UNIVERSITÀ DEGLI STUDI DI MESSINA
DIPARTIMENTO DI SCIENZE CHIMICHE, BIOLOGICHE, FARMACEUTICHE ED AMBIENTALI

DOTTORATO DI RICERCA IN SCIENZE CHIMICHE
XXXV CICLO (CHIM/01)

Exploring metal ion sequestering abilities of carnosine and carnosine derivatives in aqueous solutions for analytical applications

Chiara Abate

Supervisor
Prof.ssa Claudia Foti

Coordinator
Prof.ssa Concetta De Stefano

Academic year 2021/2022

A Stefano,
"cromoforo" della mia vita.
Alla mia famiglia,
baricentro della mia vita.
A mia mamma,
a cui devo la (mia) vita.

Correva l'anno 2020,
e tutti noi parenti,
attendenti,
il più fervente degli avvenimenti.

Correva il mio primo anno di Dottorato,
provato,
sfregiato,
da un evento indesiderato.
Dal giorno del tuo trapasso,
ogni mio passo,
ha rispettato la forma
della tua orma,
per me, radiosa
e, sempre, preziosa.
Come la tua nobile Fermezza
e la tua salda compostezza
hanno reso Te, e quel tempo trascorso con Te, una ricchezza!
Questa è la mia attuale consapevolezza
e quanto vorrei, oggi, una tua carezza!
Eri un uomo tutto d'un pezzo
e la rima era il tuo vezzo,
che hai lasciato, in eredità, ad una scarsa poetessa,
che non ha mantenuto la promessa,
ma spera di aver vinto la scommessa!

...senza troppe parole,
altro non sono che un girasole,
che, cerca e, bramosamente, vuole,
Ciccino, il Suo intramontabile Sole!

Table of Contents

Aim of the work

L-carnosine is drawn attention as a bioactive dipeptide and has been extensively studied during the last years for its promising benefits for human health [1] and employed in several research fields, such as medicine, cosmetics, nutraceuticals and food additives [2, 3]. Albeit there is no clear evidence in the literature on the specific physiological roles and mechanisms of action of carnosine, its bioactivity seems to be strictly dependent on its own metal ion coordination ability [4]. The antioxidant effect of carnosine could also be attributed to its high hydrophilicity and enhanced by its chelating properties, as it interacts with most bivalent and transition metal cations, such as Mn^{2+}, Fe^{2+}, Co^{2+}, Ni^{2+}, Cu^{2+}, Zn^{2+}, Ru^{2+} and Cd^{2+}[5-7]. Advantageously, carnosine is also a heavy metal chelator [3, 8-10]. Therefore, this thesis focuses on this ambiguous dipeptide highlighting and exploiting its chelating abilities toward metal cations, with the express purpose of using this property for analytical applications.

However, it is well known that knowledge of the total metal concentration does not sufficiently explain the effect or impact of an element in a multicomponent system and, on the other hand, a speciation study performed on a ligand, as carnosine, aims to define the different forms under which it is present in natural systems.

The starting point was an in-depth speciation study on carnosine in NaCl aqueous solutions. The study was carried out under different conditions of ionic strength ($0.15 \leq I/mol\ L^{-1} \leq 1$) and temperature ($288.15 \leq T/K \leq 310.15$) by potentiometry, UV-Vis spectrophotometry and ^1H NMR spectroscopy. Experimental data and literature ones were combined to obtain a stanch speciation model and trustworthy protonation equilibria values. In addition, structural information and fragmentation pathways of carnosine were explored by Matrix Assisted Laser Desorption

1

Ionization Mass Spectrometry (MALDI MS) and tandem Mass Spectrometry (MS/MS) techniques. Quantum-mechanical calculations were also performed to appreciate the protonation capabilities of functional groups (Chapter 3).

Once the acid-base properties of the dipeptide were defined, thermodynamic interactions parameters with bivalent metal cations (M^{2+}) were investigated, together with their dependence on ionic strength and temperature. For this purpose, a potentiometric study was performed on Ca^{2+}, Mg^{2+}, Mn^{2+}, Cu^{2+}, Zn^{2+}, Cd^{2+}, Hg^{2+} and Pb^{2+}-carnosine systems. Determination of the thermodynamic interaction parameters ($log\beta$, ΔG, ΔH, $T\Delta S$) regarding the M^{2+}-carnosine complexes was very useful for predictive purposes and allowed to simulate the distribution of the species in different real systems. Furthermore, sequestering ability of carnosine toward the metal cations under study was assessed in conditions simulating real systems, such as physiological (I = 0.15 mol L^{-1} and pH = 7.4) and seawater (I = 0.7 mol L^{-1} and pH = 8.1) solutions (Chapter 4).

During pandemic COVID-19, literature research on dipeptide electroactivity intrigued me. However, the literature data related to the voltammetric detection of carnosine are not well detailed and currently there is no clear evidence on its electrochemical mechanisms. Therefore, several tests on carnosine by voltammetry were performed during my research stay at the Department of Chemical Engineering of the *Universitat Rovira i Virgili* (Tarragona, Spain). This investigation was mainly performed using bare Screen-Printed Carbon Electrodes (SPCEs) and modifying them with suitable materials in order to improve electrochemical properties of carnosine. Although this study did not provide reproducible data neither on bare SPCEs nor on modified ones, it inputs the idea of synthetizing more electroactive carnosine derivatives and studying the sensing capability toward metal cations. Functionalization of carnosine was readily achievable as it has multiple recognition groups, such as the imidazole ring, amino

and carboxylic groups, which pose itself as an ideal candidate for modification with more versatile molecular units.

Synthetic approaches include:

1) Conjugation of carnosine (CAR) with ferrocene (Fc). This strategy is well exploited in the literature as it leads to redox-active materials with interesting electron transfer properties [11, 12] (Chapter 5).

2) Conjugation of carnosine (CAR) with Pyrene (Py). The derivative, PyCAR, has been designed as a possible fluorescent metal sensor (Chapter 5).

   Analytical approach on FcCAR and PyCAR derivatives included: *i*) Determination of the acid-base behavior by potentiometry and UV-Vis spectroscopy in NaCl aqueous solutions at I = 0.15 mol L^{-1} and T = 298.15 K. *ii*) Determination of the complexing ability toward some bivalent metal cations. FcCAR has been therefore investigated as a candidate for electrochemically recognizing metal cations and, thus, as a potential metal probe. Among the cations, FcCAR showed a greater affinity toward Hg^{2+} and Hg^{2+}-FcCAR system was used as model to study how to improve electrochemical performance. Therefore, MultiWalled Carbon NanoTubes Modified with Cyclodextrins (MWCNT-CD) dispersions were cast on Screen-Printed Carbon Electrodes (SPCEs). In this way, an amplification of the peak current signals was achieved (Chapter 5). Study on PyCAR using is still ongoing.

3) Grafting of carnosine on a commercial polyacrylamide/azlactone copolymer (AZ) and study of the resulting carnosine-based resin, AZCAR, in the Pb^{2+} removal procedures under conditions simulating natural fluids. In this case, preliminary speciation study on the Pb^{2+}-CAR system was helpful in establishing the best conditions of pH, ionic strength and temperature for adsorption experiments. The adsorption capacity of AZCAR toward Pb^{2+} was studied under conditions simulating the ionic strength and pH of various natural

waters, and the best results were obtained at pH > 7.0 and $0.001 \leq I/ \text{mol } L^{-1} \leq 0.7$ (Chapter 6).

Additional studies on further analytical applications have already been undertaken in this thesis but some aspects remain to be evaluated.

Chapter 1

Introduction

1.1 Speciation

The term "speciation" refers to the distribution of the various chemical-physical forms (isotopic composition, electronic or oxidation state, macromolecular, inorganic and organic complexes, organometallic compounds) in which an element occurs in a certain system [13]. The speciation analysis is an analytical process that allows to qualitatively identify and quantitatively determine concentration of one or more individual chemical-physical species in solution [13]. Various species of an element may differ in importance depending on the purposes for which a speciation analysis is undertaken. The distribution of an element in different inorganic compounds deeply affects its transport and bioavailability by determining its properties, such as charge, solubility and diffusion coefficient. Thus, this methodology is crucial to better understand bioavailability, toxicity and environmental impact of the chemical species of the involved elements in a system, which are affected by important parameters or conditions. pH, temperature, ionic strength, redox potential and the possible presence of organic or inorganic ligands are just some of these aspects, which can give rise to variations in the system and, thus, in the behavior of the molecule under investigation. Furthermore, the distribution of species in a system including both metal and ligand depends on their concentrations and stoichiometry, as also those of the resulting complex species.

This approach is widely used in various fields, such as toxicology, clinical and environmental chemistry, geo- and bio-chemistry [13].

Therefore, a speciation study can be crucial to assess the behavior pattern of a chelating ligand toward metal cations in natural fluids (physiological system, fresh- and seawater…) and to establish the best conditions for ligand use [14]. On the other hand, a speciation study can be pivotal to evaluate the distribution and transformation of pollutants in aquatic systems in order to improve and optimize strategies for their removal from polluted waters [15].

To perform an in-depth speciation study, different analytical techniques can be employed, including potentiometry (ISE-H^+), UV-Vis spectrophotometry, Nuclear Magnetic Resonance (NMR), voltammetry, spectrofluorimetry, calorimetry, electrophoresis, Gas Chromatography (GC), High Performance Liquid Chromatography (HPLC), and hyphenated procedures too.

Titrations with acid or base monitored by potentiometric pH measurements at different metal:ligand ratio are commonly used to determine complexes stability constants [13]. The experimental data are commonly processed by befitting computer programs, which allow to determine equilibrium constants and the best speciation model, chosen on the basis of some general criteria that are simplicity, probability, statistical parameters, formation percentages and comparison of the data with the literature ones. Knowing formations constants is important to calculate the formation percentages or the molar fractions of the species under study and to simulate the distribution of the species *vs*. pH values in certain conditions of ionic strength, ionic medium, temperature, concentration of the ligand.

1.2 L-carnosine (CAR)

L-Carnosine, referred to as CAR in this thesis (Figure 1.1), is a natural endogenous dipeptide discovered by Gulewitsch and Amiradžibi more than 100 years ago as a non-protein and nitrogen-containing compound of meat [1, 8]. This molecule was isolated from minced meat and, thus, took its name, "carnosine", from the Latin *caro*, *carnis*, namely meat [9].

It is a water-soluble (partition coefficient, $logP$ = -2.972$\pm$0.436) [16], and histidine-containing dipeptide (HCD) [17] with a molecular weight of 226.23 Da [16].
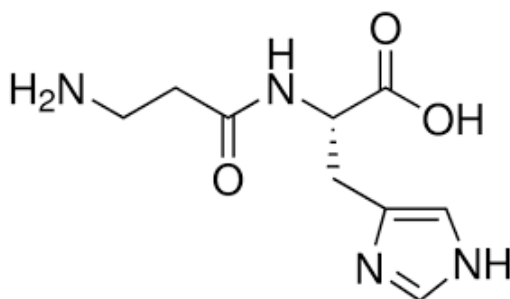
Figure 1.1. CAR structure.

CAR, (2-[(3-aminopropanoyl)amino]-3-(1H-imidazol-5-yl)propanoic acid) [4], is traditionally recognized as β-alanyl-L-histidine from the names of the precursor amino acids covalently linked [4].

It and its analogs, homocarnosine, anserine, and ophidine/balenine, are widely distributed in mammalian tissues [1]. Among them, CAR is extensively studied for its promising benefits for human health. For instance, it shows inflammation, oxidation and glycosylation resistance, and chelating properties [18], which are the focus of this thesis.

1.2.1 Distribution in the human body

Endogenic concentration of CAR is up to 20 mmol L^{-1} in skeletal muscles and brain [18], where is particularly localized in the olfactory bulb (1-2 mmol L^{-1}) [19] and cortex [1]. To a lesser degree, CAR is also present in cardiac muscles, erythrocytes, kidney, skin, eye lens, stomach and gastrointestinal tissues [1, 4, 17, 20, 21]. Interestingly, brain, skeletal and cardiac muscles show a very active oxidative metabolism [1, 22], and are the main target tissues of recently conducted in *vitro* and in *vivo* studies to evaluate the therapeutic effect of this dipeptide. Although it may be strongly marked in various chronic and cardiovascular diseases [18], the physiological role of CAR in the brain is still unclear.

Before discussing the potential of CAR, its major metabolism and transport pathways are described.

In the human body, the concentration and distribution of CAR also depend on gender, age and diet. For instance, male adults tend to have higher amounts of CAR, and the elderlies benefit from minor levels as do vegetarians [23]. Its levels, indeed, derive from dietary sources. In particular, meat, fish and dairy products are the main sources of CAR, or endogenous synthesis [24].

In skeletal muscles, kidney and brain [25], it is synthetized by the ATP-dependent *carnosine synthase* enzyme (ATPGD1, *EC 6.3.2.11*) [23] starting from β-Alanine and L-histidine amino acids. This synthesis was first described in 1950s [26, 27]. For the most part (98 %), the *carnosine synthase* plays a cytosolic activity [23] in skeletal and cardiac muscles, and in the olfactory bulb of the brain, assisted by Mg^{2+} and ATP [1, 2]. This enzyme has a C-terminal domain and was first molecularly identified by Drozak et al. [28] from chicken pectoral muscle. It was found to be a homotetramer, whose native enzyme has a molecular mass ∼ 43 kDa [2].

Both precursor amino acids have different origins in the human body; in fact, while β-Alanine is synthetized in the liver or can be obtained from the diet [1, 23], L-

histidine is not synthetized *de novo* and, thus, its origin is exogenous [1, 23]. Both can also be obtained by proteolysis of endogenous proteins and readily taken up from the circulation into the brain *via* amino acids transporters, present in the blood-brain barrier (BBB) [1, 22]. In light of this, the local CAR synthesis occurs in the brain, or rather in olfactory neurons and glial cells (particularly in mature oligodendrocytes) [1, 22]. CAR itself can cross the BBB, but most brain CAR is thought to be a product of its *de novo* synthesis localized in specific areas of the brain rather than the result of its penetration across the BBB [1, 22, 23].

In particular, brain CAR is widely used in neurons and astrocytes [1], where, in the latter, the dipeptide facilitates the export of lactate from cells, supplying metabolic support to neurons and axons through buffering protons [22]. Moreover, in astrocytes, it leads to axonal regrowth of neurons undergoing ischemic injury and, thus, functioning as a therapeutic agent for brain-related conditions [23].

CAR can also modulate the glutamatergic system through the up-regulation of glutamate transporter 1 and the reduction of glutamate levels in the central nervous system (CNS) [8, 9].

In the human body, CAR can be transported across cellular membranes by proteins belonging to the proton-coupled oligopeptide transporters (POTs) family, also named solute carrier family 15 (SLC15) [1]. These highly specific oligopeptide transporters are involved in intestinal adsorption of peptides. *PEPT1* and *PEPT2* (oligopeptide transporter 1 and 2), *PHT1* and *PHT2* (peptide/histidine transporter 1 and 2) are the mammalian members responsible for the transport of CAR and its methylated analogs. In particular, *PEPT1* plays a key role in intestinal and colonic absorption of peptides and, being a peptide/proton cotransporter, its activity is enhanced with a lower luminal/apical pH. *PEPT2* acts by transporting CAR into the brain, where it monitors the peptide trafficking and brain homeostasis [1, 23]. Analogously, it can be involved in the lungs and kidneys [23].

Regarding degradation, CAR is hydrolyzed by cytosolic non-specific dipeptidases (CNDP), named *carnosinases* (CN) or *β-Ala-His dipeptidases* [1, 29, 30], first proven and partially purified by Hanson and Smith [31] in 1949 from swine kidney. In 1968, Perry et al. [32] first described the two human hydrolytic isoforms, which belong to the M20 metalloprotease family [1, 8, 9]:

- *CN1*, or *serum carnosinase* (CN1 or CNDP1; *EC 3.4.13.20*) [1], localized in plasma, serum and brain [23, 29]. Its narrow substrate spectrum allows it to hydrolyze only histidine-containing dipeptides (HCDs) and it is mainly expressed in the liver and oligodendrocytes [1].

- *CN2*, or *tissue carnosinase* (CN2 or CNDP2; *EC 3.4.13.18*) [1] localized at the intracellular level and strongly inhibited by bestatin [29]. This has a wider substrate specificity than CN1 and exhibits ubiquitous expression in human tissues, but at very low levels in the brain [1].

These metalloproteases are activated and/or stabilized by different metals [33]. For instance, the former is probably catalyzed by two Zn^{2+} ions, and CN2 requires Mn^{2+} for its catalytic activity [1].

The greatest amount of CAR ($\geq$ 99%) is localized in skeletal muscles [23], where it has concentrations 10- to 1000-fold higher than those present in cardiac muscles, and is also found ~2-fold higher concentrations in fast-twitch fibers than in slow-twitch fibers, contributing to the physicochemical buffering of lactate, caused by exercise, and including membrane-stabilizing [34]. Its highest concentrations in skeletal muscle tissues, where CAR levels vary from 5 to 10 mmol L^{-1} in wet weight and 15-40 mmol kg^{-1} in dry weight [16], and the lack of bioavailability of CAR in serum (half-life in human serum < 5 min) [23] could be due to the presence and activity of the *carnosinase*. In fact, the latter rapidly acts, decreasing the serum levels of CAR and reducing its clinical efficiency and therapeutic uses [23]. This limitation could be overcome by joining CAR with a transporter or versatile molecule capable of protecting it from *carnosinase* degradation, or by oral

supplementation of β-Alanine [23, 29]. This, along with the orally ingested carnosine, can be practiced by athletics to increase the amino acids levels in muscles and improve performance in exercise physiology [18, 22, 23]. Indeed, since the pK_a value of the imidazole ring of CAR is close to 7.0, this moiety is particularly involved in the regulation of the hydrogen ion buffering activity [7]. As such, it acts as a more effective pH buffer than its progenitor histidine [6, 19]. This role was first proposed in 1938 by two independent groups [21]. In addition to its role as an exercise enhancer, CAR regulates calcium metabolism, decreasing lactate accumulation and optimizing energy metabolism [9, 22]. It is not only an over-the-counter food supplement to improve muscle tolerance, but CAR is also used as a component of cosmetics to exert its antioxidant and anti-aging effects [9, 35]. In fact, it upgrades mitochondrial functions, limiting systemic inflammation and oxidative stress [22, 24], and oral administration of CAR is also useful for preventing various oxidative-based disorders, including lung diseases, stroke, type-2 diabetes, cardiovascular, renal and neurodegenerative diseases [1, 36].

Despite several studies describe anti-ischemic and neuroprotective properties of carnosine, there is currently no solid evidence on its precise role in brain disorders. Therefore, possible hypotheses about the mechanisms and potential use of CAR in the prevention or management of these conditions are reported [22].

1.2.2 Physiological properties and metal ion abilities

Growing interest coming from in *vivo* and in *vitro* studies has highlighted the protective role of CAR on human diseases and aging, owing to its multimodal mechanisms of action involving several pathways and its multiple biological functions, including anti-oxidation, anti-aggregant, anti-inflammatory, anti-glycation, anti-carbonyl, anti-stress and anti-aging effects [1, 8-10, 25, 36].

Nevertheless, despite several studies describing the various health effects of CAR, its endogenous functions and molecular mechanisms of action are not fully identified [4, 36], and little in *vivo* evidence occurs in humans [37]. However, in *vitro* experiments are significant because allow an in-depth study of different mechanisms of action and give importance to specific phenomena of a molecule, which are difficult to reproduce in *vivo* [9]. For instance, in *vitro* studies reported that CAR selectivity can restrict the proliferating process of carcinoma cells [38].

An exponential growth of literature data has also confirmed that CAR can prevent and suppress oxidative stress [25, 36], which is related to more than 200 disorders and diseases [1, 24]. The main instances are atherosclerosis, hepatocellular and renal tubular epithelial cells injury, rheumatoid arthritis and myelosuppression [9, 24], but it is also studied in the prevention and treatment of numerous chronic non-communicable diseases, such as lung, renal and cardiac disorders, diabetes and its vascular developments, cancer, schizophrenia, osteoporosis and cataracts [10, 23, 36]. Interestingly, CAR is potentially employed in brain-related disorders, such as autism, Alzheimer's and Parkinson's diseases [1, 36, 39]. In fact, CAR could activate brain functions thanks to its ability to cross the blood-brain barrier (BBB), reach the brain and activate glial cells. On the other hand, in Parkinson's disease, CAR could act in the erythrocytes limiting the possible accumulation and misfolding of protein aggregates enriched of α-synuclein (ASN). This could be due to antiglycation properties of the dipeptide [23], which is also able to detoxify catecholaldehydes involved in neurodegenerative diseases, as well as cardiac complications from ischemia and diabetes [36].

The therapeutic use of CAR as an anti-inflammatory, antioxidant, anti-glycation and anti-carbonyl molecule could also be attributable to its indirect action in the activation of the Nrf2 transcription factor, which plays a key role in the transcription of more than 200 genes, having an antioxidant response element

(ARE) in the promoter region [1, 36]. The Nrf2 activation could also elucidate the anti-aging effect of carnosine, as well as its ability to inhibit the formation of anti-advanced glycation end products (AGEs), in particular derived from glyoxal (GO) and methylglyoxal (MGO). These α-dicarbonyls are the products of lipid peroxidation, glycolytic oxidation and protein glycation and, along with AGEs, are the mediators of several chronic diseases, such as diabetes, obesity, arthritis, cancer, atherosclerosis, pulmonary fibrosis, neurodegenerative diseases, aging and subsequent wrinkles [36].

The significant epithelializing and wound healing properties of CAR make it an effective and preventing anti-aging compound [4, 20]. In fact, it is used in age-related skin creams or cosmetic formulations, to avoid or prevent wrinkle forming [29, 40].

Focusing on the direct antioxidant activity of CAR, its role as carbonyl quencher, scavenger of reactive oxygen species (ROS) and reactive nitrogen species (RNS) is known in the literature [8, 9, 23, 36].

The term "ROS" refers to a wide and reactive variety of molecules and free radicals, endowed with massive harmful effects, physiologically derived from the metabolism of molecular oxygen [41]. CAR seems to be able to quench free radicals, hydroxyl radicals and superoxides [4, 17, 21], as well as single molecular oxygen [25], hypochlorite anion and hypochlorous acid (HOCl) [1]. All of these species are toxic and can modify proteins. In particular, HOCl deriving from H_2O_2 and Cl^- in mammalian cells, can react rapidly with the imidazole ring of CAR. This results in an imidazole chloramine, which limits its oxidative activity of HOCl [1].

CAR captures aldehydes, from the oxidation of lipids and sugars by a multistep mechanism, which involves the amino group and the imidazole ring, to give rise to CAR-Reactive Carbonyl Species (RCS) covalent adducts and their metabolites [1, 23, 36]. CAR somehow reacts with β-malondialdehyde (MDA) by the formation of the respective N-propenal adduct *via* Michael addition [36]. A recently detailed

progress on the direct antioxidant action of CAR was experimentally discovered by Ihara et al. [42]. A carnosine oxidation product, that is 2-oxo-carnosine, was distinguished in ex-*vivo* conditions, or better in tissue homogenates and in H_2O_2 exposed cells. This is produced by the formation of a reaction of histidyl imidazole and subsequent addition of molecular oxygen [36], and is able to remove the lipid oxidation byproducts [1, 25]. Therefore, particular attention is paid to 2-oxo-carnosine, as it shows higher antioxidant activity than other common antioxidants, such as glutathione and ascorbate [36].

In addition to the prevention of the above-mentioned lipid peroxidation of membrane lipids, CAR is also involved in the maintenance of cell membrane structure and functions.

The high water solubility of CAR makes itself an excellent antioxidant defense system in the cytosolic media, where significant concentrations of oxidation mediators, such as transition metals and ROS, occur [24]. There, CAR also works as a pH buffer, maintaining pH-balance and homeostasis, and as a chelator of divalent metal cations, in particular regulating amounts of transition metals and modulating immune cells, such as macrophages and microglia, in biological systems and tissues [8, 17, 25, 43].

Finally, CAR is progressively arousing interest for its relevant anti-glycant and antioxidant properties, along with its intriguing potential anti-tumor and anti-apoptotic functions [29].

The bioactivities of CAR are strictly related to coordination and complexation with metal cations [20]. For instance, the anti-carbonyl properties of the dipeptide could be due to its own metal chelating abilities [36]. In fact, CAR is composed of three ionizable groups: the carboxylic group, the amino segment of the β-alanine residue and two nitrogen atoms of the imidazole ring. At physiological pH (7.42), carnosine occurs mainly in a zwitterionic form, due to the presence of the carboxyl

and amino groups of β-alanine in their ionized states [7]. In this condition, Torreggiani et al. [33], by means of Raman spectroscopy, described the existence of two tautomeric forms (Figure 1.2) in equilibrium with each other, even if *Tautomer I* is energetically more stable and, therefore, the main species (75%) at pH 7.0 and 9.0 [7].

Tautomer I   *Tautomer II*
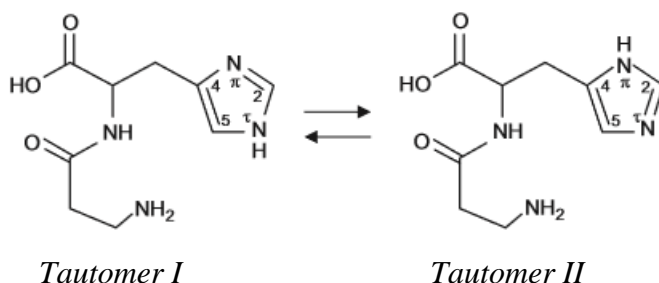
Figure 1.2. Tautomeric equilibrium of the imidazole ring of CAR [7].

The tautomeric equilibrium, described by Boldyrev et al. [7], is affected by metal ion chelation, just as the physiological behavior and protecting properties of CAR against oxidative stress [16], also depend on its metal complexation ability [4, 7]. On the other hand, it is known that living organisms, as also humans, need low amounts of iron, cobalt, copper, manganese, molybdenum, nickel, zinc, etc [44]. CAR is a polydentate ligand, having five potential metal coordinating sites, namely the two imidazole nitrogens, a carboxylate group, a peptide bound and a terminal amino group [4]. CAR coordinates numerous divalent cations, such as Cu^{2+}, Zn^{2+}, Co^{2+}, Ni^{2+}, Mn^{2+}, Ru^{2+}, Cd^{2+}, Mg^{2+}, and Ca^{2+}.The first seven metal cations, belonging to the d-block of the periodic table and ranging from biochemically active iron, copper, zinc up to the unsafe mercury [45], can exist in variable oxidation states. However, greater evidence on the chelating capacity of CAR toward bivalent metal cations (M^{2+}) is proven in the literature, and the resulting configuration of complexes depends on the size of the metal cation, the ligand:metal ratios and the ionic strength of the supporting solution [4].

Interestingly, interactions between Cu^{2+} and CAR have been studied in the last 30 years, as the dipeptide related to the regulation of anaerobic glycolysis in skeletal muscle by coordination with copper [33]. The Cu^{2+}-CAR complex could also be related to *carnosinemia*, involving a carnosinase deficiency and an excess of CAR in the urine (*carnosinuria*) [8], and Wilson's disease (WD). Both disorders provoke an accumulation of the copper in different tissues of liver, kidney and brain, giving rise to similar neurological disorders [33]. CAR was found to be able to coordinate Zn^{2+} as a quadridentate ligand, monitoring its ability in the brain and performing a neuroprotective role on Cu^{2+}- and Zn^{2+}- mediated neurotoxicity [22, 39]. In fact, CAR coordinates Cu^{2+} and Zn^{2+} and regulates the synaptic impulse [1]. The Zn^{2+}-CAR complex (*Polaprezinc* or *PepZin GI*) [10] is the first zinc-related drug approved in Japan [46], and has already been authorized by the Food and Drug Administration (FDA) [47]. It displays anti-inflammatory effect in the colon and is widely used to protect the mucosa from ulceration and to prevent *Helicobacter pylory*-related gastritis [1, 35]. It also performs a positive effect on bone metabolism and in the prevention of diseases characterized by oxidative stress and/or neurodegenerative alterations, such as diabetes, neuropathies, depression, cerebral ischemia and Alzheimer's disease (AD) [10].

Ru^{2+}-CAR could also be a suitable candidate in pharmacological applications and, thus, it was thought in drug design [4]. However, hydrophilic molecules, such as carnosine, penetrate deeper cutaneous tissues poorly [16]. For this purpose, a gel formulation based on Mg^{2+}-CAR complex species was prepared in order to improve skin bioavailability, also acting as a multifunctional agent. Among the various roles, antioxidant activity, buffering enzyme and sarcoplasmic reticulum calcium (Ca^{2+}) regulation are included [16].

Therefore, understanding the speciation of the complex species can be helpful in predicting the physiological roles of this dipeptide. For these reasons, this work has mainly focused on an overall study of the thermodynamic parameters.

Chapter 2

Experimental Section

Analytical techniques used in this research are described in the following order:

1) procedures employed to prepare each reagent,

2) analytical techniques used to perform experimental measurements,

3) computer programs for processing experimental data.

2.1 Chemicals

L-carnosine (CAR) was purchased from Sigma Aldrich and its solutions were prepared by weighing the corresponding product without further purification. Its purity was checked potentiometrically by alkalimetric titrations (always $\geq 99.0\%$), and the effective purity was taken into account in the calculations of the ligand concentration. In addition to CAR, L-Histidine (Sigma Aldrich, $\geq 98\%$) was also electrochemically tested.

Two CAR derivatives, ferrocenyl-carnosine (FcCAR) and pyrenyl-carnosine (PyCAR), were synthetized. The synthetic approach is described in Chapter 5. Stock solutions of the ligands were prepared in ultrapure water (conductivity < 0.1 μS cm^{-1}) or in high purity water (18 MΩ cm^{-1}), or in KCl (0.1 mol L^{-1}) solutions.

All metal compounds employed for the investigation are summarized in Table 2.1. Calcium, magnesium, copper, manganese, zinc, cadmium and lead solutions were standardized by titrations with EDTA (Ethylenediaminetetraacetic acid disodium salt, BioUltra, $\geq 99\%$, Sigma Aldrich) standard solution, using NET (Eriochrome

Black T) as indicator, except for the standardization of Cu^{2+}. In this case, murexide is used as indicator.

Buffer preparation procedures are described in Subparagraph 2.1.1.

Sodium hydroxide and hydrochloric acid solutions were prepared from concentrated Fluka ampoules and standardized using potassium biphthalate and sodium carbonate, respectively, previously dried in an oven at 383.15 K for at least one hour. Sodium hydroxide solutions were often prepared and always stored in dark bottles and preserved by CO_2 using soda lime traps. Sodium chloride and potassium nitrate solutions were prepared by weighing the corresponding salts (Sigma Aldrich, and BDH Chemicals, puriss.), earlier dried in an oven at 383.15 K. Potassium chloride solutions were obtained by weighing different respective salts (Scharlau, extra pure, BDH Chemicals and Sigma Aldrich, $\geq$ 99.5%). Ethanol (EtOH) absolute (Scharlau) and ammonia solution (Fischer) were also used.

Sulfuric acid, H_2SO_4, (> 95.0-98.0%) EPR, potassium ferricyanide (III), $K_3Fe(CN)_6$, powder, < 10 micron, 99+%, ferrocenecarboxylic acid (> 96.0%), N, N- Dimethylformamide (DMF) anhydrous, 99.8%, and diethyl ether anhydrous, $\geq$ 99.7% were purchased from Sigma Aldrich (Spain) and used as received. Also tetrahydrofuran, THF, 99.8%, extra dry, (Acroseal, Acros Organics), N, N'-Dycyclohexylcarbodiimide, DCC, puriss. $\geq$ 99.0% (Fluka Analytical), sodium hydrogen-carbonate, $NaHCO_3$, (Panreac) and acetone, ACS BASIC (Scharlau) were used as received. All chemicals and reagents were analytical grade and used without further purification.

Table 2.1. List of metal compounds under investigation and relative information.

Metal compounds	Formula	Purity	Sellers	Preparation	Analytical purposes
Calcium chloride dihydrate	$CaCl_2\,2H_2O$	$\geq 99.0\%$	Fluka	a)	b), c), d)
Magnesium chloride hexahydrate	$MgCl_2\,6H_2O$	$\geq 99.0\%$	Fluka	a)	b), d)
Manganese chloride tetrahydrate	$MnCl_2\,4H_2O$	$\geq 99.0\%$	Sigma Aldrich	a)	b), c), e)
Cupper chloride dihydrate	$CuCl_2\,2H_2O$	$\geq 99.0\%$	Fluka	a)	b), c), e)
Zinc chloride	$ZnCl_2$	$\geq 99.0\%$	Sigma Aldrich	a)	b), c), e), f)
Cadmium chloride	$CdCl_2$	$\geq 99.0\%$	Fluka	a)	b), f)
Mercury chloride	$HgCl_2$	$\geq 99.5\%$	Riedel-de Haën	a), g), h), i)	b), f), j)
Lead nitrate	$PbNO_3$	$\geq 99.0\%$	Fluka	a)	b), f)
Lead nitrate standard solution	$PbNO_3$	-	BDH Chemicals	h)	j)
Lead acetate trihydrate	$Pb(CH_3COO)_2\,3H_2O$	$\geq 99.0\%$	Sigma Aldrich	g), h)	j)

a) in water (conductivity $< 0.1\ \mu S\ cm^{-1}$). b) potentiometry. c) ^1H NMR spectroscopy. d) computational methods. e) Mass Spectrometry (MS). f) UV-Vis spectrophotometry. g) Voltammetry. h) in KCl ($0.1\ mol\ L^{-1}$). i) in MOPS buffer. j) weighed with the aid of a gas mask.

2.1.1 Preparation of buffers

Compounds used for the 3-(N-Morpholino)propanesulfonic acid, 4-Morpholinepropanesulfonic acid (MOPS) buffer procedure are summarized in Table 2.2. MOPS solution (pH $\cong$ 7.0) was prepared in double distilled water (18.2 MΩ cm^{-1}), obtained from a Milli-Q® system (Millipore, Madrid, Spain) and the pH was adjusted by adding sodium hydroxide solution (0.1 mol L^{-1}).

Compounds used for the preparation of Phosphate Buffer (PB) are listed in Table 2.3. PB solution (pH $\cong$ 7) was prepared in high purity water (18 MΩ cm^{-1}).

Table 2.2. List of compounds required to prepare MOPS buffer (pH = 7).

Compounds	Amount	Purity	Sellers
3-(N-Morpholino)propanesulfonic acid, 4-Morpholinepropanesulfonic acid (MOPS)	41.86 g	$\geq$ 99.5%	Sigma Aldrich
sodium acetate anhydrous (CH$_3$COONa)	4.1 g	extra pure	Scharlau
EDTA dehydrate	3.72 g	extra pure	Scharlau

Table 2.3. List of compounds required to prepare PB buffer (pH = 7).

Compounds	Amount	Purity	Sellers
Sodium phosphate dibasic (Na$_2$HPO$_4$ 12H$_2$O)	14.61 g	$\geq$ 99.0%	Sigma Aldrich
Potassium phosphate monobasic (KH$_2$PO$_4$)	3.52 g	$\geq$ 99.5%	Fluka
KCl	5 g	extra pure	Sigma Aldrich

To improve electrochemical performance of CAR, first of all, more than once the polished Screen-Printed Carbon Electrodes (SPCEs) were modified with suitable and different homogeneous dispersions. Preparation methods of which are described in the following paragraph, according to the order of use. On the other hand, SPCE surfaces were also modified with MultiWalled Carbon NanoTubes modified with Cyclodextrins (MWCNT-CD). The synthetic approach and use of MWCNT-CD are described in Chapter 5.

2.1.2 Preparation of homogeneous dispersions

In the voltammetric analysis of CAR, preparation procedures of the homogeneous dispersions are described in the order of use:

i)   Nafion solution,

ii)   Carbon Nano-Onions (CNO) in DMF dispersion.

i)   **Nafion solution**

Nafion is a sulfonated tetrafluoroethylene based fluoropolymer-copolymer. Nafion™ Perfluorinated resin solution, 5 wt% in lower aliphatic alcohols and water, containing 15-20% of water, 2-propanol and n-propanol was purchased by Sigma Aldrich. An aliquot (1 mL) of Nafion solution was dissolved in 5 mL of EtOH, in order to prepare a homogeneous Nafion (0.3 %) in EtOH:H_2O (5:1 v/v) solution. The latter was obtained to create a sensing platform for CAR molecule, or rather to produce a surface chemistry based on electropolymerization of the positive amine groups of CAR, in acid environment, assisted by the synergistic effect of a previously negative Nafion layer deposited on SPCE [48].

ii)   **CNO dispersion**

Carbon Nano-Onions (CNO) belong to the least studied family of carbon allotropes, having a hollow fullerene core surrounded by spherical or quasi-spherical concentric layers of graphene. The increasing diameters of the graphene layers are similar to onions, from which CNO take the name [49]. They occur in 2-50 nm diameter particles and are produced through the arc discharge of graphite electrodes under deionized water or during the thermal annealing of nanodiamonds in an inert atmosphere [49, 50]. According to the last procedure, the CNO used in this work were previously prepared by Fragoso et al. [51, 52].

In this work, a homogeneous dispersion of CNO in DMF (2 mg mL^{-1}) was prepared using an ultrasonic-bath for 60 min.

2.2 Potentiometry

2.2.1 General aspects [53]

Potentiometry involves all the robust electroanalytical techniques that allow to measure the electromotive force (e.m.f.) in an electrochemical cell in zero current conditions. The potential variations, in the absence of current, can be measured by an instrument, *i.e*., a potentiometer, equipped with two different electrodes diving in the electrochemical cell:

- a *reference electrode,* whose potential is constant, in the fixed ionic strength and temperature conditions, and independent of the composition of the solution containing the analyte. Among them, the most common are:
  1) Calomel reference electrode ($Hg/Hg_2Cl_2/KCl(x)$),
  2) Silver-silver chloride reference electrode (Ag/AgCl).
- an *indicator electrode*, also known as *working electrode*, whose potential depends exclusively on the activity of a single ion. In addition, it must respond quickly and reproducibly to individual variations in the ion activity of the analyte. Among the indicator electrodes can be distinguished:
  1) Metal electrodes,
  2) Ion-selective electrodes.

The last are separated from the sample solution by a membrane, which is selective for the analyte under study. In this thesis, the specific electrode for H^+ ions, ISE-H^+, also called glass electrode, was used for the determination of proton exchange in acid-base and complexation equilibria. In particular, a glass electrode like the one shown in Figure 2.1 was employed in the potentiometric measurements. It consists of a thin pH-sensitive membrane welded to the bottom of a glass or polymer tube, plunged in a diluted solution of hydrochloric acid or in a small amount of buffer, with a known concentration of H^+ ions (0.1 mol L^{-1}), and saturated with AgCl. A silver wire is also dived in this same cylindrical probe and acts as an internal reference electrode (Ag/AgCl). The cell for potentiometric

measurements also consists of a further outer reference electrode (Ag/AgCl), which gets in touch with the external solution under study.
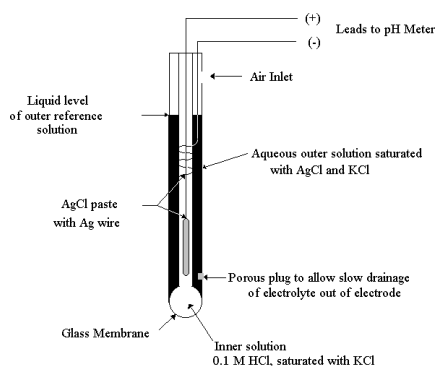
Figure 2.1. A glass electrode.

During potentiometric measurements, a potential difference is observed when a change in the proton activity occurs in the membrane interface between the inner and outer solutions. Since the H^+ ion activity is constant in the electrode, the H^+ variation only depends on the proton activity of the outer solution under study and can be described by the following Nernst equation:

$$E = E^0 - s\ log\ \frac{a_{H^+}(int)}{a_{H^+}(ext)} \tag{2.1}$$

where E is the measured potential and E^0 the formal potential. s represents the nernstian slope up to pH $\approx$ 11, which is 2.303RT/nF and equal to 59.16 and 29.58 mV for monovalent and divalent ions, respectively, at $T = 298.15$ K.

In addition to the standard electrode potential, the formal potential, E^0, is a sum of different contributions, such as the asymmetry potential and junction potential. The first is given by small differences between the two glass membrane surfaces due to some their abrasions, caused by use or determined at the time of

manufacture [54]. However, this non-ideal behavior can be worked out by calibrating the electrode with a titration of strong base or acid standard solutions. The junction potential instead develops at the interface between the salt bridge and each half-cell, due to the certain mobility of ions in solution and their different diffusion on one side of the junction surface, providing a charge separation and, therefore, a potential [54, 55]. This issue can also be solved by employing a double junction electrode as reference, in which the salt bridge owns the same ionic medium as the analyte solution.

2.2.2 Potentiometric equipment and procedure

Potentiometric measurements are performed as titrations in aqueous solution using a Metrohm model 809 Titrando potentiometer, equipped with an Orion-Ross 8102 combined glass electrode and a Metrohm Dosino 800 automatic dispenser. The titration system is automated and interconnected to a PC, which acquires experimental data and tracks the e.m.f. stability and titrant delivery by employing a specific software, named Metrohm TiAMO 2.2. In addition, this program software allows to control some important parameters, required for an accurate acquisition of experimental data, such as the time range between two readings, the maximum and minimum titrant increment and maximum number of readings and cycles necessary for amount to stability of the e.m.f. readings. The estimated error of the potentiometric system is ± 0.15 mV per e.m.f. and ± 0.002 mL for titrant volume readings, respectively.

All potentiometric measurements were carried out in NaCl aqueous solution, using thermostated glass jacket cells, at T = 298.15 $\pm$0.1 K (and also at T = 288.1 and 310.1 $\pm$0.1 K for M^{2+}-CAR systems). In addition to monitoring the temperature, using a thermometer, solutions were simultaneously kept under magnetic stirring,

to ensure continuous homogeneity of the systems, and under nitrogen bubbling to avoid possible interferences of O_2 and CO_2 inside.

A schematic instrumental apparatus is shown in Figure 2.2.
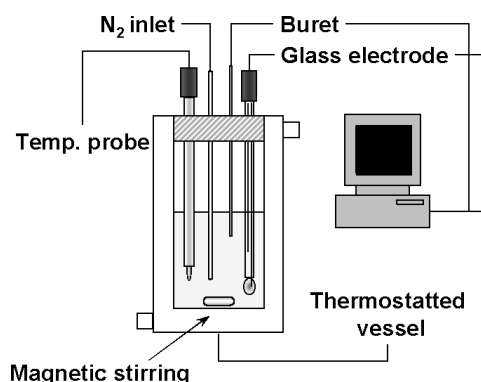
Figure 2.2. Schematization of a potentiometric apparatus.

Experimental potentiometric conditions are reported in Table 2.4. In the study of protonation equilibria, volumes of 25 mL containing CAR and the ionic medium, to reach the prefixed ionic strength values, were titrated with standard NaOH solutions over a wide pH range (2-10.5). Analogously, solutions of 10 mL, separately containing two synthetic CAR analogs, ferrocenyl-carnosine (FcCAR) and pyrenyl-carnosine (PyCAR) and the ionic medium, were titrated with standard NaOH solutions. The use of HCl was essential to fully protonate the three ligands under study. As highlighted in Table 2.4, use of EtOH (4%) was instead necessary to completely dissolve the PyCAR in aqueous solution.

In the study of the metal (M^{2+})-CAR interactions, solutions of 25 mL containing different amounts of ligand and metal cation, hydrochloric acid and the ionic medium were titrated with standard NaOH solutions.

The Hg^{2+}- and Pb^{2+}-FcCAR interactions was investigated by titrating with standard NaOH solutions of 10 mL containing different amounts of the ligand and metal

cation, HCl and the ionic medium. In detail, the experimental conditions are reported in Table 2.5.

For each experiment, independent titrations of HCl with standard NaOH solutions were carried out to determine the standard electrode potential, E^0, and pK_w values under the same experimental conditions of ionic strength and temperature as the systems under study.

Table 2.4. Experimental potentiometric conditions for the acid-base properties of CAR, FcCAR and PyCAR in NaCl ($2.5 \leq pH \leq 10.5$).

Ligand species	C_L [a)	C_{H^+} [a)	I [b)	T [c)	n [d)
CAR	1-3	5-8	0.1-1	298.15	23
	1-3	5-8	0.15	288.15	4
	1-3	5-8	0.15	310.15	4
FcCAR	1-2	10-14	0.15	298.15	4
PyCAR[e)	0.5	12	0.15	298.15	4

[a) in mmol L^{-1}. [b) in mol L^{-1}. [c) in K. [d) number of titrations. [e) dissolved in EtOH (4%) aqueous solution.

Table 2.5. Experimental potentiometric conditions for M^{2+}-ligand systems in NaCl aqueous solutions.

Systems	C_M [a]	C_L [a]	C_M/C_L	C_{H^+} [a]	pH	I [b]	T [c]	n [d]
Ca^{2+}-CAR	0.6-2	0.6-4	0.3-2	8-10	2.2-10.5	0.1-1	298.15	20
Ca^{2+}-CAR	1-2	1-3	0.3-1	8	2.3-10.5	0.1	288.15	6
Ca^{2+}-CAR	1-3	1-3	0.3-1	8-12	2.2-10.2	0.1	310.15	10
Mg^{2+}-CAR	1-2	1-4	0.3-1	8-10	2.2-10.5	0.1-1	298.15	22
Mg^{2+}-CAR	1-2	1-3	0.3-1	8	2.3-10.0	0.1	288.15	4
Mg^{2+}-CAR	1-5	1-5	0.3-1	8-12	2.3-10.0	0.1	310.15	7
Mn^{2+}-CAR	0.6-4	1-4	0.5-1	6-10	2.0-9.5	0.1-1	298.15	20
Mn^{2+}-CAR	1-2	1-4	0.4-1	6-8	2.0-9.5.0	0.1	288.15	4
Mn^{2+}-CAR	1-2	1-4	0.5-1	6-8	2.0-9.5	0.1	310.15	8
Cu^{2+}-CAR	0.5-2	1-4	0.3-1	4-12	2.2-10.5	0.1-1	298.15	17
Cu^{2+}-CAR	1-2	1-4	0.5-1	4	2.5-10.5	0.1	288.15	4
Cu^{2+}-CAR	1-2	1-4	0.5-2	4-10	2.5-10.5	0.1	310.15	9
Zn^{2+}-CAR	1-2	1-4	0.3-1	5-12	2.0-9.5	0.1-1	298.15	17
Zn^{2+}-CAR	1-2	1-3	0.3-1	8-12	2.3-9.2	0.1	288.15	7
Zn^{2+}-CAR	1-2	1-3	0.3-1	8-12	2.2-9.0	0.1	310.15	5
Hg^{2+}-CAR	1-2	1-4	0.3-1	5-12	2.0-9.5	0.1-1	298.15	22
Hg^{2+}-CAR	1-2	1-4	0.5-1	5-8	2.5-9.5	0.1	288.15	4
Hg^{2+}-CAR	1-2	1-4	0.5-1	6-10	2.0-9.5	0.1	310.15	6
Hg^{2+}-FcCAR	1	1-2	0.5-1	14	2.0-9.5	0.1	298.15	4
Pb^{2+}-CAR	0.5-2	1-4	0.3-1	5-12	2.0-9.5	0.1-1	298.15	24
Pb^{2+}-CAR	0.5-2	1-4	0.3-1	10-12	2.0-9.5	0.1	288.15	6
Pb^{2+}-CAR	0.5-2	1-4	0.3-1	10-12	2.0-9.5	0.1	310.15	6
Pb^{2+}-FcCAR	1	1-2	0.5-1	14	2.0-9.5	0.1	298.15	3
Cd^{2+}-CAR	0.5-3	1-6	0.5-1	6-12	2.3-9.5	0.1-1	298.15	21
Cd^{2+}-CAR	1-2	1-4	0.5-1	6-8	2.0-9.5	0.1	288.15	4
Cd^{2+}-CAR	1-2	1-4	0.5-1	6-8	2.0-9.5	0.1	310.15	4

[a] in mmol L^{-1}. [b] in mol L^{-1}. [c] in K. [d] number of titrations.

2.3 UV-Vis spectrophotometry

2.3.1 General aspects [53]

UV-Vis spectrophotometry is a molecular adsorption technique, widely used for the analysis of equilibria in solution. Spectrophotometric methods are based on the interactions between an incident electromagnetic radiation and matter and, in particular, on the absorption phenomena which occur between incident luminous radiations, included in the visible (Vis) (380 - 780 nm) and near ultraviolet (UV) (200 - 380 nm) spectral range, and the matter. Electromagnetic radiation, by its very dual nature, can be described as a photon or particle and, on the other hand, as a wave, whose electric and magnetic fields are perpendicular to each other and oscillating in the direction of propagation of the radiation. When an UV-Vis photon, having the same energy amount as the energy gap (ΔE) between the ground and the excited state, is absorbed by atoms or molecules, there is an increase in the internal energy of the absorbing species. On one hand, this involves vibrational, rotational and electronic transitions, from the ground state to those of higher energy and, on the other hand, it gives rise to changes in the distribution of the electron cloud of the molecule. The allowed electronic transitions ($\sigma \rightarrow \sigma^*, \pi \rightarrow \pi^*, \pi \rightarrow \sigma^*, n \rightarrow \pi^*, n \rightarrow \sigma^*$) are typically given by transition metals and molecules, endowed with double or triple bounds, or better known as "chromophores". Therefore, the UV-Vis spectrophotometric technique allows to measure the intensity of the absorbed radiation, expressed graphically in the ordinate of a spectrum as a function of the wavelength, and to obtain information on the analyte starting from quali- and quantitative analysis. The resulting spectrum is, then, compared with those present in the literature or in specific databases for the purposes of qualitative analysis. Regarding the quantitative aspect, the determination of the analyte is carried out on the basis of Lambert-Beer law, an empirical correlation among the intensity of the absorbed radiation, the concentration of the analyte and the thickness of the medium crossed. In particular,

an incident luminous radiation strikes the matter and, at the same time, undergoes an attenuation of its beam, due to the adsorption by an analyte solution, which is expressed as *Transmittance* (T):

$$T = \frac{I_1}{I_0} \qquad (2.2)$$

where I_0 and I_1 are respectively the intensity of the incident radiation and that transmitted by the solution. In more detail, the absorbed radiation is most commonly measured as *Absorbance* (A).

T and A parameters are correlated by the following relation:

$$A = log\,\frac{1}{T} = log\,\frac{I_1}{I_0} \qquad (2.3)$$

Knowing A, the concentration of the absorbent species is determined by the following Lambert-Beer law, which also correlates them.

$$A = \varepsilon b c \qquad (2.4)$$

where ε is the molar extinction coefficient (in L mol^{-1} cm^{-1}) and depends on the wavelength of the absorbed radiation, the solvent and the chemical species involved in the absorption. b is the thickness of the cell or optical path of the solution (in cm). It is usually 1 cm. c is the concentration of the absorbent species (mol L^{-1}). However, the relation (2.4) is a limit law, applied to dilute solutions (c $\leq$ 0.01mol L^{-1}).

Spectrophotometric measurements were mainly performed in the form of titrations, using an analyte chromophore, as described in the following experimental paragraph.

2.3.2 Spectrophotometric equipment and procedure

Spectrophotometric measurements were recorded in aqueous solutions using a Varian Cary 50 UV-Vis spectrophotometer, equipped with an optic fiber probe, with a fixed 1 cm path length, capable of scanning the area of the UV-Vis electromagnetic spectrum, and a Metrohm 750 combined glass electrode, for recording the pH values. The optical fiber is an appropriate tube of glass or siliceous materials for the transmission of light pulses and equipped with a cable for use over long distances. The light propagates inside it by total internal reflection and, thus, for this to happen, the transmitting fiber must be coated with a suitable material with a lower refractive index than that of the material with which the fiber was built. The spectrophotometer is connected to a PC, which acquires the experimental data (Absorbance *vs*. wavelength) using Varian Cary WinUV (model 3.00) software. The latter also controls some of the main parameters for spectrophotometric measurements, such as the previously set wavelength range, scan speed and baseline correction.

Similarly to the potentiometric measurements, the spectrophotometric ones were carried out as titrations in NaCl aqueous solutions using thermostated glass jacket cells, at T = 298.15 $\pm$0.1 K, under magnetic stirring and nitrogen bubbling. An instrumental apparatus similar to the one shown in Figure 2.2, and previously described in paragraph 2.2.2., was used for the UV-Vis spectrophotometric titrations, which were performed in a wide range of selected wavelengths ($200 \leq \lambda \leq 400$ nm) in order to detect the absorption wavelength range of CAR, FcCAR and PyCar and their molar absorption coefficients, respectively. For this purpose, 25 mL of solutions containing CAR, or FcCAR, or PyCAR, HCl and NaCl (I = 0.15 mol L^{-1}) were titrated with standard NaOH over a wide pH range (2-10). The experimental conditions for the acid-base behavior of CAR, and its synthetic analog, are summarized in Table 2.6. For the determination of the formation constants of the complex species (M^{2+} -FcCAR or -PyCAR systems), titrations

were carried out on 20 mL of solutions containing the respective ligand, metal, HCl and, the supporting electrolyte, NaCl ($I = 0.15$ mol L^{-1}) in the following selected wavelength range ($200 \leq \lambda \leq 400$ nm).

The experimental conditions, such as metal and ligand concentrations, used in the measurements at $T = 298.15$ K and $I = 0.15$ mol L^{-1} are shown in Table 2.7.

Table 2.6. Experimental conditions for the acid-base properties of the investigated ligands in NaCl aqueous solutions at $I = 0.15$ mol L^{-1} and $T = 298.15$ K.

Ligand species	C_L [a]	C_{H^+} [a]	pH	n [b]
CAR	0.01-1	5	2.0-10.0	20
FcCAR	0.04-0.1	0.7-3	2.0-9.0	5
PyCAR	0.006-0.03	1-6	2.0-9.0	5

[a] in mmol L^{-1}. [b] number of titrations.

Table 2.7. Experimental conditions for the investigated M^{2+}-ligand systems in NaCl aqueous solutions at $I = 0.15$ mol L^{-1} and $T = 298.15$ K ($2.5 \leq$ pH ≤ 9.0).

System	C_M [a]	C_L [a]	C_M/C_L	C_{H^+} [a]	n [b]
Cd^{2+}-PyCAR	0.01-0.02	0.02-0.04	0.5-1	0.2	4
Hg^{2+}-FcCAR	0.01-0.02	0.02-0.04	0.5-1	0.2	4
Hg^{2+}-PyCAR	0.01-0.02	0.02-0.04	0.5-1	0.2	4
Pb^{2+}-FcCAR	0.01-0.02	0.02-0.04	0.5-1	0.2	4
Pb^{2+}-PyCAR	0.01-0.02	0.02-0.04	0.5-1	0.2	6

[a] in mmol L^{-1}. [b] number of titrations.

2.4 ^{1}H NMR

2.4.1 General aspects [53]

Nuclear Magnetic Resonance spectroscopy (NMR) is a powerful and fast technique that exploits the magnetic properties of specific nuclei to identify, determine and clarify molecular structures and their conformations, as also to provide important information on unknown compounds, mostly organic in nature. It also allows to study particular phenomena in solution, such as tautomeric equilibria, kinetic reactions and H^+ exchanges, as well as to identify any ionizable sites present in the molecules under study.

Contrary to UV-Vis spectrophotometry, in NMR spectroscopy, the nuclei of certain atoms are involved in the absorption process, rather than the outermost electrons.

The operating principle is based on the measurement of the absorption of electromagnetic radiation in the radiofrequency region, between about 4 and 900 MHz, as a result of the interaction of the oscillating magnetic field of electromagnetic radiation in the radio wave region with the magnetic moments of the nuclei in the presence of an intense magnetic field. In particular, this phenomenon occurs when the nuclei of the analyte are immersed in a static and external magnetic field and exposed to a second oscillating magnetic ones. Therefore, only those nuclei with a specific spin value, ½, and, thus, particular magnetic properties, absorb radiofrequency radiations when they conveyed an external magnetic field. These nuclei of particular atom groups, some of which are mentioned here, such as ^1H, ^{13}C, ^{15}N, ^{19}F and ^{31}P, have the same energetic spin states with random orientation in the absence of the external magnetic field. On the other hand, when these nuclei are immersed in an intense magnetic field, they behave like small magnetic rods and, as such, can orient themselves along or against the magnetic field lines assuming two energetic levels, classified as $m = +$ ½ and m= - ½. The potential energy, E, of a nucleus in these two orientations, or quantum states, is given by:

$$E = -\frac{\gamma m h}{2\pi} B_0 \tag{2.5}$$

where γ is the *gyromagnetic ratio*, which is characteristic of each nucleus and proportional to the magnetic moment nuclear spin, μ, and spin, I. m is the magnetic quantum number, h, Planck's constant, and B_0 is the external strong magnetic field. The energy of the inferior state, corresponding to $m = + \frac{1}{2}$, is

$$E_{+1/2} = -\frac{\gamma h}{4\pi} B_0 \tag{2.6}$$

The lowest energy level ($m = + \frac{1}{2}$) is mainly populated, compared to the highest ($m = - \frac{1}{2}$), and the ΔE between them is given by the following equation:

$$\Delta E = \frac{\gamma h}{4\pi} B_0 - \left(-\frac{\gamma h}{4\pi} B_0\right) = \left(\frac{\gamma h}{2\pi}\right) B_0 \tag{2.7}$$

Transitions between energy levels (ΔE) can be promoted as a result of the adsorption or emission of electromagnetic radiation, whose frequency, ν, is correlated to ΔE by the following relation:

$$\Delta E = h\nu \tag{2.8}$$

Therefore, it follows that:

$$\nu = \left(\frac{\gamma}{2\pi}\right) B_0 \tag{2.9}$$

which represents the NMR equation relating the radiofrequency (ν) applied to the external magnetic field (B_0) with a constant of proportionality $\left(\frac{\gamma}{2\pi}\right)$. Therefore, when the enforced radiation energy is equivalent to the ΔE, equation (1.9) is

satisfied and the system is in resonance. At the same time, the NMR-active nuclei absorb the applied radiofrequency. As soon as the pulse is over, the nuclei begin to relax and return to their equilibrium position. Meanwhile, a time-domain radiofrequency signal, called free induction decay (FID), is emitted by the excited nuclei as they relax. The sum of the FID signals, detected by a coil perpendicular to the static magnetic field, is recorded and the resulting data are converted into the frequency-domain by Fourier Transform (FT) and, finally, the spectrum, *i.e.,* a graph of the intensity of the absorption peaks *vs*. frequency, is obtained.

Considering that a proton in a molecule is shielded by its electronic cloud, whose density varies with the chemical surrounding, the equation (2.9) becomes:

$$\nu = \left(\frac{\gamma}{2\pi}\right) B_0 (1 - \sigma) \tag{2.10}$$

where σ is the shielding constant deriving from the electronic cloud and its spatial distribution around the nucleus. Therefore, the shielding depends on the density of circulating electrons and on the inductive effect of the groups close to the NMR-active nuclei. As aforementioned, electrons turn over a magnetic field, thus generating a small magnetic field of their own, opposite to the one applied. For this reason, the recorded frequency is lower than the one enforced. This variation determines a difference in the absorption position of a given NMR-active nucleus with respect to that of a reference compound, whose advantageous use also allows to measure the chemical shift (δ) independently of the oscillator frequency .

2.4.2 Instrumental equipment and procedure

The proton spectra of CAR, as well as of the M^{2+}-CAR systems, were recorded in aqueous solution by a Varian 500 MHz NMR spectrometer. Presaturation ^{1}H NMR analysis was performed at T = 298.15 K and by means of a coaxial capillary, filled

with deuterated water, which was introduced into sample tubes as an external reference. The presaturation technique was used for the suppression of the water signal and 1,4-dioxane (10%) added as internal standard. The coupling constants, J, are expressed in Hz. To determine the protonation constants of CAR, ^{1}H NMR titration was performed on 25 mL of solution, containing the ligand, HCl and the ionic medium, NaCl (I = 0. 15 mol L^{-1}) and titrated with standard NaOH solution. In the study of the metal (M^{2+})-CAR interactions, similar titrations were performed on 25 mL of solutions containing different amounts of the ligand and metal cation, HCl and NaCl (I = 0. 15 mol L^{-1}). The experimental conditions are summarized in Table 2.8. The observed chemical shifts in the collected spectra and ^{1}H NMR data were processed by the HypNMR computer program [56].

Table 2.8. Experimental conditions for the formations constants of CAR systems in NaCl at I = 0.15 mol L^{-1} and T =298.15 K.

System	C_M [a]	C_L [a]	C_M/ C_L	C_{H^+} [a]	pH	%$_{D_2O}$
CAR	-	3	-	10	2.3-10.0	10
Ca^{2+}-CAR	4	6	0.7	10	3.0-10.5	10
Zn^{2+}-CAR	2	3	0.7	10	2.3-8.0	10
Cu^{2+}-CAR	2	4	0.5	10	2.8-9.0	10
Mn^{2+}-CAR	2	4	0.5	10	2.4-8.9	10

[a] in mmol L^{-1}.

2.5 Mass Spectrometry

2.5.1 General aspects [57]

Mass spectrometry (MS) is an analytical technique used to identify and quantitatively determine unknown compounds and elucidate structural and chemical properties of the molecules under study. Unlike spectroscopic techniques,

MS is a destructive analytical method and, therefore, molecules are destroyed after analysis. It is not based on the interaction between radiation and matter.

The operating principle consists in the possible separation of a mixture of ions depending on their mass/charge ratio, generally through static or oscillating magnetic fields. In more detail, the blend of ions is produced by ionizing the sample molecules, making them pass through an electron beam of known energy. After ionization, a molecule loses an electron and, thus, becomes a radical ion or better known as *molecular ion*. In turn, it is partially fragmented giving rise, on one hand, to molecules and/or neutral radicals, which are not detected by the instrument and, on the other hand, to cations and/or radical cations, that are *fragment ions*. The latter are discriminated on the basis of their mass/charge ratio and, finally, detected by a detector. The mass spectrometer is interfaced by a PC, which monitors the instrumental operations and records an MS spectrum in graphic and tabular format. The MS spectrum is given by plotting the relative abundance of the ions depending on their mass/charge ratio. On the basis of the ion separation method, this detection technique allows to measure both nominal and exact molecular mass, and to determine the specific fragmentation pathway of each compound. Regarding the ionization, two methods are known, namely hard and soft ones.

- Hard ionization operates at high energy and leads to a large fragmentation degree.
- Soft ionization operates at lower energy and results in a lesser fragmentation degree.

Among these, soft Chemical Ionization (CI) and Laser Desorption (LD) methods were employed in this experimental work. In the CI technique, molecules of a reagent gas are ionized by electron ionization. Thus, the resulting ions react with analyte molecules in the gas phase to achieve ionization. LD instead exploits a laser beam, consisting of CO_2 or CH_4, to ionize the sample that emits in the far infrared, or a Nd/YAG (neodymium/yttrium-aluminum-garnet) laser in the UV

energy region. The potentiality of the LD ionization improves when it is coupled to a support matrix (MALDI) that consists in the absorption of the sample on a matrix, which can be characterized by various materials, mainly organic in nature, such as glycerol, picolinic, succinic, caffeic, synaptic (SA) and α-Cyano-4-hydroxycinnamic acid (α-CHCA). Moreover, this matrix must have the following chemical-physical properties:

- Easy evaporation. It should not be evaporated during sample preparation or before performing measurements, obviously.
- Favorable acidity. In this case, it should act as a source of protons by promoting ionization of the analyte.
- Strong optical absorption in the UV region, to effectively absorb laser radiation.
- Hydrophilic and with possible polar groups.

When the analyte is dissolved in the solution, it is bombed by the laser beam, whose effects are attenuated by the matrix, that shields it. Therefore, the analyte is ionized and vaporized.

This MALDI technique is usually coupled with a Time-Of-Flight (TOF) analyzer spectrometer. This source, in fact, mainly gives rise to monocharged ions, allows to analyze even large molecules and provides a good m/z parameter. On the other hand, the (TOF) MS is an affordable technique that allows to observe and detect all ions without the loss associated with "scanning" processes, *i.e.*, with a high scanning speed. Therefore, a full mass-measurement cycle allows to detect very high and cram m/z range, without limits and in a short time [58, 59]. In this thesis, experiments using Matrix Assisted Laser Desorption Ionization Mass Spectrometry (MALDI MS) and tandem mass spectrometry (MS/MS) techniques were performed. The MALDI MS (TOF/TOF) technique was chosen for its high sensitivity and accuracy, short time of analysis and ability to detect different compounds in highly complex mixtures [60-62].

2.5.2 Instrumental equipment and procedure

MALDI MS and MS/MS analyses were performed using a 5800 MALDI TOF-TOF Analyzer (AB SCIEX) equipped with a neodymium/yttrium-aluminum-garnet laser (laser wavelength 349 nm), in reflection positive-ion-mode with a mass accuracy of 5 ppm. Dried droplet sample preparation was adopted to prepare samples for the MS analysis by testing two different matrixes: a-Cyano-4-hydroxycinnamic acid (α-CHCA, $CH_3CN:H_2O$, 50:50, 0.3% in TFA) and 2,5-Dihydroxybenzoic acid (DHB, $CH_3CN:H_2O$, 60:40, 0.1% in TFA). At least 3500 laser shots were typically accumulated with a laser pulse rate of 400 Hz in the MS mode. In the MS/MS mode spectra, up to 4500 laser shots were acquired and averaged with a pulse rate of 1000 Hz, with a mass accuracy of 10 ppm. CID (Collision Induced Dissociation) experiments were performed at a collision energy of 1 kV, and ambient air was used as the collision gas with a medium pressure of 10^{-6} Torr. After acquisition, spectra were handled using Data Explorer version 4.0.

2.6 Voltammetry

2.6.1 General aspects [53]

Voltammetry consists of all electroanalytical methods which are able to:

  i)   characterize and determine electrochemically accessible systems with low detection limits, and

  ii)   use cost-effective equipment, to deduce various information about an analyte, such as its stoichiometry, the rate of charge transferred at the interface, as well as the transfer rate of mass, the rate and equilibrium constants of the species involved.

Voltammetry is also useful for studying oxidation and reduction processes in various media, surface adsorption processes, as well as electron transfer mechanisms on chemically modified electrode surfaces. The operating principle is

based on the measurement of the current when the potential is applied and, thus, in conditions of polarization of a Working Electrode (WE). This is favored when the applied voltage is higher than that predicted by the Nernst equation.

Voltammetry was historically derived from polarography, conceived by the Czechoslovakian Chemist Jaroslav Heyrovsky in 1992. It differs from other voltammetric techniques in the use of a dropping mercury electrode as a Working Electrode (WE). However, the use of high amounts of mercury, the cumbersome nature of the equipment and the wide availability of faster and more convenient methods have led to a gradual lack of interest of the scientific community toward the polarography, which has lost its importance. Furthermore, the development of modern techniques, which have greatly improved the sensitivity and selectivity of the method, allow voltammetry to be an excellent tool in several areas of chemistry, biochemistry, materials science and engineering, as well as in environmental science for study of oxidation, reduction and absorption processes.

In voltammetry, an excitation signal with variable potential is enforced on the WE that gives rise to a characteristic current response. Different pulses can be applied to the WE, and the currents are measured at different times of the pulses, from which voltammetric techniques take their name. In this thesis, Cyclic Voltammetry (CV), Differential Pulse Voltammetry (DPV) and Square Wave Voltammetry (SWV) were employed, whose applied potential pulses *vs*. time and the typical resulting current responses are shown in Figure 2.3 [63]. As can be observed in A1, CV uses a ramp going back and forth between two values of potential (named *switching potentials*) in which an electrochemical process is detectable. In particular, the first potential value increases linearly up to a maximum and, then, decreases linearly toward its initial value with the same slope. The direction could also be the other way around, depending on the composition of the analyte. In this technique, important parameters are: the cathode peak potential (E_{pc}) and anode peak potential (E_{pa}), the cathode current (i_{pc}) and the anode one (i_{pa}), and scan rate

(V s^{-1}), which represents the slope for a linear voltage change during the measurement. This process can be repeated many times while recording the current *vs*. time. A complete cycle can take up 100 seconds or more, or can be completed in less than a second (1 ms), and can provide information on the voltage, kinetics and reversible, or irreversible, nature of the electrolytic process. As an example, for a reversible electrolyte process, the cathode and anode currents are almost equal in absolute value, and it follows that:

$$\Delta E_p = \left| E_{pa} - E_{pc} \right| = \frac{0.0592}{n} \tag{2.11}$$

where n is the number of electrons involved in the electrolytic reaction.

In DPV, the waveform potential, depicted in Figure 2.3 B1, shows the recording of pulsed potential signals over time and results in its combination with a linear sweep. In particular, the DPV consists in the application of a succession of voltage pulses of constant duration and amplitude, one at 16.7 ms before the pulse (S1 in Figure 2.3 B1) and the second for at least 16.7 ms at the end of the pulse (S2 in Figure 2.3 B1). These two current sampling points are chosen to allow the decay of the non-faradic (capacitive) current and, thus, optimize the signal-to-noise ratio and improve the sensitivity of the method. In the same Figure 2.3 B1, T represents the waveform period. Thus, a differential measurement of the current is obtained, which leads to the formation of a peak-shaped voltammogram, whose height is assigned with respect to the tangent and is proportional to the concentration of the analyte under study (Figure 2.3 B2).

In SWV, the potential waveform is depicted in Figure 2.3 C1, as a combination of pulses and steps-like signals. The same Figure 2.3 C1 highlights the S1 and S2 points, the potential period, T, which is about 5 ms, and the potential increment, ΔE, which is usually 10 mV. The response current, in Figure 2.3. C2 (dashed line), shows the voltammogram of a reversible process, corresponding to the forward

curve and the reverse one. Their difference gives rise to a current (solid line) proportional to the concentration of the analyte and the peak correspond to the half-wave potential. A voltammogram is obtained in less than 10 ms.
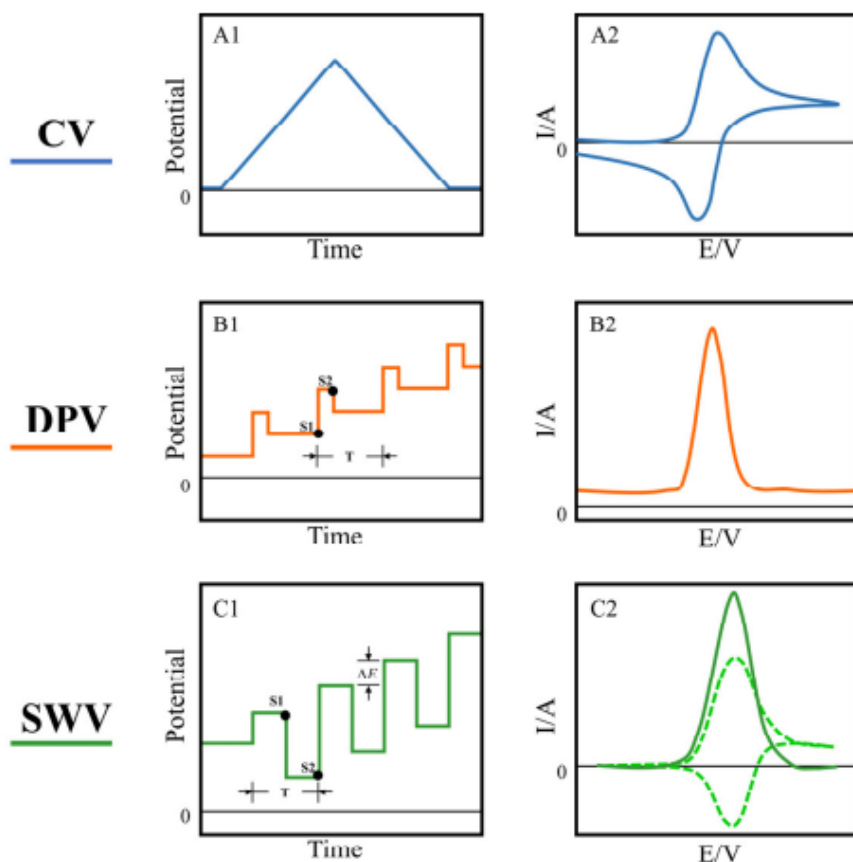

Figure 2.3. Schematization of applied potential *vs*. time and the resulting current responses in CV, DPV and SWV [63].

In any voltammetric technique, the electrochemical cell is assembled from three electrodes immersed in a solution containing the analyte, along with an excess of non-reactive electrolyte, that is the electrolyte support:

i) the Working Electrode (WE), whose potential depends on time and where the electrolytic process takes place. This electrode can be of various shape and models, as well as in various materials, such as in noble metal (Pt and Au), a carbon material (carbon paste, carbon fiber, pyrolytic graphite, glassy carbon, diamond or carbon nanotubes), a semiconductor or a metal coated with a mercury film.

ii) the Reference Electrode (RE), commonly consisting of Ag/AgCl, whose potential remains constants over time in the electrolytic process, and

iii) the auxiliary or Counter Electrode (CE), usually a platinum wire, which conducts electricity from the source to WE, turning the circuit off.

The resulting current, proportional to the potential difference between WE and RE, is conveyed in voltage as a function of time.

2.6.2 Instrumental equipment and procedure

In this thesis, voltammetric experiments were carried out at room temperature and using two different PC-controlled electrochemical workstations (PNT-10-Autolab and μAutolab potentiostat/galvanostat type III (Eco Chieme)) with two respective three-electrode cell configurations (DropSens, DRP-DSC70575, and DropSens, DRP-DSC4MM 72098). Voltammetric measurements were performed in CV, DPV and SWV, either as titrations or not, in KCl (0.1 mol L^{-1}) aqueous solutions starting from pH ≈ 3 to 9, using Screen-Printed Electrodes (SPEs).

SPEs have become increasingly important due to their advantageous characteristics, such as ease of use, low-cost and portability, also allowing fast analyses. Therefore, the screen-printed technology has significantly contributed to the shift from traditional bulky electrochemical cells to miniature portable electrodes, useful for on-site analyses. This is also possible because cleaning and/or polishing procedures of the SPEs are not needed and, thus, tedious and long

pretreatment steps are shunned. At the same time, SPEs avoid use of large amounts of reagents and samples. Although SPEs are not as robust as conventional electrodes, such as glassy carbon or gold disk, and the surface of their WE is not as perfect as that of a mirror-like polished solid electrode, their cost and size advantages, in addition to enabling rapid screenings, have led to their increasing employment in recent years as transducers in (bio)sensing, devices for biomedical applications, portable sensors for food analysis and detection of environmental contaminants [64]. SPEs usually contain a pseudo-electrochemical cell composed of three electrodes printed on a solid substrate, such as the one shown in Figure 2.4. The latter depicts a schematic representation of the Screen-Printed Carbon Electrode (SPCE) used in this thesis.
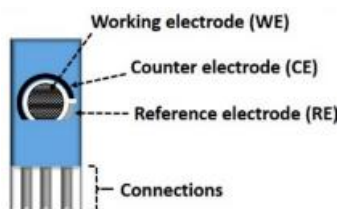
Figure 2.4. A schematic setup of the Screen-Printed Carbon Electrode (SPCE).

- Regarding the WE inks, the most common are those based on carbon (graphite, graphene, fullerene, carbon nanomaterials, etc.), due to their adequate electroanalytical features, including good conductivity, chemical inertness, ease of modification, low background currents, and a wide potential range, as well as their low costs. In addition to carbon inks, conductive metallic ones are increasingly used. Among them, gold ink is the most employed, followed by those of silver, platinum or palladium.
- The RE, usually made of Ag or Ag/AgCl ink, is a pseudo-reference or quasi-reference electrode since its potential is not as stable as that of a

conventional reference electrode. Therefore, the applied potential is not as exact and reproducible as when an Ag/AgCl electrode is used. This could be tricky for electrochemical studies, where the control of the potential is crucial; but not for sensing applications.

- The CE is normally made of the same ink as the WE.

Analytical measurements can be performed by settling a single drop of the reagent/sample solution on the SPE, dipping it into a solution or including it in a flow system [64].

The composition of the inks determines the electrochemical characteristics of the SPEs, which are also highly versatile and ease-to-modify platforms. These modifications allow to improve the electroanalytical characteristics of the SPEs (such as sensitivity, precision, operational stability, as also to enhance the immobilization of the recognition elements and units. Among the electrode modification procedures, great importance is given to the development of electrode surfaces modified with different conductive substrates, which include polymeric films, prepared by dip coating, spin coating, adsorption, electrodeposition or covalent bounds. The modified electrodes have a wide variety of applications; among them, they are used as analytical sensors for particular species or functional groups, as well as for metals [64].

For these purposes, in this thesis, electrode modification procedures are advanced more than once. In particular, SPEs based on carbon inks as working (4.0 mm diameter) and counter electrodes, and Ag/AgCl (sat) as reference electrode, were used. These bare Screen-Printed Carbon Electrodes (SPCEs) (DRP-110) were employed, as also the modified SPCEs with pristine Nafion, CNO and MWCNT-CD films. As above-mentioned, coating the working electrode (WE) in SPCEs improves electrochemical response and, thus, sensitivity in the detection of the analyte. Electrode preparations are described in the following paragraphs.

Voltammograms were deconvoluted using General Purpose Electrochemical System (GPES), version 4.9 of Eco Chemie B.V. processing software.

The SPCEs were washed in high purity water (18 MΩ cm^{-1}) or ultrapure water (conductivity < 0.1 μS cm^{-1}), plunged in H$_2$SO$_4$ solution and subsequently under a stream of nitrogen before each measurement. Electrochemical response was assessed by CV using K$_3$[Fe(CN)$_6$] (1 mmol L^{-1}) as a redox probe in KCl (0.1 mol L^{-1}) aqueous solution. It is based on the [Fe(CN)$_6$]$^{3-/4-}$ reaction in the potential window between -0.3V (*vs*. Ag/AgCl) to 0.8V and a scan rate equal to 0.1 V s^{-1}.

The CV conditions employed in this thesis were in the potential window between -1 $\leq$ E/V *vs*. Ag/AgCl $\leq$ +1.5, with a step potential equal to 0.01V (*vs*. Ag/AgCl), and varying the number of scans (between 2 and 10), conditioning potential (-0.5 $\leq$ E/V (*vs*. Ag/AgCl) $\leq$ +1), equilibration time (0 $\leq$ s $\leq$ 20) and scan rate (10 $\leq$ mV s^{-1} $\leq$ 500).

The DPV conditions used were in the potential window of -1 $\leq$ E/V *vs*. Ag/AgCl $\leq$ +1.5, and varying the parameters as follows: conditioning potential (0 $\leq$ E/V (*vs*. Ag/AgCl) $\leq$ 1.2), deposition potential (0 $\leq$ E/V (*vs*. Ag/AgCl) $\leq$ 1) between 0 to 60s at an equilibration time = 0.5 s, step potential = 10 mV, pulse amplitude = 100 mV and pulse width = 50 ms.

The SWV parameters used were set in the potential window between -1 $\leq$ E/V *vs*. Ag/AgCl $\leq$ +1.5, as follows: conditioning potential 0.5 V, without deposition potential, step potential = 15 mV and varying the pulse amplitude (10 $\leq$ E/V (*vs*. Ag/AgCl) $\leq$ 20). Electrochemical measurements were performed on variable volumes (1-10 mL) of aqueous KCl (0.1 mol L^{-1}) solutions containing L-Histidine (10^{-4} $\leq$ C$_L$/mol L^{-1} $\leq$ 10 $^{-2}$) or CAR (1 10^{-7} $\leq$ C$_L$/mol L^{-1} $\leq$ 10^{-2}) at room temperature. CV was also performed in order to understand the electrochemical behavior of ferrocenecarboxylic acid (FcCOOH) (1 $\leq$ C/mmol L^{-1} $\leq$ 5), precursor of FcCAR. Since FcCOOH is not water soluble, it was dissolved in aqueous ammonia solution (0.1 mol L^{-1}) to obtain a quaternary ammonium salt, FcCOO^{-}

NH_4^+, in KCl (0.1 mol L^{-1}) aqueous solution. Experimental measurements of FcCAR (0.01 ≤ C_L/mmol L^{-1} ≤ 10) in KCl (0.1 mol L^{-1}) aqueous solutions were performed in CV and DPV, in a wide pH range (3 ≤ pH ≤ 9). Variable volumes (1-10 mL) of aqueous KCl (0.1 mol L^{-1}) solutions containing FcCAR (1 mmol L^{-1}) were titrated with mercury (C_{Hg}^{2+} = 0.3-3 mmol L^{-1}. C_M/ C_L = 0.3-3) and lead (C_{Pb}^{2+} = 0.2-3 mmol L^{-1}. C_M/ C_L = 0.3-3) solutions, previously prepared in MOPS buffer (pH ≈7).

2.6.3 Electrode preparation

In this work, the exclusive use of SPCE is attributable to their many advantages, which include the possibility of their modification with a wide variety of materials, thus improving their sensitivity and lower limit of detection [65]. Carbon nanomaterials, metal oxides, conductive polymers and also hybrid materials, that are resulting from the combination of more than one substrates, have emerged for these analytical purposes. In fact, the chemical-physical properties of these materials, such as high surface area, good electrical conductivity, electrocatalytic properties, result in an improvement in the analytical performance of a sensor [65]. For all these reasons, Nafion and carbon nanomaterials were employed to enhance sensitivity of SPCEs, whose preparation procedures are described in the following order:

i)   Electrode preparation with Nafion,

ii)   Electrode preparation with CNO,

iii)   Electrode preparation with MWCNT-CD.

Nafion/SPCE and CNO/SPCE were used for the electroactivity of CAR (Chapter 3), while the MWCNT-CD/SPCE was employed in the electrochemical analysis of FcCAR (see Chapter 5).

i)   Electrode preparation with Nafion

The aim of this tool was to deposit a thin Nafion (0.3 %) layer on the surface of the working electrode (WE) to favor the interaction with totally protonated CAR species (H_3L^+). Prior to modification, bare SPCE was first washed in Milli-Q® water and dried under a stream of nitrogen. 1 μL of Nafion (0.3 %) in EtOH:H_2O (5:1 v/v) was drop-casted on the WE, air-dried to evaporate the solvent (approximatively 15 min) [48], and also under a stream of nitrogen (10s). No further aliquots of Nafion solution (0.3 %) were drop-casted on the SPCE.

Electrochemical response of the modified SPCE was assessed by CV using $K_3[Fe(CN)_6]$ (1 mmol L^{-1}) as redox probe, in KCl (0.1 mol L^{-1}). This Cyclic Voltammogram (CV) is compared with that obtained on the bare SPCE in Figure 2.5. Electrochemical measurements were performed on variable volumes (1-10 mL) of solutions containing CAR ($1 \ 10^{-3} \leq C_L/ \text{mol L}^{-1} \leq 10^{-2}$), H_2SO_4 (0.1 mol L^{-1}) to fix the pH ($\approx$ 3) and KCl (0.1 mol L^{-1}) as a supporting electrolyte.
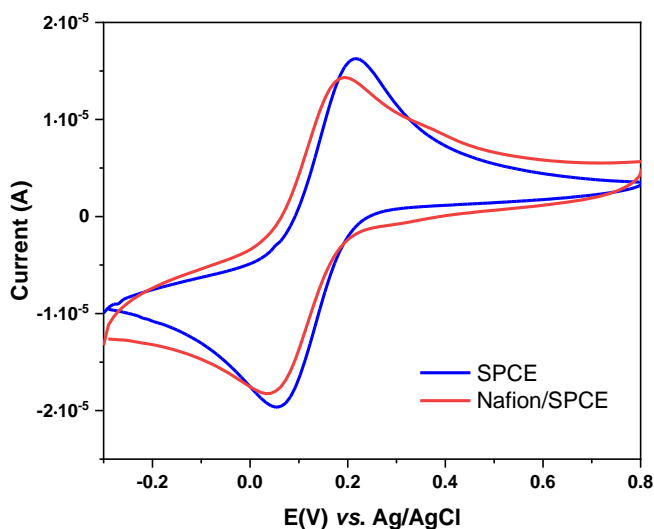
Figure 2.5. CVs of $[Fe(CN)_6]^{3-/4-}$ (1 mmol L^{-1}) in KCl (0.1 mol L^{-1}) aqueous solution obtained with bare SPCE (blue line) and Nafion/SPCE (red line). Scan rate: 0.1 V s^{-1}.

On the other hand, the incorporation of nanomaterials on electrochemical platforms leads to an improvement of the sensitivity, as well as of the limit of detection [66]. For this purpose, Carbon Nano-Onions (CNO) and MultiWalled Carbon NanoTubes modified with CycloDextrins (MWCNT-CD) dispersions were employed in this thesis.

ii)   *Electrode preparation with Carbon Nano-Onions (CNO)*

The enhanced surface area and electron transfer rate of the CNO make them emerging candidates in a wide variety of electrochemical applications, as electrochemical immunosensor, biosensor and capacitors [49, 50, 66]. The polished SPCE was sonicated in Milli-Q® water for 5 min and dried under a stream of nitrogen. The polished SPCE was further dried in vacuum (T = 353.15 K) for 60 min, prior to modification. SPCE was modified by drop-casting a homogeneous dispersion of CNO in DMF (2 mg mL^{-1}) prepared using an ultrasonic-bath for 30 min. To obtain a thin layer of CNO, 1 µL of the dispersion was cast twice times on the surface of the electrodes and dried in an oven at T = 353.15 K under DMF atmosphere for 30 min. This procedure was used to avoid the formation of the so-called coffee-ring effect, which results in non-homogeneous films [49]. Electrochemical response of the modified SPCE was assessed by CV using $K_3[Fe(CN)_6]$ (1 mmol L^{-1}) as redox probe, in 0.1mol L^{-1} KCl aqueous solution. Cyclic Voltammograms (CVs) are compared in Figure 2.6.
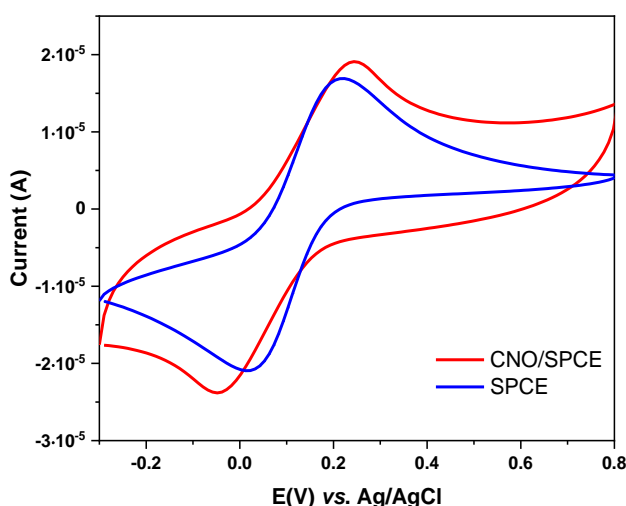
Figure 2.6. CVs of $[Fe(CN)_6]^{3-/4-}$ (1 mmol L^{-1}) in KCl (0.1 mol L^{-1}) aqueous solution obtained with bare SPCE (blue line) and CNO/SPCE (red line). Scan rate: 0.1 V s^{-1}.

iii)   *Electrode preparation with MultiWalled Carbon NanoTubes modified with CycloDextrins (MWCNT-CD)*

Similar dispersions of MultiWalled Carbon NanoTubes modified with CycloDextrins (MWCNT-CD) were used in the electrochemical analysis of FcCAR. For the synthetic approach of MWCNT-CD, electrode preparation and practical function see Chapter 5, subparagraph 5.6.1.

2.7 Computational methods

2.7.1 Quantum-mechanical calculations and *Ab Initio* Molecular Dynamics (AIMD)

Nowadays, supercomputing resources are capable of efficiently solving quantum-mechanical laws for complex molecules in solution. Quantum chemical methods can be used for evaluating the ground-state structures and the associated potential

energy surface of selected molecules. In particular, standard quantum-mechanical approaches solve the Schrödinger equation for the electrons while treating the nuclei as classical entities. By exploiting the Density Functional Theory (DFT) formalism, it is possible to obtain optimized molecular geometries under implicit solvation conditions. However, approximating the solvent to its dielectric constant may provide only a crude description of the local molecular environment with respect to methods explicitly solving the DFT equations for the solvent, as in *Ab Initio* Molecular Dynamics (AIMD) simulations. In AIMD methods, indeed, the solvating species (*e.g.*, water molecules) are rigorously treated at the same level of theory of the solute (*e.g.*, carnosine (CAR) complexes). The term *ab initio* or, equivalently, "from first-principles" refers to the fact that these molecular dynamics approaches employ a limited number of parametrization – as compared to historical classical force-fields techniques – by solving "on the fly" the Schrödinger equation for the electrons within the Kohn-Sham formalism of DFT. In particular, the Born-Oppenheimer molecular dynamics method here adopted relies upon the evaluation of the electronic potential energy surface, which uniquely determines the forces acting on the nuclei. As usual, due to their larger masses and shorter associated de Broglie wavelength, these latter are treated as Newtonian particles. In such a way, complex molecular systems simulated *via* AIMD spontaneously evolves over time and space allowing to calculate fundamental properties with atomistic resolution.

In this thesis, both static traditional quantum-mechanical calculations with implicit solvation and prolonged AIMD simulations in the presence of the explicit solvent were performed. As for the static calculations, the direct addition of protons to all the relevant functional groups of CAR were considered to evaluate its own capabilities in accepting and donating protons. In this way, the Proton Affinity (PA) of different molecular sites offered by both CAR zwitterionic tautomeric forms was determined. On top of these quantum-mechanical calculations,

dynamical averages associated to the CAR behavior were gathered *via* a series of AIMD simulations of two numerical samples composed by CAR in the presence of common cations in bulk liquid water at room temperature. Owing to the employment of molecular dynamics techniques, it is possible to study the temporal evolution of interacting atoms and molecules in explicit solvation. Therefore, AIMD simulations allow to clarify the dynamical behavior of proteins and their complexes in solution and to determine fundamental biochemical properties.

2.7.2 Computational methodology

All static calculations were performed by means of the Gaussian 09 software [67], which exploits the Density Functional Theory (DFT) formalism. The latter allows to evaluate, among other things, the ground-state structures of molecular species. The B3LYP [68-71] hybrid exchange and correlation functional was used with 100% of exact exchange. Geometry optimizations of different molecular structures were performed in gas phase and under implicit solvation employing the 6-311++G(2d,2p) atomic basis set for all atoms. To simulate the solvent, the conductive polarizable continuum model (CPCM) [72] was employed by setting parameters mimicking the water electrostatics. Once the structural relaxation to the ground state occurred, vibrational calculations were performed not only to establish the correctness of the previous calculations (*i.e.*, absence of imaginary frequencies), but also to obtain the zero-point energy (ZPE) associated with each optimized molecular structure. ZPE values are also critical in the determination of the proton affinity (PA), which is defined as the negative of the change in enthalpy for the exemplary following reaction:

$$H^+ + B \rightarrow H^+B \qquad . \qquad (2.12)$$

To have a comprehensive scenario on the CAR capabilities in accepting and donating protons, quantum-mechanical calculations were performed on both carnosine zwitterionic tautomeric forms of the imidazole ring and for different initial protonation states, involving all the possible molecular protonation sites. Neutral, cationic and anionic carnosine species are also included in the simulations to estimate the PA values for the successive protonation steps, in line with the laboratory experiments reported in the current thesis. In this way, the PA values were obtained by calculating the energy difference between the optimized protonated and neutral (neutral and deprotonated) molecules at the B3LYP/6-311++G(2d,2p) level of theory, using the following equation [73, 74]:

$$PA = -\Delta H = -\Delta E - \Delta ZPE + \Delta Ev(T) + C \quad , \qquad (2.13)$$

where the ΔZPE term indicates the difference between the electronic energies and the corrected ones by the difference between the ZPE of the species. The second and third terms in equation (2) are obtained from the frequencies of the normal modes of vibration. The last term, C, introduces the correlation for translational and rotational energy changes taking into account the classical behavior and the ΔnRT term, necessary to convert an energy into enthalpy assuming an ideal gas behavior. All these calculations, albeit being conducted under implicit solvent conditions, were carried out explicitly considering the addition of protons to all the significant molecular functional groups, namely the carboxylic group of the zwitterion (COO^-), the bare nitrogen atom (N) and the nitrogenous group (NH) of the imidazole ring. On the other hand, as for the removal of protons from the globally neutral zwitterionic carnosine species, the functional group involving the protonated amino group of the β-alanine residue of the zwitterion (NH_3^+) was taken into consideration in the quantum-mechanical calculations.

Several *ab initio* molecular dynamics (AIMD) simulations were performed with the CP2K code [75] on two numerical samples composed by CAR, calcium cation

(Ca^{2+}) and liquid water, on the one hand, and by CAR, magnesium cation (Mg^{2+}) and liquid water, on the other. Both samples were composed of one carnosine molecule, one cation (either Ca^{2+} or Mg^{2+}) and 128 water molecules, resulting in a total of 413 atoms present in each system. The simulated conditions *via* AIMD produce much higher CAR and metal ion concentration (≈ 0.3 M) than those reported in potentiometric titrations (mM region). However, the size and time scale of the simulated samples represent a computational upper-bound nowadays achievable with powerful academic supercomputing resources. In this way, respective cubic super-cells with edges of 16.22 Å and 16.19 Å of the Ca^{2+}- and the Mg^{2+}-containing samples were simulated. Periodic boundary conditions were applied along the three Cartesian axes. Initial atomic configurations of the CAR species complexed with the two investigated metal cations were preliminarily structurally optimized at the B3LYP/6-311++G(2d,2p) [68-71] DFT level under implicit water solvation conditions. The optimized Ca^{2+}-CAR and Mg^{2+}-CAR structures were later and separately hydrated with 128 water molecules each. During the AIMD simulations, wavefunctions of each atomic species were expanded in double-zeta-valence-plus-polarization (DZVP) basis sets with the Goedecker–Teter–Hutter pseudopotentials [76] using the so-called GPW method. A plane-wave cutoff of 400 Ry was adopted. Exchange and correlation effects were treated *via* the Perdew-Burke-Ernzerhof (PBE) [77] density functional. To consider dispersion interactions, which are pivotal in correctly simulating the liquid water behavior and its hydration capabilities, the dispersion-corrected version PBE-D3 [78, 79] was used. All AIMD simulations were performed at the nominal temperature of 300 K, which was kept fixed through a CSVR thermostat [80]. In this way, an isothermal-isochoric (NVT) ensemble was simulated whilst the nuclei dynamics was classically propagated through the Verlet algorithm with a time-step of 0.5 fs. To gather relevant statistics, multiple AIMD simulations were performed by choosing slightly different initial atomic configurations of the aqueous

environment, as well as of the initial atomic velocities of the simulated systems. Furthermore, to obtain almost independent trajectories and to monitor the cations-carnosine complexation processes in an unbiased manner, pseudo-random initial atomic velocities taken from Maxwell-Boltzmann distributions were assigned. Consequently, 5 independent 30-ps-long AIMD simulations per system were performed. Finally, statistical assessments of the most stable hydrated complexes structures were executed *via* AIMD simulations.

2.8 Data analysis

2.8.1 Computer programs

Depending on the instrumental analytical techniques used, the collected experimental data were processed by various computer programs in order to determine the protonation and complex formation constant values, as well as the thermodynamic parameters and their dependence on the ionic strength and temperature.

In more detail, computer programs are depicted below:

- <u>STACO</u> and <u>BSTAC</u> [81] were employed in the elaboration of the potentiometric data. These programs, using the method of non-linear least squares minimization, allow to calculate analytical parameters from potentiometric measurements, both at constant and different ionic strength, considering that the latter can also undergo variations during titrations. The two programs enable to calculate the stoichiometry of the species, as well as the thermodynamic values of the protonation and formation constants, refining the parameters for the dependence of the stability constants on the ionic strength. As far as the refinement is concerned, STACO minimizes the sum of the quadratic residues, equivalent to the relative volumes of titrant

added. Analogously, BSTAC proceeds with the minimization on the e.m.f. measured. Both procedures refer to the following equations:

$$U_V = \sum_n w_n (v_n^{\exp} - v_n^{calc})^2 \qquad \text{(STACO)} \qquad (2.14)$$

$$U_E = \sum_n w_n (E_n^{\exp} - E_n^{calc})^2 \qquad \text{(BSTAC)} \qquad (2.15)$$

where

$$w_n = 1 \big/ \sigma_n^2 \qquad (2.16)$$

$$\sigma_n^2 = \sigma_V^2 + (\delta v_i / \delta E_i)^2 \sigma_E^2 \qquad \text{(STACO)} \qquad (2.17)$$

$$\sigma_n^2 = \sigma_E^2 + (\delta E_i / \delta v_i)^2 \sigma_v^2 \qquad \text{(BSTAC)} \qquad (2.18)$$

For both programs, two refinement procedures can be performed, in which the first process uses the unit weight and the second the weight in equation (2.16), where σ originated in the first cycle. This means that, in the second refinement process, the data result in a lesser weight, with respect to the first cycle, in which they are affected by higher errors (σ).

- LIANA [81], refers to Linear and Nonlinear Analysis, is a calculation program in Pascal code, useful for optimizing experimental data and getting general fits. In particular, it has a large number of equation libraries and is employed in the following purposes:
  1. Calculation of parameters of linear and non-linear equations,
  2. Detachment of an equation into several partial equations,
  3. Submission of the equations in the same input, as parameters can also be found in different equations,
  4. Awarding of different weights to various variables,
  5. Resolution of multi-variable fits, as well as more than two linear systems simultaneously,

6. View graphs for faster evaluation of results.

- HYPSPEC [82] is a computer program used to determine equilibrium constants, starting from spectrophotometric data. This software is able to process UV-Vis, Raman, Infrared, luminescence and fluorescence data, considering that the spectral intensity of each chemical species is proportional to their concentration in solution. Spectral data can be acquired by titration or a set of individual solutions, which are batch data. It is also able to perform a manual simulation in order to optimize the stability constants values or the results of a refinement cycle.

- HYPNMR [83] is a computer software used to determine equilibrium constants, starting from chemical shifts (δ) obtained in NMR spectra. Equilibrium is assumed to be achieved quickly on the NMR time-scale, and the observed chemical shift for a certain nucleus results in the average of the chemical shifts of that nucleus in the different species present, weighted by their fractional populations. The data input consists of the frequencies, *i.e.*, the chemical shifts of the NMR peaks, with respect to the analytical concentration of the species in solution and, optionally, the pH. The refinement process provides the values of equilibrium constants and the respective chemical shift of each nucleus in every chemical compound. Once each cycle refined, the chemical shifts of the respective species are processed by linear test least-squares, taking into account the set stability constants. The output file includes information about the refined stability constants of each species, as well as their concentration and calculated chemical shifts.

- HYSS [84] is a computer program able to perform titration simulations, taking into account a speciation model, which bases on a set of equilibrium constants. As far as the titration is concerned, it is simulated by setting titration conditions and calculating the concentrations of each species, as a
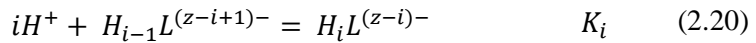
titration evolves. This software is also enable to calculate species concentrations, starting from a model and a set of conditions, as the pH range.

2.8.2 Equilibrium constants

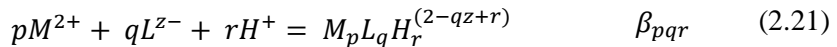In this thesis, the protonation constants are reported as decimal logarithms and referred to the following reactions:
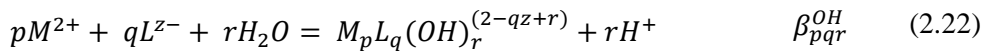
$$iH^+ + L^{z-} = H_iL^{(z-i)-} \qquad \beta_i \qquad (2.19)$$

or

$$iH^+ + H_{i-1}L^{(z-i+1)-} = H_iL^{(z-i)-} \qquad K_i \qquad (2.20)$$
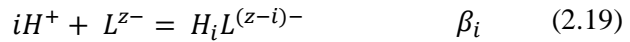
where i is the protonation step.

The formation constants of the metal:ligand complex species are related to the following reactions:

$$pM^{2+} + qL^{z-} + rH^+ = M_pL_qH_r^{(2-qz+r)} \qquad \beta_{pqr} \qquad (2.21)$$

or for hydrolytic species:

$$pM^{2+} + qL^{z-} + rH_2O = M_pL_q(OH)_r^{(2-qz+r)} + rH^+ \qquad \beta_{pqr}^{OH} \qquad (2.22)$$

2.8.3 Dependence of the formation constants on the ionic strength

Of significant importance is the effect that the ionic strength has on solution equilibria. As far as the thermodynamic parameters are concerned, referring to the ligand protonation, as well as metal hydrolysis, and species formation equilibria

can be affected by notable variations in ionic strength. First of all, the latter affects the activity coefficients (γ_x) of the chemical species present in a solution, which, in turn, is related to the molar concentration $[X]$ and the activity (a_x) of the species according to the following relationship:

$$a_x = \gamma_x [X] \tag{2.23}$$

In an ideal system, $\gamma_x = 1$ is assumed and the activity of a component (a_x) corresponds to its concentration $[X]$. Therefore, the equilibrium constants are calculated taking into account the concentrations of the species in solution. In a real system, based on the attractive or repulsive forces of electrolytes in solution, the ions are affected each other and, thus, cannot themselves be considered independent. Therefore, also in very diluted solutions, the concentration does not correspond to the activity (a_x) of the species. The last term indicates the effective number of particles taking part in a given phenomenon, and the linearity deviation of the real system, from the ideal one, is clarified by the Debye-Hückel (DB) theory. According to which, the ions in solutions are point-like masses with exclusively electrostatic interactions and the activity coefficient is related to the ionic strength, as expressed in the following equation:

$$log\gamma_x^{\pm} = -A|z^+ \cdot z^-|\sqrt{I_m} \tag{2.24}$$

where A, constant factor, depends on the temperature and solvent ($A = 0.5100$ mol$^{-1/2}$ kg$^{1/2}$ at T $=298.15$K), z^+ and z^- are the ionic charges and I_m represents the ionic strength in molal concentration scale. However, this is a limit law because it is valid up $I \leq 0.001$mol L^{-1}. Considering that the ions cannot approach at distances lower than the sum of their radii, a further extension of the DB theory was admitted and valid up $I \leq 0.01$mol L^{-1}.

$$log\gamma_x^{\pm} = -A\frac{|z^+\cdot z^-|\sqrt{I_m}}{1+1.5\sqrt{I_m}} \tag{2.25}$$

Davis added an empirical parameter to the previous equation, denoted as $L(I)$ or $C(I)$, depending on the electrolyte and ionic strength.

$$log\gamma_x^{\pm} = -A\frac{|z^+\cdot z^-|\sqrt{I_m}}{1+1.5\sqrt{I_m}} + L(I) \tag{2.26}$$

In this thesis, to evaluate the dependence of the formation constants on the ionic strength, the following Debye-Hückel type equation was used as a mathematical model:

$$log\beta = log\beta^0 - A\frac{z^*\sqrt{I}}{1+1.5\sqrt{I}} + C(I) \tag{2.27}$$

where β corresponds to the protonation or formation constant, β^0 is the protonation or formation constant at infinite dilution and the empirical parameter, $C(I)$, depends on the charges involved in the reaction.

Finally, $\qquad z^* = \sum(charges)^2_{reactans} - \sum(charges)^2_{products}$.

2.8.4 Dependence of the formation constants on the temperature

As the ionic strength, temperature can also affect equilibria in real systems, such as natural waters and biological fluids. The dependence of the equilibrium constants on the temperature can be assessed by the following Van't Hoff equation:

$$log^T\beta = log\beta_\theta + \frac{1}{2.303R}\Delta H_\theta^0 \left(\frac{1}{\theta} - \frac{1}{T}\right) \qquad (2.28)$$

where $log^T\beta$ is the equilibrium constant at a given temperature, expressed in Kelvin, $log\beta_\theta$ corresponds to the equilibrium constant at the reference temperature (θ) and, thus, at T = 298.15 K. R is 8.314472 J K^{-1} mol^{-1} when ΔH_θ refers to J mol^{-1}. The equation (2.29) allows to determine the enthalpy changes for a given species on the basis of the $log\beta$ values at different temperatures and it can be employed in molar and molal concentration scales. The Gibbs free energy, ΔG_i, and $T\Delta S_i$ values can be calculated by the following reactions and knowing the formation constants of the given species, $log\beta_i$.

$$\Delta G_i = -RTln\beta_i \qquad (2.29)$$

$$\Delta G_i = \Delta H_i - T\Delta S_i \qquad (2.30)$$

The Van't Hoff equation is valid when the enthalpy changes, ΔH_i, are approximatively constant in a given temperature range.

2.9 Sequestering ability

Evaluating the sequestering ability of a metal ion chelator is crucial in different research fields and in many environmental and medical applications, where chelating ligands can be used in the heavy metals removal from real and contaminated samples or also in chelation therapy. For the same purpose, in this treatment, chelating ligands are employed to detoxify tissues and, thus, organism from toxic metal ions. The assessment of the sequestering ability of a certain ligand

toward metals requires the knowledge of several factors, such as temperature, ionic strength, ion medium, acid-base behavior of the ligand, as well as of the metal, and competitive equilibria, which can be occurred among metals and ligands present in the real matrix simultaneously. All these aspects can act varying the formation yields of the species [14], and since all these interactions and phenomena should be considered in the determination of the sequestering ability of a ligand toward investigated metals, the research group promoted a semi empirical parameter in 2006 [85-87]. The previous pL_{50} [88, 89] is currently evolved in the $pL_{0.5}$ and corresponds to the total ligand concentration needed to sequester 50 % of a metal ion present in traces under specific conditions of pH, temperature and ionic strength, and also in the simultaneous presence of other components in the system. The $pL_{0.5}$ can be calculated using an usual speciation program following the procedure reported in Crea et al. [90], and obtained by plotting the sum of the molar fraction (χ) of the metals complexed by the ligand *vs*. pL, that is cologarithm ($pL = -logC_L$) of the total ligand concentration (C_L). It is a sigmoidal curve, getting by the following Boltzmann type equation with asymptote 1 for $pL \rightarrow -\infty$ and asymptote 0 for $pL \rightarrow +\infty$ [90, 91]:

$$\chi = \frac{1}{1+10^{(pL-pL_{0.5})}} \tag{2.31}$$

The greatest $pL_{0.5}$ value means the greatest efficiency of the ligand in sequestering the metal cation.

Using this approach, the sequestering ability of CAR, as well as of its derivatives, toward the investigated metal cations was assessed at different experimental conditions, which are summarized in Table 2.9.

Table 2.9. Experimental conditions for the determination of the sequestering ability of ligands toward metal cations.

Ligand Species	Metal species	pH	I [a]	T [b]
CAR	Ca^{2+}	7.4	0.1	310.15
	Mg^{2+}	7.4	0.1	310.15
	Cu^{2+}	7.4	0.1	310.15
	Mn^{2+}	7.4	0.1	310.15
	Zn^{2+}	7.4	0.1	310.15
CAR	Hg^{2+}	5.0-9.0	0.001-0.7	298.15-310.15
FcCAR	Hg^{2+}	7.0-9.0	0.1	298.15
PyCAR	Hg^{2+}	7.0-9.0	0.1	298.15
CAR	Pb^{2+}	5.0-9.0	0.001-0.7	298.15-310.15
FcCAR	Pb^{2+}	7.0-9.0	0.1	298.15
PyCAR	Pb^{2+}	7.0-9.0	0.1	298.15
CAR	Cd^{2+}	5.0-9.0	0.001-0.7	298.15-310.15
FcCAR	Cd^{2+}	7.4	0.1	298.15
PyCAR	Cd^{2+}	7.0-9.0	0.1	298.15

[a] in mmol L^{-1}. [b] in K.

Chapter 3

L-Carnosine (CAR) acid-base properties

CAR, as widely highlighted in Chapter 1, plays several roles in biological systems. The mechanisms of action and biochemical pathways of CAR, albeit unclear, depend firstly on its charge and, thus, on its own acid-base behaviour and distribution [92]. The protonation of the amino group, imidazole ring and carboxylate moiety occurs at different pH values, and the protonation state of any these sites can critically modify the proton-binding ability of the other functional groups and the charge-distribution over the whole CAR molecule [92]. Understanding the site- and species-specific protonation properties of CAR is therefore important to thoroughly elucidate its biochemical and physiological functions. The protonation state of a biologically active molecule, such as CAR, can also affect the binding process with other molecules and ions. On the other hand, acting as a pH buffer, CAR protonation and, thus, deprotonation do not influence metabolic processes [93].

However, considering the importance of fully understanding the role of CAR and its acid-base properties, and taking into account the importance of a speciation study, debated in Chapter 1, knowing the thermodynamic properties of the CAR molecule was crucial not only to understand and clarify its behaviour in aqueous solution, but also to evaluate its interactions with the solvation shells, to describe activity of its functional groups and its own intermolecular interactions.

For these reasons, a synergic combination of experimental and computational techniques was employed to determine the thermodynamic protonation parameters of CAR in NaCl aqueous solution and obtain a comprehensive and accurate

thermodynamic picture, structural information and proton capabilities of CAR molecule.

Determination of the protonation constant values of CAR was first of all achievable by the robust potentiometric measurements, performed as titrations in different ionic strength ($0.1 \leq I/ \text{ mol L}^{-1} \leq 1$), temperature ($288.15 \leq T/ \text{ K} \leq 310.15$) conditions and concentrations ($1 \leq C_L/ \text{ mmol L}^{-1} \leq 3$). Potentiometric data, processed by means of BSTAC and STACO computer programs, were confirmed by those acquired by UV-Vis spectrophotometric and ^{1}H NMR titrations at $I = 0.15$ mol L^{-1} and T = 298.15 K. HYSPEC and HYPNMR software were respectively used to process the UV-Vis spectrophotometric and ^{1}H NMR spectroscopic data.

Both experimental data and literature ones [94-96] were combined, in order to obtain reliable data on the protonation equilibria, evaluate the dependence of the stability constants on ionic strength and temperature, and thus deduce a consistent speciation model. Structural information and fragmentation pathways of CAR were clarified by means of Matrix Assisted Laser Desorption Ionization Mass Spectrometry (MALDI MS) and tandem mass spectrometry (MS/MS) techniques.

Quantum-mechanical calculations were also performed to quantitatively estimate the protonation capabilities of the various functional groups of CAR by means of the Gaussian 09 software [67].

3.1 Protonation constants determination [97]

The protonation constants values, obtained by potentiometry, are listed in Table 3.1, and reported as global formation constants β, and as stepwise formation constants K, referred, respectively, to the following reactions:

$$i\text{H}^+ + \text{L}^- = \text{H}_i\text{L}^{i-1} \qquad\qquad \beta \qquad (3.1)$$

$$H^+ + H_{i-1}L^{i-2} = H_iL^{i-1} \qquad\qquad K \qquad (3.2)$$

Stepwise formation constants are useful for evaluating the functional group involved in each protonation equilibria. CAR has three ionizable groups: the carboxylate (COO^-), the nitrogenous group (NH) of the imidazole ring, and the amino group of the β-alanine residue (NH_2). The $logK$ values of the three protonation steps are quite different from each other. Comparing them with the literature data of similar functional groups, the first protonation step ($9.03 \leq logK \leq 9.79$, depending on the conditions) is attributable to the amino group of the β-alanine residue, the second protonation step ($6.65 \leq logK \leq 6.99$) to the nitrogenous of the imidazole ring and the third one ($2.57 \leq logK \leq 2.81$) to the carboxylic group.

Table 3.1. CAR protonation constants values, obtained by potentiometry, in NaCl aqueous solutions in different ionic strength and temperature conditions.

Reaction	$log\beta$ [a]					
	T = 298.15 K				**288.15 K**	**310.15 K**
	I = 0.15 [b]	**I = 0.50** [b]	**I = 0.73** [b]	**I = 0.98** [b]	**I = 0.15** [b]	**I = 0.15** [b]
$L^- + H^+ = LH^0$	9.178±0.006 [c]	9.490±0.005 [c]	9.231±0.006 [c]	9.187±0.009 [c]	9.79±0.02 [c]	9.03±0.05 [c]
$L^- + 2H^+ = LH_2^+$	15.918±0.009	16.427±0.008	16.061±0.008	16.02±0.01	16.78±0.02	15.68±0.05
$L^- + 3H^+ = LH_3^{2+}$	18.49±0.02	19.24±0.01	18.76±0.01	18.63±0.02	19.37±0.02	18.45±0.04

	$logK$ [a]					
	T = 298.15 K				**288.15 K**	**310.15 K**
	I = 0.15 [b]	**I = 0.50** [b]	**I = 0.73** [b]	**I = 0.98** [b]	**I = 0.15** [b]	**I = 0.15** [b]
$L^- + H^+ = LH^0$	9.178	9.490	9.231	9.187	9.79	9.03
$LH^0 + H^+ = LH_2^+$	6.740	6.937	6.827	6.83	6.99	6.65
$LH_2^+ + H^+ = LH_3^{2+}$	2.57	2.81	2.70	2.61	2.59	2.77

[a] ref. [97]. [b] in mol L^{-1}. [c] ± 3 std. dev.

3.1.1 Dependence on the ionic strength

The dependence of the protonation constants on the ionic strength was determined by the Debye-Hückel type equation (2.27) and studied by taking into account the literature data (Table 3.10) and the experimental values reported in the Table 3.1. The equation (2.27) also allowed to obtain the $log\beta^0$ and the empirical parameter C, at T = 298.15K. All these values are collected in Table 3.2.

Table 3.2. Formation constant values at infinite dilution and C parameters for the dependence on the ionic strength (equation 2.27), at T = 298.15 K.

Reaction	$log\beta^{0}$ [a]	C [a]
$L^- + H^+ = LH^0$	9.62 ± 0.04 [b]	0.01
$L^- + 2H^+ = LH_2^+$	16.41 ± 0.04	0.08
$L^- + 3H^+ = LH_3^{2+}$	18.89 ± 0.06	-0.17

[a] ref. [97]. [b] $\pm$ 3 std. dev.

The influence on the ionic strength is also visible on the species distribution, as can be observed in Figure 3.1.
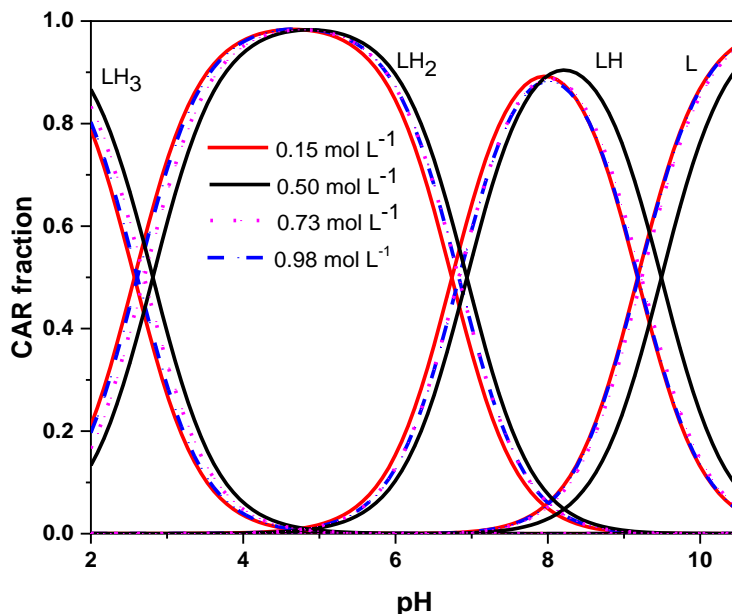
Figure 3.1. Speciation diagram *vs*. pH of the CAR (L)-H$^+$ system (charges omitted for simplicity) in NaCl aqueous solutions at I = 0.15 mol L^{-1} (solid red line), I = 0.50 mol L^{-1} (solid black line), I = 0.73 mol L^{-1} (dot magenta line), I = 0.98 mol L^{-1} (dashed blue line), and at T = 298.15 K (C$_L$ = 1 mmol L^{-1}).

The protonation process of CAR was described by M. Jozanovic et al. [98], and showing that, at low pH values, all groups are protonated and the molecule holds an overall positive charge. For intermediate pH values (isoelectric point) the peptide is found as the common dipolar zwitterion, exhibiting a total net charge equal to zero whilst, and upon increasing the pH, the molecule shows a globally negative charge.

The distribution diagram reported in Figure 3.1 clearly displays that for $5.0 \leq pH \leq 8.0$, range of interest for most biological fluids, the equilibrium involved is the second one, *i.e.*, $LH^0 + H^+ = LH_2^+$. In fact, CAR is present as LH_2^+ or LH^0 species, whose formations reach a maximum at pH = 5.0 and 8.0, respectively. It is necessary to consider pH < 4.0 for the protonation of the carboxylic group (formation of LH_3^{2+} species) and pH > 9.0 for the deprotonation of the amino group

of the β-alanine residue (L$^-$ species). The effect of the ionic strength on the protonation constant values, even though not very marked, cannot be neglected. As an example, *logK* values referred to the first protonation step vary at most from 9.178 (at I = 0.15 mol L^{-1}) to 9.490 (at I = 0.50 mol L^{-1}). This implies a shift of 0.5 pH units for species formation, as can be noticed in Figure 3.1. In terms of CAR fraction, this means that at pH = 7.0 and I = 0.15 mol L^{-1}, there are ∼0.34 of LH$_2$ and ∼0.64 of LH. Keeping constant that given pH value but varying the ionic strength to I = 0.5 mol L^{-1}, the fraction of both species is ∼0.5. Looking again on Figure 3.1, the increase in the ionic strength from I = 0.15 mol L^{-1} to I = 0.98 mol L^{-1} does not give rise to a significant change in the curves. A different profile is evident at I = 0.50 mol L^{-1}, whose shift toward higher pH values is more pronounced than the species distribution at I = 0.73 mol L^{-1}.

The knowledge of the parameters in Table 3.2 is useful to evaluate the protonation constant values in conditions that differ from the experimental ones. By way of example, the calculated protonation constant values at different ionic strength and T = 298.15 K are reported in Table 3.3.

Table 3.3. Calculated protonation constant values of CAR (L$^-$) at different ionic strengths and T = 298.15 K.

Reaction	*logβ* [a]				
	I = 0.15 [b]	I = 0.25 [b]	I = 0.5 [b]	I = 0.75 [b]	I = 1 [b]
L$^-$ + H$^+$ = LH^0	9.38±0.03[c]	9.34±0.03[c]	9.28±0.03[c]	9.25±0.05[c]	9.23±0.07[c]
L$^-$ + 2H$^+$ = LH$_2^+$	16.17±0.03	16.14±0.03	16.10±0.04	16.09±0.06	16.08±0.08
L$^-$ + 3H$^+$=LH$_3^{2+}$	18.86±0.04	18.84±0.04	18.80±0.04	18.76±0.06	18.72±0.08

[a] ref. [97]. [b] in mol L^{-1}. [c] ± 3 std. dev.

To document the consistency of the data, some examples of calculated constant values, along with the respective errors, *vs.* ionic strength are reported in Figure 3.2. As can be observed, a slight decrease is occurred in the pattern as the ionic strength increases. Moreover, the fitting curves obtained by calculating the parameters of Table 3.2 are shown in Figure 3.3.
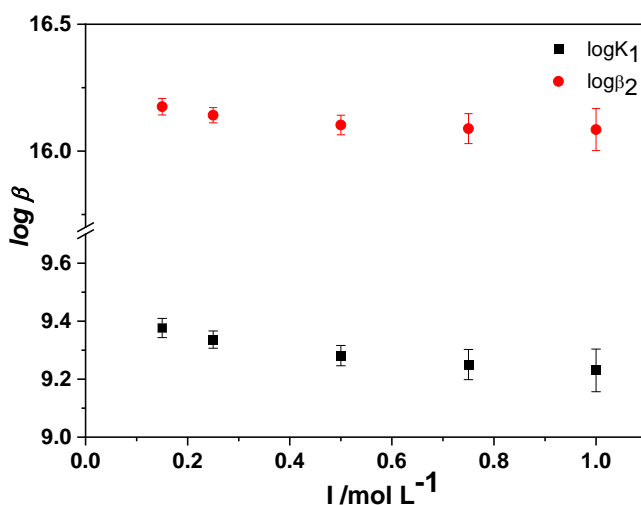
Figure 3.2. Calculated protonation constant values of CAR *vs.* ionic strength.
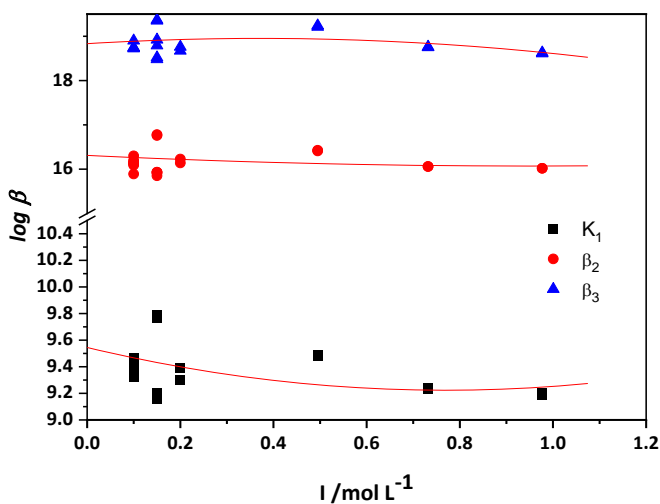
Figure 3.3. Fitting curves obtained in the calculation of the parameters of Table 3.2 for the main text for the protonation constants of CAR.

3.1.2 Dependence on the temperature

The dependence of the protonation constants on the temperature was determined by the Van't Hoff equation (2.28), at I = 0.15 mol L^{-1}, taking into account the literature data (Table 3.10) and the experimental values reported in Table 3.1, In this way, a complete thermodynamic picture was obtained and the ΔH changes, along with ΔG and $T\Delta S$ values, are summarized in Table 3.4. In particular, ΔG and $T\Delta S$ values were derived from equations (2.29) and (2.30) respectively.

Table 3.4. Thermodynamic formation parameters of CAR (L^-) species in NaCl at I = 0.15 mol L^{-1}.

Reaction	ΔG [a), b)]	ΔH [a), b)]	$T\Delta S$ [a), b)]
$L^- + H^+ = LH^0$	-52.4±0.03[c)]	-46±8 [c)]	6±8 [c)]
$L^- + 2H^+ = LH_2^+$	-90.9±0.05	-66±9	25±9
$L^- + 3H^+ = LH_3^{2+}$	-105.5±0.1	-36±11	70±11
$L^- + H^+ = LH^0$	-52.4	-46	6
$LH^0 + H^+ = LH_2^+$	-38.5	-20	19
$LH_2^+ + H^+ = LH_3^{2+}$	-14.7	30	45

[a)] In kJ·mol^{-1}. [b)] ref. [97]. [c)] ± 3 std. dev.

To better distinguish among the different molecular functional groups, thermodynamic parameters concerning the stepwise equilibria (equation 3.2) are also shown in Table 3.4, through which various considerations on the equilibria can be made. As far as the protonation is concerned, for the first one, *i.e.*, the equilibrium involving the protonation of the amino group of the β-alanine residue, the process is exothermic (ΔH = -46 kJ mol^{-1}) with a typical value referred to an amino group, where the main contribution to the free energy is enthalpic ($T\Delta S$ = 6 kJ mol^{-1}); the second protonation step (protonation of the nitrogenous of the imidazole ring) is also exothermic (ΔH = -20 kJ mol^{-1}), but enthalpy and entropy

equally contribute to the free energy ($T\Delta S = 19$ kJ mol^{-1}). The most acidic protonation step, *i.e.*, that referring to the protonation of the carboxylic group, is endothermic ($\Delta H = 30$ kJ mol^{-1}) with a main entropic contribution to the free energy ($T\Delta S = 45$ kJ mol^{-1}).

As for the dependence on the ionic strength, similar considerations can be made on the temperature dependence, whose effect is marked on the three protonation equilibria. In particular, in the first protonation step, the *logK* varies from 9.79 (at T = 288.15 K) to 9.03 (at T = 310.15 K), in the second one, the *logK* value is 6.99 (at T = 288.15 K) and 6.65 (at T = 310.15 K). In the third protonation step, the *logK* increases from 2.59 (at T = 288.15 K) to 2.77 (at T = 310.15 K).
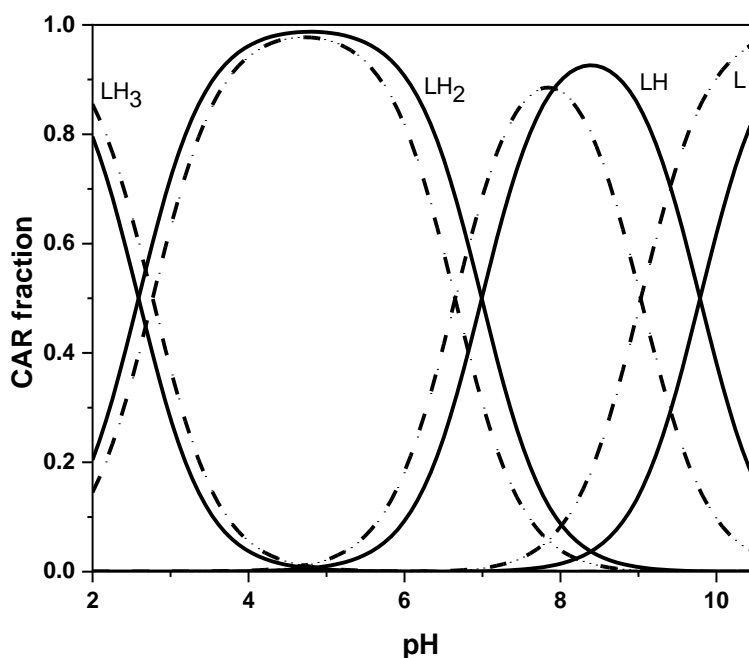
Figure 3.4. Speciation diagram *vs*. pH of the CAR (L)-H$^+$ system (charges omitted for simplicity) in NaCl aqueous solution at I = 0.15 mol L^{-1}, T = 288.15 K (solid line), and T = 310.15 K (dashed line), (C_L = 1 mmol L^{-1}).

The distribution diagram reported in Figure 3.4 clearly shows that an increase in temperature, from T = 288.15 K to T = 310.15K, causes a shift of the protonated species (LH_3^{2+}) toward higher pH values and a pronounced shift of the monoprotonated (LH^0) and deprotonated (L^-) species toward lower pH values.

The possibility to calculate the protonation constants at different temperatures, as well as at various ionic strength, from those under investigation allows to simulate the distribution of the species in various natural fluids. Obviously, all this information also allows to calculate the formation constant values at different temperatures, which are reported in Table 3.5.

Table 3.5. Calculated protonation constants values of CAR (L^-) at different temperatures and I = 0.15 mol L^{-1}.

Reaction	$log\beta$ [a]				
	278.15 K	288.15 K	308.15 K	310.15 K	318.15 K
$L^- + H^+ = LH^0$	9.9±0.1[b]	9.65±0.08 [b]	9.12±0.07 [b]	9.07±0.08 [b]	8.9±0.1 [b]
$L^- + 2H^+ = LH_2^+$	17.0±0.1	16.58±0.08	15.80±0.08	15.73±0.08	15.4±0.1
$L^- + 3H^+ = LH_3^{2+}$	19.3±0.2	19.08±0.10	18.66±0.09	18.62±0.09	18.5±0.2

[a] ref. [97]. [b] ± 3 std. dev.

As far as the dependence of the calculated constant values on the ionic strength is concerned, Figure 3.5 shows some examples of the calculated constant values, along with the respective errors, *vs*. temperature. A slight decrease is observed in the pattern as the temperature decreases. The fitting curves were also obtained by calculating the parameters of Table 3.4 and depicted in Figure 3.6.
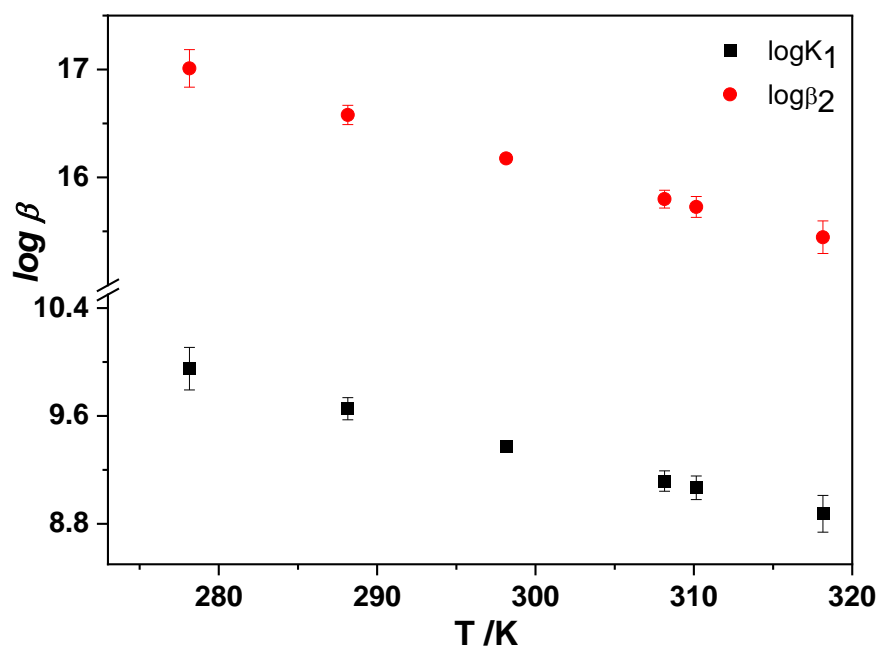
Figure 3.5. Calculated protonation constant values of CAR *vs*. temperature.
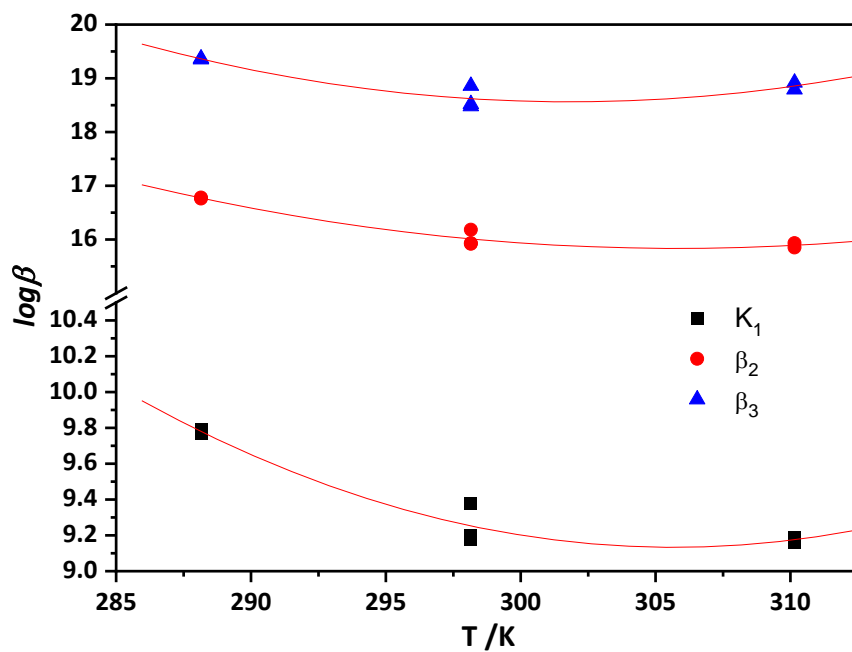
Figure 3.6. Fitting curves obtained in the calculation of the parameters of Table 3.4 for the main text for the protonation constants of CAR.

3.2 UV-Vis spectrophotometric and ^{1}H NMR spectroscopic results

UV-Vis spectrophotometric and ^{1}H NMR data were elaborated using the HYSPEC and HypNMR computer programs, respectively. Both allowed to calculate protonation constants, but also the molar Absorbance and the chemical shift of each species, respectively.

UV-Vis spectrophotometric and ^{1}H NMR spectroscopic titrations were performed from pH ≈ 2.5 to pH ≈ 10.5, as depicted in Figures 3.7 and 3.9, respectively. In the literature, the UV absorption spectrum of CAR (0.88 mmol L^{-1}) is reported, with bands at 264.5, 214, and 209 nm, assigned to n–p*, p–p*, and p–p* electronic transitions, respectively [4]. Branham et al. [4] also described that at much lower concentrations (0.08 mmol L^{-1}), there is only the broad band around 214 nm and the peak at 264.5 nm disappears completely.

However, at the concentrations used in this study, CAR displays a single UV band with a fairly broad shape in acidic environment and reaches a maximum of absorption at λ = 209 nm (Figure 3.7). As the pH increases, and thus the deprotonation degree of the CAR molecule, a gradual gain in Absorbance occurs. Similar considerations can be made by focusing on Figure 3.8, which shows the calculated values of molar Absorbance for each CAR species as a function of the wavelength. As can be observed, ε/ mol^{-1} cm^{-1} L increases as the pH grows and, thus, the deprotonation degree of CAR species.
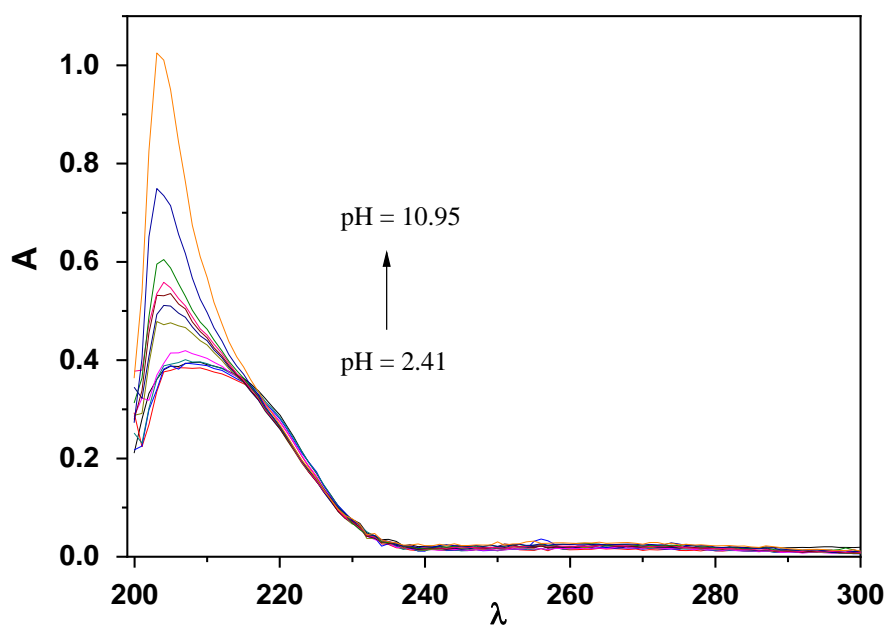
Figure 3.7. UV-Vis spectrophotometric titrations of CAR in NaCl at I = 0.15 mol L^{-1} and T = 298.15 K (C$_L$ = 0.02 mmol L^{-1}).
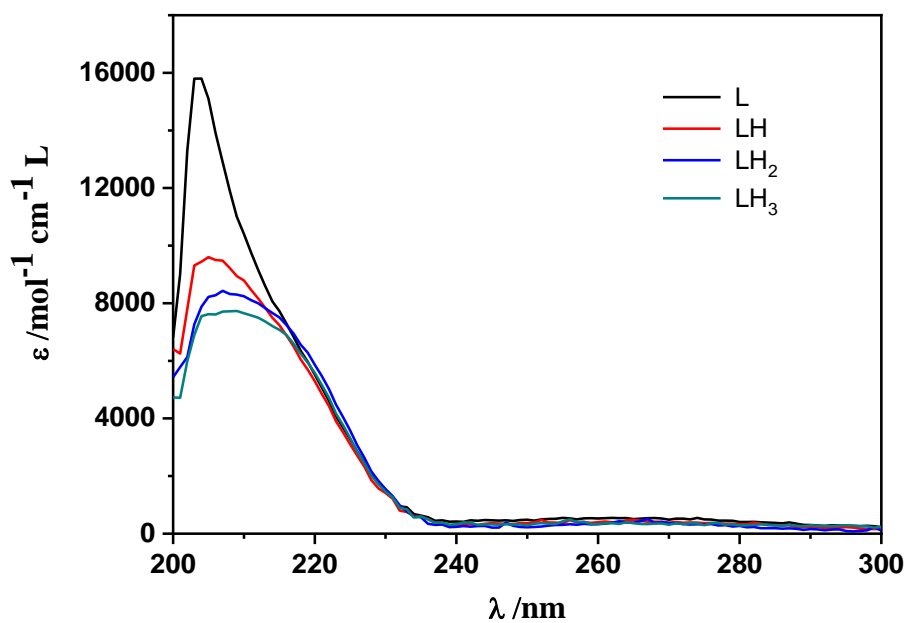
Figure 3.8. Molar absorption coefficients of CAR (L) species, as a function of the wavelength.

From the ^{1}H NMR analysis of CAR in different pH solutions, an evident variation in the chemical shift of the imidazole protons (CH-2 and CH-4) can be noticed, starting from pH > 4.0 (Figure 3.9). In correspondence with the disappearance of the NH-8 amide signal, it can reasonably be stated that from pH > 4.0, first the carboxylic group and then the NH imidazole proton are deprotonated. This clearly affects the chemical shift of the heterocyclic protons ($\Delta\delta \sim 1$ ppm). Minimal chemical shift variations are appreciated for the other protons CH-10 and CH-11, highlighting a non-involvement of the amino group NH_2 in the equilibria at pH < 9.0.

The calculated values of the chemical shift for each species are given in Table 3.6.
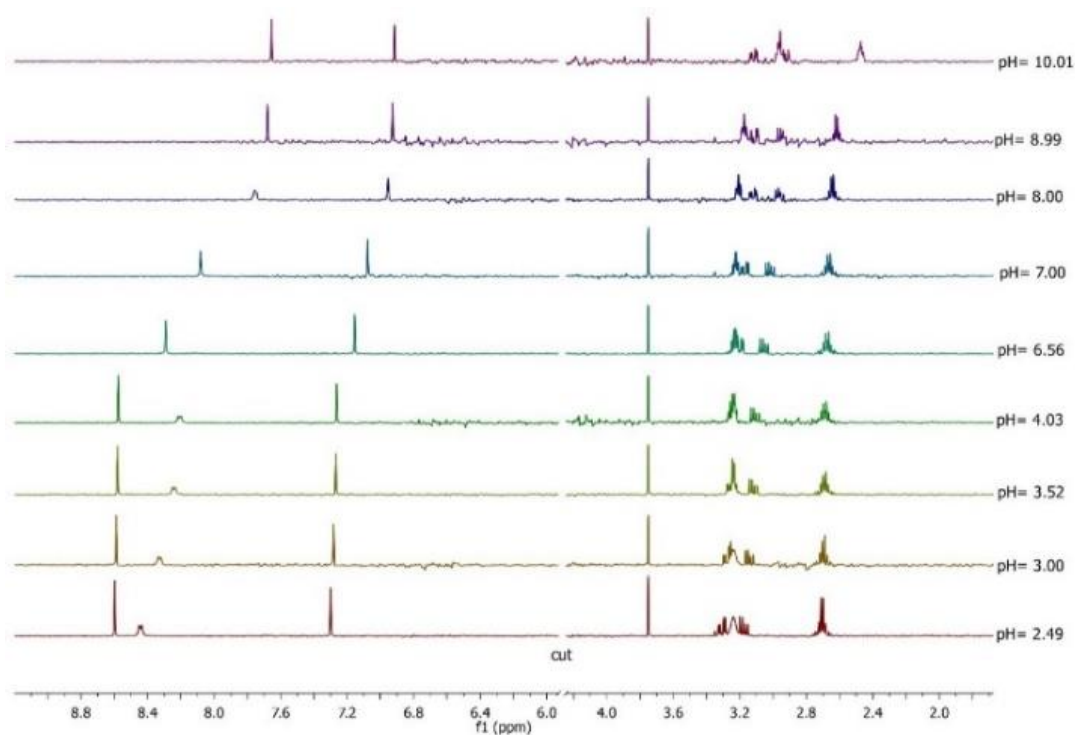
(a)
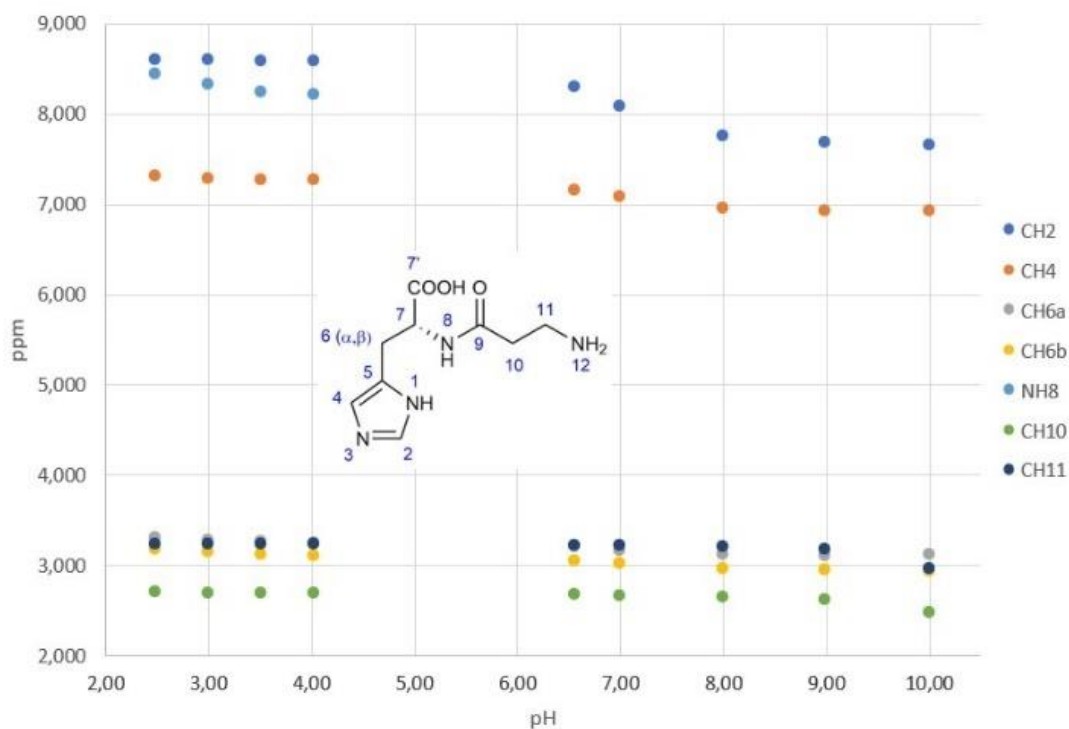
(b)

Figure 3.9. (a) ^{1}H NMR titrations of CAR in water ($C_L = 3$ mmol L^{-1}), from pH $\approx$ 2.5 to pH $\approx$ 10.0 and **(b)** spreadsheet of chemical shifts of CAR protons as a function of pH.

Table 3.6. Chemical shifts for each nucleus.

δ [a]	L	LH	LH_2	LH_3
CH2	$7.64\pm0.01^{[b]}$	$7.70\pm0.01^{[b]}$	$8.58\pm0.01^{[b]}$	$8.61\pm0.01^{[b]}$
CH4	6.910 ± 0.038	6.930 ± 0.048	7.260 ± 0.038	7.320 ± 0.038
$CH6_\alpha$	3.12 ± 0.09	3.11 ± 0.09	3.25 ± 0.09	3.34 ± 0.09
$CH6_\beta$	2.93 ± 0.04	2.95 ± 0.04	3.10 ± 0.04	3.22 ± 0.04
CH10	2.460 ± 0.034	2.660 ± 0.034	2.680 ± 0.034	2.720 ± 0.033
CH11	2.92 ± 0.08	3.24 ± 0.08	3.23 ± 0.08	3.25 ± 0.08

[a] ref. [97]. [b] $\pm$ 3 std. dev.

78

Despite both the UV-Vis spectrophotometric and ^{1}H NMR data were collected starting from pH $\approx$ 2.5, it was not possible to calculate the protonation constant concerning the formation of the LH_3^{2+} species and, therefore, the value obtained by the potentiometric technique was used. The protonation constants values, obtained by processing the UV-Vis spectrophotometric and ^{1}H NMR data at I = 0.15 mol L^{-1} and T = 298.15 K, are reported in Table 3.7. As far as the third protonation step, which regards the formation of the LH_3^{2+} species, the respective value obtained by potentiometry is listed in the same Table 3.7, for comparison. A perfect agreement was found for the second protonation step, while quite slight discrepancies can be observed for the first one.

Table 3.7. CAR protonation constants values in NaCl aqueous solution at I = 0.15 mol L^{-1} and T = 298.15 K, obtained by different experimental techniques.

Reaction	$log\beta$ [a]	
	UV-Vis spectrophotometry	^{1}H NMR spectroscopy
$L^- + H^+ = LH^0$	9.57±0.05 [b]	9.13±0.03 [b]
$L^- + 2H^+ = LH_2^+$	15.97±0.05	15.986±0.001
$L^- + 3H^+ = LH_3^{2+}$	(18.49)	(18.49)

[a] ref. [97]. [b] ± 3 std. dev.

3.3 Mass spectrometry results [99]

Experimental studies were performed on the CAR molecule using Matrix Assisted Laser Desorption Ionization Mass Spectrometry (MALDI MS) and tandem mass spectrometry (MS/MS) techniques. As discussed in Chapter 2, the MALDI MS (TOF/TOF) technique was chosen for its high sensitivity and accuracy, as well as its short analysis time and ability to detect different compounds in highly complex mixtures [60-62]. The first issue was to identify the most suitable MALDI matrix for analyses. In fact, the choice and use of an adequate matrix leads to highly

resolved spectra with excellent signal-to-noise (S/N) ratio, negligible analyte fragmentation, and modest matrix background in the mass range of the analyte. These aspects are particularly important for small molecules, as in the case of the dipeptide under study. In the experimental conditions for the detection and characterization of CAR, an aliquot (1μL) of solution (1mM) was analyzed by MS experiments in positive ionization mode using traditional matrices (α−CHCA, DHB). The best results were obtained with the use of 2,5-Dihydroxybenzoic acid (DHB), as interference between the matrix and analyte is minimal. CAR was also analyzed by Collision Induced Dissociation (CID) MS/MS in order to obtain a deeper understanding of its fragmentation pathways, which are shown in Figure 3.10. The resulting CID MS/MS spectrum of CAR (m/z 227.11; $[C_9H_{15}N_4O_3]^+$) is depicted in Figure 3.11, and the relative MS and MS/MS fragment ions are collected in Table 3.8. The relative molecular formula of the fragments can be interpreted partially according to Peiretti et al. [100], and partly as the dipeptide backbone fragmentation. In the CID MS/MS spectrum of CAR (Figure 3.11), peaks of m/z 210.09 ($[C_9H_{12}N_3O_3]^+$), 209.10 ($[C_9H_{13}N_4O_2]^+$), and 156.08 ($[C_6H_{10}N_3O_2]^+$) were detected as the most abundant fragment ions from the precursor ion (m/z 227.11; $[C_9H_{15}N_4O_3]^+$). The ammonia loss is the most intense process and the [LH-17+H]$^+$ ion results in the formation of the peak of m/z 210.09 ($[C_9H_{12}N_3O_3]+$), which gives rise two main products by the elimination of water (m/z 192.08; $[C_9H_{10}N_3O_2]^+$) and cycloprop-2-en-1-one (m/z 110.07; $[C_5H_8N_3]^+$; schematic in Figure 3.10). The water loss from the precursor ion leads to the formation of the m/z 209.10 ion ($[C_9H_{13}N_4O_2]^+$), followed by elimination of the β-alanine moiety, in order to obtain the ion of m/z 138.07 (z1(+1) ion, $[C_6H_8N_3O]^+$). The direct fragmentation of the precursor ion also results in the formation of m/z 156.08 (y1(+1) ion, $[C_6H_{10}N_3O_2]^+$), by cleavage of the peptide bond. Finally, the low-mass ions could be attributable to fragmentation of the histidine side chain (Figures 3.10 and 3.11, Table 3.8).
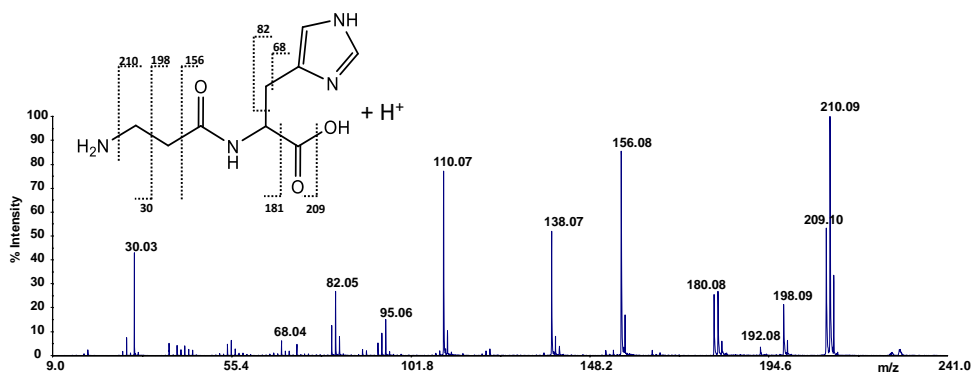
Figure 3.10. CID MS/MS fragmentation pathways of CAR (m/z 227.11; $[C_9H_{15}N_4O_3]^+$).

Figure 3.11. CID MS/MS spectrum of CAR (LH) (m/z 227.11; $[C_9H_{15}N_4O_3]^+$).

Table 3.8. MS and MS/MS fragment ions of CAR (LH) (m/z 227.11; $[C_9H_{15}N_4O_3]^+$).

Carnosine	Composition	Detected Mass	Δppm
[LH+H]$^+$	$[C_9H_{15}N_4O_3]^+$	227.11	5.0
MS/MS fragments	$[C_9H_{12}N_3O_3]^+$	210.09	6.0
	$[C_9H_{13}N_4O_2]^+$	209.10	7.0
	$[C_8H_{12}N_3O_3]^+$	198.09	8.0
	$[C_9H_{10}N_3O_2]^+$	192.08	9.0
	$[C_8H_{10}N_3O_2]^+$	180.08	7.5
	$[C_6H_{10}N_3O_2]^+$	156.08	9.0
	$[C_6H_8N_3O]^+$	138.07	8.0
	$[C_5H_8N_3]^+$	110.07	7.5
	$[C_5H_7N_2]^+$	95.06	6.0
	$[C_4H_6N_2]^{\bullet+}$	82.05	6.5
	$[C_3H_4N_2]^{\bullet+}$	68.04	8.0
	$[CH_4N]^+$	30.03	5.0

3.4 Electrochemistry of CAR

As pointed out in Chapter 1, the aim of the work was to exploit the metal chelating ability of CAR and, thus, its sensing properties in the detection of certain metal cations. For this purpose, electrochemical methods are widely employed to study amino acids and peptides.

However, to date, there is no clear evidence for the electrochemical activity of CAR, as there is for its precursor amino acid, L-Histidine. The latter was studied electrochemically by M. Medvidović-Kosanović et al. [44] in a pH range of 4.0 to 10.0 by CV and DPV. They found that L-histidine is not electroactive in CV, but shows an oxidation peak ($E_{p,a}$ = 0.860 V) at pH = 10.0 in DPV. However, more precisely, the last peak corresponds to the oxidation of the imidazole ring of the L-Histidine, which is not found to be electroactive in the investigated pH range. In more detail, the totally deprotonated species (L^-) of histidine was found to be involved in the oxidation reaction, unlike the partially deprotonated species (LH_2^+ and LH^0), which were not involved in the redox process [44]. These results are in agreement with the following deconvoluted voltammograms on SPCE in KCl (0.1 mol L^{-1}) aqueous solution (Figures 3.12, 3.13 and 3.14). As can be observed in Figures 3.13 and 3.14, a slight band is visible around $E_{p,a}$ = 1.150 V, which could be attributable to the imidazole ring. The other peak, at $E_{p,a}$ = 1.36 V, is attributable to the blank solution.
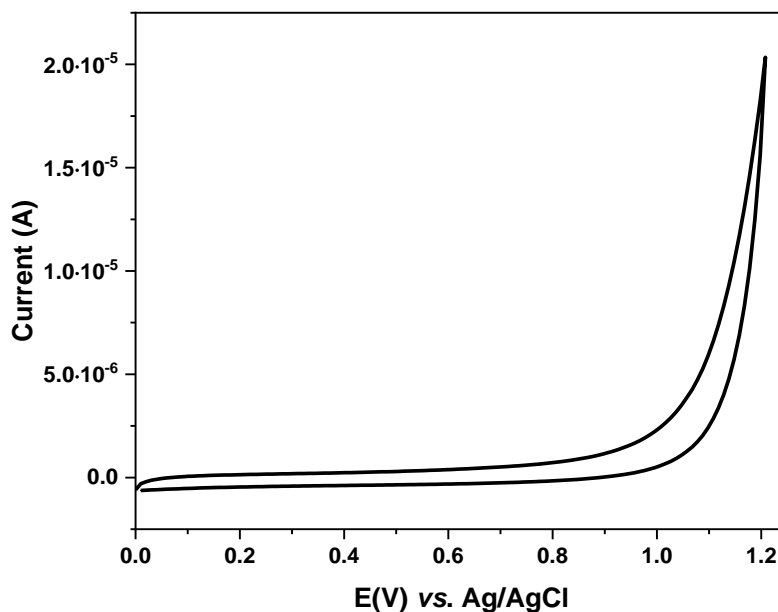
Figure 3.12. CV of L-Histidine (C_L = 1 mmol L^{-1}) in KCl (0.1 mol L^{-1}) aqueous solution on SPCE. Scan rate: 0.1 V s^{-1}.
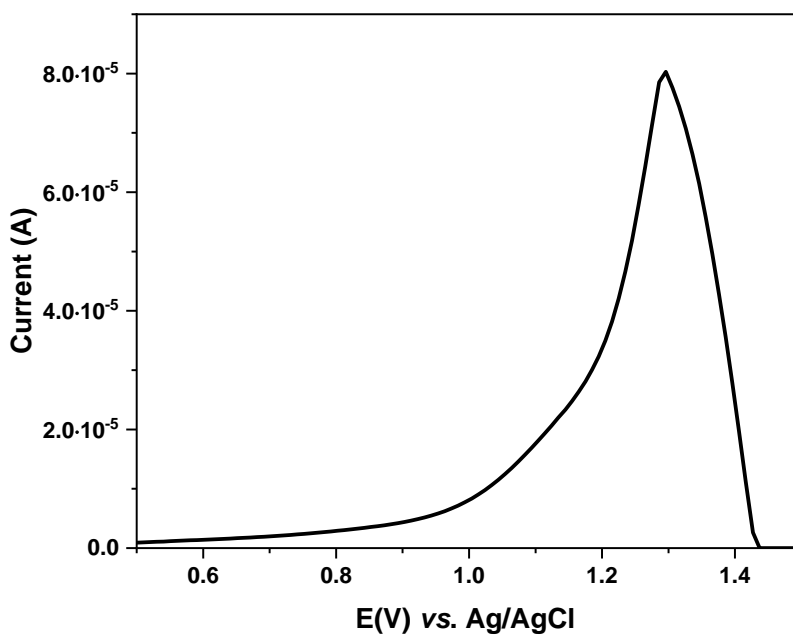
Figure 3.13. DPV of L-Histidine (C_L = 1 mmol L^{-1}) in KCl (0.1 mol L^{-1}) aqueous solution on SPCE.
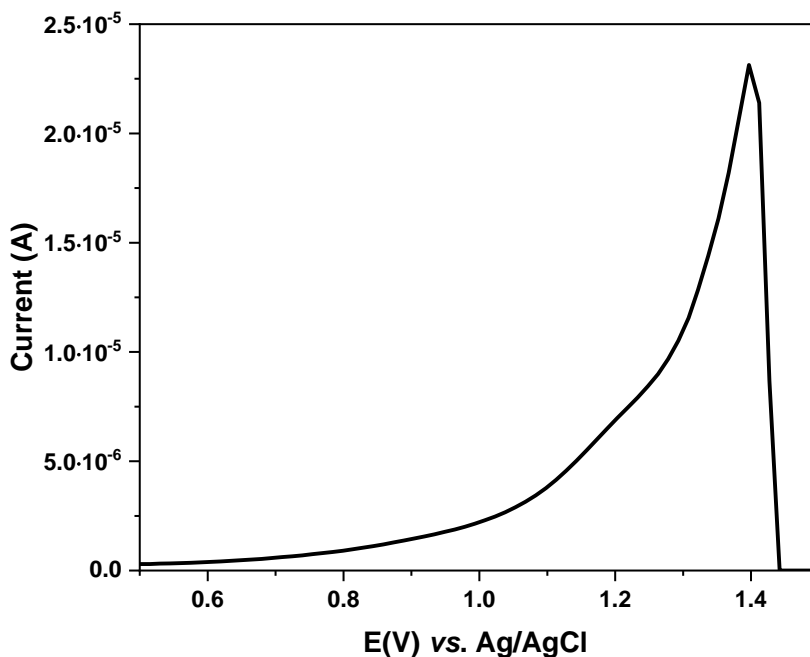
Figure 3.14. SWV of L-Histidine (C_L = 1 mmol L^{-1}) in [1] KCl (0.1 mol L^{-1}) aqueous solution on SPCE.

Considering that a high concentration of histidine was used for electrochemical analysis, the data obtained were rather scarce and unsatisfactory. Similar results, not many reproducible, are consequently obtained in the voltammetric study of CAR, performed in a wide pH range from 4.0 to 10.0 on SPCE. CAR, as its precursor, shows nearly inert electroactivity.

Therefore, to improve the electrochemical performance of CAR on SPCE, a strategic approach was adopted using two different dispersions, already described in Chapter 2.

    i)   Nafion.

    ii)   CNO.

The aim of this work was to develop a highly sensitive voltammetric method for carnosine determination. Thus, Nafion and CNO were used to improve sensitivity of SPCE [65]. Voltammetric tests for CAR were performed on modified SPCEs with respective Nafion and CNO dispersions in a wide pH range ($3.0 \leq pH \leq 10.0$). DPVs obtained for CAR on the individual modified electrodes are shown in Figures 3.15 and 3.16 in acid and alkaline environments, respectively. The DPV scans in Figure 3.15 reveal a slight oxidation peak ($E_{a,p} \cong 1.09$ V) for CAR (1 mmol L^{-1}) in KCl (0.1 mol L^{-1}) at pH $\cong$ 3.0. This result was obtained for preconcentration potential and time equal to 0.8 V and 60 s, respectively. Only this oxidation value is in line with the oxidation peak for CAR ($E_{a,p} = 1.15$ V), obtained on bare SPCE, described by Jozanović et al. [101]. However, the oxidation peak disappears as the CAR concentration increases, and the KCl peak shifts toward the cathodic potential range when the solution pH is acidic (Figure 3.15). On the other hand, DPV in Figure 3.16 reveals an oxidation peak ($E_{a,p} = 0.735$ V), which could be attributable to the CAR molecule at the highest concentration (10 mmol L^{-1}). The oxidation peak tends to decrease, up to disappear, as the number of scans increases. For instance, this effect is shown in Figure 3.16.

Therefore, the data obtained are neither clear nor reproducible. However, these results have given rise to the idea of synthetizing a more electroactive and versatile CAR derivative, with the aim of searching for its electrochemical properties, as well as its sensing capability toward metal cations.
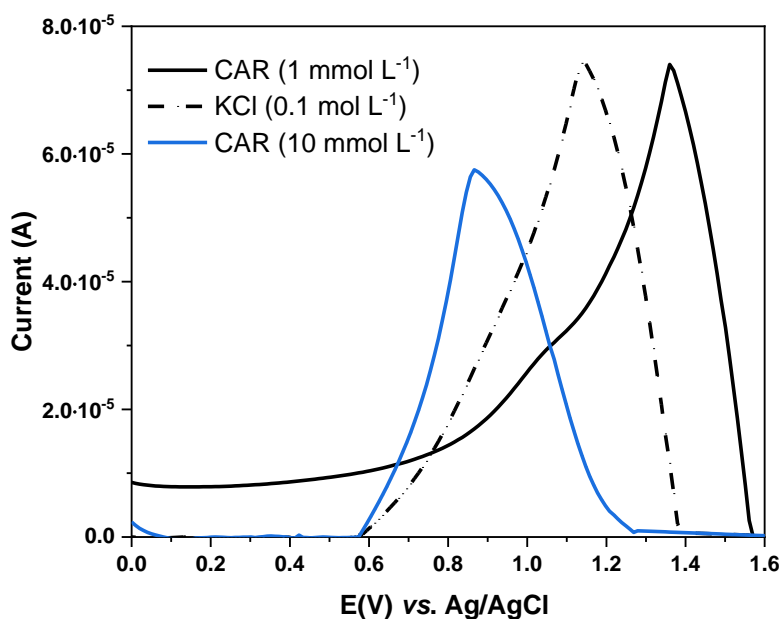
Figure 3.15. DPV scans of CAR ($1 \leq C_L/$ mmol $L^{-1} \leq 10$) in KCl (0.1 mol L^{-1}) aqueous solution on Nafion/SPCE (pH $\cong$ 3.0).
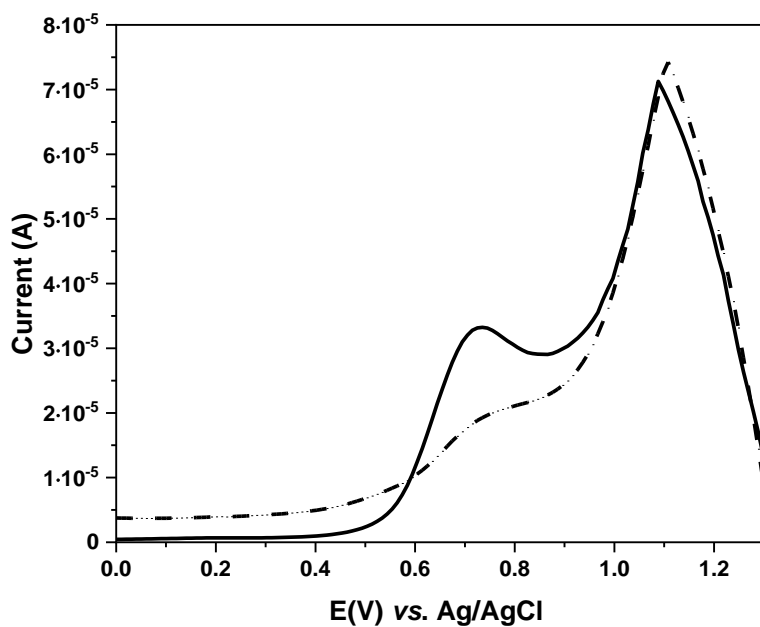

Figure 3.16. First (solid line) and second (dashed line) DPV scan of CAR ($C_L = 10$ mmol L^{-1}) in KCl (0.1 mol L^{-1}) aqueous solution on CNO/SPCE (pH $\cong$ 10.0).

3.5 Computational results [97]

As pointed out in Chapter 2, both CAR tautomeric forms of the imidazole ring were considered for the quantum-mechanical computational analyses. However, the very small total energy difference between the two tautomers makes the presentation of the respective results redundant for both forms. Therefore, this thesis uniquely refers to the tautomer depicted in Figure 3.17. The quantum-mechanical calculations results are in line with the indications obtained from the literature, on the basis of the values of the stepwise formation constants referred to the different nature of the functional groups. Indeed, the Proton Affinity (PA) shown by the amino group of the β-alanine residue of the CAR molecule solvated in water is the largest one (*i.e.*, ≈ 1189 kJ mol^{-1}). Quantum-mechanical calculations highlighted that the large PA of the NH_2 group of the β-alanine residue can be ascribed to two main factors: *(i)* the presence of the nearby CH_2 group, which repels electrons, and *(ii)* the presence of the oxygen atom of the CO group of the CAR molecule. The latter acts as a stabilizer of the extra charges not only when protons are in excess, *via* the formation of an internal H-bond, but also when an extra electron is present, due to proton deficiency on the NH_2 group, as shown in Figure 3.17.

In addition to the well-known significant PA of the amino group of the β-alanine residue, other functional groups are suitable candidates for accepting protons in acid conditions. In particular, as shown in Table 3.9, a PA similar to that observed for the amino group of the alanine residue is also found for the bare nitrogen atom of the imidazole ring, protonated species labeled as H_2L^+ (2) (*i.e.*, ≈ 1184 kJ mol^{-1}). As depicted in Figure 3.18 (column H_2L^+ (2)), the nitrogen atom, once the proton is accepted, forms a strong H-bond with the nucleophilic oxygen atom of the nearest CO group, hence, stabilizing the whole protonated molecular structure and increasing the PA value relative to this functional group. Furthermore, the relaxed molecular structure also benefits from the presence of an internal H-bond between

the NH_3^+ group and the deprotonated carboxylic one. Similar considerations also apply to the protonation of the carboxylic group of the CAR molecule, as shown in Figure 3.18 (column $H_2L^+(1)$). However, once the structural relaxation occurs, the COOH group partially loses the excess proton in favor of the bare nitrogen atom of the imidazole ring, establishing a strong H-bond with the latter. This circumstance does not alter the previously existing H-bond between the NH_3^+ group and the CAR carbonyl one, under the globally neutral zwitterionic state, as visible in Figure 3.18 (column H_2L^+ (1)). The presence of the two internal H-bonds results into a PA equal to ≈ 1151 kJ mol^{-1}, as listed in Table 3.9. Therefore, it is not so surprising that this value is close to that exhibited by the bare nitrogen atom, due to the fact that this latter is fully involved in the stabilization process of the cationic state of the CAR molecule both when it is directly protonated and when protonation is forced on the COO$^-$ zwitterion group. Once again, this aspect sheds light on the strong propensity carried by the bare nitrogen atom of the imidazole ring to attract protons. Finally, another possible protonation site is constituted by the nitrogenous group (NH) of the imidazole ring. However, since this event corresponds to a PA equal to ≈ 984 kJ mol^{-1} (Table 3.9), it is so far the least likely. In fact, as shown in Figure 3.18 (column H_2L^+ (3)), the stable molecular configuration associated with the protonation of this functional group completely hinders the possibility of forming an internal H-bond additional to that normally established between the NH_3^+ group and the carboxylic one. It is noteworthy that all static calculations were performed under implicit solvation conditions and representing the ground-state molecular structure of differently protonated states of the CAR molecule, as predicted by quantum-mechanical (Density Functional Theory, DFT) laws.
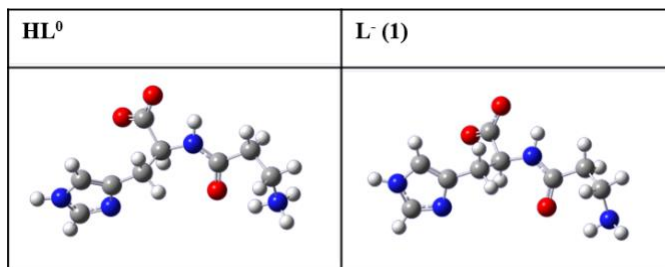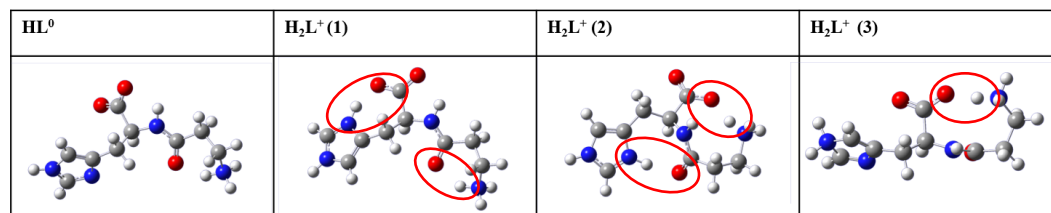
Figure 3.17. Ground-state structures of the CAR molecule for different protonation states, as determined by DFT calculations performed at the B3LYP/6-311++G(2d,2p) level under implicit water solvation. HL^0, neutral zwitterion; $L^-(1)$, deprotonated. Deprotonation has been executed on the NH_3^+ group ($H_2L^+(1)$).

Table 3.9. Total energies (in a.u., first row) and Proton Affinity (PA, in kJ·mol^{-1}, second row) of CAR, determined both from cationic and neutral zwitterionic species, calculated at the B3LYP/6-311++G(2d,2p) DFT level in water for the protonation of the COO^- group ($H_2L^+(1)$), of the nitrogen atom of the imidazole ring ($H_2L^+(2)$), and of the nitrogenous group NH of the imidazole ring ($H_2L^+(3)$).

CAR (L)	HL^0	$H_2L^+(1)$	$H_2L^+(2)$	$H_2L^+(3)$
Water	-796.11	-796.56	-796.57	-796.50
PA	-	1151	1184	984

Figure 3.18. Ground-state structures of the CAR molecule for different protonation states, as determined by DFT calculations performed at the B3LYP/6-311++G(2d,2p) level under implicit water solvation. HL^0, neutral zwitterion; H_2L^+, protonated. Protonation has been executed on the COO^- group ($H_2L^+(1)$), the nitrogen atom of the imidazole ring ($H_2L^+(2)$), and the NH group of the imidazole ring ($H_2L^+(3)$). Red circles identify internal H-bonds stabilizing the protonated molecular structures.

3.6 Literature comparisons

The characterization of protonation equilibria of CAR was carried out in different literature reports [44]. The values of CAR protonation constants reported in the literature are summarized in Table 3.10. However, the dependence on the ionic strength and temperature was not investigated thoroughly. Therefore, this in-depth study was performed in order to elucidate, first of all, the thermodynamic parameters of CAR and also the protonation capabilities of its functional groups.

As just written in Paragraph 3.1, the consistency of the data was also proved in the synergic combination of the experimental and literature data, in particular in the calculation of the dependence of CAR protonation constants values on the ionic strength and temperature.

Moreover, structural information and fragmentation pathway of CAR were elucidated by Matrix Assisted Laser Desorption Ionization Mass Spectrometry (MALDI MS) and tandem mass spectrometry (MS/MS) techniques.

Table 3.10. Literature protonation constant values of CAR.

Ionic medium	T /K	I /mol L^{-1}	$log\beta_1$	$log\beta_2$	$log\beta_3$	Ref.
NaClO$_4$	298.15	0.1	9.397	16.20	17.493	[102]
	298.15	0.1	9.35	16.09	18.72	[103]
	298.15	0.1	9.32	15.89	-	[104]
NaCl	298.15	0	9.37	16.14	18.73	[93]
KCl	298.15	0.1	9.372	16.146	18.740	[105]
	298.15	0.2	9.30	16.14	18.67	[106]
	298.15	0.2	9.39	16.23	18.76	[107]
	310.15	0.15	9.20	15.89	18.65	[92]
KNO$_3$	298.15	0.1	9.372	16.15	18.74	[108]
	298.15	0.1	9.466	16.30	18.90	[109]
	298.15	0.1	9.36	16.12	-	[110]
	298.15	0.1	9.40	16.18	18.75	[111]
	310.15	0.15	9.04	15.83	18.37	[112]
	310	0.15	9.04	15.62	18.26	[113]

3.7 Final remarks

The synergy of the various techniques, together with the analysis of literature data, allowed to obtain robust thermodynamic parameters on the acid-base properties of CAR.

- In particular, potentiometry allowed firstly to explore the acid-base behavior of the CAR molecule over a wide range of ionic strength and temperature.
- In this way, thermodynamic parameters (ΔH, ΔG and $T\Delta S$) were calculated by equations (2.28), (2.29) and (2.30).
- Protonation constants values, obtained by potentiometry, were in accordance with those derived from the processing of UV-Vis spectrophotometric and ^{1}H NMR data.
- The thermodynamic investigation was also enriched by the computational results, which allowed to determine the Proton Affinity (PA) of the functional groups of the CAR molecule.
- On the other hand, mass spectrometry provided structural information and fragmentation pathways of CAR.
- However, the voltammetric activity of CAR could not be known. This molecule, indeed, shows an irreversible and nonreproducible redox process.
- Therefore, electrochemical methods were used to study a more electroactive carnosine derivative, ferrocenyl-carnosine (FcCAR). The latter was synthetized in Tarragona under the supervision of Prof. Fragoso.

In this thesis, the synthesis and analysis of FcCAR are reported in Chapter 5.

Chapter 4

M^{2+}-L-Carnosine (CAR) interactions

Metals are an essential part of the entire ecosystem, whether they are alkalis, alkaline-earth cations, or transitions metals [45], which also have different oxidation states. All metals are found in biological and environmental fields, both in elemental and ionic forms. Metal ions are widely employed for industrial and analytical purposes, as they are involved in many biochemical processes within the living body. Metal cations are, indeed, ubiquitous in biological systems, where they take part at the cellular and extracellular levels and in the central nervous system [45].

Complexes of metal cations with amino acids or peptides can be used as models to study the pharmacological effects of drugs [44]. As far as carnosine is concerned, various works report its remarkable metal ion chelating properties, particularly marked with respect to bivalent cations (M^{2+}) [5, 7, 18, 114]. However, there was no clear evidence in the literature on the interactions between the dipeptide and bivalent metal cations. For this reason, and as written for the protonation determination of CAR, an in-depth thermodynamic study was necessary to understand the M^{2+}-CAR interactions, as well as the formation constants values and their dependence on the ionic strength and temperature. This effect is also important, as metal complexes can affect both mechanistic pathways and physiological roles of CAR itself.

To study M^{2+}-CAR interactions, a combination of experimental techniques was employed. First of all, potentiometric titrations were performed under different conditions of ionic strength ($0.1 \leq I/ \text{ mol L}^{-1} \leq 1$), temperature ($288.15 \leq T/K \leq$

310.15) and metal:ligand ratios. As reported in Chapter 2 (Paragraph 2.2.2), equilibrium constant values of all the metal cations under study are known from the literature [115-121] and, consequently, were not experimentally investigated in this thesis.

Therefore, the strength of interactions, the presence of complex species and their stoichiometry, were defined along with the formation constants and speciation models for each M^{2+}-CAR system. In particular, the speciation models were chosen on the basis of some general criteria, such as simplicity, species formation rates, standard and mean deviation of the fit. For each system studied, the speciation models are summarized in Table 4.1. Formation constants values of the M^{2+}-CAR complex species, obtained by potentiometry, are given as β_{pqr}, or β_{pqr}^{OH}, according to the equations (2.21) or (2.22).

Once a complete thermodynamic picture was established for each M^{2+}-CAR system, ^{1}H NMR spectroscopic titrations were performed on some of the M^{2+}-CAR systems investigated. In particular, for the Ca^{2+}-, Mn^{2+}-, Cu^{2+}- and Zn^{2+}-CAR systems, ^{1}H NMR spectroscopic measurements were carried out to confirm the speciation models, previously determined by potentiometric ones. The experimental conditions adopted are summarized in Table 2.8. However, the processing of the ^{1}H NMR data yielded only the formation constants values of the Ca^{2+}- and Zn^{2+}-CAR systems. In fact, the paramagnetic nature of the Mn^{2+}- and Cu^{2+}- ions did not allow reliable ^{1}H NMR information to be obtained in the same experimental conditions used for the Ca^{2+}- and Zn^{2+}-CAR systems.

In this thesis, the M^{2+}-CAR interactions are debated according to the nature of the metal cations under study, namely in the following order:

- 4.1. Alkaline-earth metals, Ca^{2+} and Mg^{2+}.

  For both cations, *ab initio* molecular dynamics (AIMD) simulations also clarified the complexation mechanisms of Ca^{2+} and Mg^{2+} to the dipeptide by explicitly treating, at the quantum level, the role of the water solvation.

- 4.2. First transition metal cations series, Mn^{2+}, Cu^{2+} and Zn^{2+}.

  For these metal cations, integration with further investigation by High Resolution (HR) Matrix Assisted Laser Desorption Ionization (MALDI) Mass Spectrometry (MS) elucidated the Mn^{2+}-, Cu^{2+}- and Zn^{2+}- CAR chelating modes.

- 4.3. Cd^{2+} as a metal of the second transition metal cation series.

- 4.4. Third transition metal cations series, Hg^{2+} and Pb^{2+}.

The resulting synergistic effect of the experimental and computational methods was crucial to better distinguish the structural and coordination features of the M^{2+}-CAR complex species.

Finally, for all these metal cations studied, the sequestering ability of the CAR was determined according to the equation (2.31). The resulting sequestering diagrams, simulated according to the experimental conditions given in Table 2.9, are shown in Figures 4.28 and 4.29.

Table 4.1. Experimental formations constants values of M^{2+}-CAR (L^-) systems, obtained by potentiometry, in NaCl aqueous solutions in different ionic strength and temperature conditions.

				logβ			
				T = 298.15 K			288.15 K	310.15 K
M^{2+}	Species	I = 0.15 [a]	I = 0.50 [a]	I = 0.73 [a]	I = 0.98 [a]	I = 0.15 [a]	I = 0.15 [a]
Ca^{2+} [b]	ML^+	2.97±0.03 [c]	3.26±0.04 [c]	3.57±0.04 [c]	3.50±0.05 [c]	2.87±0.03 [c]	3.09±0.05 [c]
	MLH^{2+}	12.13±0.05	12.18±0.03	12.49±0.03	12.75±0.03	11.97±0.02	12.19±0.04
	MLH_2^{3+}	18.74±0.07	18.93±0.05	18.99±0.04	19.41±0.05	18.61±0.04	18.95±0.06
Mg^{2+} [b]	ML^+	2.74±0.04	-	-	-	2.86±0.07	2.49±0.05
	MLH^{2+}	11.77±0.04	11.64±0.03	11.78±0.04	11.82±0.04	12.05±0.06	11.30±0.05
	MLH_2^{3+}	18.38±0.05	18.36±0.04	18.70±0.03	18.82±0.04	18.91±0.06	17.74±0.05
		I = 0.15 [a]	I = 0.49 [a]	I = 0.72 [a]	I = 0.98 [a]	I = 0.15 [a]	I = 0.15 [a]
Mn^{2+} [d]	ML^+	3.34±0.05 [c]	3.40±0.04 [c]	3.53±0.05 [c]	3.35±0.03 [c]	3.44±0.02 [c]	4.52±0.05 [c]
	MLH^{2+}	12.56±0.02	12.05±0.05	12.22±0.05	12.12±0.03	12.05±0.02	13.12±0.04
	MLH_2^{3+}	19.33±0.03	18.34±0.07	18.80±0.05	18.41±0.04	18.36±0.04	19.41±0.03
Cu^{2+} [d]	ML^+	8.27±0.01	7.87±0.01	7.77±0.01	7.58±0.02	8.44±0.04	8.01±0.02
	MLH^{2+}	13.46±0.02	13.33±0.01	13.34±0.02	13.40±0.02	13.80±0.05	13.08±0.04
	ML_2H^+	21.10±0.03	20.49±0.07	20.42±0.08	20.35±0.08	21.4±0.2	20.61±0.04

	MLOH	2.65±0.01	2.376±0.006	2.315±0.009	2.27±0.01	2.80±0.02	2.31±0.02
	$ML(OH)_2^-$	-8.38±0.02	-8.62±0.02	-8.51±0.02	-8.90±0.04	-8.04±0.04	-8.05±0.06
Zn^{2+} [d]	MLH^{2+}	12.63±0.03	12.24±0.02	12.20±0.04	12.23±0.03	12.90±0.06	12.08±0.04
	MLH_2^{3+}	18.81±0.03	18.35±0.03	17.8±0.1	17.33±0.08	18.83±0.06	18.66±0.02
	MLOH	-2.85±0.03	-3.40±0.02	-3.63±0.04	-3.73±0.03	-3.09±0.02	-3.21±0.03
		I = 0.15 [a]	**I = 0.49** [a]	**I = 0.72** [a]	**I = 0.96** [a]	**I = 0.15** [a]	**I = 0.15** [a]
Cd^{2+}	ML^+	3.11±0.07 [c]	3.68±0.05 [c]	3.90±0.05 [c]	4.13±0.06 [c]	4.22±0.04 [c]	3.42±0.08 [c]
	MLH^{2+}	12.17±0.03	12.69±0.03	12.96±0.06	13.15±0.03	13.07±0.03	11.80±0.07
	MLH_2^{3+}	18.85±0.03	-	-	-	-	-
Hg^{2+}	ML^+	17.28±0.01	17.61±0.02	18.08±0.03	18.36±0.01	17.49±0.08	16.81±0.02
	MLH^{2+}	24.37±0.02	25.20±0.04	26.03±0.07	25.60±0.07 [c]	25.26±0.02	23.63±0.07
	MLOH	9.46±0.03	8.90±0.02	9.03±0.02	9.07±0.02 [c]	10.38±0.04	8.95±0.02
		I = 0.15 [a]	**I = 0.5** [a]	**I = 0.75** [a]	**I = 0.977** [a]	**I = 0.15** [a]	**I = 0.15** [a]
Pb^{2+}	ML_2^0	8.65±0.08 [c]	8.89±0.08 [c]	8.88±0.07 [c]	8.3±0.1 [c]	10.05±0.07 [c]	8.44±0.08 [c]
	ML_2H^+	18.06±0.02	17.76±0.02	17.58±0.03	17.44±0.03	18.65±0.04	17.57±0.04
	MLH_2^{3+}	18.31±0.02	-	-	-	-	-

[a] in mol L^{-1}. [b] ref. [97]. [c] ± 3 std. dev. [d] ref. [99].

Table 4.2. Experimental formation constants values of Ca^{2+}- [97] and Zn^{2+} - [99] CAR (L^-) systems, obtained by ^1H NMR spectroscopy, in NaCl aqueous solutions at $I = 0.15$ mol L^{-1} and $T = 298.15$ K.

Reaction	$log\beta$
$Ca^{2+} + L^- = CaL^+$	(2.97) [a]
$Ca^{2+} + L^- + H^+ = CaLH^{2+}$	12.11 ± 0.04 [b]
$Ca^{2+} + L^- + 2H^+ = CaLH_2^{3+}$	18.87 ± 0.04
$Zn^{2+} + L^- + H^+ = ZnLH^{2+}$	12.5 ± 0.4
$Zn^{2+} + L^- + 2H^+ = ZnLH_2^{3+}$	19.18 ± 0.02
$Zn^{2+} + L^- + H_2O = ZnLOH^0 + H^+$	-2.9 ± 0.3

[a] value obtained by potentiometry. [b] $\pm$ 3 std. dev.

4.1 Alkaline-earth metals, Ca^{2+}- and Mg^{2+}-, with CAR

Although CAR does not belong to the metalloproteinases, its intriguing metal ion chelating ability has caused the dipeptide to be increasingly studied. Considering the potential beneficial properties of CAR, more emphasis has been placed on bivalent metal cations of biological interest. In fact, high concentrations of Ca^{2+} and CAR in biological tissues can lead to important complex species [122].

As written in Chapter 1, 99% of CAR is found in skeletal muscle tissues, where it plays different roles in homeostasis during anaerobic respiration [92], acting as a pH buffer [7], and increasing the Ca^{2+} sensitivity of contractile units [123]. Moreover, taking advantage of the anti-glycating, anti-aging and dermocosmetic properties of CAR, its supplementary uses have also shown positive effects on the skin. In particular, Mg^{2+}-CAR complex species provided a superior delivery of CAR in the lower skin layers, up to 60% with respect to the free CAR [16].

Therefore, considering that the biological and physiological roles of CAR are strongly based on its acid-base properties and its interactions with bivalent metal ions, studying the speciation of the M^{2+}-CAR systems was pivotal to better

understand the activities of the resulting complex species. Moreover, no literature data reported the dependence of the formation constants values of M^{2+}-CAR systems on the ionic strength and temperature. Thus, as above-mentioned, this effect was investigated potentiometrically for all M^{2+}-CAR systems studied in this thesis.

4.1.1 Ca^{2+}-CAR complexes

In Table 4.1, the speciation model includes species with 1:1 metal-ligand ratio at each value of ionic strength and temperature. Three metal complex species are formed, namely ML^+, MLH^{2+} and MLH_2^{3+}, whose $log\beta$ values tend to increase as ionic strength and temperature growth. In particular, for the ML^+ species, the $log\beta$ value varies from 2.97 (at I = 0.15 mol L^{-1}) to 3.50 (at I = 0.98 mol L^{-1}), and from 2.87 (at T = 288.15 K) to 3.09 (at T = 310.15 K). For the MLH^{2+} species, the trend is $12.13 \leq log\beta$ value ≤ 12.75 in the following ionic strength range $0.15 \leq$ I/ mol L^{-1} ≤ 0.98 and $11.97 \leq log\beta$ value ≤ 12.19 for that concerning the temperature, $288.15 \leq$ T/ K ≤ 310.15. A greater increase is found for the MLH_2^{3+} species, whose $log\beta$ ranges from 18.74 (at I = 0.15 mol L^{-1}) to 19.41 (at I = 0.98 mol L^{-1}), and from 18.61 (at T = 288.15 K) to 18.95 (at T = 310.15 K). Figure 4.1 shows the species distribution *vs*. pH at two different ionic strength values. As can be noticed, M^{2+} is coordinated with CAR throughout the pH range investigated and at the two ionic strength values considered. The free M^{2+} fraction decreases by about 0.3 units passing from I = 0.15 mol L^{-1} (solid line) to I = 0.98 mol L^{-1} (dashed line). On the other hand, the molar fraction of the metal is approximatively 0.6 as MLH_2^{3+} (for $3.5 \leq$ pH ≤ 6.0). The MLH^{2+} and ML^+ species also reach 0.6 at I = 0.15 mol L^{-1}, and 0.8 at I = 0.98 mol L^{-1}, at pH = 8.0 and pH = 10.0, respectively. Figure 4.2, instead, shows the species distribution *vs*. pH at two different temperature values. In both cases, as can be observed, the formation of the three complex species occur.

However, M^{2+} is much coordinated to CAR at T = 310.15K (dashed line), and only an amount (~ 0.2) of free metal is found throughout the pH range. An amount of about 0.8 free M^{2+} fraction is present up to pH $\sim$ 6.0 at T = 288.15 K (solid line). In this condition, the metal molar fraction is approximatively 0.2 in the form of MLH_2^{3+} (for $3.5 \leq pH \leq 6.5$), 0.3 and greater than 0.5 in the MLH^{2+} (at pH = 8.0) and ML^+ species (for pH $\geq$ 10.0), respectively. At T = 310.15 K, the MLH_2^{3+} species amounts to 0.8 in the following pH range ($3.8 \leq pH \leq 5.0$), the MLH^{2+} and ML^+ ones reach 0.6 at pH = 8.0 and pH = 10.0, respectively.

In order to confirm the speciation model provided for potentiometry, ^{1}H NMR spectroscopic measurements were also performed as titrations, and the corresponding spectra of Ca^{2+}-CAR solutions, at different pH values, are depicted in Figure 4.3. The spectra of carnosine (Figure 3.9 (a)) and Ca^{2+}-CAR system (Figure 4.3) are very similar [97]. The proton signals in the complexes are affected by a faint downfield effect ($\Delta\delta \sim 0.1$) in regard to the free ligand. The variations involved six chemical shift signals which allowed to determine the formation constants values (Table 4.2) and confirm the speciation model previously defined by potentiometric titrations.

The formation constants values of the $CaLH^{2+}$ and $CaLH_2^{3+}$ species are achieved taking into account that obtained by potentiometry relative to the CaL^+ species, which is 2.97. In light of the expected speciation model, the good agreement between the experimental and calculated chemical shifts is depicted in Figure 4.4. However, it is not possible to distinguish well between free and coordinated ligand because, as written, the species that took part in the equilibria were rapidly exchanging on the NMR time scale [97]. Therefore, no relevant assumptions were made about the nature and amount of complex species. In spite of the weakness of Ca^{2+}-CAR interactions, to assess its effect on the ligand speciation, a simulated distribution diagram at "real" concentrations is shown in Figure 4.5. As highlighted in Chapter 1, CAR may amount to 20 mmol L^{-1} in skeletal muscle tissues and to

very low concentrations in plasma ($80 \leq$ nmol L$^{-1} \leq 125$), where it can reach 140 µmol L^{-1} after beef consumption [97]. In this condition, Ca^{2+}-CAR complexes are important; in particular, 0.55 of the ligand molar fraction is found to be in the MLH^{2+} form at physiological pH (7.4) (Figure 4.5). This diagram was derived from the thermodynamic data at $I = 0.15$ mol L^{-1} and $T = 310.15$ K, that are the physiological conditions of the plasma. However, the data shown in Tables 3.1 and 4.1. allow to simulate the respective speciation of CAR and M^{2+}-CAR systems at different experimental conditions of element concentration, ionic strength and temperature.
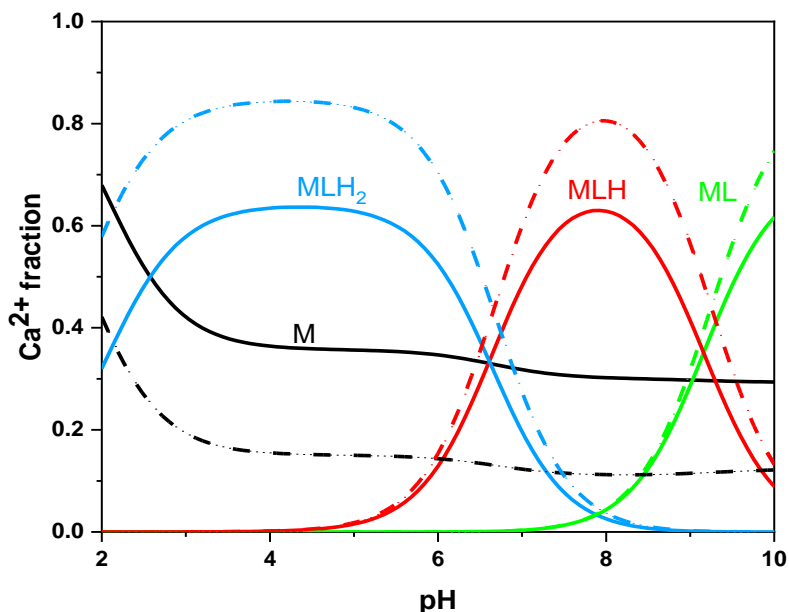
Figure 4.1. Speciation diagram *vs*. pH of the Ca^{2+}-CAR (L) system (charges omitted for simplicity) in NaCl aqueous solution at I = 0.15 mol L^{-1} (solid line) and I = 0.98 mol L^{-1} (dashed line), T = 298.15 K (C_M = 2 mmol L^{-1}, C_L = 4 mmol L^{-1}).
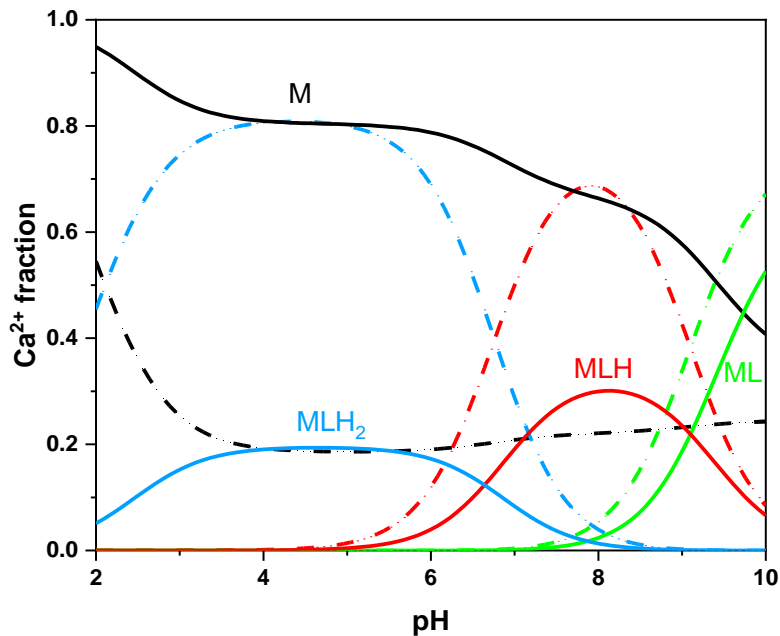
Figure 4.2. Speciation diagram *vs*. pH of the Ca^{2+}-CAR (L) system (charges omitted for simplicity) in NaCl aqueous solution at T = 288.15 K (solid line) and T = 310.15 K (dashed line), I = 0.15 mol L^{-1} (C_M = 2 mmol L^{-1}, C_L = 4 mmol L^{-1}).
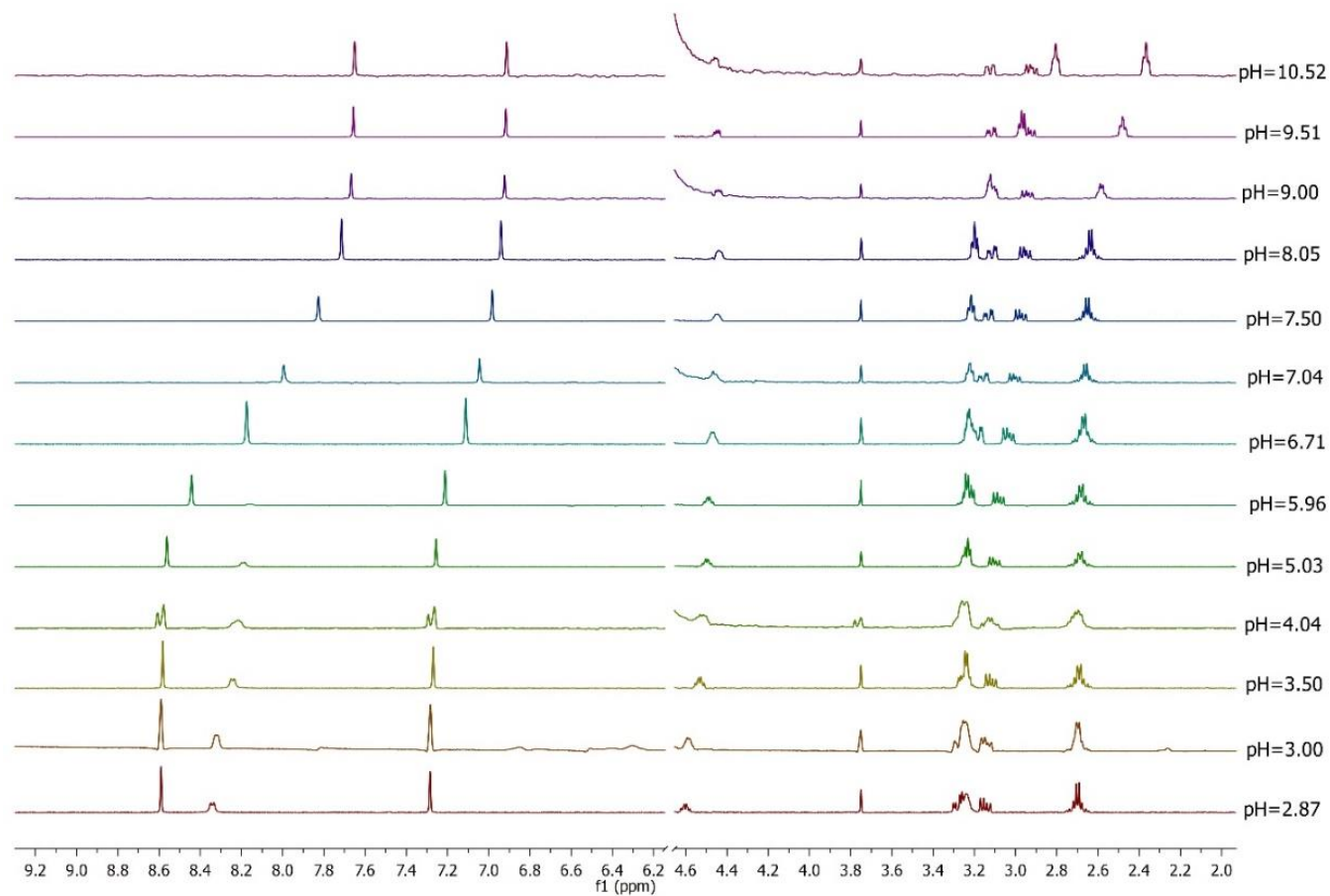
Figure 4.3. ^{1}H NMR titrations of the Ca^{2+}-CAR system in aqueous solution in the following pH range, $2.5 < \text{pH} < 10.5$ ($C_M = 4$ mmol L^{-1}, $C_L = 6$ mmol L^{-1}).
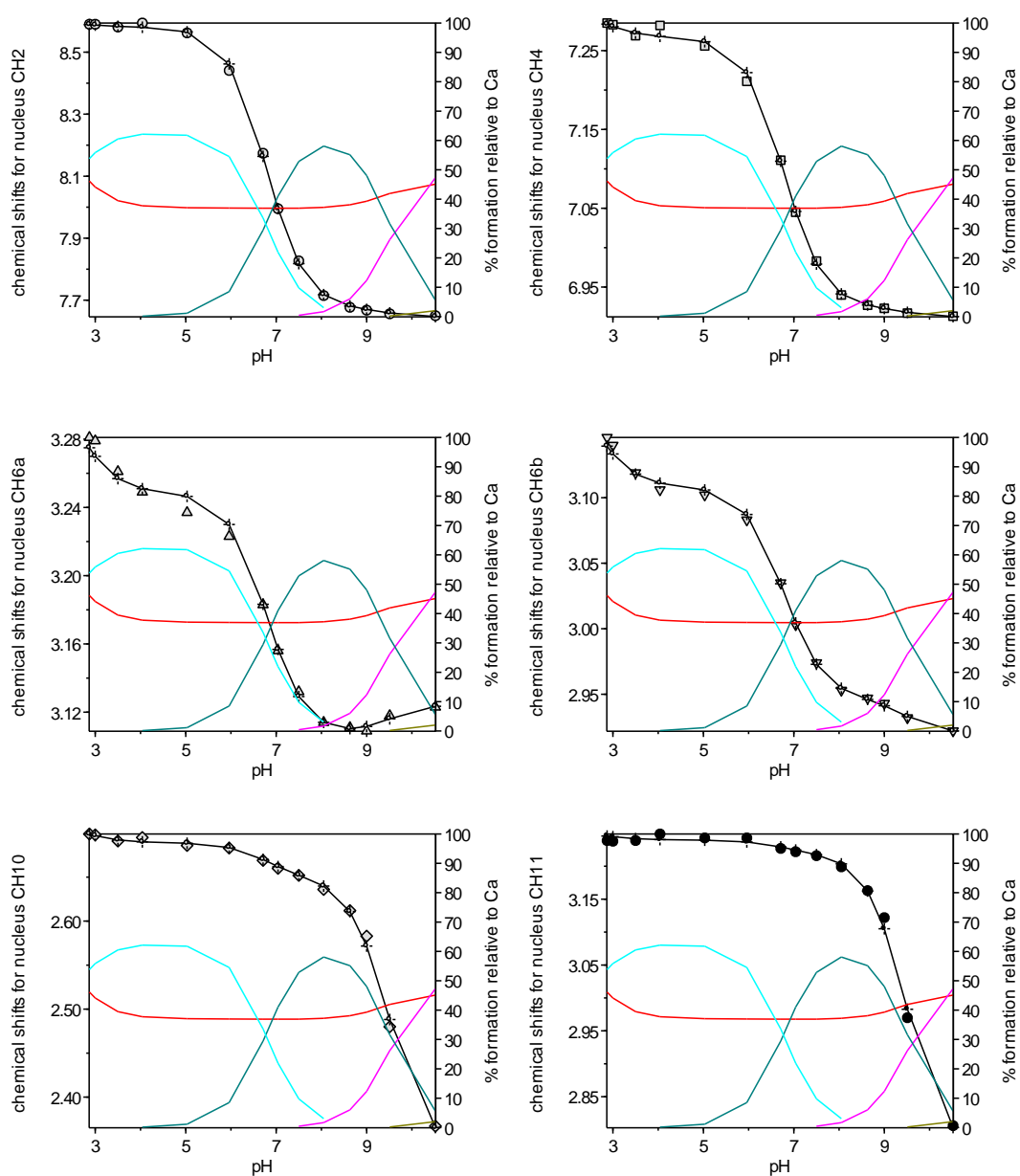
Figure 4.4. Experimental and calculated chemical shifts *vs.* pH of the Ca²⁺-CAR system, along with the formation percentages of CaLH₂ (cyan), CaLH (green), CaL (magenta) and free Ca²⁺ (red) species.
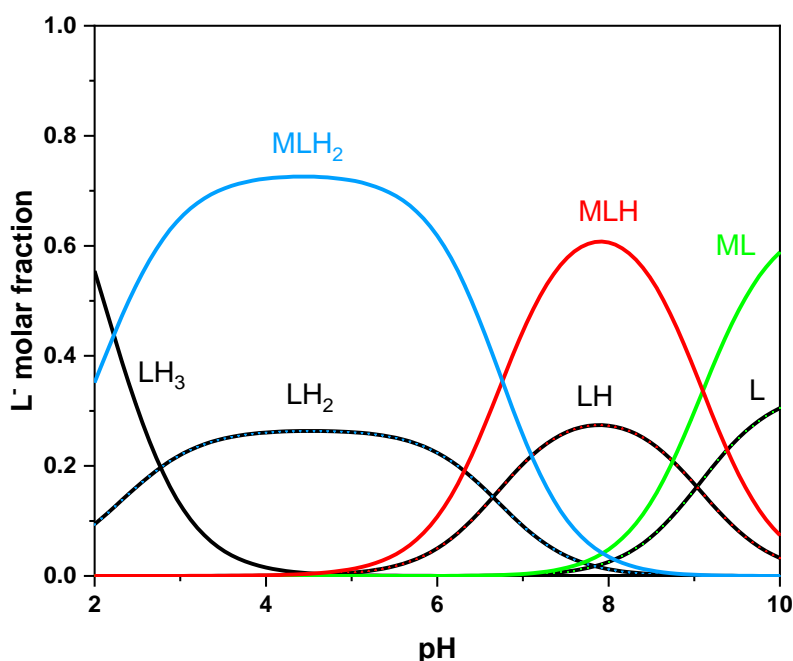
Figure 4.5. Speciation diagram *vs*. pH of the Ca^{2+}-CAR (L) system (charges omitted for simplicity) at I = 0.15 mol L^{-1} and T = 310.15 K ($C_{Ca^{2+}}$ = 2 mmol L^{-1}, C_{L^-} = 0.14 mmol L^{-1}).

4.1.2 Mg^{2+}-CAR complexes

In the adopted experimental conditions (Table 2.5), the most trustworthy speciation model for the Mg^{2+}-CAR system was defined and reported in Table 4.1. The formation of three metal complex species, namely ML^+, MLH^{2+} and MLH_2^{3+} was found only at I = 0.15 mol L^{-1}. The speciation model of the Mg^{2+}-CAR system is similar to that of the Ca^{2+}-CAR system, except for the deprotonated ML^+ species, which was determined only at I = 0.15 mol L^{-1}. Instead of Ca^{2+}, in the presence of Mg^{2+}, precipitation phenomena occurred at pH ~ 10.0. However, it did not affect the formation and determination of the ML^+ species at the lowest ionic strength value (I = 0.15 mol L^{-1}). At this ionic strength value, the *logβ* of the ML^+ species is 2.74 (at T = 298.15 K), 2.86 (at T = 288.15 K) and 2.49 (at T = 310.15 K). Figure

4.6, which describes the species distribution *vs.* pH at I = 0.15 mol L^{-1} (solid line) and I =0.98 mol L^{-1} (dashed line), shows that of the ML$^+$ species formation begins at pH = 8.0 (T = 298.15 K). At higher ionic strength, there is a slight shift in the formation curves toward higher pH values, which also implies the presence of the ML$^+$ species. In fact, the latter occurs at slightly higher pH values, closer to the precipitation region, where the potentiometric determination is elusive. Therefore, the ML$^+$ formation was not taken into account in the speciation model because its low fraction and the extreme error associated with its determination were reached below the physiological pH value (7.4). This is also confirmed by Figure 4.6, which depicts the species distribution *vs.* pH at T = 288.15 K (solid line) and at T = 310.15 K (dashed line).

However, M^{2+} is coordinated with CAR throughout the pH range investigated, as can be observed in Figures 4.6 and 4.7. In the first, the MLH$_2^{3+}$ species reaches a fraction of 0.46 at I = 0.15 mol L^{-1} (for 3.8 ≤ pH ≤ 5.2) and 0.6 at I = 0.98 mol L^{-1} (for 3.4 ≤ pH < 6.0), and its *logβ* value varies from 18.38 (at I = 0.15 mol L^{-1}) to 18.82 (at I = 0.98 mol L^{-1}), respectively. In the second, the MLH$_2^{3+}$ fraction is ∼ 0.3 at T = 288.15 K (for 3.6 ≤ pH ≤ 5.7) and 0.27 at T = 310.15 K in the following pH range, 3.9 ≤ pH < 5.3, and its *logβ* value varies from 18.91 (at T = 288.15 K) to 17.74 (at T = 310.15 K). The *logβ* value of the MLH^{2+} species ranges from 11.77 (at I = 0.15 mol L^{-1}) to 11.82 (at I = 0.98 mol L^{-1}) at T = 298.15 K, and from 12.05 (at T = 288.15 K) to 11.30 (at T = 310.15 K) at I = 0.15 mol L^{-1}. As visible in Figure 4.6, at this ionic strength value, the MLH^{2+} fraction reaches an amount of 0.51 at pH ∼ 8.0. A slight shift in pH toward the acidic environment is observed at I = 0.98 mol L^{-1}, in which the MLH^{2+} fraction is 0.48 at pH ∼ 7.8. This trend can also be observed in Figure 4.7, whose MLH^{2+} profiles decrease to 0.33 at both T = 288.15 K (pH ∼ 8.0) and T = 310.15 K (pH ∼ 7.7).

As discussed for the Ca^{2+}-CAR system, Mg^{2+}-CAR interactions are also weak. Despite this, to evaluate its effect on the ligand speciation, a simulated distribution

diagram at "real" concentration is shown in Figure 4.8 [97]. The CAR fractions, complexed by Mg^{2+}, are very low (< 0.1) compared to the free ligand species at any pH value. This diagram, as well as the one in Figure 4.5, were constructed using the thermodynamic data at $I = 0.15$ mol L^{-1} and $T = 310.15$ K, simulating the physiological conditions of the plasma. On the basis of the data listed in Table 4.1, it is possible to know the speciation of CAR under different experimental conditions.

In this thesis, Ca^{2+}- and Mg^{2+}-CAR interactions were investigated in parallel. Since the Ca^{2+}-CAR complexes have higher stability constants than those of Mg^{2+}-CAR, as well as their relevance, the ^1H NMR spectroscopic study was neglected on this Mg^{2+}-CAR system.
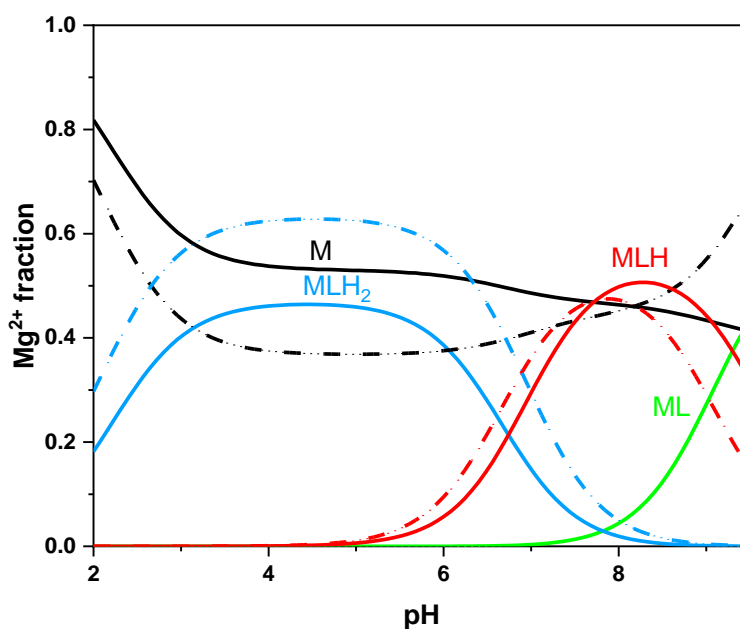
Figure 4.6. Speciation diagram *vs*. pH of the Mg^{2+}-CAR (L) system (charges omitted for simplicity) in NaCl aqueous solution at $I = 0.15$ mol L^{-1} (solid line) and $I = 0.98$ mol L^{-1} (dashed line), $T = 298.15$ K ($C_M = 2$ mmol L^{-1}, $C_L = 4$ mmol L^{-1}).
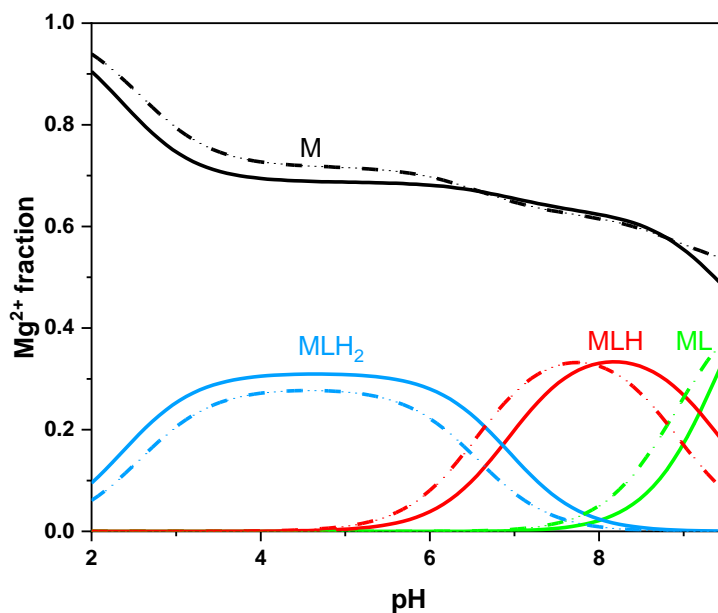
Figure 4.7. Speciation diagram *vs*. pH of the Mg^{2+}-CAR (L) system (charges omitted for simplicity) in NaCl aqueous solution at T = 288.15 K (solid line) and T = 310.15 K (dashed line), I = 0.15 mol L^{-1} (C_M = 2 mmol L^{-1}, C_L = 4 mmol L^{-1}).
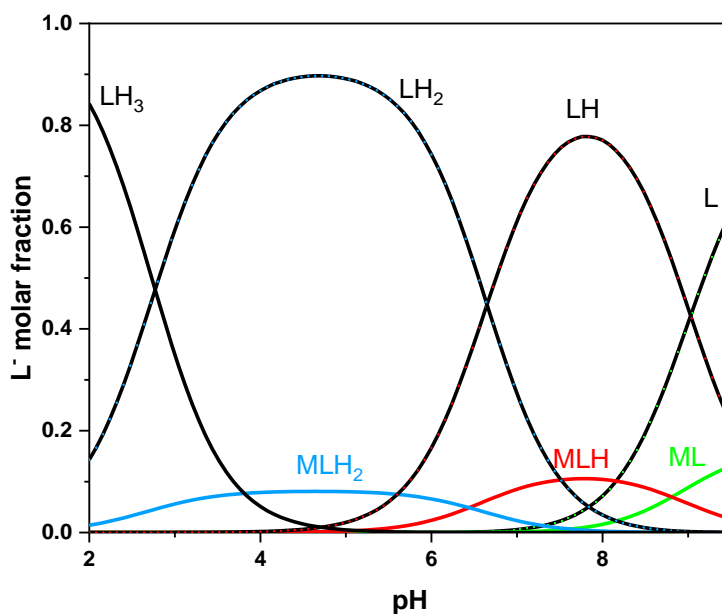
Figure 4.8. Speciation diagram *vs*. pH of the Mg^{2+}-CAR (L) system at I = 0.15 mol L^{-1} and T = 310.15 K ($C_{Mg^{2+}}$ = 0.9 mmol L^{-1}, C_{L^-} = 0.14 mmol L^{-1}).

4.1.3 Computational results [97]

In addition to the experimental study, a computational investigation was carried out on Ca^{2+}- and Mg^{2+}-CAR systems with the aim of defining atomistic details by performing state-of-the-art *ab initio* molecular dynamics (AIMD) simulations. Generalized structures for the lowest-energy species for the doubly deprotonated CAR molecule complexed with Ca^{2+} and Mg^{2+} were performed at the B3LYP/ 6-311++G(2d,2p) Density Function Theory (DFT) level of the neutral Ca^{2+}- and Mg^{2+}-CAR complexes under implicit solvation simulated with the conductive polarizable continuum model (CPCM) [72]. A tetra-coordinated complex structure was obtained, whose interactions concern the divalent cation and *(i)* an oxygen of the COO$^-$ group, *(ii)* the bare nitrogen atom of the imidazole ring, *(iii)* the amino group of the alanine moiety (NH_2), and *(iv)* the bare nitrogen of the histidine. However, this is true only if the description of the solvating environment is approximated to its dielectric constant, as it is customary in static quantum-mechanical calculations (see, *e.g.*, computations reported in Chapter 3). In fact, when evoking an explicit treatment of the water environment – achievable *via* AIMD simulations – around the cations–carnosine complexes, a completely different situation occurs in the solvation modalities. As depicted in Figure 4.9, the metal cation is only tri-coordinated to the CAR molecular structure through interactions with *(i)* an oxygen of the COO- group, *(ii)* the bare nitrogen atom of the imidazole ring, and *(iii)* that of the histidine residue. Moreover, as also shown in Figure 4.9, the achievement of the complexation process occurs by directly involving 4 water molecules from the local environment.

The scenario considerably changes in the magnesium case. As can be observed from Figure 4.9 b), the Mg^{2+} complex with the doubly deprotonated CAR molecule is closer to the predictions of static quantum-mechanical calculations, as a tetra-coordinated structure is noticed. Furthermore, 2 water molecules of the first hydration shell also actively participate in the complexation mechanism of Mg^{2+}.

That is to say, a hepta-coordinated Ca^{2+} complex, with CAR acting as a tridentate ligand, and a hexa-coordinated Mg^{2+}complex, with CAR acting as a tetra-dentate ligand, are observed in AIMD simulations.

The differences recorded in the coordination modalities of the Ca^{2+} and Mg^{2+} cations can be directly attributable to their different sizes and electron densities. In fact, the first cation, being larger than Mg^{2+}, provides a more ''opened'' structure of the CAR molecule, as shown by the typical interaction lengths, falling on average in the interval [2.5-2.7 Å], and described in Figure 4.9 a). This results into the possible insertion of a larger number of hydrating water molecules close to the Ca^{2+} cation. On the other hand, Mg^{2+} is a very small cation that forces the CAR structure to fold around the latter, establishing interactions, whose lengths fall at shorter distances (*i.e.*, in the interval [2.1-2.3 Å]) with the active atomic sites of CAR. This circumstance limits the inclusion of large quantities of water molecules. As for the Ca^{2+} case, the involvement of a more expanded solvation shell comprising greater amounts of water molecules is in compliance with the experimental result relating to the entropic nature of the stabilization process of the Ca^{2+}-CAR complex. Furthermore, Ca^{2+} is also a weaker ''structure-maker'' cationic agent than Mg^{2+}. In fact, while the entropy changes associated with Mg^{2+} are very small (if not negative), those attributed to the Ca^{2+} turn out to be quite large, as shown in Table 4.5. From a microscopic point of view, the involvement of a greater number of water molecules - as predicted by several AIMD simulations starting from significantly different initial conditions, and as depicted in Figure 4.9 - gives rise to the Ca^{2+}- CAR complex a larger entropy than the Mg^{2+}- CAR complex.
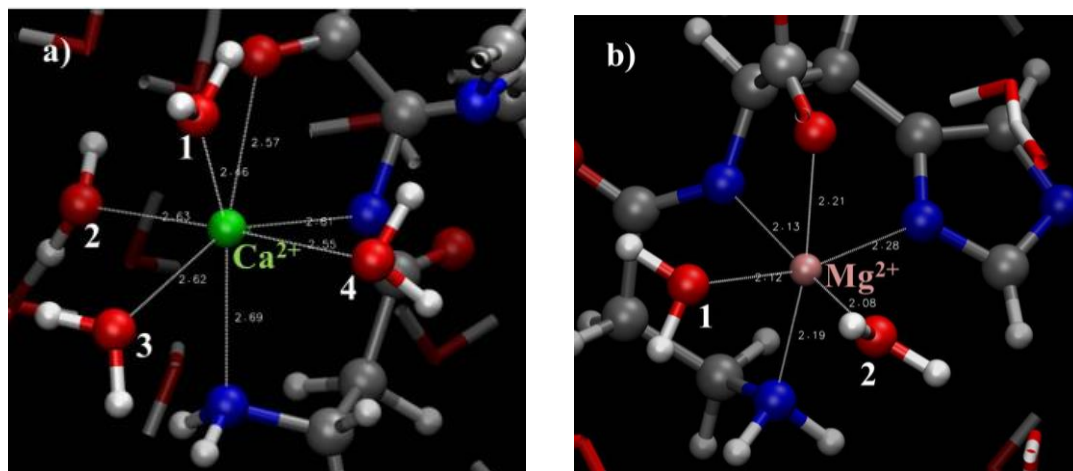
Figure 4.9. Stable hydrated structures of doubly deprotonated CAR complexes formed with divalent cations, such as **a)** Ca^{2+} and **b)** Mg^{2+}, as determined by AIMD simulations. Typical distances of the established interactions (represented with dashed white lines) are shown in Å. For the sake of clarity, first-neighbor water molecules, which solvate the metal cations, are numbered.

4.2 First transitions metal cations series, Mn^{2+}-, Cu^{2+}- and Zn^{2+}-, with CAR [99]

The antioxidant role of CAR could be attributed to its high hydrophilicity and enhanced by its chelating properties. CAR is able to coordinate most of bivalent and transitions metal cations, such as Mn^{2+}, Fe^{2+}, Co^{2+}, Ni^{2+}, Cu^{2+}, Zn^{2+}, Ru^{2+} and Cd^{2+}, thus forming different complex species [6, 7, 124].

Mn^{2+}, Cu^{2+} and Zn^{2+} cations are found coordinated to proteins and are supposed to be potential risk co-factors in neurodegenerative disorders [125]. CAR can coordinate all the three metal cations, protecting the neuro- and mitochondrial functions and preventing copper-, manganese- and zinc-induced neurotoxicity [5, 6, 22, 126]. Studying the importance of the functions of these metal cations in neurodegenerative processes requires understanding their interactions with peptides [99]. In particular, in the literature, several works have been reported on the Cu^{2+}- and Zn^{2+}- chelating ability of CAR. However, no thermodynamic data provide the

dependence of the formation constants on the ionic strength and temperature. For this reason, a comprehensive thermodynamic study was necessary to understand the complex species and, thus, speciation models involving M^{2+} and CAR. Among the cations in the first series of transition metals, Mn^{2+}, Cu^{2+} and Zn^{2+} ions and their interactions with CAR were investigated.

4.2.1 Mn^{2+}-CAR complexes

As expected, since Mn^{2+} shares similar ionic radii and coordinating properties as the Ca^{2+} cation [127], the Mn^{2+}-CAR speciation model also includes species with 1:1 metal:ligand ratio. The speciation models including Ca^{2+}- and Mn^{2+}-CAR species resemble each other, as do the values of their equilibrium constants. The latter refer to the formation of three complex species, namely ML^+, MLH^{2+} and MLH_2^{3+}. The $log\beta$ of the ML^+ species varies from 3.34 to 4.52 at I = 0.15 mol L^{-1}, the MLH^{2+} species ranges from 12.05 to 13.12, and the MLH_2^{3+} from 18.34 to 19.41. The speciation diagram vs. pH is shown in Figure 4.10 at T = 298.15 K. At the lowest ionic strength value (I = 0.15 mol L^{-1}), the MLH_2^{3+} species reaches a molar fraction of ~0.8 in the range $3.5 \leq pH \leq 5.0$. At I = 0.98 mol L^{-1}, it is ∼ 0.43 in the acid environment and the MLH^{2+} species occur in the $5.0 \leq pH \leq 9.0$, amounting a fraction of 0.6 at pH $\cong$ 7.5 in both ionic strength values. The ML^+ species form starting from pH $\geq$ 7.0. Its determination was feasible, despite precipitation phenomena occurred at pH ∼ 9.5 [99]. Figure 4.11 also describes the speciation profiles of the Mn^{2+}-CAR system vs. pH at T = 288.15 K (solid line) and T = 310.15 K (dashed line). At the lowest temperature value, a large amount of free M^{2+} (0.75) is present in solution up to pH = 6.9, while a smaller fraction of the metal (0.12) is found to be coordinated to CAR up to pH ∼ 6.2. The ML^+ species take place starting from pH ∼ 7.0 at the simulated temperature values. At

113

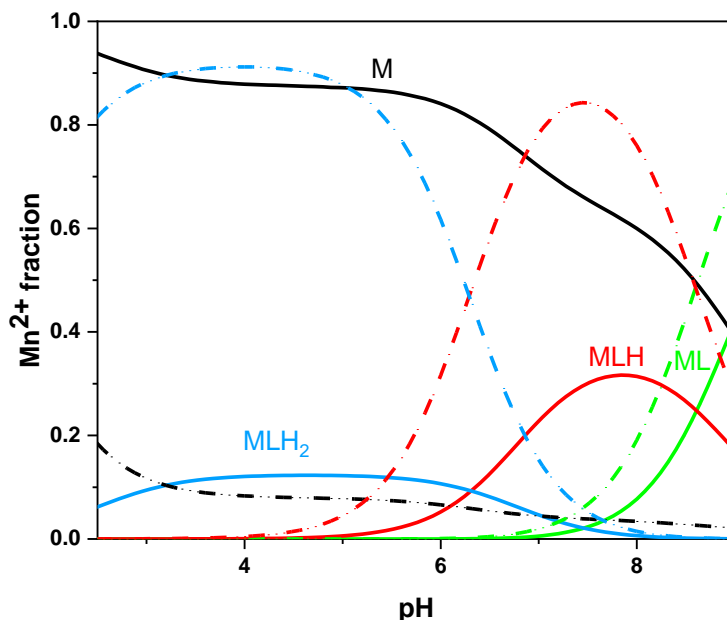T = 310.15 K, the metal is almost totally coordinated to the dipeptide as MLH_2^{3+} and MLH^{2+} species.
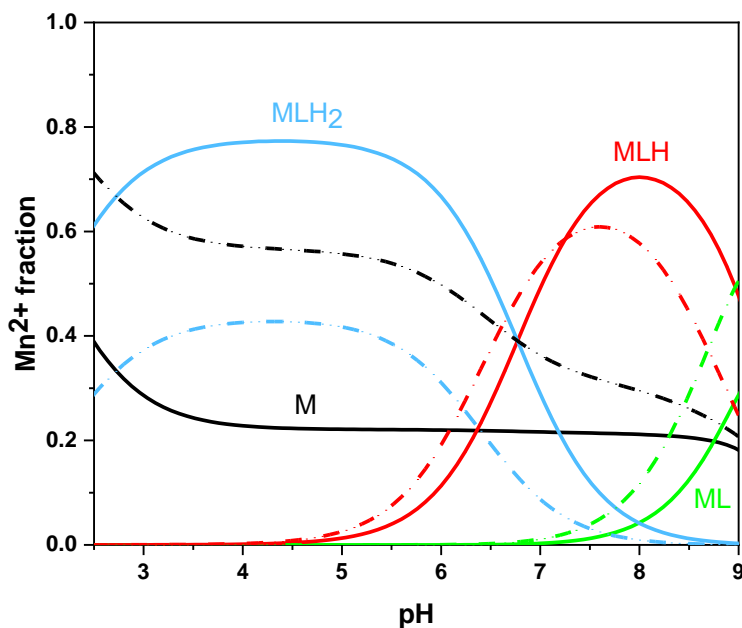
Figure 4.10. Speciation diagram *vs*. pH of the Mn^{2+} -CAR (L) system (charges omitted for simplicity) in NaCl aqueous solution at I = 0.15 mol L^{-1} (solid line) and I = 0.98 mol L^{-1} (dashed line), T = 298.15 K (C_M = 2 mmol L^{-1}, C_L = 4 mmol L^{-1}).
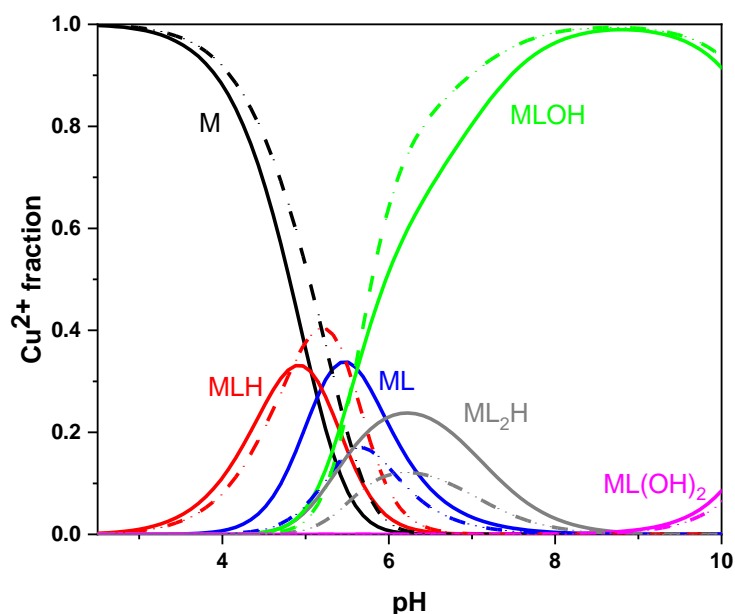
Figure 4.11. Speciation diagram *vs*. pH of the Mn^{2+}-CAR (L) system (charges omitted for simplicity) in NaCl aqueous solution at $T = 288.15$ K (solid line) and $T = 310.15$ K (dashed line), $I = 0.15$ mol L^{-1} ($C_M = 2$ mmol L^{-1}, $C_L = 4$ mmol L^{-1}).

4.2.2 Cu^{2+}-CAR complexes

CAR is highly localized in human skeletal muscle, where it is also found in one-third of the copper present in the body (20-47 nmol Kg^{-1}) [33]. Although the antioxidant mechanisms of CAR remain unclear, its capacity to inhibit metallic and nonmetallic lipid oxidation and to protect phages from γ irradiation, preventing oxidative DNA damage, seems to be expressed because it is assisted by copper [33]. Therefore, understanding these metal:ligand interactions is of biological importance and could be helpful in the evaluation of some bioactivities concerning this system, considering that Cu^{2+}-CAR can also be useful as a model system in metal-enzyme studies [33]

The most reliable speciation model, with 1:1 and 1:2 Cu^{2+}-CAR ratios, is described in Table 4.1, where five complex species, namely ML^+, MLH^{2+} and ML_2H^+, $MLOH^0$ and $ML(OH)_2^-$, are shown at each ionic strength and temperature.

Dinuclear species have also been described in the literature [43, 108, 111, 128], whose formation was not significant under the adopted experimental conditions (Table 2.5). Therefore, following the general criteria for choosing the speciation model (simplicity, standard and mean deviation of fit, formation percentages of the species), the formation of dinuclear species was neglected in this thesis. On the other hand, no further investigations were carried out either, since copper concentrations are lower than those of CAR in living organisms, and the existence of dimers is, indeed, unconvincing.

As reported in Table 4.1, the $log\beta$ of the complex species tend to decrease as the ionic strength increases. A similar trend can be seen as temperature growths. The speciation behavior, depicted in Figures 4.12 and 4.13, better highlights the formation of the complex species throughout the pH, taking into account the ionic strength and temperature ranges and proving the binding ability of CAR toward Cu^{2+} under the investigated experimental conditions. The fairly high stability constants of this system allow suppression of hydrolysis of the metal cation. However, free M^{2+} is present in solution at $I = 0.15$ mol L^{-1}, whose molar fraction is nearly 0.4 at pH $\sim$ 5.0 (T = 298.15, in Figure 4.12) and ($288.15 \leq T/ K \leq 310.15$, in Figure 4.13). The MLH^{2+} fraction is 0.33 at pH $\sim$ 4.8 and $I = 0.15$ mol L^{-1}, but it undergoes a slight shift to higher pH values and, thus, amounts to 0.4 at pH $\sim$ 5.2 and $I = 0.98$ mol L^{-1}. Its fractions are less than 0.3 in Figure 4.13. Starting from pH $\sim$ 4.0, the ML^+ species take place, whose molar fraction reaches a maximum of 0.34 and 0.17 at $5.5 \leq pH \leq 5.7$, $I = 0.15$ mol L^{-1} and 0.98 mol L^{-1}, respectively. Their highest fractions (≥ 0.3) are shown in Figure 4.13. Minor fractions of the ML_2H^+ species are present, while the highest amounts occur at $I = 0.15$ mol L^{-1}, and at T = 298.15 K and T = 310.15 K. The $MLOH^0$ species are preponderantly found in alkaline environments, as is the $ML(OH)_2^-$ species, which forms from pH $\sim$ 8.0.
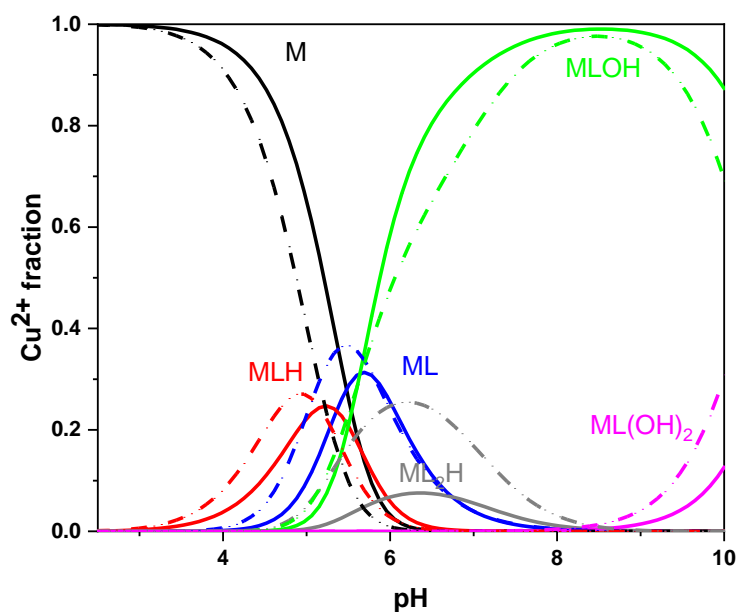
Figure 4.12. Speciation diagram *vs*. pH of the Cu^{2+}-CAR (L) system (charges omitted for simplicity) in NaCl aqueous solution at I = 0.15 mol L^{-1} (solid line) and I = 0.98 mol L^{-1} (dashed line), T = 298.15 K (C_M = 2 mmol L^{-1}; C_L = 4 mmol L^{-1}).

Figure 4.13. Speciation diagram *vs*. pH of the Cu^{2+}-CAR (L) system (charges omitted for simplicity) in NaCl aqueous solution at T = 288.15 K (solid line) and T = 310.15 K (dashed line), I = 0.15 mol L^{-1} (C_M = 2 mmol L^{-1}; C_L = 4 mmol L^{-1}).

4.2.3 Zn^{2+}-CAR complexes

As written in Chapter 1, a zinc-L-carnosine complex, (zinc N-(3- aminopropionyl)-L-histidine, or *polaprezinc*) [18, 129], was found to protect the gastric mucosa from experimental ulceration in *vivo* and to be effective against *Helicobacter pylori*-associated gastritis [6]. *Polaprezinc* is soluble in acid, and it can adhere to ulcerous sites much better than zinc or CAR alone in the stomach [130]. However, it goes from the small intestine to the colon, and thus its concentration tends to decrease over time in the small intestine [131]. It is also administered in preventing radiation-induced intestinal damage in these patients undergoing radiotherapy. In this case, a helpful combination of employment both *polaprezinc* and hyperbaric oxygen may give rise to advantageous effects on the reduction of radiation-induced intestinal damage due to their different mechanisms of action [131]. Albeit the evidence supporting the application of *polaprezinc* in maintaining, preventing and treating mucosal damage, as well as epithelial tissues, further trials are required to study the anticancer effects and mechanisms as anti-carcinoma adjuvant drugs [18]. In view of these facts, the Zn^{2+}-CAR is a very interesting biological system. Therefore, an in-depth speciation study may be pivotal to better elucidate the bioavailability and mechanisms of action of this system. Speaking of which, the best possible speciation model is described in Table 4.1. It includes species with 1:1 metal:ligand ratio, that are MLH^{2+}, MLH_2^{3+} and $MLOH^0$. The *logβ* of the MLH^0 species ranges from 12.08 to 12.90 at the lowest ionic strength value (I = 0.15 mol L^{-1}), those concerning the MLH_2^{3+} and $MLOH^0$ species decrease as ionic strength increases. This trend is also found as temperature increases. For instance, the *logβ* of the MLH_2^{3+} varies from 18.81 (at I = 0.15 mol L^{-1} and T = 298.15 K) to 17.33 (at I = 0.98 mol L^{-1} and T = 298.15 K) and the *logβ* of the MLH^0 species ranges from -2.85 (at I = 0.15 mol L^{-1} and T = 298.15 K) to -3.73 (at I = 0.98 mol L^{-1} and T = 298.15 K). Figure 4.14 shows the distribution profile of the Zn^{2+}-CAR species, from I = 0.15 mol L^{-1} (solid line) to I = 0.98 mol L^{-1} (dashed line). Zn^{2+} is

coordinated to the dipeptide in the pH range investigated, although to a lesser extent at I = 0.98 mol L^{-1}. In fact, at this ionic strength value, zinc exists in solution as free M^{2+}, with a fraction of 0.5, up to pH ~ 6.5. The MLH_2^{3+} species reach the maximum fraction (nearly 0.7) in the range $3.0 \leq pH \leq 5.5$ at I = 0.15 mol L^{-1}, remaining less than 0.1 at I = 0.98 mol L^{-1}. The MLH^{2+} species form starting from pH = 4.0 in both ionic strength conditions. The MLH^{2+} species amount to the fraction of 0.72 and 0.65 in the physiological pH range at I = 0.15 mol L^{-1} and I = 0.98 mol L^{-1}, respectively. Although precipitation phenomena took place at pH ~ 9.0, the formation of the MLOH species was also found in this system. It starts from pH = 7.0 and their fractions, at pH ~ 8.8, are 0.5 and 0.9 at I = 0.15 mol L^{-1} and I = 0.98 mol L^{-1}, respectively.

Figure 4.15 shows the speciation model of the Zn^{2+}-CAR system *vs*. pH at T = 288.15 K (solid line) and T = 310.15 K (dashed line). In this case, free M^{2+} (0.46) is present in solution up to pH = 6.56 at T = 288.15 K. At this temperature value, zinc also occurs as MLH_2^{3+} (0.27) (3.84 $\leq$ pH $\leq$ 5.0), as MLH^{2+} (0.66), in the physiological pH range, and as the species $MLOH^0$ (0.97) (pH ~ 9.0). The latter, in particular, forms starting from pH ~ 7.0. At T = 310.15 K, a molar fraction (~ 0.3) of the free metal is found up to pH ~ 6.0. On the other hand, Zn^{2+} is coordinated with CAR in the form of MLH_2^{3+} (0.70) (3.6 $\leq$ pH $\leq$ 5.5), MLH^{2+} (0.54) (pH ~ 7.3) and $MLOH^0$ (> 0.9) at pH $\geq$ 8.3.

To confirm the speciation model defined through potentiometric titrations, ^{1}H NMR spectroscopic ones on Zn^{2+}-CAR solutions were performed under the experimental conditions given in Table 2.8. ^{1}H NMR spectra are shown in Figure 4.16. The experimental ^{1}H NMR data, elaborated by HyNMR software, allowed calculation of the Zn^{2+}-CAR formation constant values, which are reported in Table 4.2, along with those of the Ca^{2+}-CAR system. The ^{1}H NMR signals of CAR, previously analyzed, are summarized in Figure 3.9 and Table 3.6. Comparison of the chemical shift (δ) values of the free ligand and the Zn^{2+} -CAR mixture as the

pH varies points out a slight downfield effect ($\delta \sim 0.1$ ppm), resulting in weak interactions. However, the ^{1}H NMR titrations fully confirm the speciation model obtained through potentiometry, as also visible by comparing the formation constants values, reported in Table 4.2, with those in Table 4.1, for the Zn^{2+}-CAR system.
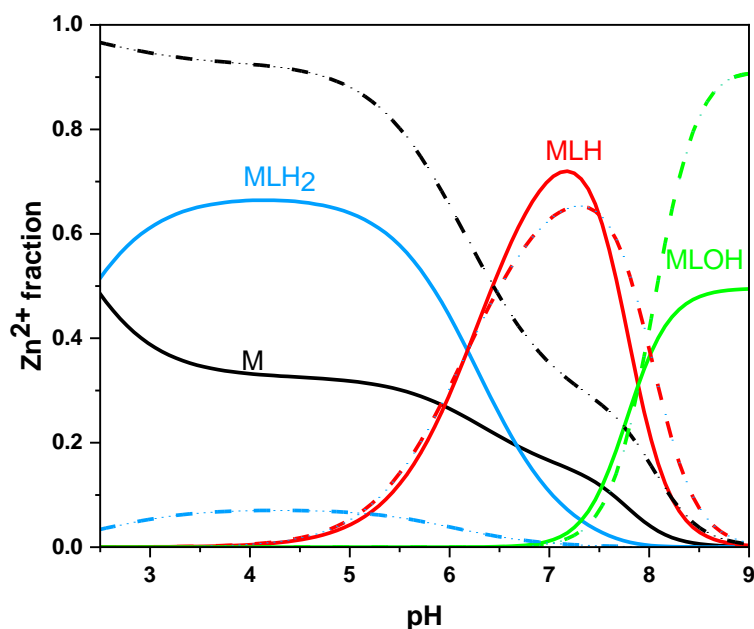

Figure 4.14. Speciation diagram *vs.* pH of the Zn^{2+}-CAR (L) system (charges omitted for simplicity) in NaCl aqueous solution at I = 0.15 mol L^{-1} (solid line) and I = 0.98 mol L^{-1} (dashed line), T = 298.15 K (C_M = 2 mmol L^{-1}, C_L = 4 mmol L^{-1}).
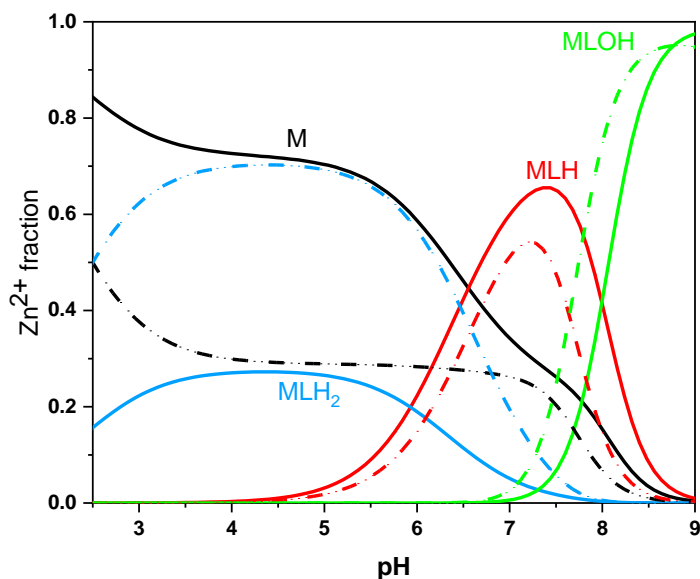
Figure 4.15. Speciation diagram *vs.* pH of the Zn^{2+}-CAR (L) system (charges omitted for simplicity) in NaCl aqueous solution at T = 288.15 K (solid line) and T = 310.15 K (dashed line), I = 0.15 mol L^{-1} (C_M = 2 mmol L^{-1}, C_L = 4 mmol L^{-1}).
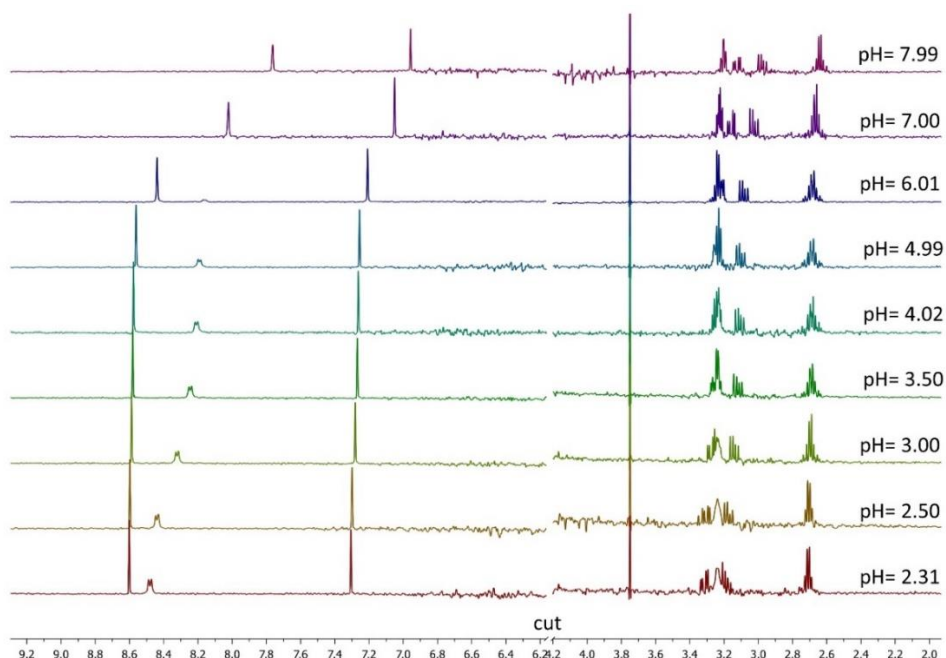
Figure 4.16. ^1H NMR titrations of the Zn^{2+}-CAR (L^-) system in H_2O, external coaxial D_2O, referenced to dioxane at 3.70 ppm (C_M = 2 mmol L^{-1}, C_L = 3 mmol L^{-1}).

4.2.4 Mass Spectrometry results [99]

The Mn^{2+}-, Cu^{2+}- and Zn^{2+}-CAR complexes were further investigated by High Resolution (HR) Matrix Assisted Laser Desorption Ionization (MALDI) Mass Spectrometry (MS). The M^{2+}-CAR complexes ([LH, Mn^{2+}]; [LH, Cu^{2+}]; [LH, Zn^{2+}];) were prepared by dissolving the metal chloride (1 mmol) in water. A solution of ligand (2 equivalents) was added slowly with stirring. An aliquot (1 µL) of the resulting reaction mixtures was directly analyzed by positive-ion mode mass spectrometry using 2,5-Dihydroxybenzoic acid (DHB, $CH_3CN:H_2O$, 60:40, 0.1% in TFA). Figure 4.17 shows the spectra of the three M^{2+}-CAR systems. All species were efficiently identified by the reported high resolution mass-to-charge (m/z) values, isotopic distribution and signal intensity. In Figure 4.17 (a), the spectrum concerning the Zn^{2+}-CAR system describes the formation of signals of m/z 289.03, 311.01 and 326.98. The first is attributable to the complex species with 1:1 (metal:ligand) stoichiometry containing $[Zn^{2+}L]^+$ ($[C_9H_{13}N_4O_3Zn]^+$, m/z 289.03). The other two species are sodiated ($[C_9H_{12}NaN_4O_3Zn]^+$, m/z 311.01) and potassiated ($[C_9H_{12}KN_4O_3Zn]^+$, m/z 326.98), respectively.

Comparison of the measured experimental isotopic distribution with the calculated theoretical distribution of the expected summary formula (Figure 4.17. (b)) confirms the isotopic distribution and elemental formula. In Figure 4.17. (c) the spectrum corroborates similar information about the Mn^{2+}-CAR complex. In particular, the ionic species of m/z 280.04 ($[C_9H_{13}N_4O_3Mn]^+$) corresponds to the complex with 1:1 (metal:ligand)stoichiometry, and again, the comparison of the measured experimental isotopic distribution with the theoretically calculated one confirms the isotopic distribution and elemental formula, as shown in Figure 4.17 (d). Comparable results are also obtained for the Cu^{2+}-CAR complex and the observed ion of m/z 289.04 in Figure 4.17 (e) can be attributable to a radical cation species ($[C_9H_{14}CuN_4O_3]^{•+}$) with 1:1 (metal:ligand) stoichiometry, as confirmed by the theoretically calculated distribution of the expected summary formula (Figure

4.17 (f)). The isotope distribution and elementary formulas are confirmed for the three divalent M^{2+}-CAR systems, whose formation of complexes with stoichiometry 1:1 and 1:2 (metal:ligand) is detected. No dimeric species were observed under the adopted experimental conditions. However, these data are not sufficient to assign the metal coordination sites, and for this reason, CID (MS/MS experiments were performed for the complexes with stoichiometry 1:1 and 1:2 (metal:ligand). The resulting fragments are reported in Table 4.3.

Figure 4.18.A depicts the CID MS/MS spectrum of the ionic species of m/z 280.04 ($[C_9H_{13}N_4O_3Mn]^+$), which showed an extensive fragmentation of the precursor with charge retention on the metal (Table 4.3), and displaying ionic peaks arising from the direct and consecutive fragmentation pathways. The neutral losses of 18 ($[C_9H_{11}MnN_4O_2]^+$, m/z 262.03) and 44 ($[C_8H_{13}MnN_4O]^+$, m/z 236.05) from the parent ion $[Mn^{2+}L]^+$ gave rise to the two most intense fragment ions in the spectra (direct fragmentation) and confirmed the presence of a free OH group. In this case, the absence of ammonia loss, which was the most intense process in the CID experiment performed on the free ligand (Figure 3.11), suggests the full involvement of the β-NH_2 moiety in coordination with Mn^{2+}. All other fragment ion signals can be attributable to fragmentation and rearrangement of the ligand, as discussed in Tables 4.3 and 3.8. On the one hand, the data point out that the ligand chelates Mn^{2+} *via* the β-NH_2 termini with an assistance of lone pairs of the amidic nitrogen, as shown in Figure 4.18.A, probably leading to a six-membered ring locating charge on the metal and, on the other hand, with a partial assistance of the lone pairs of the carboxyl acid moiety oxygen.

Figure 4.18.B shows the CID MS/MS spectrum of the ionic species of m/z 506.14 ($[C_{18}H_{27}N_8O_6Mn]^+$) that can be ascribable to the complex with 1:2 (metal:ligand) stoichiometry, whose spectrum describes the formation of ionic products of m/z 462.15 ($[C_{17}H_{27}MnN_8O_4]^+$) and 435.11 ($[C_{15}H_{22}MnN_7O_5]^+$) related to the direct loss of 44 (COO) and 71 (β-alanine residue, -C_3H_5NO, y1-type fragment in the free

123

ligand), respectively. The formation of the ions of m/z 418.16 ($[C_{15}H_{19}MnN_6O_5]^+$) and 389.10 ($[C_{14}H_{20}MnN_7O_3]^+$) resulted in the loss of 17 (NH$_3$) and 46 (HCOOH) amounts from the ion of m/z 435. As can be observed in the CID MS/MS spectrum in Figure 4.18.B, when an entire ligand is lost, the ion of m/z 280.04 ($[Mn^{2+}L]^+$ complex) is formed. All other low molecular weight signals can be correlated to the fragments of the complex having 1:1 stoichiometry. Therefore, all the data suggested that the carboxyl groups are not directly involved in metal coordination. The first ligand goes more stably into the Mn^{2+} coordination sphere and the second can stabilize the metal *via* the involvement of the imidazole ring. The absence of specific ionic products, deriving from the involvement of the imidazole ring and the direct loss of the β-alanine residue, proposed the coordination of the metal through NH$_2$-β-amine group with an assistance of the N-imidazole.

The Zn^{2+}-CAR system was also analyzed by CID tandem mass spectrometry. The CID MS/MS spectra of the ionic species of m/z 289.03 ($[C_9H_{13}N_4O_3Zn]^+$) and 515.13 ($[C_{18}H_{27}N_8O_6Zn]^+$) can be ascribable to the $[Zn^{2+}L]^+$ and $[Zn^{2+}L_2+H]^+$ complexes, respectively, as can be observed in Figure 4.19 and Table 4.3. In particular, the fragmentation of the precursor ion of m/z 289.03 shows the direct neutral losses of 18 ($[C_9H_{11}N_4O_2Zn]^+$, m/z 271.02) and 44 ($[C_8H_{13}N_4OZn]^+$, m/z 245.04) and, thus, confirms the presence of a free OH group (Figure 4.19.A). The ion of m/z 204.01 can be attributable to the formation of the $[C_6H_{10}N_3OZn]^+$ species, while the other ions are originated from fragmentation of the ligand. These data also suggested that the β-amino group is directly involved in the coordination of the metal, similar to that observed for the Mn^{2+}-CAR in the 1:1 stoichiometric system. The CID MS/MS spectrum of the ionic species of m/z 515.13 ($[C_{18}H_{27}N_8O_6Zn]^+$) in Figure 4.19.B depicts the fragmentation of the complex having 1:2 (metal:ligand) stoichiometry. The spectrum also shows few ionic products and the formation of the m/z 471.14 ($[C_{17}H_{27}N_8O_4Zn]^+$) and 289.03 ($[C_9H_{13}N_4O_3Zn]^+$) species, which are related to the respective direct losses of 44

(COO) and ligand amount. The low molecular weight region described fragmentation patterns similar to those observed for similar Mn^{2+}-containing species.

The Cu^{2+}-CAR system was also investigated by tandem mass spectrometry. Literature data report that the interaction between CAR and copper is strictly pH dependent and the equilibrium is shifted toward the formation of dimeric species at pH > 6.7, while complexes with 1:1 and 1:2 (metal:ligand) stoichiometry are favored at acid pH values [132]. Under the adopted experimental conditions, no dimeric species were observed. However, the complexes with 1:1 and 1:2 stoichiometry were detected and characterized by MS and MS/MS analysis. The CID MS/MS technique on the ion of m/z 289.03 ($[C_9H_{14}N_4O_3Cu]^{\bullet+}$) reported the formation of several ionic products, as can be observed in Table 4.3 and Figure 4.20. The formation of the species of m/z 271 ($[C_9H_{12}N_4O_2Cu]^{\bullet+}$) and m/z 260 ($[C_8H_{11}N_3O_3Cu]^{\bullet+}$) are respectively associated with the direct losses of one water molecule and 29, corresponding to an amount equal to CH_2NH. The ion of m/z 243 ($[C_8H_{10}N_3O_2Cu]^+$) is derived from consecutive losses of amounts equal to 29 (CH_2NH) and 17 ($OH^{\bullet}$), starting from the precursor. As depicted in Figures 4.20 and 4.21, the formation of the ion of m/z 218 is attributable to the copper coordination with the oxygen of the carboxylic group. In particular, as shown in Figure 4.21, the subsequent loss of HCOOH, results in the ion of m/z 171 and the formation of a six-membered, imidazole-assisted ring, followed by cross-ring fragmentations and chemical rearrangements. These data highlighted that the ligand chelates the Cu^{2+} through the β-NH_2 termini with the assistance of the oxygen of the carboxylic group (Figure 4.20). The fragmentation pattern shown in Figure 4.21 also revealed an important effect, played by the imidazole ring, especially in the stabilization of intermediates.

Several distinctive ion products were also detected in the CID MS/MS spectrum of the ion of m/z 513.13, which originated from the precursor ion $[C_{18}H_{26}N_8O_6Cu]^{\bullet+}$,

as reported in Table 4.4 and Figure 4.22. The two most abundant peaks are originated from two different fragmentation pathways, starting from the precursor. The neutral loss of 46 (HCOOH), resulting in the formation of the ions of m/z 467 ($[C_{17}H_{24}N_8O_4Cu]^{\bullet+}$) and m/z 379 ($[C_{12}H_{20}N_4O_6Cu]^{\bullet+}$), is due to the loss of the two imidazole rings, which point outward the complex. All the observed fragment ions were efficiently identified and reported in Table 4.3 and Figure 4.22. The data bring to light that two CAR molecules chelate Cu^{2+} through the β-NH_2 moiety with the assistance of the oxygen lone pairs of the carboxylic group.

Finally, the results just discussed suggest that a hypothetical assembly structure, in which imidazole rings of different units face each other to form H-bonds, is favored. However, this assumption requires further experimentation.
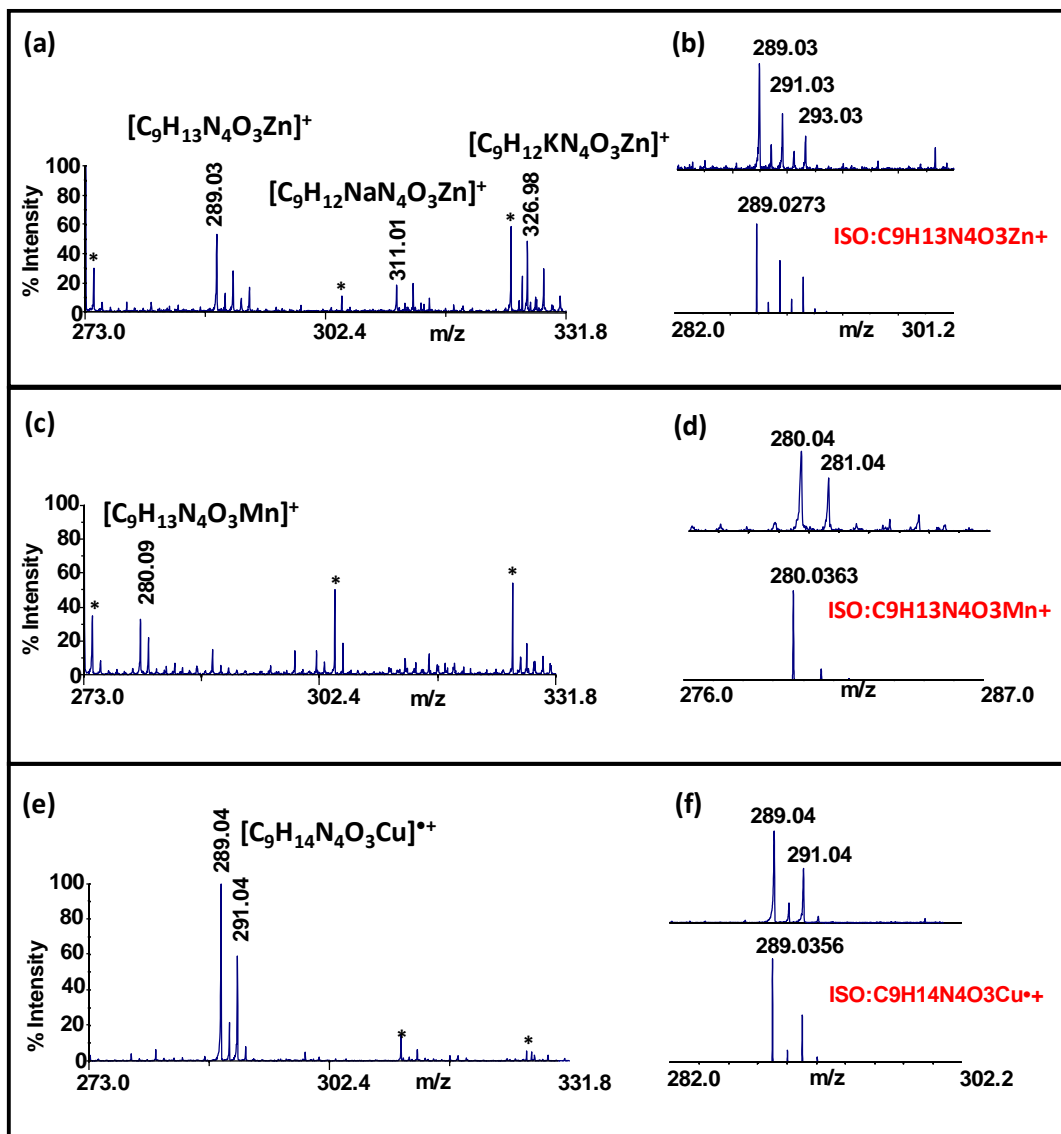
Figure 4.17. MALDI (+)-MS spectra of: (a) MALDI MS and (b) theoretical distribution of the isotope cluster ions of Zn^{2+}-CAR complex; (c) MALDI MS and (d) theoretical distribution of the isotope cluster ions of Mn^{2+}-CAR complex; (e) MALDI MS and (f) theoretical distribution of the isotope cluster ions of Cu^{2+} - CAR complex. (*) matrix clusters.

Table 4.3. MALDI MS and MS/MS fragments of $[Zn^{2+}L]^+$ and $[Zn^{2+}L_2+H]^+$; $[Mn^{2+}L]^+$ and $[Mn^{2+}L_2+H]^+$; $[Cu^{2+}LH]^{\bullet+}$ and $[Cu^{2+}L_2]^{\bullet+}$.

	Composition	Detected Mass	Δppm		Composition	Detected mass	Δppm
$[Zn^{2+}L]^+$	$[C_9H_{13}N_4O_3Zn]^+$	289.03	4	**$[Zn^{2+}L_2+H]^+$**	$[C_{18}H_{27}N_8O_6Zn]^+$	515.13	5
MS/MS	$[C_9H_{11}N_4O_2Zn]^+$	271.02	5	**MS/MS**	$[C_{17}H_{27}N_8O_4Zn]^+$	471.14	6
fragments				**fragments**			
	$[C_8H_{13}N_4OZn]^+$	245.04	6		$[C_9H_{13}N_4O_3Zn]^+$	289.03	4
	$[C_6H_{10}N_3OZn]^+$	204.01	8		$[C_9H_{11}N_4O_2Zn]^+$	271.02	5
	$[C_8H_{13}N_4O]^+$	181.11	7		$[C_8H_{13}N_4OZn]^+$	245.04	6
	$[C_6H_{10}N_3O_2]^+$	156.08	8		$[C_8H_{13}N_4O]^+$	181.11	7
	$[C_6H_8N_3O]^+$	138.07	9		$[C_5H_8N_3]^+$	110.07	5
	$[C_5H_8N_3]^+$	110.07	5		$[C_4H_6N_2]^{\bullet+}$	82.05	7
	$[C_4H_6N_2]^{\bullet+}$	82.05	7				
$[Mn^{2+}L]^+$	$[C_9H_{13}MnN_4O_3]^+$	280.04	4	**$[Mn^{2+}L_2+H]^+$**	$[C_{18}H_{27}MnN_8O_6]^+$	506.14	5
MS/MS	$[C_9H_{11}MnN_4O_2]^+$	262.03	6	**MS/MS**	$[C_{17}H_{27}MnN_8O_4]^+$	462.15	6
fragments				**fragments**			
	$[C_8H_{13}MnN_4O]^+$	236.05	7		$[C_{15}H_{22}MnN_7O_5]^+$	435.11	7
	$[C_8H_{13}N_4O]^+$	181.11	7		$[C_{15}H_{19}MnN_6O_5]^+$	418.08	7
	$[C_6H_{10}N_3O_2]^+$	156.08	8		$[C_{14}H_{20}MnN_7O_3]^+$	389.10	8

|	Formula	Mass	N		Formula	Mass	N
	$[C_3H_6MnN_2O]^+$	140.99	6		$[C_9H_{13}MnN_4O_3]^+$	280.04	6
	$[C_3H_6MnNO]^+$	126.98	7		$[C_8H_{13}MnN_4O]^+$	236.05	7
	$[C_5H_8N_3]^+$	110.07	5		$[C_8H_{13}N_4O]^+$	181.11	7
	$[C_4H_6N_2]^{•+}$	82.05	7		$[C_6H_{10}N_3O_2]^+$	156.08	8
	$[C_3H_5N_2]^+$	69.04	5		$[C_5H_8N_3]^+$	110.07	5
	$[C_3H_7O]^+$	59.05	5				
$[Cu^{2+} LH]^{•+}$	$[C_9H_{14}N_4O_3Cu]^{•+}$	289.03	4	**$[Cu^{2+}L_2]^{•+}$**	$[C_{18}H_{26}N_8O_6Cu]^{•+}$	513.13	5
MS/MS	$[C_9H_{12}N_4O_2Cu]^{•+}$	271.02	5	**MS/MS**	$[C_{17}H_{24}N_8O_4Cu]^{•+}$	467.12	7
fragments				**fragments**			
	$[C_8H_{11}N_3O_3Cu]^{•+}$	260.01	6		$[C_{12}H_{20}N_4O_6Cu]^{•+}$	379.07	6
	$[C_8H_{10}N_3O_2Cu]^+$	243.01	8		$[C_{10}H_{20}N_5O_5Cu]^+$	353.07	8
	$[C_6H_9N_3O_2Cu]^{•+}$	218.00	9		$[C_9H_{17}N_4O_4Cu]^+$	308.05	5
	$[C_5H_7N_3Cu]^{•+}$	171.99	8		$[C_9H_{14}N_4O_3Cu]^{•+}$	289.03	4
	$[C_4H_5N_3Cu]^{•+}$	157.98	7		$[C_9H_{12}N_4O_2Cu]^{•+}$	271.02	5
	$[C_3H_3N_3Cu]^{•+}$	143.96	8		$[C_8H_{10}N_3O_2Cu]^+$	243.01	8
	$[C_5H_8N_3]^+$	110.07	5		$[C_4H_5N_3Cu]^{•+}$	157.98	7
	$[C_4H_5N_2]^+$	81.04	6		$[C_5H_8N_3]^+$	110.07	5
	$[CH_4N]^+$	30.03	7				
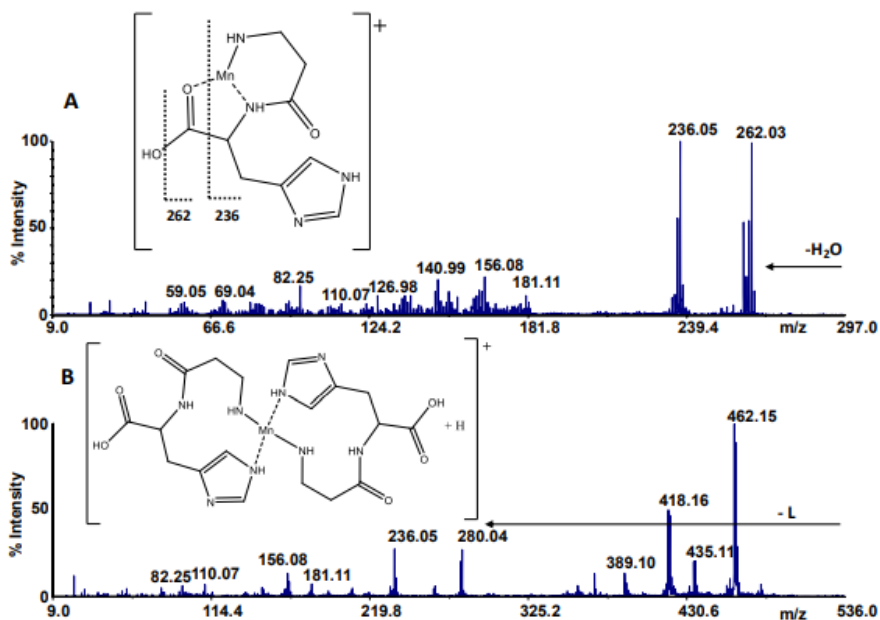
Figure 4.18. CID MS/MS spectra of the complexes: **(A)** $[Mn^{2+}L]^+$, m/z 280.04; **(B)** $[Mn^{2+}L_2+H]^+$, m/z 506.14.
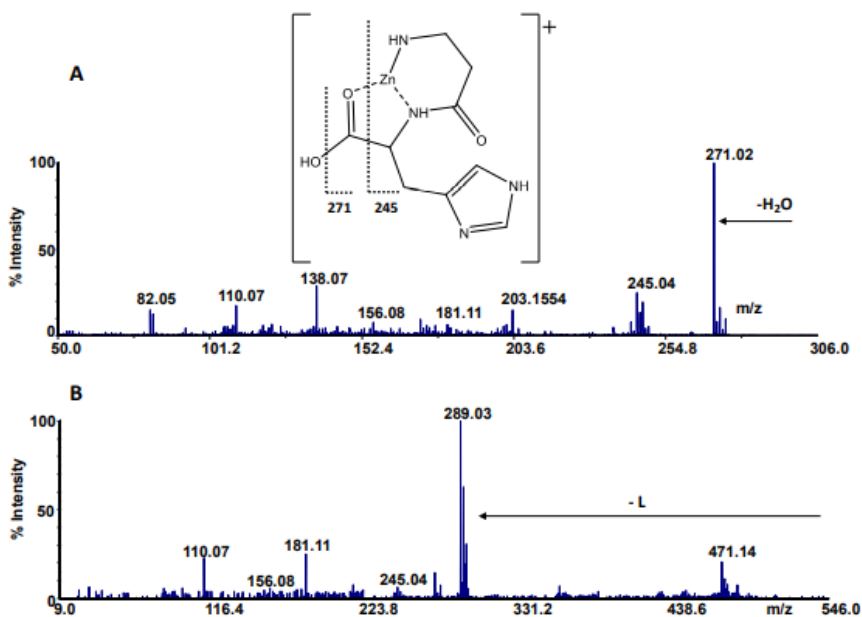

Figure 4.19. CID MS/MS spectra of the complexes: **(A)** $[Zn^{2+}L]^+$, m/z 289.00; **(B)** $[Zn^{2+}L_2+H]^+$, m/z 515.13.
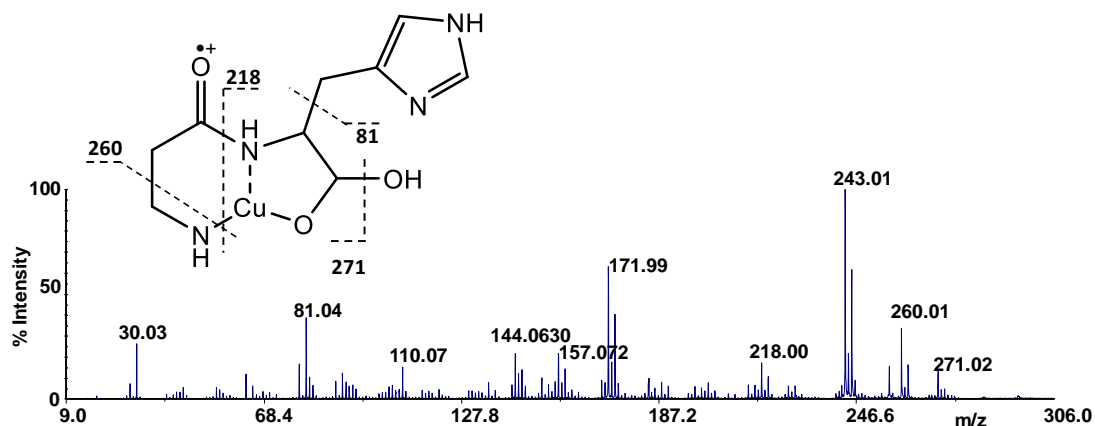
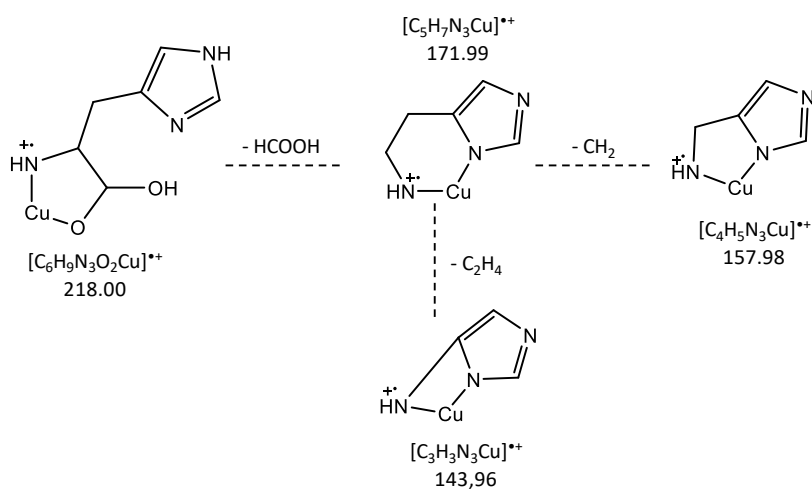**Figure 4.20**. CID MS/MS spectra of the complexes: [Cu^{2+}LH]$^{•+}$, m/z 289.03.

Figure 4.21. Fragmentation pattern of [Cu^{2+}LH]$^{•+}$ (m/z 289.03).
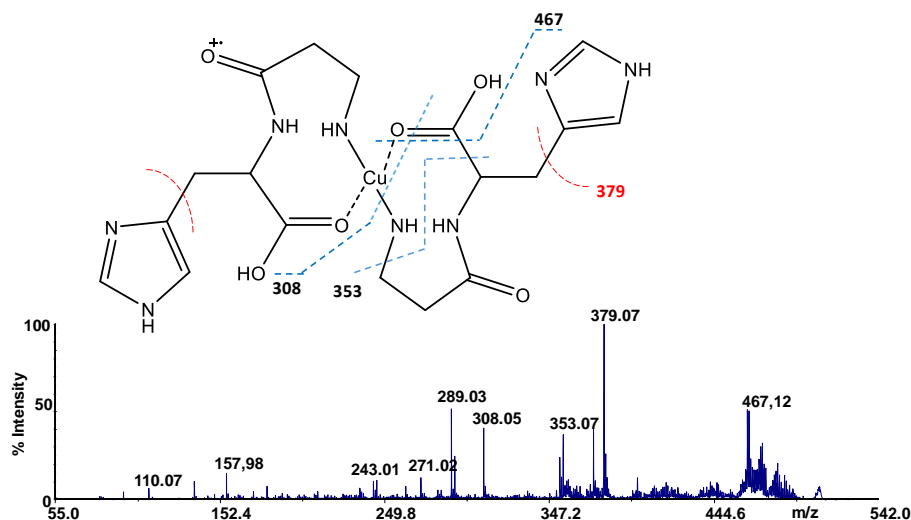
131

Figure 4.22. CID MS/MS spectra of the complexes $[Cu^{2+}L_2]^{\bullet+}$ m/z 515.13.

4.3 Cd^{2+}- CAR complexes

Metals are generally defined as *i)* essential, when they are needed for the maintenance of cell survival *ii)* beneficial, due to they can provide an organism with improved health, *iii)* neutral, if their presence does not give rise to beneficial or toxic effects, and *iv)* toxic, when they are exclusively harmful. In this thesis, a wide variety of metal cations was concerned in order to evaluate their thermodynamic interactions with CAR and, in particular, the M^{2+}-CAR systems are discussed here based on the nature of the metals investigated. Therefore, once defining the thermodynamic interactions among metal cations of biological interest and CAR, its coordination ability involving the potentially toxic metal cations was investigated.

Among the second transition metals series, Cd^{2+} was considered to study thermodynamic interactions with CAR.

This speciation model includes species with 1:1 metal-ligand ratio. The formation of three complexes, ML^+, MLH^{2+} and MLH_2^{3+}, is just achievable at I = 0.15 mol

L^{-1} and T = 298.15 K. Under these conditions, the *logβ* value of the MLH$_2$$^{3+}$ species corresponds to 18.85±0.03. As can be observed in Table 4.1, the *logβ* values of the ML$^+$ and MLH^{2+} species increase as the ionic strength raises, and range from 3.11 (at I = 0.15 mol L^{-1}) to 4.13 (at I = 0.96 mol L^{-1}), and from 12.17 (at I = 0.15 mol L^{-1}) to 13.15 (at I = 0.96 mol L^{-1}), respectively. At the lowest temperature value (T = 288.15 K), the *logβ* values of the ML$^+$ and MLH^{2+} species are 4.22 and 13.17, and decrease to 3.42 and 11.80 at T = 310.15 K, respectively. Although precipitation phenomena take place at pH ∼ 9.0, determination of the speciation model and, thus, the formation constants values at each ionic strength and temperature, was feasible. However, the distribution profile *vs.* pH (Figure 4.23) concerning the Cd^{2+}- CAR system is significantly different. In fact, the lower formation percentages of the species are always less than 0.2 at each ionic strength and temperature value considered, and an amount of free cadmium (0.1) is always present throughout the pH range, just as the Cd^{2+}-(Cl$^-$)$_x$ species prevail.

The speciation diagrams *vs.* ionic strength and temperature are disregarded because of the complex species formation is always less than 0.2. Therefore, to avoid redundant figures, the distribution diagram of the Cd^{2+}-CAR system is described only at I = 0.15 mol L^{-1} and T = 298.15 K.
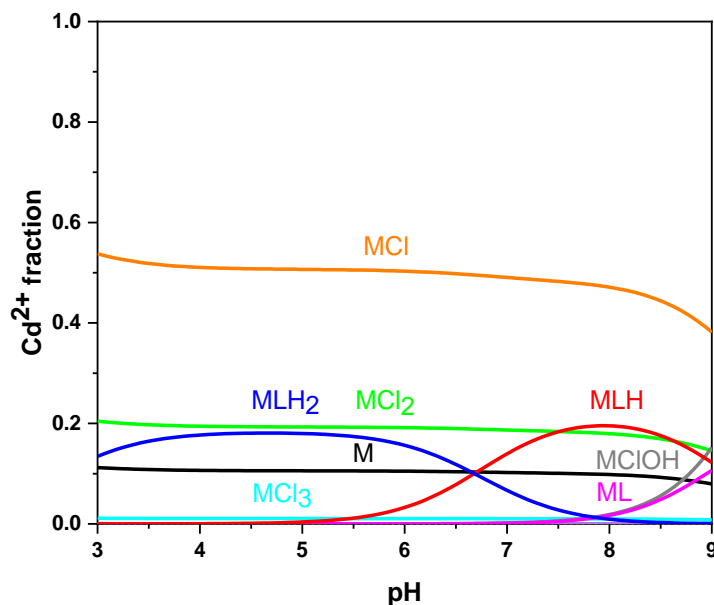
Figure 4.23. Speciation diagram *vs*. pH of the Cd^{2+}-CAR (L) system (charges omitted for simplicity) in NaCl aqueous solution at I = 0.15 mol L^{-1} and T = 298.15 K (C_M = 2 mmol L^{-1}; C_L = 4 mmol L^{-1}).

4.4 Third transitions metal cations series, Hg^{2+}-, and Pb^{2+}-, with CAR

Besides Cd^{2+}, most metal ions, belonging to the third series of transition metal cations, are particularly toxic. Environmental contamination by heavy metals can endanger human and ecological health, and among the main contaminants found in aquatic systems, as well as in air and solid waste, are mercury and lead [133].

On the one hand, mercury has many uses, and on the other hand, it also has many toxic effects. However, both metals are particularly detrimental even at low concentrations and, along with their byproducts, emitted into the soil, air, and aquatic environments by manufacturing, anthropogenic, and industrial activities, can reach ground- and surface waters, where they have non-biodegradable and bio-accumulation features [134-137].

Bioaccumulation of mercury provokes disruption in cellular processes, including growth, cell proliferation, differentiation, damage repair and programmed cell

death [137]. On the other hand, lead is particularly harmful for aquatic and human life, where it is difficult to metabolize and its actions target most organs (in particular, the liver, heart and kidneys [34, 126, 138] and the endocrine, reproductive and hematological systems [126, 135, 136].

Toxicity and side effects on living organisms require the removal of Hg^{2+} and Pb^{2+} from water. In respect to the latter metal cation, a removal procedure is advanced in Chapter 6 of this thesis.

The thermodynamic interactions of Hg^{2+}- and Pb^{2+}-CAR systems are analyzed here.

4.4.1 Hg^{2+}-CAR complexes

The speciation model, including 1:1 metal:ligand ratio species, is shown in Table 4.1. The formation of three complex species, namely ML^{+}, MLH^{2+} and $MLOH^{0}$, occurs at each ionic strength and temperature value. The stability of ML^{+} species increases as the ionic strength grows, and vice versa, it decreases from T = 288.15 K to T = 310.15 K. The $log\beta$ values of the ML^{+}, MLH^{2+} and $MLOH^{0}$ species decrease as temperature increases. At the lowest temperature value, the $log\beta$ values of the ML^{+}, MLH^{2+} and $MLOH^{0}$ species are 17.49, 25.26 and 10.38; and 16.81, 23.63 and 8.95 at T = 310.15 K, respectively.

Figure 4.24 shows the speciation profile *vs*. pH at two different ionic strength values relative to the Hg^{2+}-CAR system, which better highlights the formation of the metal complex species throughout the pH considered. Their determinations were obtained despite precipitation phenomena occurring at pH ~9.0. Moreover, the fairly high stability constants of Hg^{2+}-CAR allow suppression of hydrolysis of the metal cation. Instead, the Hg^{2+}-Cl^{-} species prevail up to pH $\cong$6.0. At the lowest ionic strength (I = 0.15 mol L^{-1}), the MLH^{2+} species forms in the acid environment and reaches the 0.35 molar fraction at pH $\cong$ 6.7. This species is present to a lesser

extent (0.1) at I = 0.96 mol L^{-1}, reaching the maximum at pH ~ 7.5. The ML^+ molar fraction turns out to be 0.45 at pH $\cong$ 7.6 and I = 0.15 mol L^{-1}. At this ionic strength value, the $MLOH^0$ complex is present starting from pH $\cong$ 6.5 and totally prevails at pH = 9.0. At the highest ionic strength value, all profiles undergo a shift toward the alkaline environment.

Figure 4.25 shows the speciation diagram *vs.* pH at two different temperature values, at T = 288.15 K (solid line) and T = 310.15 K (dashed line). Three complexes, ML^+, MLH^{2+} and $MLOH^0$, are formed starting from pH ~ 4, 6, and 6.5, respectively. The MLH^{2+} species amounts to 0.52 at pH = 6.9, a minor fraction (0.16) of the ML^+ species occurs at pH ~ 7.6, and the metal is totally coordinated as the $MLOH^0$ in alkaline environment at T = 288.15 K (solid line). At the highest temperature value (T = 310.15 K), ~ 0.2 of the MLH^{2+} species is present at pH ~ 6.7, and an amount of 0.46 is achieved at pH ~ 7.6 . Finally, the $MLOH^0$ complex occurs preponderantly starting from pH $\approx$ 7.0, again at T = 310.15 K.

Figure 4.24. Speciation diagram *vs.* pH of the Hg^{2+}-CAR (L) system (charges omitted for simplicity) in NaCl aqueous solution at I = 0.15 mol L^{-1} (solid line) and I = 0.96 mol L^{-1} (dashed line) at T = 298.15 K (C_M = 2 mmol L^{-1}, C_L = 4 mmol L^{-1}).
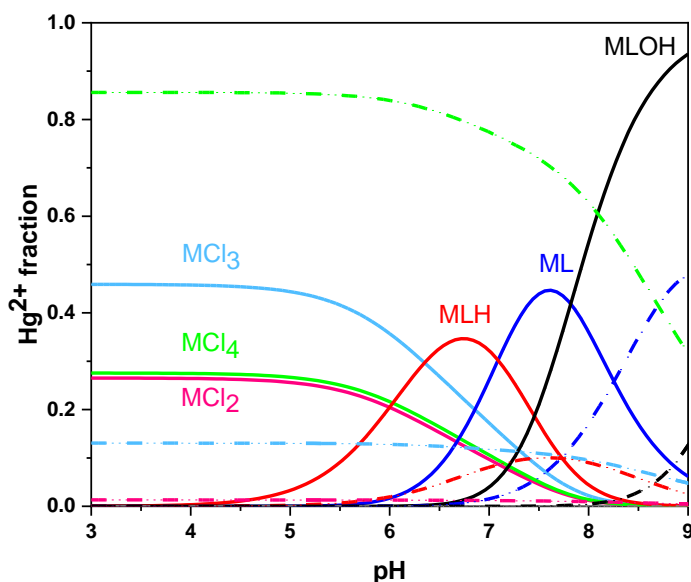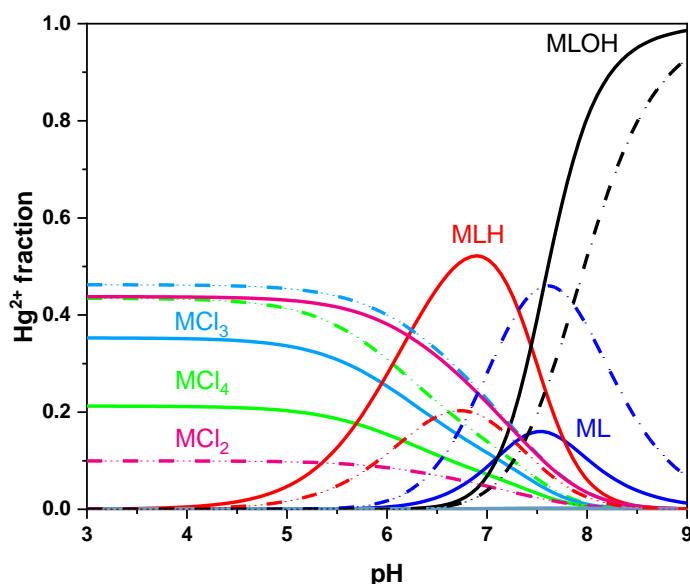
Figure 4.25. Speciation diagram *vs*. pH of the Hg^{2+}-CAR (L) system (charges omitted for simplicity) in NaCl aqueous solution at $I = 0.15$ mol L^{-1} (solid line) and $I = 0.96$ mol L^{-1} (dashed line) at $T = 298.15$ K ($C_M = 2$ mmol L^{-1}, $C_L = 4$ mmol L^{-1}).

4.4.2 Pb^{2+}-CAR complexes

The potentiometric data yielded a speciation model that includes species with 1:1 and 1:2 metal:ligand ratios, as can be observed in Table 4.1. However, the unique 1:1 species, MLH_2^{3+}, is defined only at $I = 0.15$ mol L^{-1} and $T = 298.15$ K, due to it is formed in negligible quantities. Therefore, the MLH_2^{3+} species cannot be considered in this speciation model. On the other hand, the ML_2^0 and ML_2H^+ species are described for each ionic strength and temperature value investigated. The *logβ* values of the ML_2^0 complex vary from 8.3 at $I = 0.977$ mol L^{-1} to 10.05 at $I = 0.15$ mol L^{-1} and $T = 288.15$ K. The stability constant value of the ML_2H^+ species decreases as the ionic strength and temperature increase. For instance, its *logβ* value ranges from 18.65 to 17.57 at $I = 0.15$ mol L^{-1} and $288.15 \leq$ T/ K $\leq$ 310.15. The distribution diagrams *vs*. pH are shown under variable conditions of

ionic strength and temperature. In particular, Figure 4.26 shows the speciation behavior of the Pb^{2+}-CAR system *vs.* pH at I = 0.15 mol L^{-1} (solid line) and I = 0.977 mol L^{-1} (dashed line). Precipitation phenomena occur at pH $\sim$ 6.5, probably due to the formation of the ML_2^0 species. However, this did not affect the formation and determination of ML_2H^+ and ML_2^0 complexes, which show a similar pattern at the two different ionic strength values. A different distribution is observed for the MLH_2^{3+} species, whose molar fraction reaches $\sim$ 0.4 up to pH $\sim$ 5.7. As discussed earlier, it occurs at I = 0.15 mol L^{-1} and T = 298.15 K and, as a consequence, at this ionic strength value, less free Pb^{2+} is present in solution than at I = 0.977 mol L^{-1}. In fact, under this condition, the free metal totally prevails in solution up to pH $\sim$ 5.7.

More marked is the distribution speciation of the Pb^{2+}-CAR system *vs.* pH, described in Figure 4.27, at two different temperature values. In particular, at T = 288.15 K (solid line), the free metal is present in solution with a molar fraction of $\sim$ 0.6 up to pH $\sim$ 6.7. The ML_2H^+ species begins to form at pH $\cong$ 5.5 and achieves a maximum ($\sim$ 0.75) at pH $\cong$ 7.5 at T = 310.15 K. Its molar fraction is less than 0.6 at the lowest temperature value. The ML_2^0 species form starting from pH $\geq$ 7.0.

Considering the above-mentioned toxicity of this metal cation and its interactions with the naturally occurring dipeptide, a study was performed on this system in order to evaluate both the sequestering ability of CAR toward the Pb^{2+} and its removal and, thus, adsorption capacity when it is grafted on a porous resin. This approach is described in Chapter 6 of this thesis.
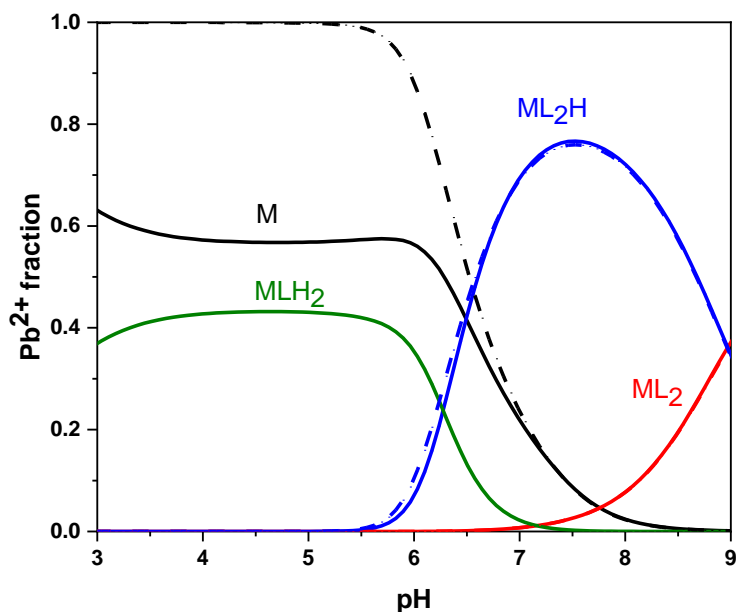
Figure 4.26. Distribution diagrams of the Pb^{2+}-CAR (L) system *vs*. pH in NaCl aqueous solution at I = 0.15 mol L^{-1} (solid line) and I = 0.977 mol L^{-1} (dashed line), T = 298.15 K (C_M = 2 mmol L^{-1}, C_L = 4 mmol L^{-1}).
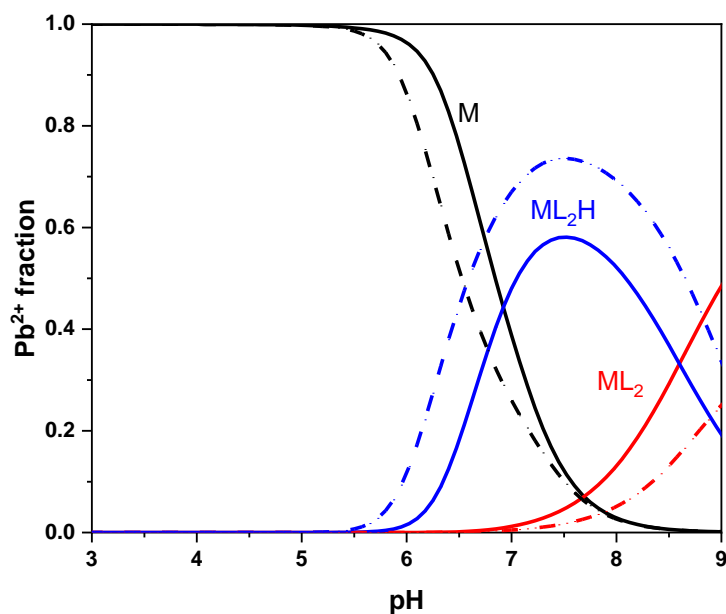

Figure 4.27. Speciation diagram *vs*. pH of the Pb^{2+}-CAR (L) system (charges omitted for simplicity) in NaCl aqueous solution at I = 0.15 mol L^{-1} (solid line) and I = 0.977 mol L^{-1} (dashed line), T = 298.15 K (C_M = 2 mmol L^{-1}, C_L = 4 mmol L^{-1}).

4.5 Dependence of the formation constants on the ionic strength

Variations in ionic strength affect the species distribution, as it influences the ligand protonation, hydrolysis of the metals and, thus, the stability constants of the complex species [139, 140].

Ionic strength effects on the speciation diagrams of the M^{2+}-CAR systems are shown and widely discussed in the respective paragraphs.

The dependence on the ionic strength was determined by the Debye–Hückel type equation (2.27), widely used in the following range $0 \leq I/ \text{mol } L^{-1} \leq 1$ [97]. The formation constants values at infinite dilution and the empirical parameter, C, calculated for each complex species, are given in Table 4.4. In turn, these parameters allow to determine the formation constant values under different conditions. All the C values are positive for the Ca^{2+}-, Mg^{2+}-, Cd^{2+}- and Hg^{2+}-CAR systems. Considering the Ca^{2+}- and Mg^{2+}-CAR systems, the species most affected by variations in ionic strength is ML^+ for the former, whose a higher C value was obtained than for the other species. However, the highest C values are found for the ML^+ and MLH^{2+} species in the Cd^{2+}- and Hg^{2+}-CAR systems. On the other hand, all the C values are negative for the Mn^{2+}-, Zn^{2+} and Pb^{2+}-CAR systems. TheCu^{2+}-CAR system also shows negative C values, except for the MLH species, whose C value is higher than that of the other species. Similar considerations can be made for the MLH_2^{3+} of the Zn^{2+}-CAR system. The same contribution of the C values, corresponding to 0.24, is observed in the Pb^{2+}-CAR system.

Table 4.4. Formation constant values at infinite dilution and C parameters for the dependence on the ionic strength (equation (2.27)), at T = 298.15 K.

M^{2+}	Species	$log\beta^0$ [a]	C
Ca^{2+} [b]	ML^+	3.31 ± 0.06 [c]	1.18
	MLH^{2+}	12.18 ± 0.04	0.95
	MLH_2^{3+}	18.42 ± 0.05	0.46
Mg^{2+} [b]	ML^+	-	-
	MLH^{2+}	11.95 ± 0.04	0.30
	MLH_2^{3+}	18.01 ± 0.05	0.41
Mn^{2+} [d]	ML^+	4.23 ± 0.09	-0.1
	MLH^{2+}	12.77 ± 0.08	-0.3
	MLH_2^{3+}	18.74 ± 0.09	-0.8
Cu^{2+} [d]	ML^+	8.82 ± 0.04	-0.45
	MLH^{2+}	13.64 ± 0.03	0.16
	ML_2H^+	21.89 ± 0.05	-0.40
	$MLOH^0$	3.13 ± 0.03	-0.06
	$ML(OH)_2^-$	-8.10 ± 0.04	-0.29
Zn^{2+} [d]	MLH^{2+}	12.79 ± 0.07	-0.21
	MLH_2^{3+}	18.91 ± 0.07	-2.04
	$MLOH^0$	-2.31 ± 0.06	-0.67
Cd^{2+}	ML^+	3.44 ± 0.12	1.6 ± 0.2
	MLH^{2+}	12.26 ± 0.11	1.4 ± 0.2
Hg^{2+}	ML^+	17.54 ± 0.01	1.8 ± 0.1
	MLH^{2+}	24.42 ± 0.02	2.1 ± 0.2
	$MLOH^0$	9.75 ± 0.01	0.1 ± 0.1
Pb^{2+}	ML_2^0	9.93 ± 0.09	-0.24 ± 0.15
	ML_2H^+	18.91 ± 0.05	-0.24 ± 0.09

[a] referred to the equations (2.21) or (2.22). [b] ref. [97]. [c] $\pm$ 3 std. dev. [d] ref. [99].

4.6 Dependence of the formation constants on the temperature

Temperature is another factor that affects the complexes speciation. To have a comprehensive thermodynamic picture, the dependence on the temperature was determined by the Van't Hoff equation (2.28). For all the M^{2+}-CAR systems studied, ΔH changes are summarized in Table 4.5, along with the Gibbs free energy, ΔG_i, and $T\Delta S_i$ values, calculated by the reactions (2.30) and (2.31), respectively.

For the Ca^{2+}- and Mn^{2+}-CAR (L) complexes, all the ΔH values are endothermic and the free energy changes are mainly entropy driven. This trend is characteristic of electrostatic interactions.

For the Mg^{2+}-, Cu^{2+}-, Zn^{2+}, Cd^{2+}-, Hg^{2+}- and Pb^{2+}-CAR (L) complexes, the enthalpy change values (ΔH) are exothermic, except for the ML^+ in Mg^{2+}-CAR system and for the respective $ML(OH)_2^-$ and $MLOH^0$ species in Cu^{2+}- and Zn^{2+}-CAR systems. This can be attributed to an increase in order due to solvation processes.

In the Mg^{2+}-CAR complexes, the main contribution to stability is enthalpy, as also for the other M^{2+}-CAR systems considered. For the Cu^{2+}-CAR system, enthalpy and entropy tend to contribute in a similar extent to the free Gibbs energy, especially in the ML^+, MLH^{2+} and ML_2H^+ species. Most complex species in the Cd^{2+}-, Hg^{2+}- and Pb^{2+}- systems benefit from a negative $T\Delta S$, due to solvation processes, and a higher extent of the enthalpy contribute to the free Gibbs energy (ΔG).

The different thermodynamic behavior of M^{2+}-CAR systems in water may be due to the various coordination modes of the CAR molecule toward metal cations, as proven by *ab initio* molecular dynamics simulations in the case of Ca^{2+} and Mg^{2+} (Paragraph 4.1.3).

Table 4.5. Thermodynamic formation parameters of M^{2+}-CAR (L^-) species in NaCl at I = 0.15 mol L^{-1} and T = 298.15K.

M	Species	ΔG [a), b)]	ΔH [a), b)]	$T\Delta S$ [a), b)]
Ca^{2+} [c)]	ML^+	-16.9±0.2 [d)]	17±9 [d)]	34±9 [d)]
	MLH^{2+}	-69.2±0.3	17±6	86±6
	MLH_2^{3+}	-107.0±0.4	27±9	134±9
Mg^{2+} [c)]	ML^+	-15.6±0.2	-29±4	-13±4
	MLH^{2+}	-67.2±0.2	-59±5	8±5
	MLH_2^{3+}	-104.9±0.3	-91±3	14±3
Mn^{2+} [e)]	ML^+	-19.1±0.3	76±12	95±12
	MLH^{2+}	-71.7±0.1	74±12	146±12
	MLH_2^{3+}	-110.3±0.2	77±12	187±12
Cu^{2+} [e)]	ML^+	-47.2±0.06	-29±4	18±4
	MLH^{2+}	-76.8±0.1	-48±5	29±5
	ML_2H^+	-120.4±0.2	-56±10	64±10
	$MLOH^0$	-15.1±0.06	-24±7	-9±7
	$ML(OH)_2^-$	47.8±0.1	16±11	-32±11
Zn^{2+} [e)]	MLH^{2+}	-72.1±0.02	-53±7	19±7
	MLH_2^{3+}	-107.4±0.02	-12±7	95±7
	$MLOH^0$	16.3±0.02	4±7	-12±7
Cd^{2+}	ML^+	-17.8±0.4	-60±40	-42±40
	MLH^{2+}	-69.5±0.2	-98±30	-29±30
Hg^{2+}	ML^+	-98.6±0.06	-65±10	34±10
	MLH^{2+}	-139.1±0.1	-162±14	-23±14
	$MLOH^0$	-54.0±0.2	-118±11	-64±11
Pb^{2+}	ML_2^0	-56.7±0.5	-122±14	-65±14
	ML_2H^+	-107.9±0.3	-87±8	21±8

[a)] referred to the equations (2.21) or (2.22). [b)] In kJ·mol⁻¹. [c)] ref. [97]. [d)] ≥ 95% of confidence interval. [e)] ref. [99].

4.7 Sequestering ability

To complete the investigation of CAR with bivalent metal cations, its sequestration ability toward them was assessed. Its determination was achievable through the empirical parameter, $pL_{0.5}$, extensively described in Paragraph 2.9, under different experimental conditions (Table 2.10).

For each M^{2+}-CAR system, the resulting $pL_{0.5}$ values and sequestration diagrams are reported in Figures 4.28 and 4.29 under different pH, ionic strength and ionic strength conditions.

In Figure 4.28, simulated at physiological conditions, the best sequestering ability of CAR is achieved toward Cu^{2+}, whose $pL_{0.5}$ value is 7.88. In particular, the $pL_{0.5}$ decreases in the following order:

$$Cu^{2+} \gg Mn^{2+} > Cd^{2+} > Zn^{2+} > Pb^{2+} > Hg^{2+} > Ca^{2+} > Mg^{2+}$$

The sequestration profile of CAR changes in conditions simulating natural waters, or rather seawaters (Figure 4.29). In these cases, the $pL_{0.5}$ decreases in the following order:

$$Cu^{2+} > Hg^{2+} \gg Zn^{2+} > Pb^{2+} > Ca^{2+} > Mn^{2+} > Mg^{2+} > Cd^{2+}$$
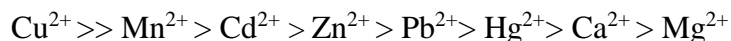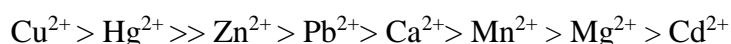
This aspect was crucial in evaluating CAR as an ideal candidate for *(i)* detection and *(ii)* removal metal cations. Starting from which, the dipeptide was thought in several applications, which are discussed in the following chapters. However, as it turns out, the thermodynamic Ca^{2+}-, Mg^{2+}- and Cd^{2+}-CAR interactions are rather weak, as is the sequestering ability of CAR toward them.
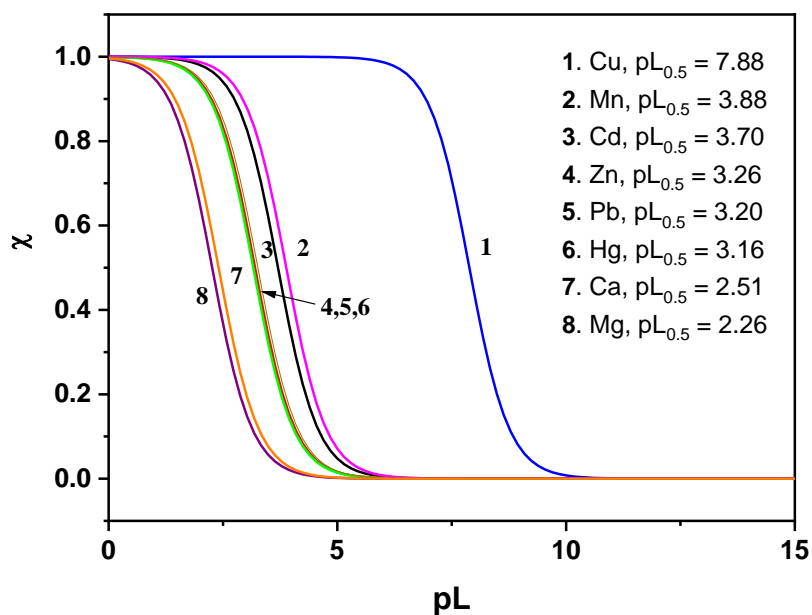
Figure 4.28. Sequestration diagram of CAR toward the metal cations (M^{2+}) studied at pH = 7.4; I = 0.15 mol L^{-1} and T = 310.15 K.
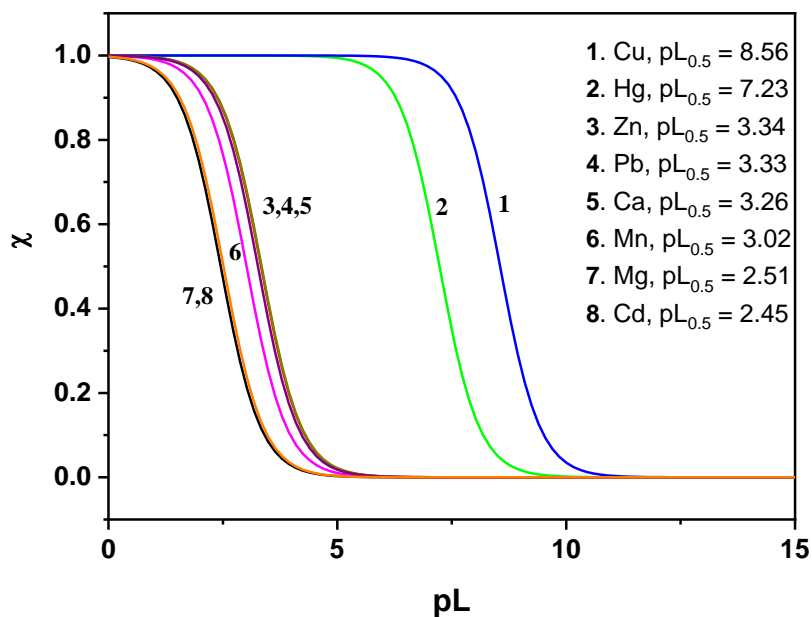

Figure 4.29. Sequestration diagram of CAR toward the metal cations (M^{2+}) studied at pH = 8.1.; I = 0.7 mol L^{-1} and T = 298.15 K.

4.8 Literature comparison

The metal ion chelating ability of CAR is one of the most studied features of this dipeptide, also included in this thesis. Several models are reported in the literature concerning, in particular, the structures of the Cu^{2+}- and Zn^{2+}-CAR complex species [7, 94, 141]. Since 1955 [142], investigations of the Cu^{2+}-CAR system in aqueous solutions have continued. The Cu^{2+} complexes with multidentate ligands, containing imidazole groups, have been extensively studied [143], due to the fact that they are potentially endowed with donor and acceptor abilities. These peculiar aspects result in the formation of coordination and hydrogen bounds. In particular, the donor ability of the imidazole ring is inhibited at acid pH values (below its dissociation constant values) and no assembly processes are observed. Under alkaline conditions, instead, the imidazole ring is able to coordinate the cupper ion of an adjacent group or generate hydrogen-bonds with an adjacent imidazole. In fact, controversial data concern the existence of some species in certain pH values [33], whose formation depends on pH and metal:ligand ratio. In particular, literature data propose that the dimeric form, $[Cu_2H_{-2}L_2]^0$, exists in equilibrium with the monomeric ones ($[CuLH]^{2+}$ and $[CuL]^+$) in solution, and that this equilibrium is shifted toward the dimer at neutral and basic pH and in a 1:1 molar ratio [33]. Although several studies have been performed on the characterization of the Cu^{2+}-CAR complexes, the presence of the dimeric form was not predictable in living organisms because it is relevant in alkaline environment (pH ≥ 8.0), and not under physiological conditions, in which low copper concentrations and competitive ligands occur. In turn, the latter would lead to monomeric species with mixed ligands [7, 33]. Although the literature data report the presence of Ca^{2+}-, Cu^{2+}-, and Zn^{2+}- CAR dimers in solution, no dimeric forms are obtained under the experimental conditions adopted in this thesis.

Furthermore, literature data report generalized structures for the lowest energy species for the doubly deprotonated CAR molecule complexed with divalent

cations, such as Ca^{2+} and Mg^{2+} [144]. Moustafa et al. [144] describe a tetra-coordinated complex structure, where interactions are between the divalent cation and (i) one oxygen of the COO^- group, (ii) the bare nitrogen atom of the imidazole ring, (iii) the amino group of the alanine residue (NH_2), and (iv) the bare nitrogen atom of the histidine residue. Analogously, in the Paragraph 4.1.3, the same results are discussed.

Little evidence was also provided on the formation constants values, which were not defined under different conditions of ionic strength and temperature. Therefore, this thesis provides the stability constants values of all the M^{2+}-CAR systems investigated and their dependence on ionic strength and temperature.

4.9 Final remarks and future perspectives

This intriguing dipeptide, carnosine, is paid particular attention for its numerous beneficial properties and functions. Among these, although the metal ion chelating ability of CAR is well-known in the literature, no clear evidence has been revealed. For these reasons, it was important to define the speciation of CAR and its interactions with the main metal cations. On the other hand, it was necessary to determine the formation constants values and to study their dependence on ionic strength and temperature. This analysis was mainly performed by potentiometry, through which robust results were obtained. The latter, along with literature data and combinatorial use of techniques, are strengthen the speciation models expected for each system investigated.

Therefore,

- Thermodynamic parameters (ΔH, ΔG and $T\Delta S$) were also determined by means of equations (2.28), (2.29) and (2.30).
- The sequestering ability of CAR toward the investigated metals was calculated. In light of this, the subsequent applicative study takes shape. In

particular, the outstanding sequestering ability of CAR was exploited to study its sensing properties toward metal cations under physiological conditions.

- However, since the electrochemical study on the free ligand did not provide insight into its voltammetric behavior, a more electroactive CAR derivative, FcCAR, was synthetized.

- On the other hand, another analog, PyCAR, thought to be a potential agent for the detection of metal cations, was produced.

  Both synthetic approaches are described in Chapter 5 of this thesis. Furthermore, sensing properties of the two CAR derivatives were also focused on and discussed in Chapter 5.

- Moreover, CAR was covalently grafted on an azlactone–activated, polyacrylamide resin (AZ) in order to study its Pb^{2+} removal capacity.

Chapter 5

L-Carnosine (CAR) as metal ion probe

5.1 General aspects

So far the complexing and sequestering abilities of CAR toward different bivalent metal cations have been highlighted. However, one of the purposes of this work should not overlooked that, starting from speciation studies, concerns the use of CAR as a potential sensor for the detection of bivalent metal cations in various environments.

Speaking of metal ion sensors, many factors should be taken into account before their production. First of all, the concentration of a probe should not exceed that of metal ions because, otherwise, it could impound the whole metal amount [45]. However, the concentration of the sensor should be considerable to be highly selective and, thus, avoid competitive exchange with endogenous metal complex species. Furthermore, in the fabrication of a sensor, the modulation of ion-selectivity and electronic densities involved in the interactions among molecules should be considered, as well as the monitoring of the surrounding medium and, thus, of the solvent, the ionic strength and pH where it works [45]. Moreover, a potential probe should benefit from:

   i)   photophysical properties, *i.e*., brightness, photostability and wavelength range;

   ii)   electrochemical properties and, thus, it should give a variation in redox potential or current intensity;

   iii)   biochemical properties, *e.g*., affinity and specificity for the metal target.

However, there is still a lack of an empirical rule for an easy and appropriate realization of a specific metal ion probe, and a useful and strategic approach consists in the formation of a binding unit, which includes at least a moiety responsible for metal ion binding and one or more signaling residues. The latter should be a fluorophore or a redox active unit to point out the binding phenomena through change in color or photophysical properties and, thus, variations in Absorbance or Emission, or redox potential [45]. Sometimes the signaling unit is located next to the binding one, other times they are outdistanced by a space or linker. In some cases, the binding site, which includes at least a heteroatom, also corresponds to the signaling unit, that is the fluorophore or redox active molecule.

In order to design efficient CAR-based sensors, ferrocene (Fc) and pyrene (Py) units were introduced into the molecule to obtain an electrochemical and a fluorescent sensor, respectively.

i)   Among various materials, Fc-based sensors have drawn attention for the unique peculiarities of this molecule that provides sensitive, selective, cost-effective and easy-to-make probes for metal cations [45]. Fc is the most studied redox active molecule since 1951, year of its discovery. The chemical properties of Fc, as well as its remarkable electroanalytical activity, are related to its sandwich structure and, in particular, to d-π interactions between Fe^{2+} and the cyclopentadienyl (Cp) rings. Fc displays a reversible oxidation to ferrocenium ion that is, in turn, assisted by the lower oxidation potential of ferrocene to lose an electron, giving rise to two stable redox states (Fe^{2+}/Fe^{3+} for Fc/Fc^+). Moreover, Fc has several benefits, including thermal and photochemical stability, low biotoxicity and commercial availability. The electrochemical properties of Fc are fully preserved even when it is modified. Indeed, its easy functionalization on one or both Cp moieties, along with the above-mentioned advantages, make Fc a versatile

molecule in a wide variety of applications, such as biophysics, medicines, biomedical engineering, switchable liquid cristable, burning rate catalysis, biosensors, chemosensors, optical devices, radiation absorption and bioelectronics [45].

ii)   Pyrene (Py-) derivatives have recently attracted attention because their Py moiety, belonging to the polycyclic aromatic hydrocarbons (PAHs), can give rise to both covalent and donor-acceptors (D-A) systems. This D-A unit is conducive to the fine-tuning electronic interactions and charge transfer efficiencies [145]. Therefore, these Py-based materials can be employed in technological applications, as they can accomplish multifunctional optoelectronic properties by regulating the electronic structures. In fact, they also allow an efficient monitoring of absorption and emission properties through regioselective replacements of functional groups in pyrene active sites [145, 146]. Since the emission color tuning of these chromophores is readily controlled by the functional groups modification, they are outstanding candidates as light-emitting materials with high emission quantum yields both in solution and in the solid state [146]. Furthermore, the planar geometry of the Py unit results in intermolecular π-π interactions, making aggregation, fluorescence quenching, red-shift characteristics and broad emission bands. Among these properties, molecular aggregation and fluorescence quenching have recently been employed to develop fluorescence sensors. The selective recognition and sensing of aromatic systems are due to the fluorescence resonance energy transfer (FRET) mechanism[146]. Due to its sensitivity and sensing speed, fluorescence is a useful method for selective applications of chemosensors, especially based on the fluorescence quenching approach.

In more detail, Pal et al. [45] described the most likely mechanisms of sensing in the Fc-based chemosensors, schematized in Figure 5.1.
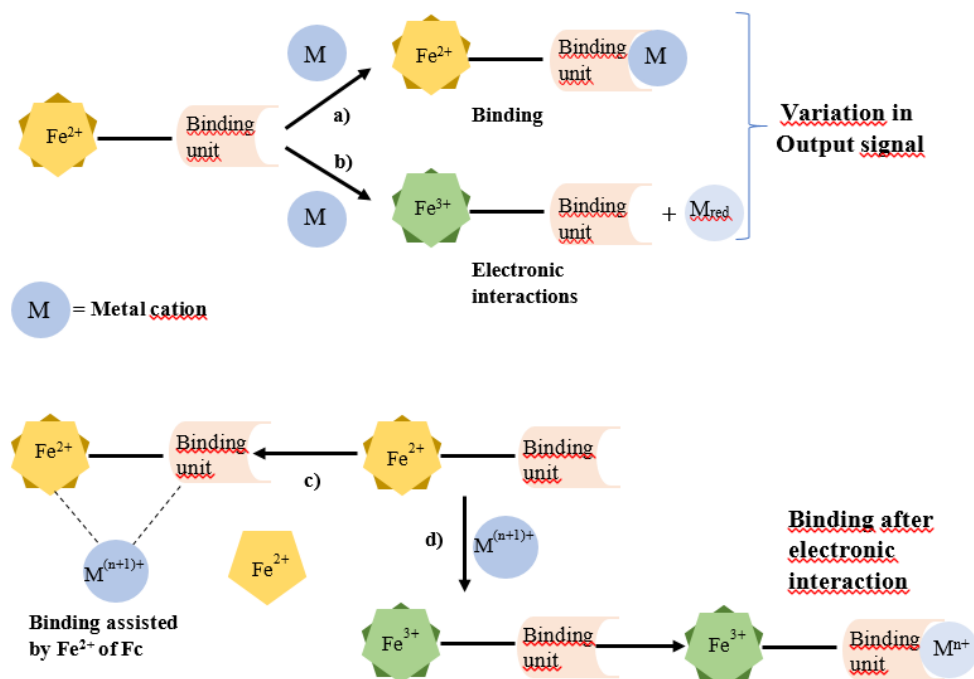

Figure 5.1. Schematic representation of the common sensing pathways of Fc derivatives.

In the pathway

a) The electron density is drifted from the N-binding unit to the guest metal ion in the course of binding, and the electronic density on the ferrocenyl unit is reduced. In particular, this phenomenon occurs if it is conjugated to the binding unit through double or triple bonds. This leads to further difficult oxidation of the ferrocenyl unit, which undergoes an anodic shift in electrochemical measurements. Therefore, it is cleaver to synthetize a probe with the binding unit close to the Fc in order to provide a perceivable variation in the electrochemical signal upon interaction with the guest.

b) An electronic redox reaction occurs between the host Fc unit and the guest metal cation. The metal ion is reduced by one electron and the Fe^{2+} of the Fc unit is oxidized by one electron to form Fc^+ ion, having Fe^{3+}. In these cases, electrochemical measurements undergo cathodic shifts. Cu^{2+}/Fe^{3+} and Hg^{2+}/Fe^{3+} give rise to this kind of electrochemical behavior, as they can reduce to Cu^+/Fe^{2+} or Hg^+/Fe^{2+} [45].

c) The Fc unit directly takes part in the binding of the metal ion, as does the probe. In this case, the d electrons of the Fe^{2+} center of Fc interact with the guest metal ion with original oxidation state and, thus, this binding mechanism is assisted by the Fc moiety of the probe. Electrochemical measurements undergo relevant anodic shifts due to the electronic cloud goes from the Fc center to the vacant orbitals of the guest metal.

d) The redox path b) can be followed by a binding interaction between the oxidized Fc probe and the reduced metal ion at the binding unit, containing heteroatoms. These interactions were found in the case of Cu^{2+}, which reduces to Cu^+ and binds to the oxidized probe.

Pathways **a)** and **b)** are the most common sensing mechanisms in Fc derivatives. Pal et al. [45] also reported that the binding of alkali cations promotes that of their counter ions to cation-bound sensors. However, cation sensing phenomena are not dependent on the presence of other competitive metal ions.

To demonstrate the sensing properties of fluorescent, colorimetric, and redox-selective metal ion chemosensors toward certain metal cations, traditional analytical techniques, such as UV-Vis spectroscopy and Cyclic Voltammetry (CV) are usually used [147]. Both methods were employed in this thesis to investigate the behavior of the two CAR derivatives toward Hg^{2+} and Pb^{2+}. Since they are the most toxic environmental pollutants responsible for a wide variety of adverse health problems, the development and employment of suitable, sensitive and

selective chemosensors for the detection of these toxic metal cations has become of considerable importance.

## 5.2 Synthesis of ferrocenyl-carnosine (FcCAR)

The redox active ferrocenyl-carnosine derivative (**3**) FcCAR was synthesized by a coupling reaction of free CAR with the *N*-hydroxysuccinimide activated ferrocene (**2**) under mild experimental conditions (Scheme 1). The ferrocenecarboxylic acid (**1**) was activated by reacting with N-hydroxysuccinimide to form the corresponding ester (**2**), which was treated at room temperature (r.t.) with CAR in the presence of sodium bicarbonate to afford FcCAR (**3**) in an overall yield of 64%. Given the amphiphilic characteristics of FcCAR, the selection of a suitable mixture of water/aprotic solvent for the coupling reaction (*i.e.,* water/DMF) and in the purification by crystallization (water/acetone) was crucial to the success of the synthesis [45]. The ^{1}H NMR spectrum of the FcCAR shows three distinct regions of signals, which are those of the imidazole protons of the histidine residue at 7.0 ppm and 7.9 ppm; the typical peaks of the ferrocenyl unit at 4.5 ppm and the peptidyl aliphatic region between 2.5-3.5 ppm.
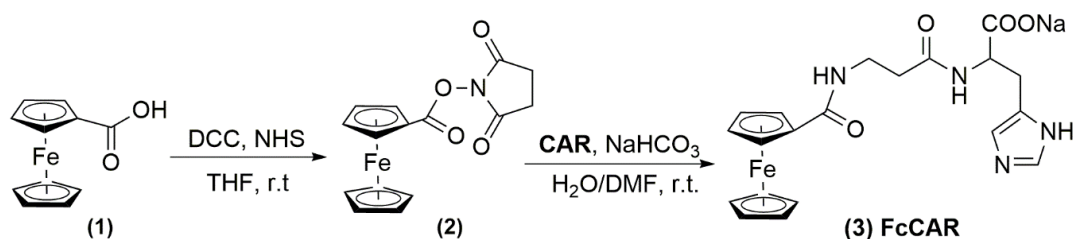
Scheme 1. Synthesis of the ferrocenyl-carnosine (FcCAR).

5.3 Synthesis of pyrenyl-carnosine (PyCAR)

To exploit the sensing properties of CAR toward metal cations, conjugation of CAR with pyrenacetic acid was achieved. The pyrenyl carnosine derivative (**5**) PyCAR was synthesized by a coupling reaction of free CAR with pyrenacetic acid (**4**) under mild experimental conditions (Scheme 2). The coupling reaction was carried out in the presence of peptide coupling reagents (EDCI, HOBt) (Scheme 2). The structure of PyCAR (**5**) was confirmed by ^{1}H NMR analysis. In particular, the signals of pyrenyl protons were detected at 7.75 (2H, d), 7.55 (2H, d), 7.25 (5H, m) ppm in the ^{1}H NMR spectrum. The imidazole peaks of the histidine moiety were detected as doublets at 6.8 and 7.7 ppm, whereas the L-histidine methyne proton was detected at 3.4 ppm as a multiplet.
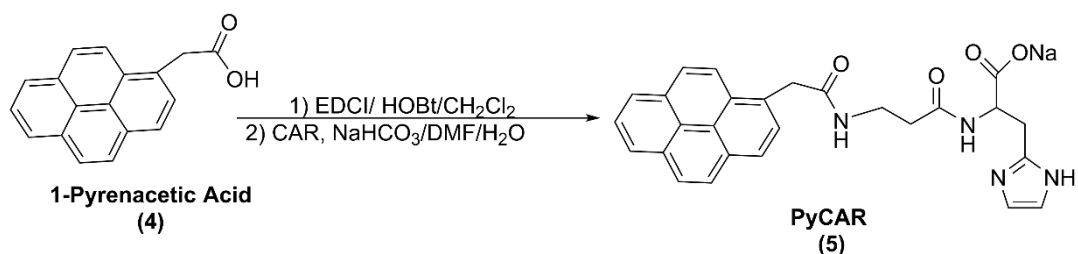
Scheme 2. Synthesis of pyrenyl-carnosine (PyCAR).

5.4 Acid-base properties

Before evaluating the electrochemical and fluorimetric properties of the two CAR derivatives, a speciation study was undertaken aimed, first of all, at determining the thermodynamic interaction parameters with some of the metals considered in this thesis, and selecting those with respect to which the two derivatives show the greatest sequestering abilities.

The starting point was the analysis of the acid-base properties. As discussed in Chapter 3, CAR has three ionizable groups. Its amino group of the β-Ala residue is

conjugated with the lipophilic Fc and Py moieties, respectively, in the two derivatives under study. Therefore, FcCAR and PyCAR have two ionizable groups, consisting of the carboxylic one and the imidazole ring.

The study of the equilibria of both CAR derivatives in NaCl aqueous solutions was performed by potentiometric and UV-Vis spectrophotometric titrations at $I = 0.15$ mol L^{-1} and $T = 298.15$ K. The latter measurements were carried out in a wide selected wavelength range ($200 \leq \lambda \leq 400$ nm), from pH ≈ 3.0 to 9.0.

For FcCAR, the spectrophotometric titrations and ε *vs*. λ diagram are shown in Figure 5.2. The spectrum of FcCAR is characterized by a broad band around 205 nm and a slight one around 260 nm. Both are attributable to n-π^* and π-π^* electronic transitions, respectively. As the pH increases, and thus the deprotonation degree of the molecule, a gradual gain in Absorbance occurs. Moreover, the ε of the deprotonated FcCAR species is also higher than that of protonated ones.
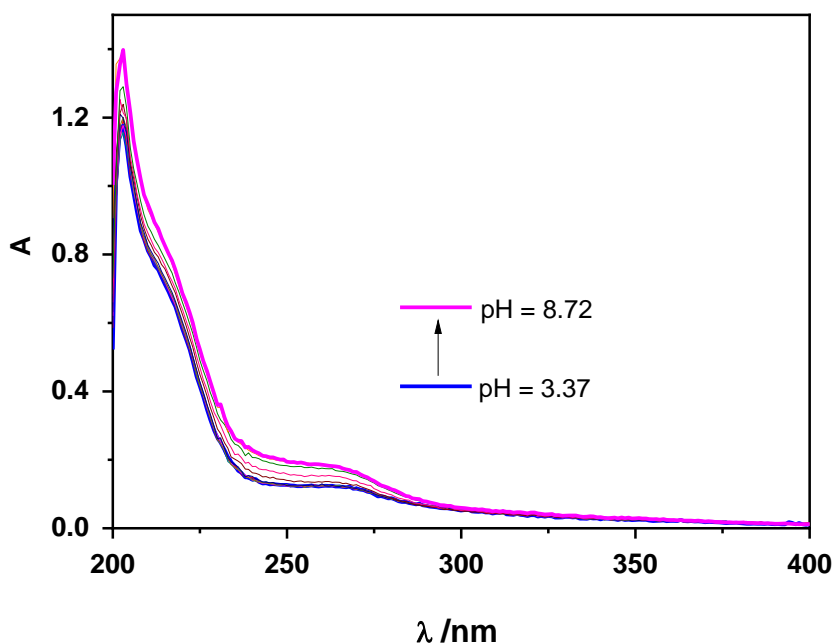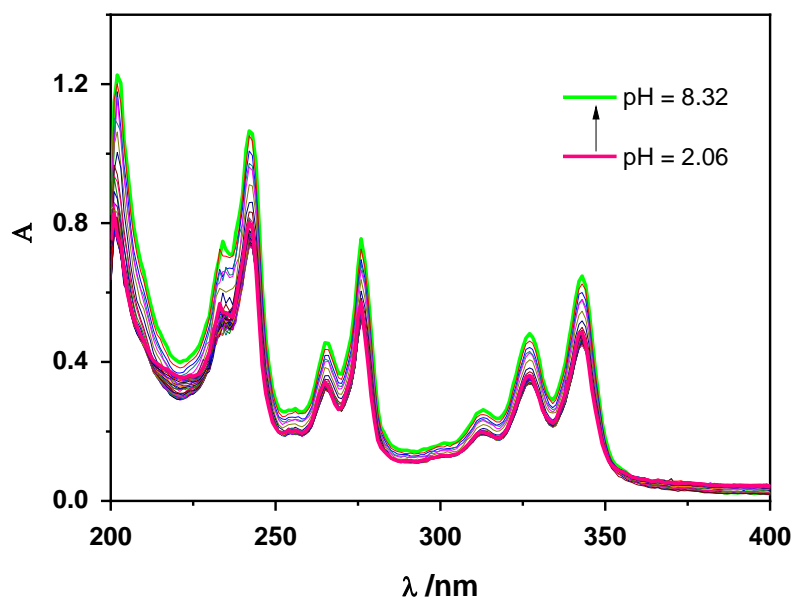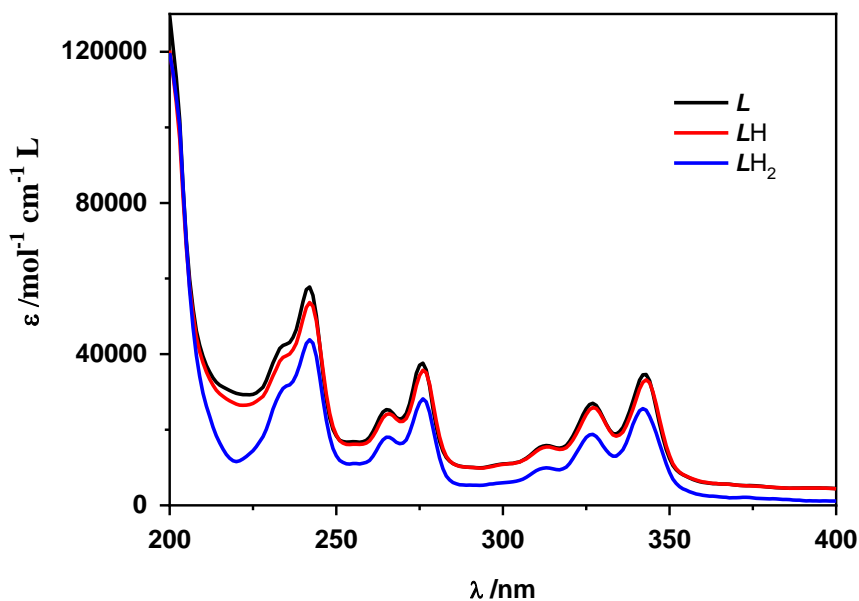

(a)
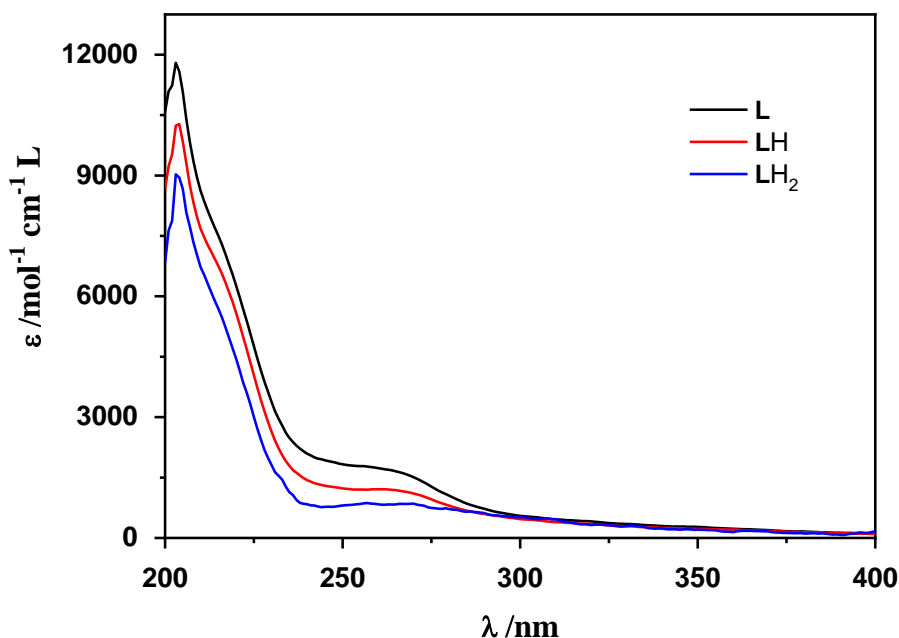
(b)

Figure 5.2 (a) Spectrophotometric titrations of FcCAR (**L**) (0.1 mmol L^{-1}) in NaCl aqueous solution at I = 0.15 mol L^{-1} and T = 298.15 K. **(b)** ε *vs.* λ of the differently protonated FcCAR (**L**) species in NaCl aqueous solution at I = 0.15 mol L^{-1} and T = 298.15 K.

For PyCAR, the spectrophotometric titrations and ε *vs.* λ diagram are shown in Figure 5.3. The spectrum of PyCAR is characterized by numerous bands in the wavelength range (200 ≤ λ ≤ 400 nm), whose maxima around 240, 274 and 340 nm are attributable to n-π* and π-π* electronic transitions, respectively. As the pH, and thus the deprotonation degree of the molecule, increases, there is a gradual gain in Absorbance, just as in FcCAR. Analogously, the ε of the deprotonated PyCAR species is also greater than that of protonated ones.

(a)

(b)

Figure 5.3 (a) Spectrophotometric titrations of PyCAR (*L*) (0.025 mmol L^{-1}) in NaCl aqueous solution at I = 0.15 mol L^{-1} and T = 298.15 K. **(b)** ε *vs.* λ of the differently protonated PyCAR (*L*) species in NaCl aqueous solution at I = 0.15 mol L^{-1} and T = 298.15 K.

The protonation constants, obtained from the processing of potentiometric and spectrophotometric data using the BSTAC and HYSPEC programs respectively, are collected in Table 5.1 along with those of CAR, for comparison. The overall protonation constants, β, are defined as average of the data resulting from the synergistic combination of the two techniques. The same Table shows the stepwise formation constants, K, which are useful for evaluating the functional groups involved in each protonation equilibrium.

The first protonation step of FcCAR and PyCAR, related to the imidazole ring, has a lower value ($logK = 6.45$ and $logK = 6.66$, respectively) than that of CAR ($logK = 6.79$). On the other hand, the second equilibrium step pertains to the carboxylic group, whose $logK_2$ value is 3.00 for FcCAR and ~0.3 fold higher than that of CAR ($logK_3 = 2.69$). A similar value is supplied by PyCAR, whose $logK_2$ value is 2.79. Comparing the protonation constant values of both derivatives, as well as the nature and size of the lipophilic conjugates, it was found that the Fc moiety undergoes a greater withdrawal effect on the CAR residue.

The distribution diagrams of FcCAR and PyCAR (Figure 5.4) show that for $5.0 \leq$ pH ≤ 8.0, range of interest for most natural fluids, FcCAR and PyCAR are present as HL^0 and L^- species, whose formations reach a maximum at pH ~ 4.5-5.0 and 9.0, respectively.
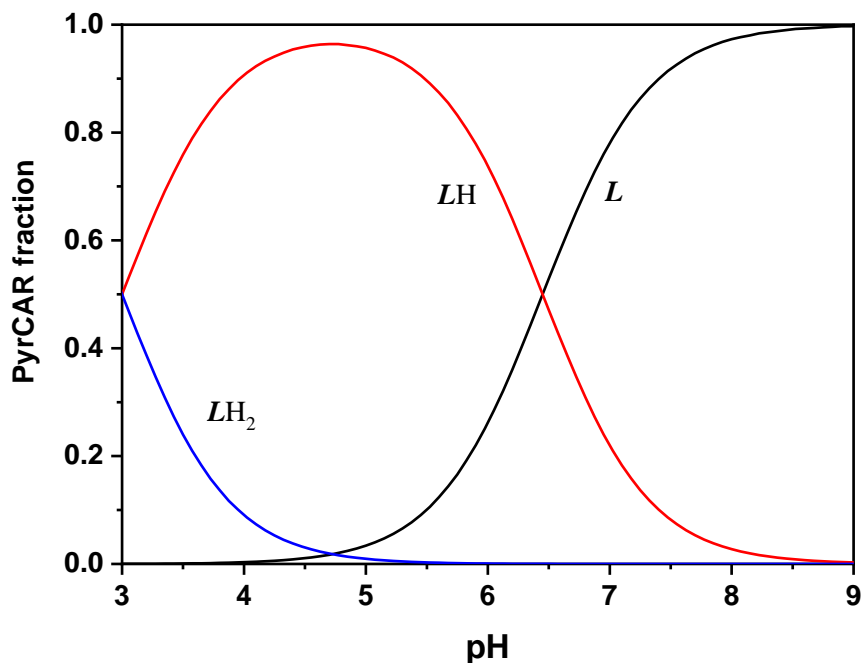
Table 5.1. Protonation constant values of CAR, FcCAR and PyCAR in NaCl aqueous solution at $I = 0.15$ mol L^{-1} and $T = 298.15$ K.

| Reaction	CAR [a]	FcCAR	PyCAR
	logβ		
$L^- + H^+ = LH^0$	9.38	6.45±0.04[a]	6.66±0.02[a]
$L^- + 2H^+ = LH_2^+$	16.17	9.45±0.06	9.45±0.03
$L^- + 3H^+ = LH_3^{2+}$	18.86	-	-
	logK		
$L^- + H^+ = LH^0$	9.38	6.45	6.66
$LH^0 + H^+ = LH_2^+$	6.79	3.00	2.79
$LH^+ + H^+ = LH_3^{2+}$	2.69	-	-

[a] ± 3 std. dev.
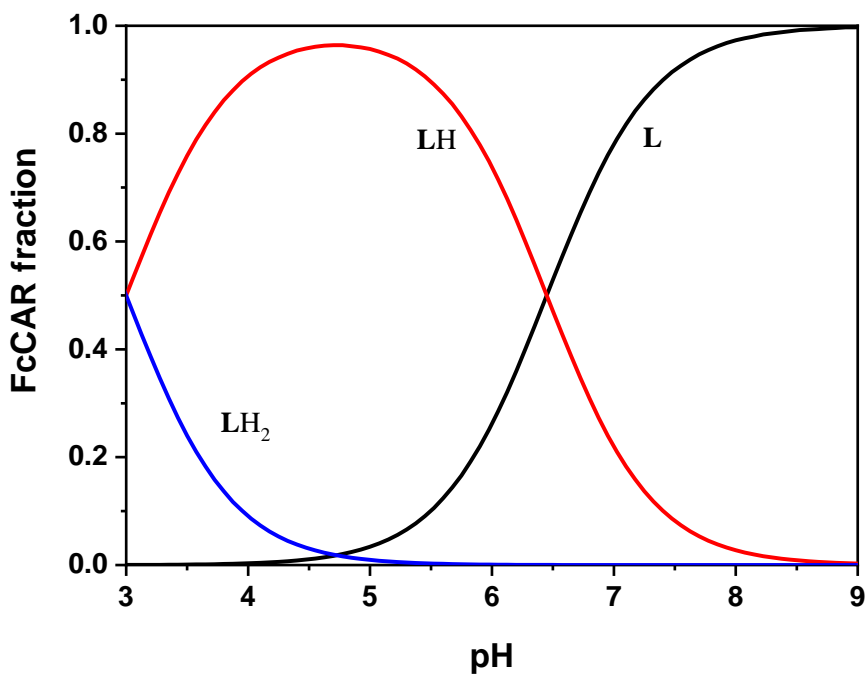
(a)

(b)

Figure 5.4. Speciation diagrams *vs*. pH of **(a)** FcCAR (**L**) and **(b)** PyCAR (*L*) (charges omitted for simplicity) in NaCl aqueous solution at I = 0.15 mol L^{-1} and T = 298.15 K (C$_L$ = 0.1 mmol L^{-1}).

5.5 M^{2+}-ligand interactions

To determine the complexing ability of the two CAR derivatives with respect to three potentially toxic metal cations, Cd^{2+}, Hg^{2+} and Pb^{2+}, UV-Vis spectrophotometric titrations of solutions containing variable metal:ligand ratios, were performed in the ranges $200 \leq \lambda \leq 400$ nm and $2.5 \leq pH \leq 8.5$. The experimental conditions are shown in Table 2.7 However, the results with Cd^{2+} were affected by high errors, probably because the formation fractions of the complex species were not significant under the experimental conditions used for UV-Vis spectrophotometry. For this reason, they are not reported in this thesis.

Concerning the FcCAR systems, in the presence of Hg^{2+}, the UV-Vis spectra of the molecule are affected by a significant variation, as can be observed in Figure 5.5, where ε /mol^{-1} cm^{-1} L *vs.* λ /nm of the Hg^{2+}- and Pb^{2+}-FcCAR systems are shown. On the other hand, the presence of Pb^{2+} results in a gradual increase in Absorbance, without significant changes in the shape of the spectrum. Analogously for the PyCAR systems, the presence of Hg^{2+} or Pb^{2+} leads to an increase in Absorbance and no effect on the shape of the spectra is observed in Figure 5.6, where the ε values of the Hg^{2+}- and Pb^{2+}- PyCAR species are shown.

(a)

(b)
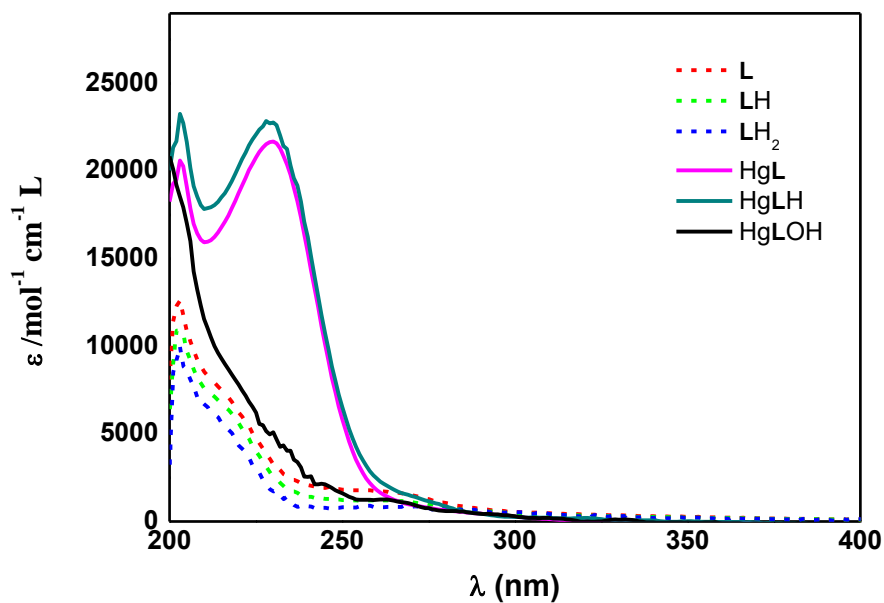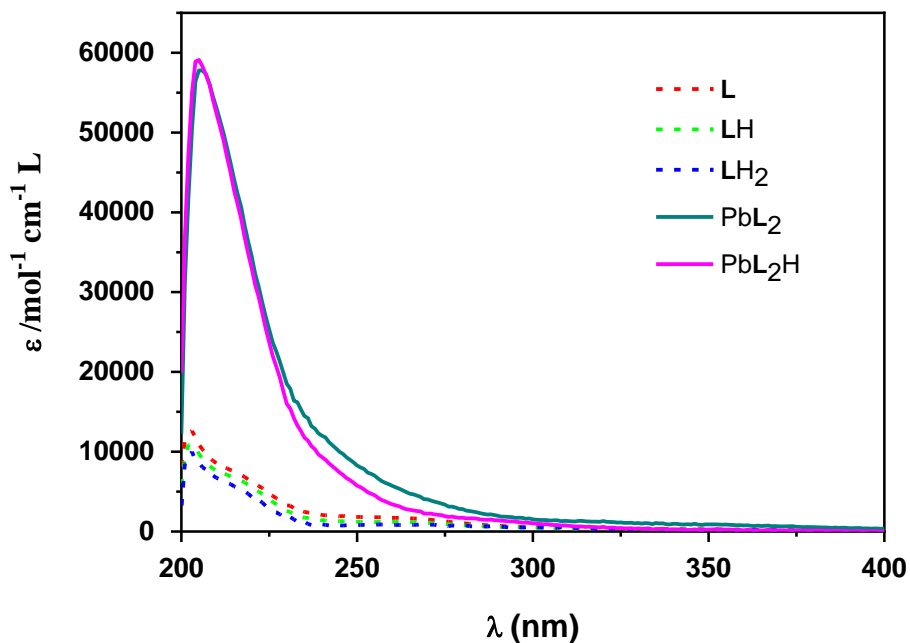
Figure 5.5. ε *vs.* λ of FcCAR (**L**) (dashed lines) compared with the **(a)** Hg^{2+}-FcCAR (**L**) (solid lines) and **(b)** Pb^{2+}-FcCAR (**L**) (solid lines) systems, in NaCl aqueous solution at I = 0.15 mol L^{-1} and T = 298.15 K.
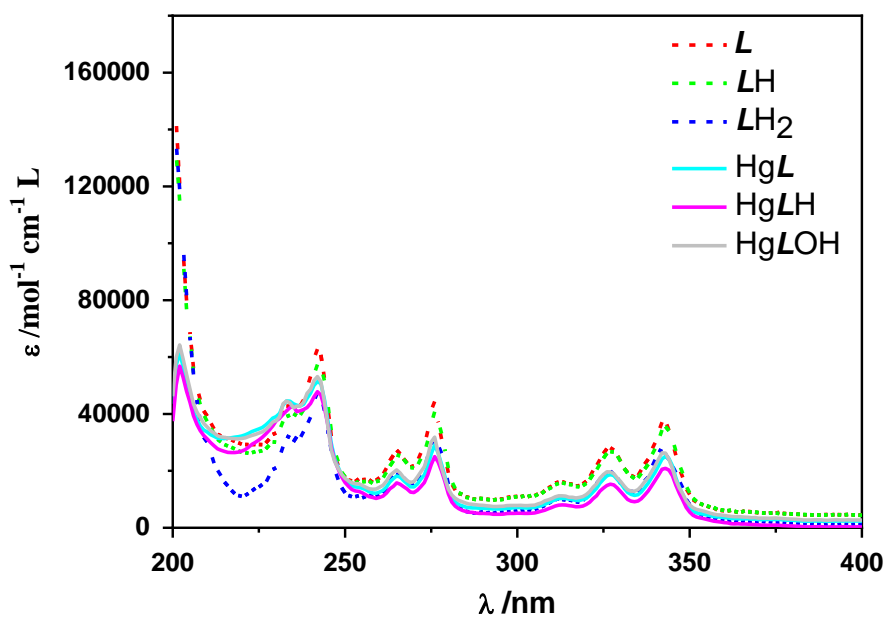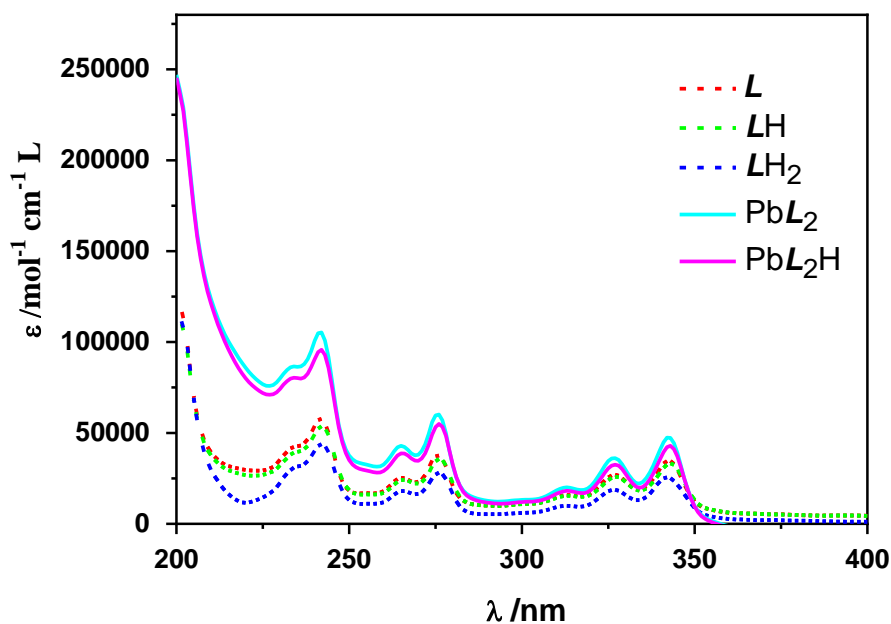
(a)

(b)

Figure 5.6. ε *vs.* λ of PyCAR (*L*) (dashed lines) compared with the **(a)** Hg^{2+}-PyCAR (solid lines) and **(b)** Pb^{2+}-FcCAR (solid lines) systems, in NaCl aqueous solution at I = 0.15 mol L^{-1} and T = 298.15 K.

Overall formation constants values, obtained by processing UV-Vis spectrophotometric data using the HYSPEC program, are shown in Table 5.2. The most reliable speciation models obtained for each system include species with a 1:1 metal:ligand ratio, with the exception of Pb^{2+}. This metal cation forms with both ligands 1:2 complex species, as for the CAR system. In more detail, the formation of three complexes, namely ML^+, MLH^{2+} and $MLOH^0$, occurs for the Hg^{2+}-FcCAR system, while the formation of two complex species, ML_2^0 and ML_2H^+, is described for the Pb^{2+}-FcCAR system. For both systems, the speciation diagrams in Figures 5.7 and 5.8 describe a strong chelating ability of FcCAR and PyCAR toward the two metal cations. In particular, Hg^{2+} is totally coordinated with FcCAR in the form of MLH^{2+} in acid environment, and the ML^+ species reaches a maximum of nearly 0.9 at pH 7.5. The $MLOH^0$ species forms starting from pH $\geq$ 7.0. On the other hand, Pb^{2+} is totally coordinated by FcCAR in the ML_2H^+ and ML_2^0 species in acid and basic environments, respectively.

A different distribution of the Hg^{2+}-PyCAR system can be observed in Figure 5.8. The molar fraction of Hg^{2+} reaches a maximum of 0.8 in the acid pH range and prevails in the ML^+ species at pH $\sim$ 6.5, amounting almost 0.97. The $MLOH^0$ species takes place starting from pH $\sim$ 6.0, predominating in the alkaline environment. The Pb^{2+}-PyCAR speciation is similar to that of the Pb^{2+}-FcCAR system and, thus, Pb^{2+} is totally coordinated by PyCAR in the ML_2H^+ and ML_2^0 species in acid and basic environments, respectively. Both species achieve the 0.5 fraction at pH = 6.0.

The high complexing capacities of FcCAR and PyCAR are also reflected in the sequestering ability. Figure 5.9 shows the comparison of the sequestering ability of CAR, PyCAR and FcCAR with respect to Hg^{2+} and Pb^{2+} cations. An increase in the pL_{05} value by at least three orders of magnitude was obtained in both systems.

Table 5.2 Formation constant values of the Hg^{2+}-, Pb^{2+}-FcCAR and -PyCAR systems, in NaCl aqueous solution at I = 0.15 mol L^{-1} and T = 298.15 K.

Reaction	FcCAR	PyCAR
	logβ	
$Hg^{2+} + L^- = HgL^+$	18.72±0.02 [a]	18.80±0.03 [a]
$Hg^{2+} + L^- + H^+ = HgLH^{2+}$	24.85±0.04 [a]	23.46±0.03 [a]
$Hg^{2+} + L^- + H_2O = HgL(OH)^0$	9.81±0.06 [a]	10.83±0.05 [a]
$Pb^{2+} + 2L^- = PbL_2^0$	16.29±0.08 [a]	15.88±0.05 [a]
$Pb^{2+} + 2L^- + H^+ = PbL_2H^+$	23.19±0.04 [a]	21.95±0.05 [a]

[a] ≥ 95% of confidence interval.
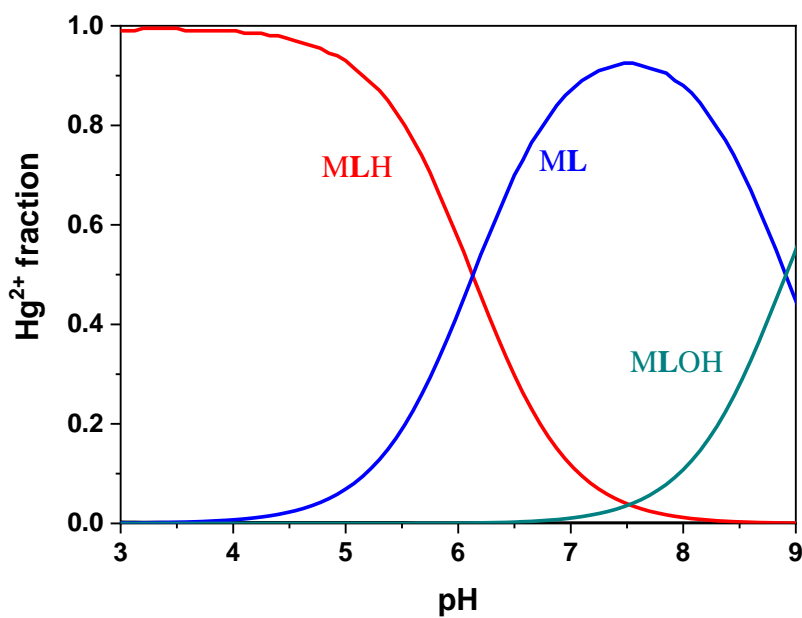
(a)
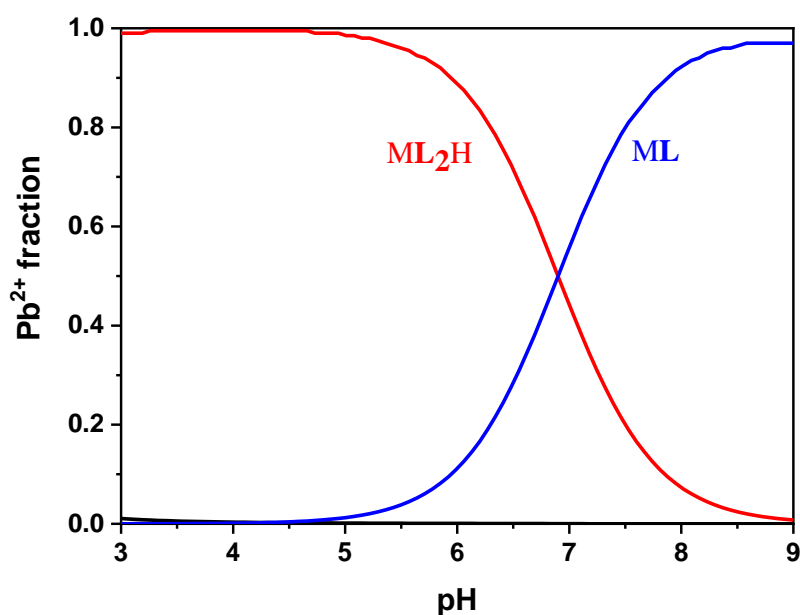
(b)

Figure 5.7. Speciation diagrams *vs*. pH of the **(a)** Hg^{2+}- and **(b)** Pb^{2+}- FcCAR (**L**) systems (charges omitted for simplicity) in NaCl aqueous solution at I = 0.15 mol L^{-1} and T = 298.15 K (C$_M$ = 0.2 mmol L^{-1}, C$_L$ = 4 mmol L^{-1}).

(a)
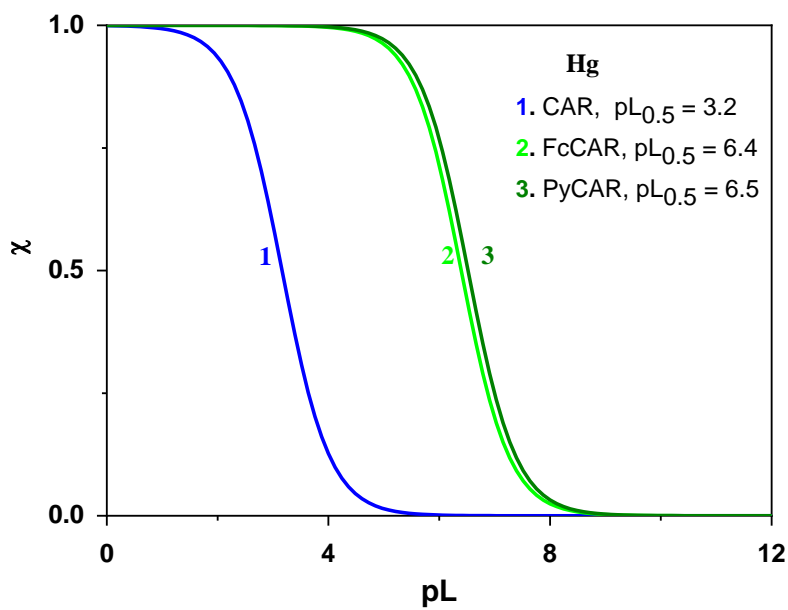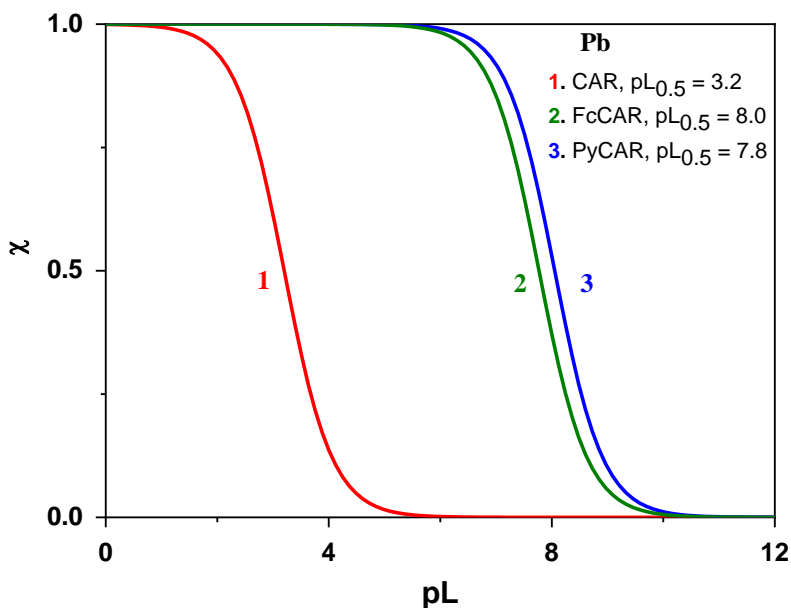
167
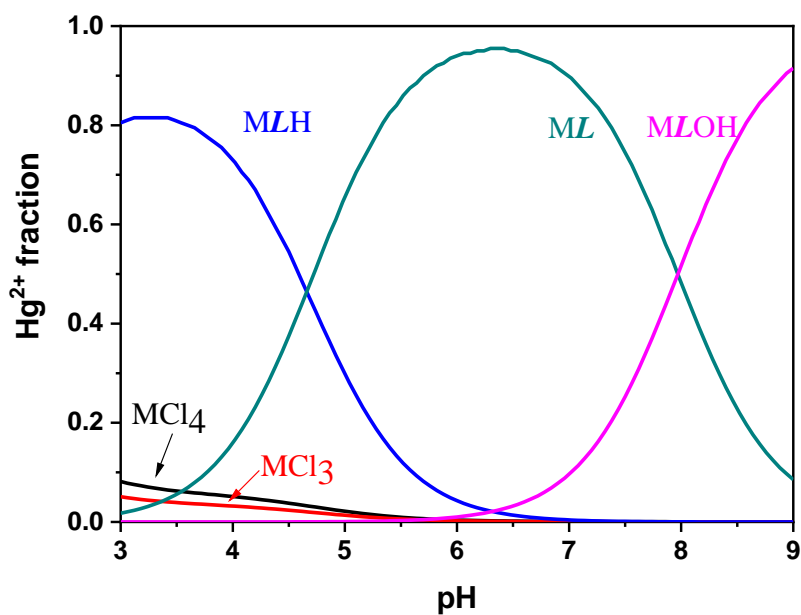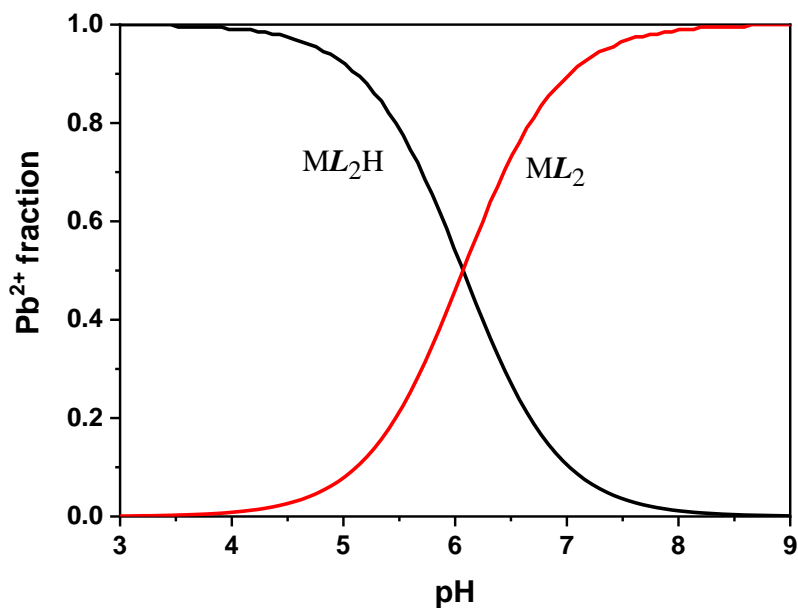
(b)

Figure 5.8. Speciation diagrams *vs*. pH of the **(a)** Hg^{2+}-PyCAR (*L*) and **(b)** Pb^{2+}-PyCAR (*L*) systems (charges omitted for simplicity) in NaCl aqueous solution at $I = 0.15$ mol L^{-1} and $T = 298.15$ K ($C_M = 0.2$ mmol L^{-1}, $C_L = 4$ mmol L^{-1}).

(a)

(b)

Figure 5.9. Sequestration diagrams of CAR, FcCAR and PyCAR toward **(a)** Hg^{2+} and **(b)** Pb^{2+} in NaCl aqueous solution at pH = 7.4, I = 0.15 mol L^{-1} and T = 298.15 K.

5.6 Electrochemical analysis

As written in Chapter 2, electrochemical sensing consists of a robust analytical tool that allows rapid response, high specificity and sensitivity, inexpensive and accurate analysis, even in heterogeneous matrixes [45]. In this context, voltammetric techniques are mainly employed because interactions are interpreted as variations in half-wave potential or current intensity. Since electroanalytical sensors are progressively emerging, FcCAR and PyCAR have been studied electrochemically. Electrochemical response of Screen-Printed Carbon Electrodes (SPCEs) was assessed by means of Cyclic Voltammetry (CV) using $K_3[Fe(CN)_6]$ (1 mmol L^{-1}) in KCl (0.1 mol L^{-1}) aqueous solutions at room temperature. Scan rate: 0.1 V s^{-1}.

Similarly, electrochemical activities of FcCAR and PyCAR on SPCEs were investigated by means of CV in KCl (0.1 mol L^{-1}) aqueous solutions at room temperature. CV was performed in different potential windows (-1 ≤ E(V) *vs.* Ag/AgCl ≤ +1), pH (3.0 ≤ pH ≤ 9.0 at scan rate: 0.1 Vs^{-1}) and scan rate ranges (10 ≤ mV s^{-1} ≤ 100 at pH = 7.0). However, PyCAR can give rise to dimeric species in aqueous solution which, dropping off on the electrode surface, do not give reproducible data. For these reasons and since all the analyses debated in this thesis were performed in aqueous solutions, electrochemical characterization of PyCAR was not taken into account. On the other hand, FcCAR was determined electrochemically with a limit of detection (LOD) of 10 nmol L^{-1}, and its Cyclic Voltammogram (CV) is compared with that of the ferrocenecarboxylate (FcCOO^{-}) precursor in Figure 5.10.

Figure 5.11 shows, instead, different ΔE_p values as a function of pH and, as can be observed, there are no significant changes in ΔE_p as pH changes. This is also confirmed in Figure 5.12, where the CVs as a function of pH are depicted. The anodic peaks are at +0.355 V, +0.366 V, +0.355 V and +0.375 V (*vs.* Ag/AgCl) as pH increases. The cathodic peaks are at +0.304 V, +0.294 V, +0.304 V and +0.304 V (*vs.* Ag/AgCl), respectively. The CV recorded at pH = 5.0 undergoes a different cathodic effect. Curiously, the CV of FcCAR revealed one oxidation peak at E = +0.526 V (*vs.* Ag/AgCl) and pH = 9.0, which could match to the oxidation of the imidazole ring, as reported in the literature [148]. The dependence of CVs on scan rate is shown in Figure 5.13, in which the one-electron reversible process is depicted. A slight shoulder can also be observed at E = +0.606 V (*vs.* Ag/AgCl) and pH = 7.0, attributable to oxidation of the imidazole ring.
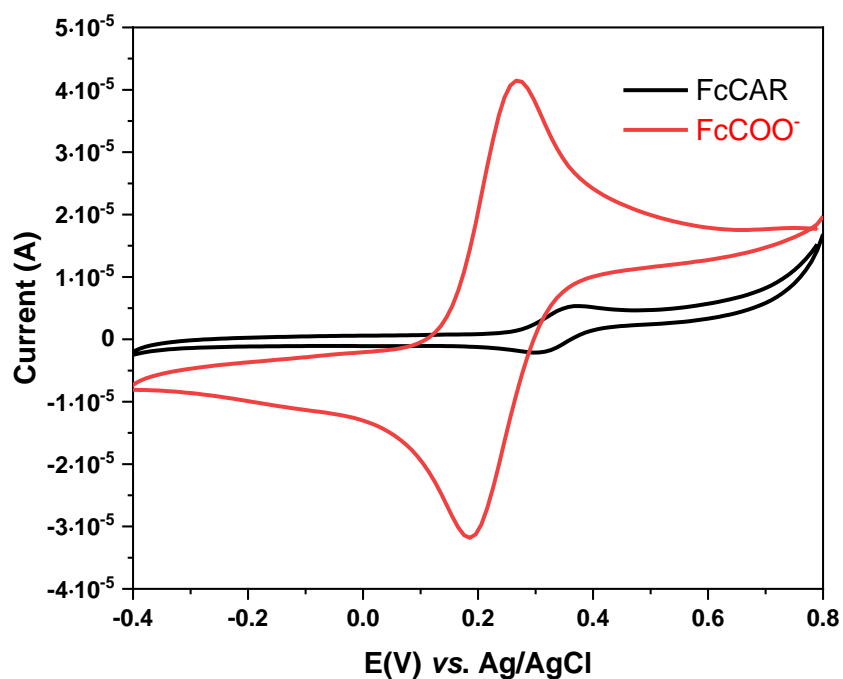
Figure 5.10. CVs of FcCOO⁻ (5 mmol L⁻¹) and FcCAR (5 mmol L⁻¹) in KCl (0.1 mol L⁻¹) aqueous solution on SPCE and at room temperature (scan rate: 0.1 V s⁻¹).
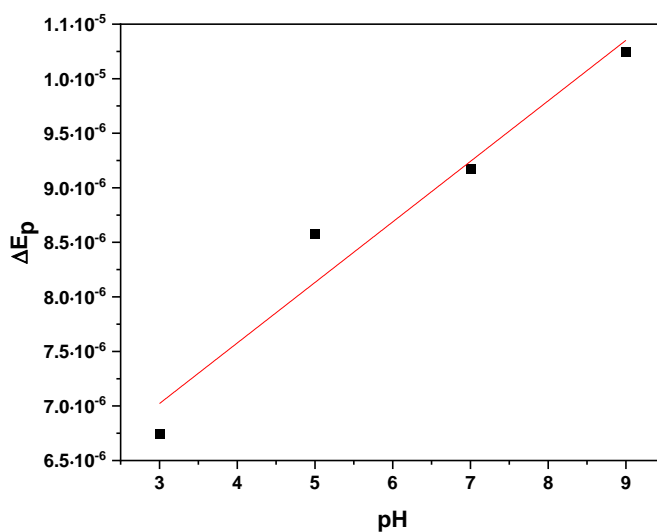
Figure 5.11. Dependence of ΔE_p *vs.* pH of FcCAR (1 mmol L⁻¹) in KCl (0.1 mol L⁻¹) aqueous solution on SPCE and at room temperature (scan rate: 0.1 V s⁻¹).

Figure 5.12. CVs of FcCAR (1 mmol L^{-1}) in KCl (0.1 mol L^{-1}) aqueous solution in the following pH range (3.0 ≤ pH ≤ 9.0) on SPCE and at room temperature (scan rate: 0.1 V s^{-1}).
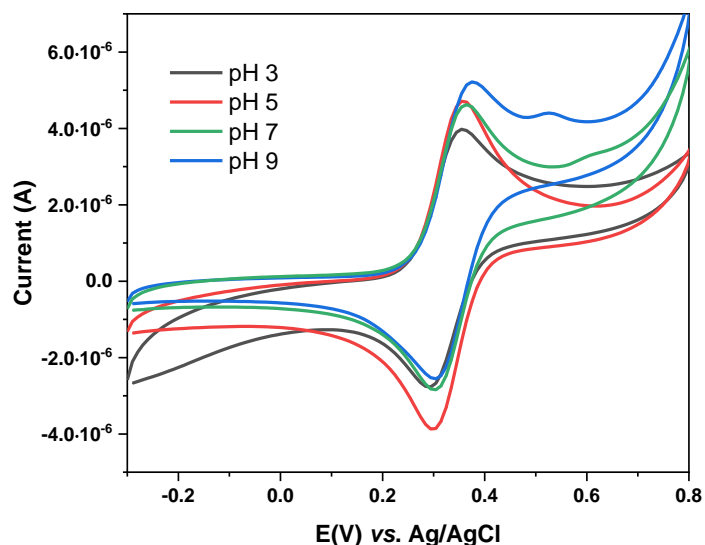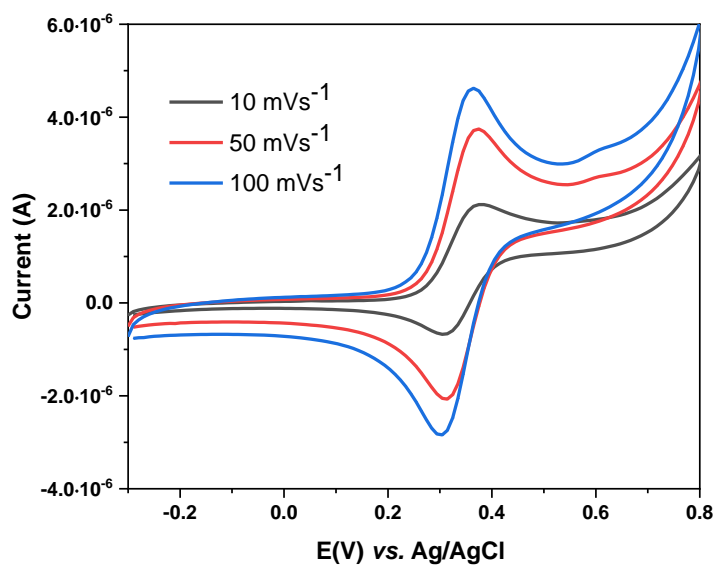

Figure 5.13. CVs of FcCAR (1 mmol L^{-1}) in KCl (0.1 mol L^{-1}) aqueous solution on SPCE and at room temperature (pH = 7.0 and scan rate:10 mV s^{-1}, 50 mV s^{-1} and 100 mV s^{-1}).

To evaluate the sensing properties of FcCAR in regard to Hg^{2+} and Pb^{2+}, voltammetric measurements were performed. In particular, electrochemical titrations were carried out in KCl (0.1 mol L^{-1}) aqueous solutions containing FcCAR by adding Hg^{2+} or Pb^{2+}, previously prepared in MOPS buffer (pH = 7.0). The resulting voltammograms from CV and DPV of FcCAR solutions titrated with Hg^{2+} are shown in Figures 5.14 and 5.15. As can be observed, the FcCAR peaks reduce linearly as the metal concentration increases. The CV and DPV studies exhibited a slight shift of the voltammograms toward the cathodic current, indicating that the addition of the Hg^{2+} ion promotes the oxidation of FcCAR with its concomitant reduction to Hg^+. Visually, an orange to yellow color change of the ligand in the presence of the metal ion was realized, along with a low amount of gray precipitate. The latter could be due to the formation of some Hg^+ complex with Cl^-.

The trend is instead different in the voltammograms resulting from CV and DPV of FcCAR solutions titrated with Pb^{2+} (Figures 5.16 and 5.17). In particular, in CV, the FcCAR peaks in the presence of Pb^{2+} do not appear to depend on the metal concentration. In DPV, the anodic and cathodic peak currents of FcCAR *vs*. metal concentration give rise to different electrochemical responses. The cathodic behaviour of FcCAR in Figure 5.17 (b) was considered up to a Pb^{2+} concentration of 1.5 mmol L^{-1}, due to a narrower linearity range was found for the cathodic peaks of FcCAR in the presence of Pb^{2+}. These deviations, starting from C = 1.7 mmol L^{-1}, are highlighted in Figure 5.18 (b), and compared with the dependence of the cathodic peaks of FcCAR on the Hg^{2+} concentration.
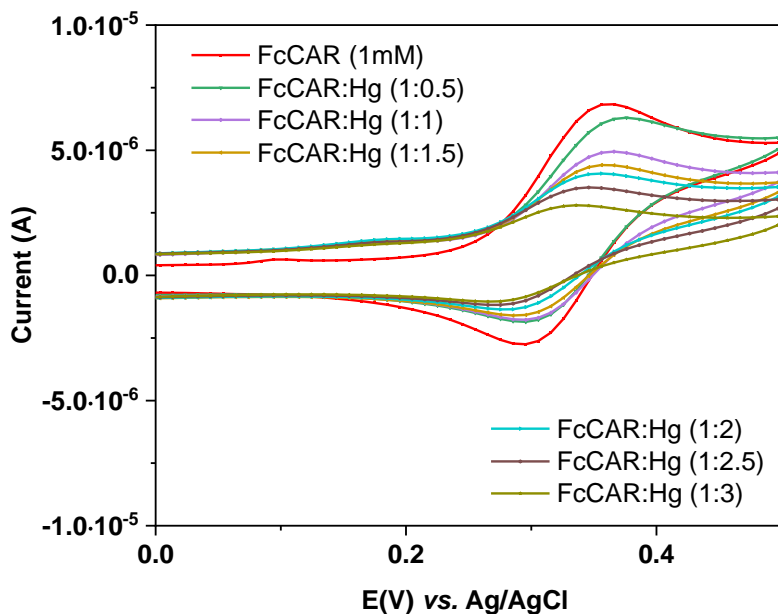
Figure 5.14. CVs of FcCAR (1 mmol L^{-1}) in KCl (0.1 mol L^{-1}) aqueous solution, titrated with Hg^{2+} on SPCE and at room temperature (pH = 7.0 and scan rate: 0.1 V s^{-1}. $0.5 \leq C_M/$ mmol L$^{-1} \leq 3$).
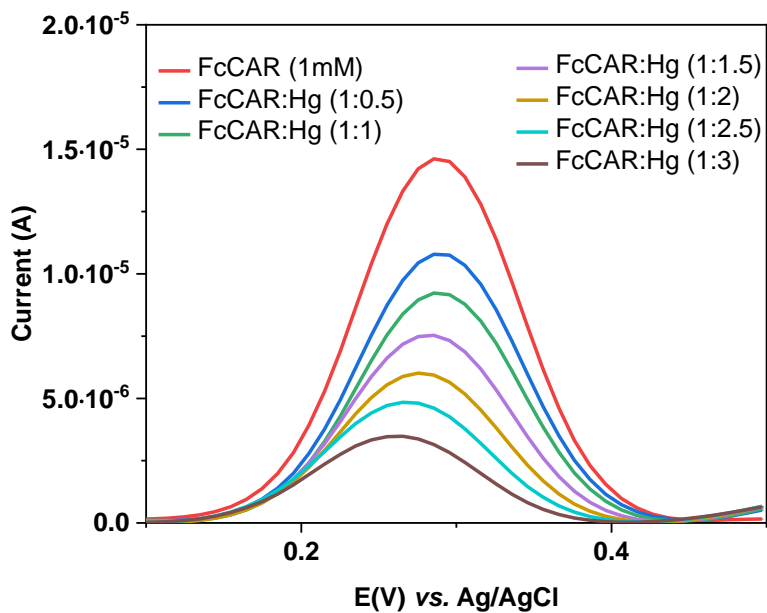
(a)
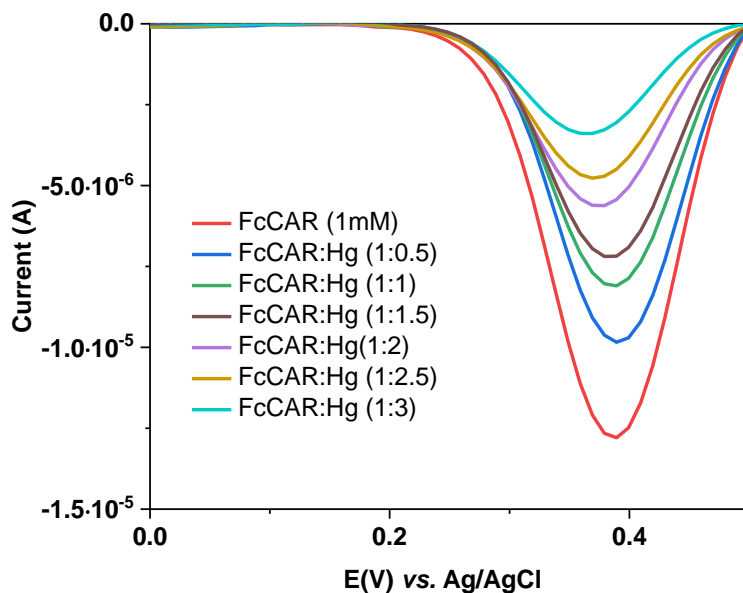
(b)

Figure 5.15. (a) Anodic and **(b)** cathodic peaks of FcCAR (1 mmol L^{-1}) in the presence of Hg^{2+} in KCl (0.1 mol L^{-1}) aqueous solution (pH = 7.0, $0.5 \leq C_M$ mmol L$^{-1} \leq 3$) on SPCE and at room temperature.
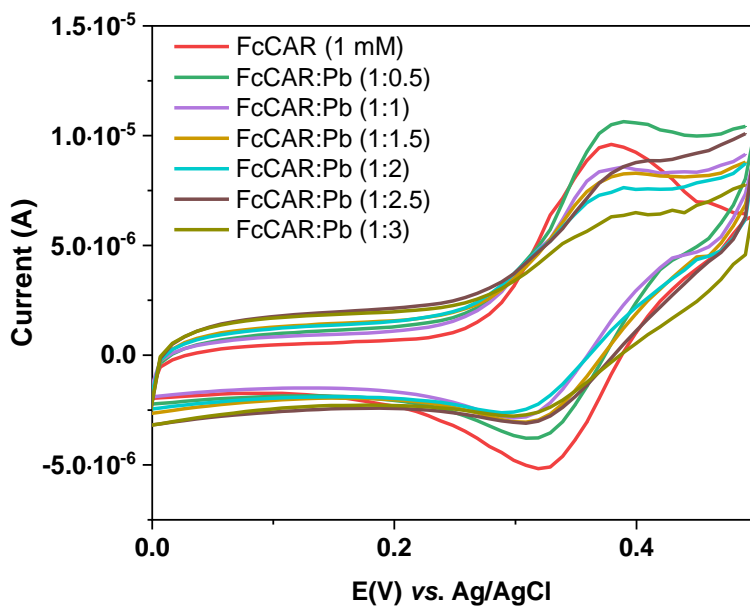
Figure 5.16. CVs of FcCAR (1 mmol L^{-1}) in KCl (0.1 mol L^{-1}) aqueous solution, titrated with Pb^{2+} on SPCE and at room temperature (pH = 7.0 and scan rate: 0.1 V s^{-1}. $0.5 \leq C_M$ mmol L$^{-1} \leq 3$).

175
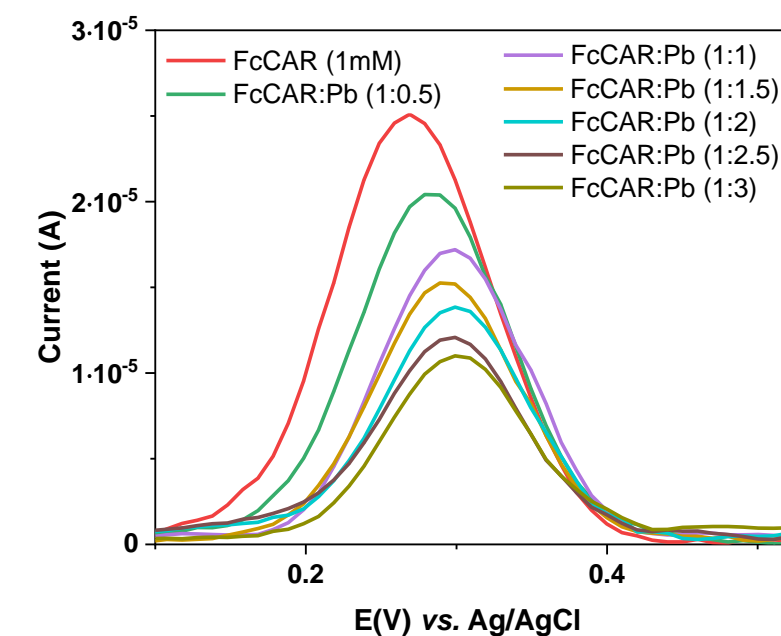
(a)
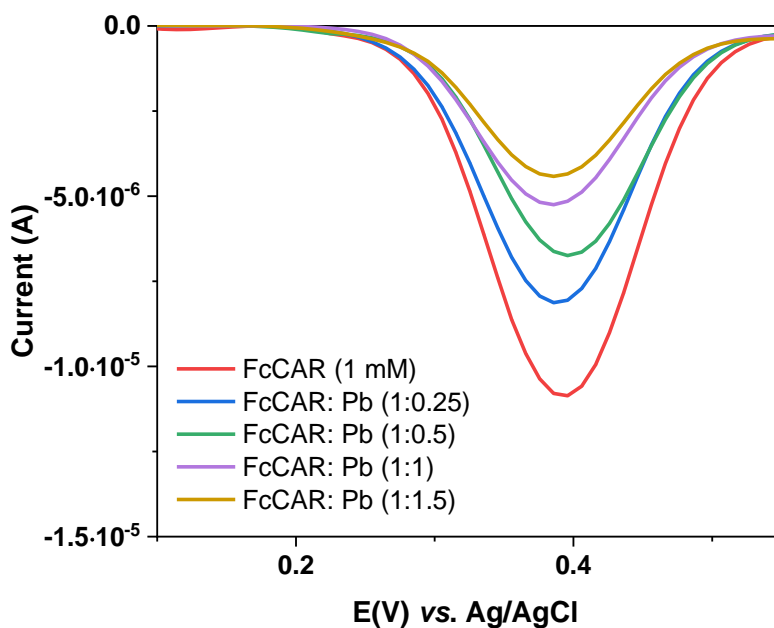
(b)

Figure 5.17. (a) Anodic and **(b)** cathodic peaks of FcCAR (1 mmol L^{-1}) in the presence of Pb^{2+} in KCl (0.1 mol L^{-1}) aqueous solution (pH = 7.0, $0.5 \leq C_M$ mmol L$^{-1} \leq 3$) on SPCE and at room temperature.

(a)   **(b)**
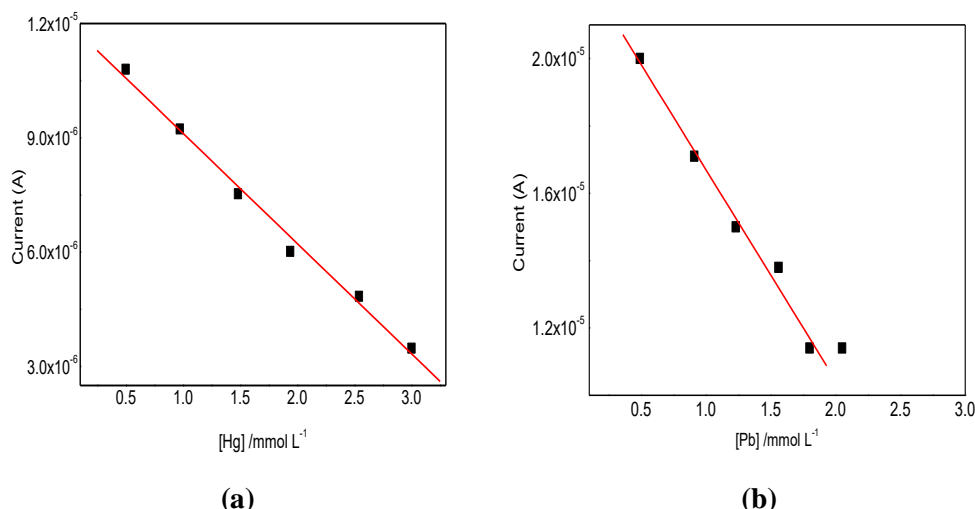
Figure 5.18. Dependence of cathodic peak currents of FcCAR with **(a)** Hg^{2+} and **(b)** Pb^{2+} in KCl (0.1 mol L^{-1}) aqueous solutions (pH = 7.0, $0.5 \leq C_M$ mmol $L^{-1} \leq 3$ and $C_L = 1$ mmol L^{-1}) on SPCE and at room temperature.

Although these electrochemical studies did not allow to understand and identify metal recognition processes, the effect of Hg^{2+} is much more pronounced than the other metal cations discussed. Moreover, its linearity concentration range is wider than that of the FcCAR-Pb^{2+} system.

Both aspects were exploited to improve the electrochemical performance of FcCAR as a mercury sensor. For this purpose, Screen-Printed Carbon Electrodes (SPCEs) were modified with MultiWalled Carbon Nanotubes (MWCNT), previously synthetized by Prof. Piperno et al.

5.6.1 Multiwalled Carbon Nanotubes covalently functionalized with cationic β-cyclodextrins (MWCNT-CD)

Carbon Nanotubes (CNT) are intriguing materials proposed for a wide range of applications, including nanotechnology-related devices, water treatment and sensors [149-151]. CNT are considered as rolled-up sheets of graphene forming

single or multiwalled seam-less cylinders with diameters ranging from a few to hundreds of nanometers, (SW- and MWCNT, respectively). They generally present a length/diameter ratio higher than 10^6 and have exceptional electrical, thermal, mechanical and optical properties [152, 153]. Although their excellent properties give CNT great potential in many practical applications, their non-dispersibility in solvents weakens their competitive strength in the synthesis of composites, semiconductors, and sensors. CNT functionalization is considered a key step to improve their dispersibility and processability, and to assist their combination/incorporation with other classes of compounds to produce high-performance multifunctional materials. Moreover, their combination with other organic or inorganic compounds, such as polymers, drugs, and inorganic nanoparticles, through covalent and/or noncovalent approaches, results in new hybrid nanomaterials endowed with unique properties [154, 155]. The latter are not the simple addition of the starting properties of the native materials, but in many cases new ones appear as originating from the synergistic action of the components.

In the ongoing research program at the SYMAT Laboratories of the University of Messina, aimed at developing high-performance multifunctional materials, new carbon-based nanomaterials were developed by covalently functionalizing graphene or carbon nanotubes with β-cyclodextrins (CD) [156].

The functionalization of carbon nanomaterials with CD units improved the biocompatibility, process ability and colloidal stability. Moreover, CD grafted on nanomaterials furnished new molecular recognition sites (*i.e.,* lipophilic CD cavities and hydrophilic CD rims). In line with this research topic, the synthesis and characterization of MWCNT functionalized with cationic β-cyclodextrins (MWCNT-CD, Scheme 3) are herein described. Moreover, exploiting the high affinity of CD cavities [157] for a ferrocennyl unit ($K \approx 10^3$ mol L^{-1}), MWCNT-CD were used to modify Screen-Printed Carbon Electrodes (SPCEs).

Commercially available carboxylated MWCNT were functionalized with alkyne terminated moieties by Tour reaction. CD units were grafted on MWCNT sidewalls by click chemistry reaction between CNT-Alk and *per*-azido β-cyclodextrins. The residual azido groups were reduced to amine groups and recovered as hydrochloric salt (MWCNT-CD, Scheme 3).
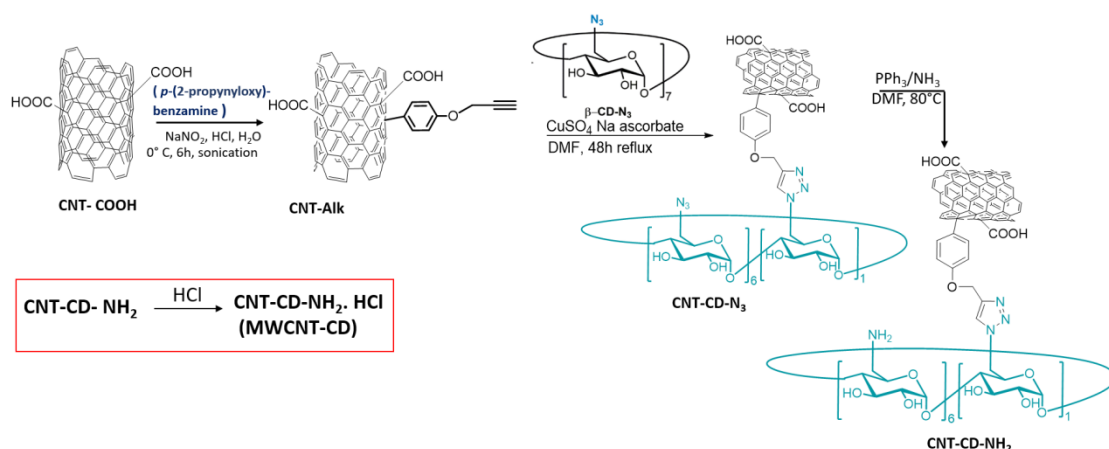
Scheme 3. Schematic representation of the synthesis of MWCNT-CD.

The degree of functionalization (Δm%) of the CD-modified MWCNT was estimated by thermogravimetric analysis (TGA) under argon atmosphere (Figure 5.19). Comparing the weight residue (%) at 400 ∘C, between CNT-ALK and CNT-CD-NH$_2$, a CD content of 6.5 % w/w was found, which roughly corresponds to 0.0522 mmol g^{-1}. This result is in agreement with the amount of free amino groups estimated by the ninhydrin assay (0.0607 mmol/g) (Figure 5.20). The ninhydrin assay was carried out using the commercial Kaiser test kit consisting of three solutions as follows: (a) phenol (0.5 g mL^{-1}) in absolute EtOH; (b) 2 mL of potassium cyanide (1 mmol L^{-1}, aqueous solution) dissolved in 98 mL of pyridine; (c) ninhydrin (0.05 g mL^{-1}) in absolute EtOH. Briefly, 0.5 mg of CNT-N$_3$ or CNT-NH$_2$ were treated in sequence with 75 μL of solution (a), 100 μL of solution (b)

179

and 75 µL of solution (c). The dispersion was sonicated in a water bath and then heated at 120 °C for 5 min, diluted with 4750 µL of absolute EtOH and centrifuged at 14.000 rpm. The absorbance at 570 nm of supernatant was correlated to the amount of free amine groups on the CNT surface (NH_2 loading (mmol g^{-1})) using the following equation:

$$[free\ amines] = \frac{([A]\ dilution\ 1000)}{(\varepsilon b\ sample\ weight)} \tag{5.1}$$

where dilution was fixed at 5 mL; ε was 15.000 mol L^{-1} cm^{-1}; b, the optical path, was 1 cm and the sample weight was 0.5 mg [158].
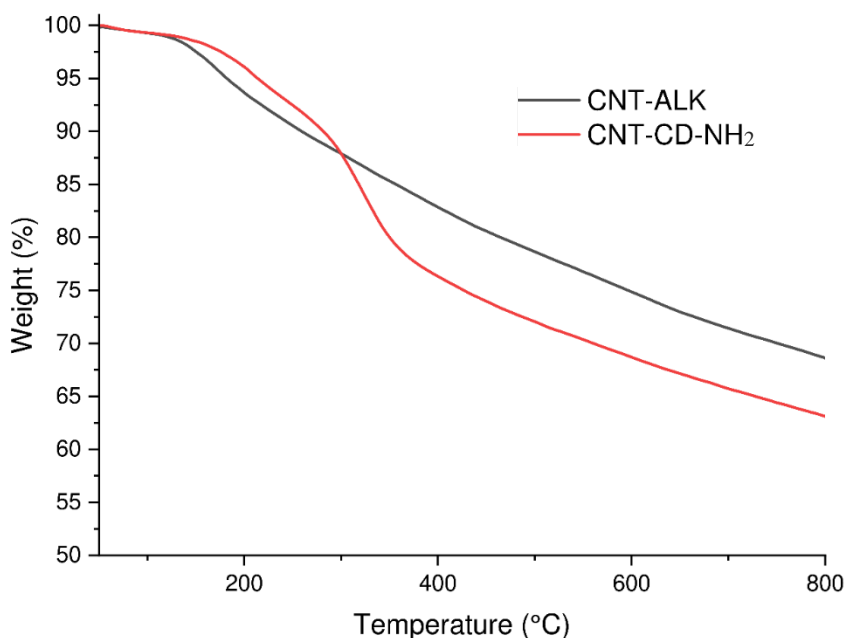
Figure 5.19. TGA under argon atmosphere of CNT-ALK and CNT-CD-NH_2.
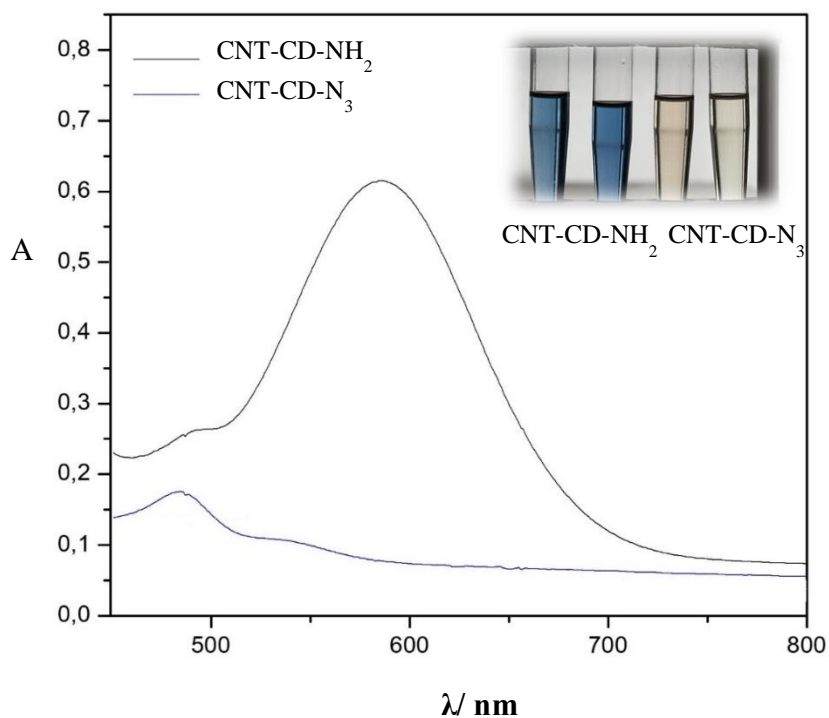
Figure 5.20. UV-Vis absorption spectra of CNT-CD-NH$_2$ and CNT-CD-N$_3$ sample after the ninhydrin test.

The morphology of MWCNT functionalized with CD by STEM technique is currently under investigation. The starting material, CNT-COOH, showed a clear multi-walled tubular structure with a diameter close to 10 nm, corresponding to a number of 8-10 layers.
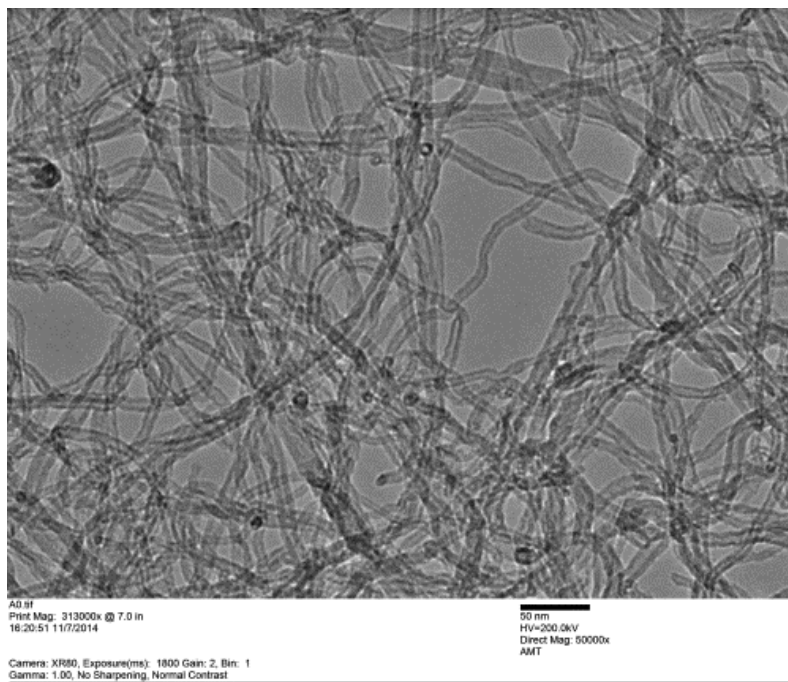
Figure 5.21. TEM image of CNT-COOH reproduced with permission of ref.[158].

As accomplished with CNO (Chapter 3, Paragraph 2.6.3), the incorporation of MWCNT-CD on the electrode surface is based on a simple and fast procedure, consisting in the preparation of a homogeneous dispersion and subsequent noncovalent functionalization on SPCEs. In this case, multiple dispersions were prepared and cast on SPCEs, in order to investigate the electrochemical signal. The first homogeneous dispersion of MWCNT-CD in DMF (1 mg mL^{-1}) was not sufficient to obtain promising electrochemical performance. Therefore, an additional homogenous dispersion of MWCNT-CD in DMF (3 mg mL^{-1}) was prepared and used for the analytical purposes of this work.

The polished SPCEs were sonicated in Milli-Q® water for 5 min and dried under a stream of nitrogen. The SPCEs were modified by drop-casting a homogeneous dispersion of MWCNT-CD in DMF (3 mg mL^{-1}) prepared using an ultrasonic-bath for 30 min. To obtain a thin layer of MWCNT-CD, 1 µL of the dispersion was cast

four times on the surface of the electrodes and dried in an oven at 80 °C under DMF atmosphere for 30 min. This procedure was used to avoid the formation of the so-called coffee-ring effect, which results in non-homogeneous films [49]. After each casting, the electrochemical responses of $K_3[Fe(CN)_6]$ (1 mmol L^{-1}) in KCl (0.1 mol L^{-1}) on MWCNT-CD modified electrodes were analyzed at different degrees and depicted in Figure 5.22. As increasing the MWCNT-CD layering on SPCEs, a signal amplification is observed, due to the deposition of the conductive MWCNT-CD material inducing a capacitive behavior on the electrode surface. The MWCNT-CD dispersion was cast up to 4 μL, after which no further changes in the CV were observed, indicating a complete coverage of the surface. The slight increase in the ΔE_p from bare (115 mV) to the modified (130 mV) could be due to repulsive interactions between the anionic $[Fe(CN)_6]^{3-}$ and carboxylate groups on the surface of the MWCNT-CD/SPCE, resulting in a hindered electron transfer. Therefore, the electrochemical responses of $K_3[Fe(CN)_6]$ (1 mmol L^{-1}) in KCl (0.1 mol L^{-1}) aqueous solution on bare and MWCNT-CD modified electrodes were studied, and the CVs are compared in Figure 5.23. The $[Fe(CN)_6]^{3-}$ redox probe was chosen to assess the effect of the oxidation degree of MWCNT-CD on their electrochemical properties. The voltammetric behavior presented above reveal that the electroactivity of $[Fe(CN)_6]^{3-/4-}$ is enhanced on the MWCNT-CD modified electrodes, as well as the electrochemical responses.
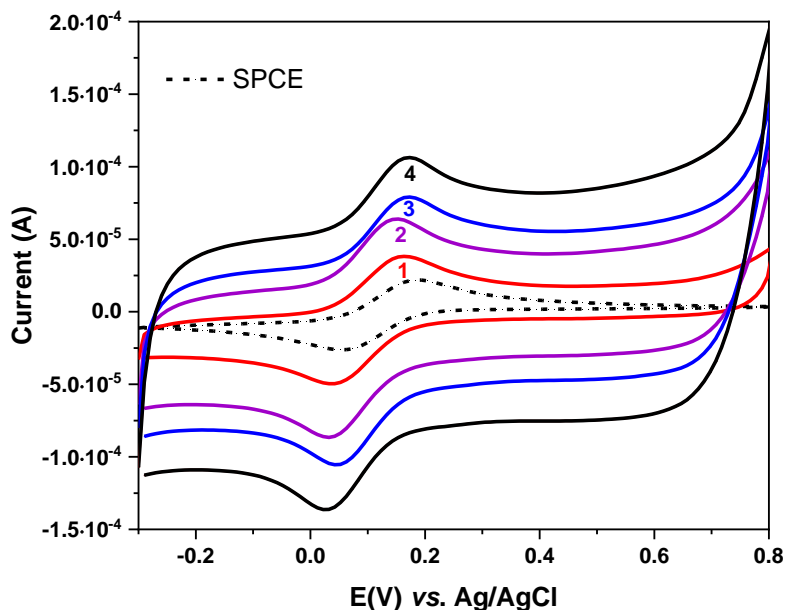
Figure 5.22. CVs of $[Fe(CN)_6]^{3-/4-}$ (1 mmol L^{-1}) in KCl (0.1 mol L^{-1}) aqueous solution obtained on bare SPCE and MWCNT-CD/SPCE, after each dispersion casting. Scan rate: 0.1 V s^{-1}.
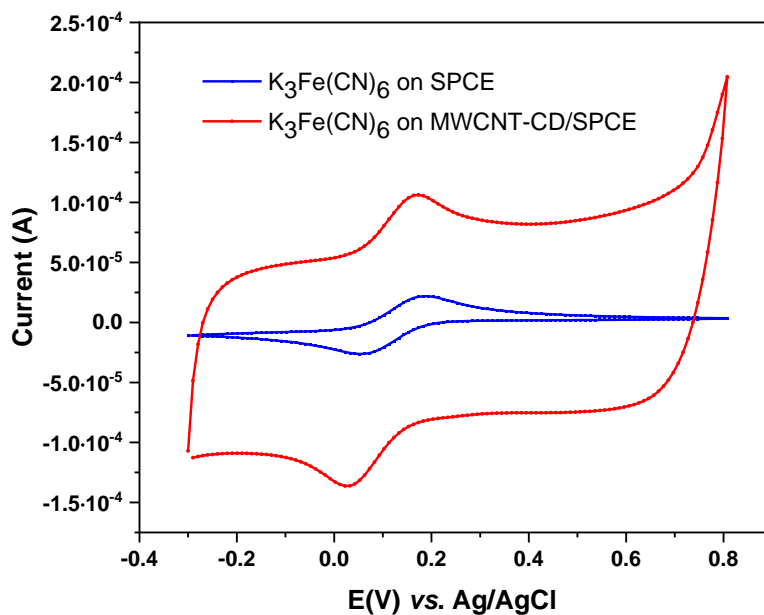
Figure 5.23. CVs of $[Fe(CN)_6]^{3-/4-}$ (1 mmol L^{-1}) in KCl (0.1 mol L^{-1}) aqueous solution obtained on bare SPCE (blue line) and MWCNT-CD/SPCE (red line) (pH = 7.0 and at room temperature). Scan rate: 0.1 V s^{-1}.

184

5.6.2 Electrochemical behavior of FcCAR toward Hg^{2+} on modified Screen-Printed Carbon Electrodes (SPCEs) with MultiWalled Carbon Nanotubes covalently functionalized with cationic β-cyclodextrins (MWCNT-CD)

The electrochemical behavior of FcCAR was analyzed on bare SPCE and MWCNT-CD/SPCE. Figure 5.24 shows Cyclic Voltammograms (CVs) for the electrochemical activity of FcCAR (1 mmol L^{-1}) in KCl (0.1 mol L^{-1}) aqueous solution on bare and MWCNT-CD modified SPCEs. In both cases, FcCAR undergoes one-electron reversible redox process. However, on the modified electrodes, CVs exhibit a pseudo-rectangular shape, which is characteristic of the electric layer capacitive behavior of MWCNT-CD, and the capacitive current increases with the oxidation degree of MWCNT-CD, due to the presence of functional groups on their surface.

In addition to the capacitive current, anodic and cathodic peaks of FcCAR at 0.373 V and 0.312 V (*vs*. Ag/AgCl), respectively, are observed in the CVs of the bare and MWCNT-CD modified electrodes (Figure 5.24). These values did not shift due to the modification strategies.

The peak currents vary linearly with the scan rate, indicating that the redox process is due to redox species confined on the surface of MWCNT-CD (Figure 5.25). The anodic and cathodic peak currents obtained on MWCNT-CD/SPCE were higher than those on bare SPCE, indicating better electrochemical activity toward this molecule. The best resolved response for FcCAR was obtained on the MWCNT-CD/SPCE compared to the SPCE.

DPV studies for FcCAR require further experimental investigation, due to a change in shape that occurs on MWCNT-CD/SPCE. This is more pronounced in the anodic peak, as can be observed in Figure 5.26 (a). Therefore, the intriguing nature of the Fc/Fc^+ moiety of the FcCAR probe could give rise to interactions on the MWCNT-CD/SPCE, which are currently unexplored.
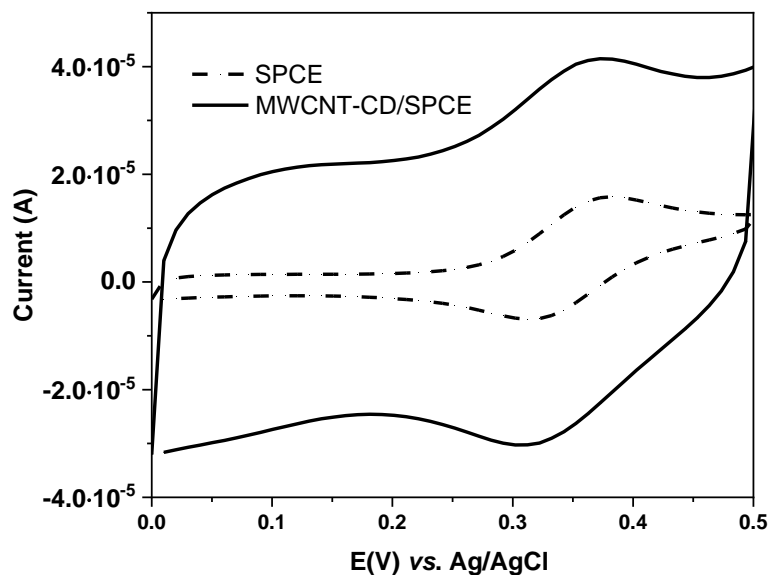
Figure 5.24. CVs of FcCAR (1 mmol L^{-1}) in KCl (0.1 mol L^{-1}) aqueous solution obtained on bare SPCE (dashed line) and MWCNT-CD/SPCE (pH = 7.0 and at room temperature). Scan rate: 0.1 V s^{-1}.
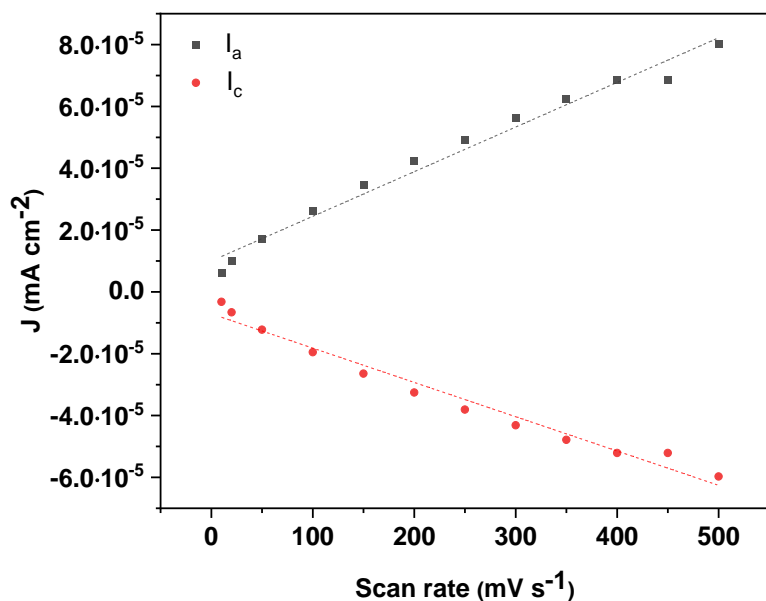
Figure 5.25. Dependence of anodic and cathodic peak currents of FcCAR with scan rate observed on MWCNT-CD/SPCE in KCl (0.1 mol L^{-1}) aqueous solution.
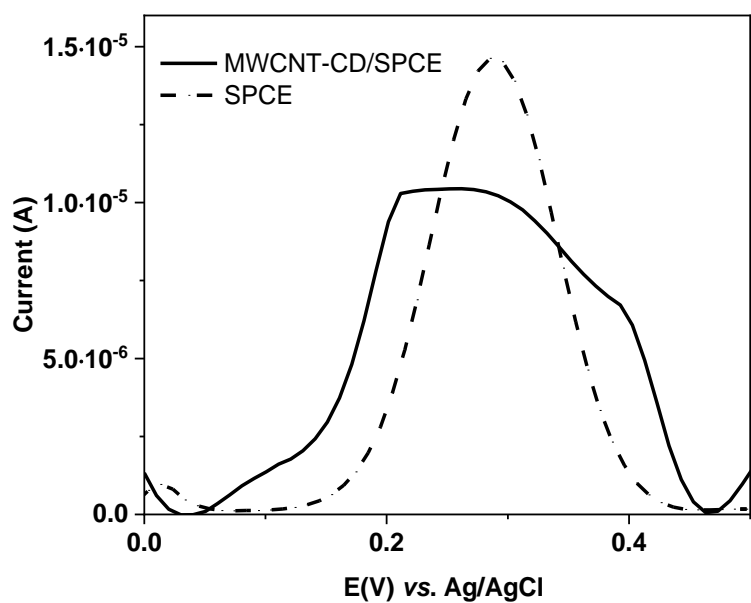
(a)
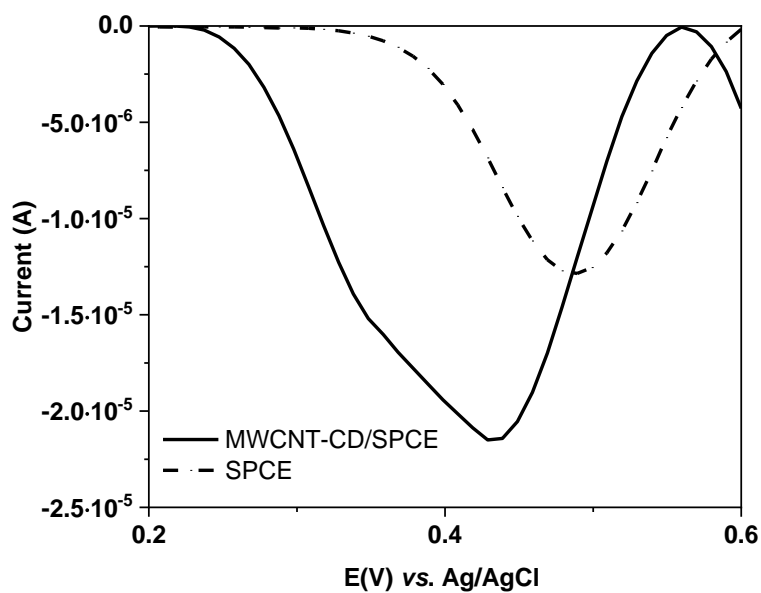
(b)

Figure 5.26. (a) Anodic and **(b)** cathodic peak currents of FcCAR (1 mmol L^{-1}) in KCl (0.1 mol L^{-1}) aqueous solution on bare SPCE (dashed line) and MWCNT-CD/SPCE (solid line) (pH = 7.0 and at room temperature). Scan rate: 0.1 V s^{-1}.

Electrochemical measurements were performed as titrations in KCl (0.1 mol L^{-1}) aqueous solution containing FcCAR by addition of Hg^{2+} solution, previously prepared in MOPS buffer (pH = 7.0). The resulting voltammograms from CV and DPV on MWCNT-CD/SPCE are depicted in Figures 5.27 and 5.28. In the latter, the peak currents of free FcCAR are neglected.

No deposition phenomena were observed. The FcCAR peak currents decrease linearly as the Hg^{2+} concentration increases, qualitatively amplifying the electrochemical signals and also indicating a good affinity of the molecule for mercury. This aspect is better clarified in Figure 5.29, which shows the dependence of the anodic peak of FcCAR *vs*. Hg^{2+} concentration on SPCE and MWCNT-CD/SPCE, highlighting a good response and amplification of the signal on the modified electrode surface.
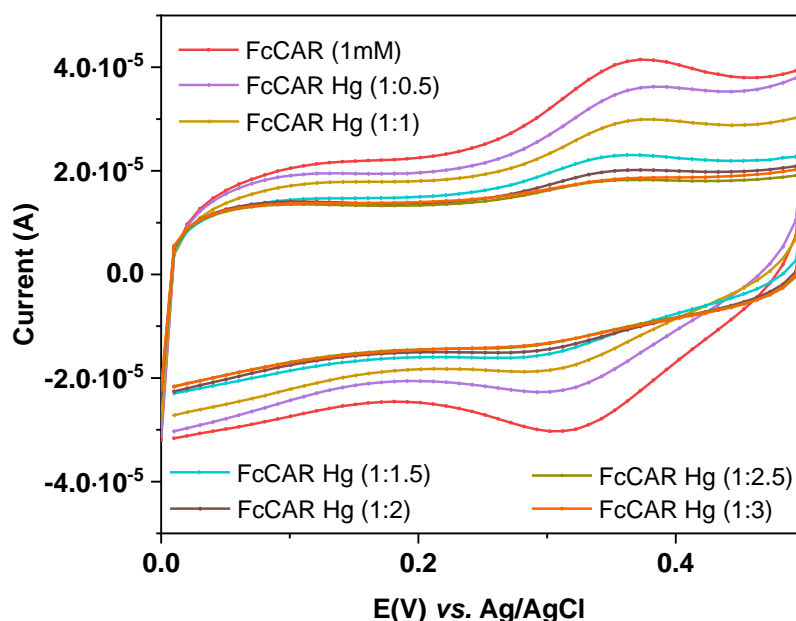
Figure 5.27. CVs of FcCAR (1 mmol L^{-1}) in KCl (0.1 mol L^{-1}) aqueous solution, titrated with Hg^{2+} on MWCNT-CD/SPCE and at room temperature (pH = 7.0 and scan rate: 0.1 V s^{-1}. $0.5 \leq C_M$ mmol $L^{-1} \leq 3$).
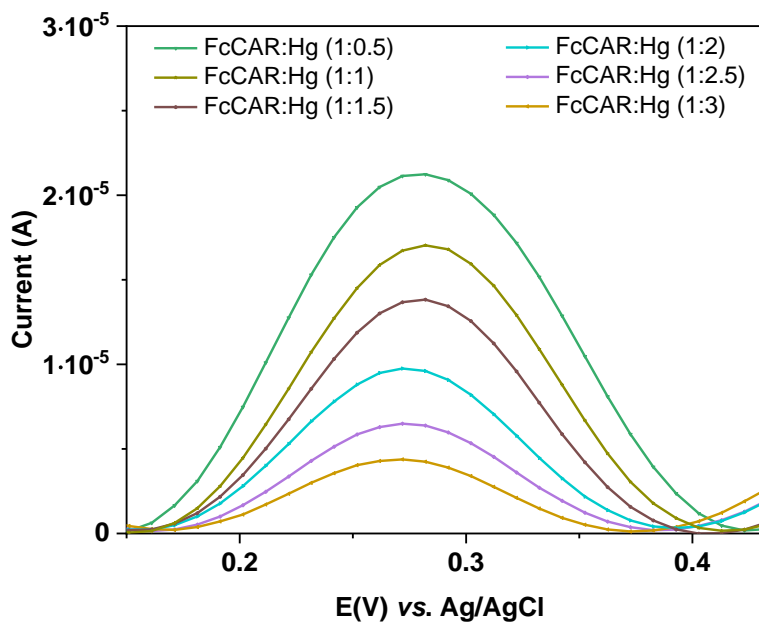
(a)
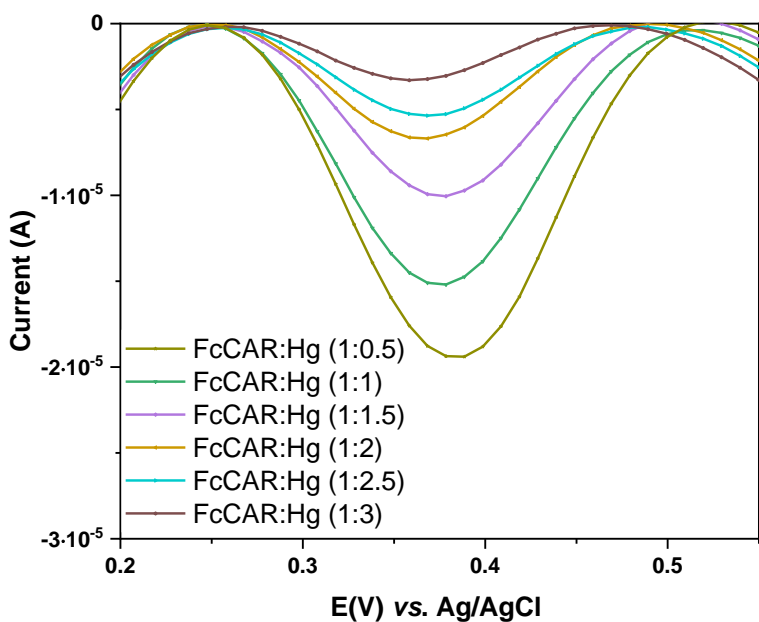
(b)

Figure 5.28. (a) Anodic and **(b)** cathodic peak of FcCAR (1 mmol L^{-1}) in the presence of Hg^{2+} in KCl (0.1 mol L^{-1}) aqueous solution on MWCNT-CD/SPCE and at room temperature (pH = 7.0, $0.5 \leq C_M$ mmol $L^{-1} \leq 3$).
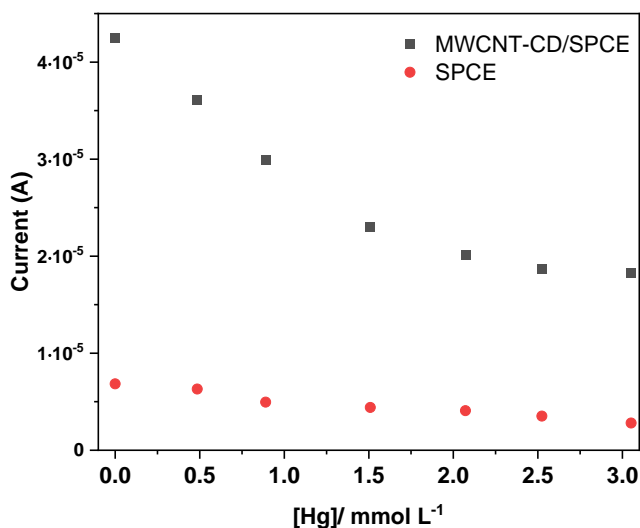
Figure 5.29. Dependence of anodic peak of FcCAR (1 mmol L^{-1}) *vs*. Hg^{2+}/ mmol L^{-1} in KCl (0.1 mol L^{-1}) aqueous solution on SPCE and MWCNT-CD/SPCE, and at room temperature (pH = 7.0, $0.5 \leq C_M$ mmol $L^{-1} \leq 3$).

5.7 Final remarks and future perspectives

The synthesis of the two CAR derivatives allowed them to be studied and evaluated as potential sensors. However, while a voltammetric approach has been efficiently feasible on FcCAR, it has not been so on PyCAR, as the latter gives rise to dimeric species in aqueous solution, which can easily drop off on the SPCE surface. Rather, the pyrene-based compounds show high quantum emission yields, which can be easily monitored by the functional groups modification [146]. Therefore,

- the PyCAR should be investigated by fluorimetric techniques. This study, though, disregards this thesis, where only the UV-Vis spectrophotometric analysis on PyCAR is debated.
- On the other hand, UV-Vis spectrophotometric measurements were also performed, as titrations, on the FcCAR.

190

- The resulting UV-Vis spectra highlighted the Absorbance *vs*. Concentration and ε of the two CAR derivatives, that are PyCAR and FcCAR, and their complex species investigated.

- Moreover, the latter was qualitatively studied by voltammetric techniques in order to assess its sensing properties. Other aspects, including quantitative determination and electrochemical characterization, need further study.

5.8 MATERIALS AND METHODS

Synthesis of ferrocenyl-carnosine (FcCAR)

A solution of ferrocenecarboxylic acid (**1**) (655.0 mg; 2.85 mmol) and NHS (360.0 mg; 3.13 mmol) in 30 mL of anhydrous THF was added to a stirring solution of DCC (603.8 mg; 2.93 mmol) in 10 mL of THF. The mixture was stirred at room temperature (r.t.) for 24 h, the brown solid was removed by filtration and the organic solvent was evaporated, to give (**2**). The chemical structure and the purity of (**2**) were confirmed by ^{1}H NMR analysis and compared with the literature data [159]. The ferrocenyl intermediate (**2**) (821.0 mg; 2.50 mmol) was dissolved in DMF (25 mL) and slowly added, under stirring, in an ice bath, to a CAR (678.9 mg; 3.0 mmol) and NaHCO$_3$ (210.3 mg; 2.50 mmol) H$_2$O/DMF (1:1) solution. The reaction mixture was stirred at room temperature for 20 h. The solvent was evaporated under vacuum, and the brown solid was purified by crystallization from water/acetone to obtain (**3**) in an overall yield of 64%.

Chapter 6

L-Carnosine (CAR) in removal procedure

6.1 General aspects

In this work, the bivalent metal ion complexing and sequestering abilities of CAR in aqueous solutions were extensively explored and exploited. The outstanding complexing ability of CAR toward potentially toxic metal cations was firstly investigated for analytical applications.

Heavy metals are inorganic pollutants with long-range persistence and -transport, and marked toxic properties [160]. They and their by-products are also resistant to chemical, photolytic and biological biodegradation and tend to bio-accumulate and bio-magnify in aquatic ecosystems [160]. Among heavy metals, lead is one of the most toxic even at low concentrations [135, 161], and because of its massive impact in the environment, many attempts have been made to study Pb^{2+} sensors [45].

Lead and its byproducts are released into the soil, air, and aquatic environments from manufacturing, anthropogenic and industrial activities, reaching ground- and surface waters. Lead-toxicity is particularly harmful to aquatic and human life because the metal is difficult to metabolize and tends to non-biodegrade and bio-accumulate [134-136, 160]. Therefore, its actions target most organs (in particular, liver, heart and kidney [34, 126, 138]), and the endocrine, reproductive and hematological systems [126, 135, 136]. Lead-toxicity can also have dangerous effects on brain development, giving rise to a slower nerve conduction velocity and behavioral problems in childhood [135]. As a consequence, lead has been classified

192

as a feasible human carcinogen by the International Agency for Research on Cancer (IARC) and US Environmental Protection Agency (USEPA), that settled its action level at 15 μg/L in drinking water [135]. Health Canada also determined that the maximum acceptable concentration (MAC) of lead in drinking water is 5 μg/L, based on the principle of "as low as reasonably achievable" (ALARA) [135]. The European Community Directive and the World Health Organization (WHO) set that the MAC of lead in tap water is 10 μg/L [135]. Literature data reported various methods for the Pb^{2+} removal from aquatic systems, such as chemical precipitation, coagulation-flocculation, ion-exchange, sedimentation, membrane separation, adsorption, reverse osmosis, electrodialysis, solid phase microextraction (SPME), chelating ligands [135, 162-166]. Among all of them, adsorption is one of the most common methods to remove contaminants from wastewater due to its application feasibility and higher effectiveness [135]. This physical, chemical and biological process is based on boundaries between two different phases and, in particular, occurs when molecules of the analyte in an aqueous solution are distributed on the surface or porous space of a solid material [167]. In this way, they are the adsorbate and adsorbent, respectively. The adsorption phenomena depend on several factors, such as the structure, quantity, nature, physico-chemical properties of an adsorbent, as well as the pH, concentration and temperature of the solution. Each parameter and its effects on adsorption phenomena must be investigated. In particular, pH plays a key role in these processes because it can influence the solubility, ionization and chemistry of the adsorbate, which represents the extracted contaminants under study. In general, ideal adsorbent materials should have a regular and large specific surface area, high porosity to increase adsorption capacities, high selectivity, fast kinetics, good mechanical, thermal and chemical stabilities, non-swelling properties and non-toxicity. They should also preferably be low-cost, available and abundant in nature adsorbents, with easy to use and process

[135, 162, 165]. A great variety of natural and synthetic adsorption materials were investigated and used in water treatment for metal ion removal [135, 167].

In this thesis, a commercial hydrophilic Thermo Scientific UltraLink Biosupport was employed. In more detail, it is an enduring, preactivated porous resin, consisting of a beaded-polyacrylamide/azlactone copolymer, that is charge-free, slightly hydrophobic in its active form, and highly cross-linked [168]. "Azlactones" is the classical term for oxazolones or oxazol-5-(4H)-ones, which consist of five-membered heterocycles with one nitrogen and two oxygen atoms [169]. They play a key role in the synthesis of tiny chemical molecules, such as amino alcohols, amino acids, thiamine, amides, peptides and polyfunctional compounds. The resulting derivatives have various biological and pharmacological activities and can also be used as immunomodulatory, biosensors, heterocyclic precursor or as devices for proteins [169]. The reactivity of oxazolones depends on the substituents present at the C-2 and C-4 sites. For instance, the rate of the ring-opening reaction of oxazolones decreases as the electron-donor nature of the phenyl ring substituent at the C-2 position increases [169]. The chemistry of oxazolones is intriguing because of their propensity to undergo a ring-opening reaction, whose active sites in a saturated one are depicted in Figure 6.1.
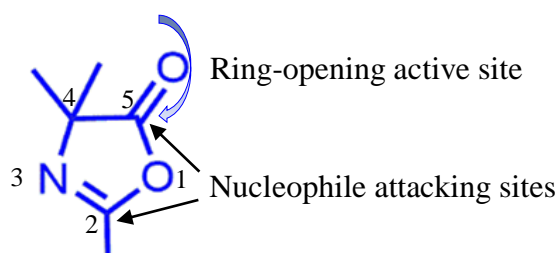
Figure 6.1. Active sites of a saturated oxazolone.

The saturated polyacrylamide/azlactone copolymer (AZ), (**2**) in Scheme 4, was chosen as an ideal support to covalently linked the CAR molecule, since this specific resin is able to covalently bond primary amine biomolecules [168],

proteins and amine-containing ligands through a ring-opening reaction [170, 171], as above-mentioned. In particular, this coupling reaction results in stable amide bonds without toxic chemical by-products. Scheme 4 shows the synthetic scheme between CAR (**1**) and AZ (**2**) to produce the CAR-based resin named AZCAR (**3**). The adsorption capacity of AZCAR was investigated under conditions simulating the ionic strength and pH of different natural waters. However, this study was performed on the basis of the previous thermodynamic investigation reported in Chapter 4. In fact, considering that the adsorption processes depend on the pH, concentration, composition, ionic strength and temperature of the solution containing the adsorbent under study, defining the speciation of the Pb^{2+}-CAR system was very useful in predicting the behavior of lead. Furthermore, the potentiometric study, performed in different ionic strength and temperature ranges, was useful to define and evaluate the best conditions under which the molecule shows the greatest complexing capacities. In regard to the speciation model, the possibility of using CAR in removal techniques for Pb^{2+} was assessed by determining the $pL_{0.5}$. A sequestration diagram is reported in Figure 6.2 under certain ionic strength and pH conditions simulating natural fluids. This profile clearly describes the highest sequestering ability of the CAR toward Pb^{2+} in ionic strength and pH conditions of sea waters (curve **1**), blood (curve **2**), and freshwater (curve **3**). In the last case, CAR shows the lowest sequestering ability toward Pb^{2+}. The $pL_{0.5}$ value was also calculated keeping the ionic strength and pH constant one at a time in order to evaluate whether the effect was due to one or both of the experimental parameters. The results show that the pH has a greater influence on the sequestering ability, while the ionic strength variation provides a lesser effect. In fact, a slight decrease in the sequestering capacity occurs as the ionic strength increases. These impressive results turned out to be extremely useful for planning and reducing the number of experimental measurements for batch tests and for optimizing removal procedures.
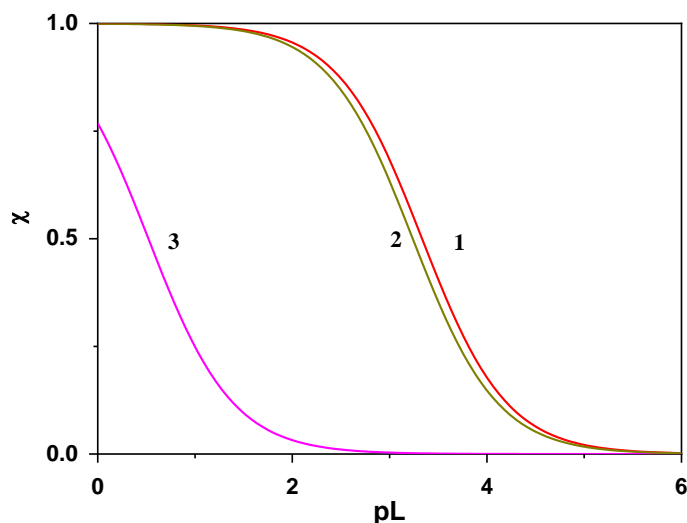
Figure 6.2. Sequestration diagram of CAR (L) toward Pb^{2+}.
 Experimental conditions:
    1) pH = 8.1, I = 0.7 mol L^{-1} and T = 298.15 K,
    2) pH = 7.4, I = 0.15 mol L^{-1} and T = 310.15 K,
    3) pH = 5, I = 0.001 mol L^{-1} and T = 298.15 K.
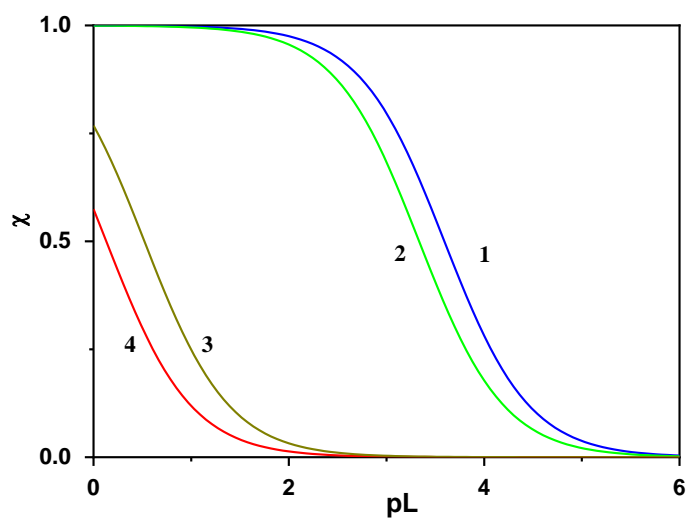
Figure 6.3. Sequestration diagram of CAR (L) toward Pb^{2+}.
 Experimental conditions:
    1) pH = 8.1, I = 0.001 mol L^{-1} and T = 298.15 K,
    2) pH = 8.1, I = 0.7 mol L^{-1} and T = 298.15 K,
    3) pH = 5, I = 0.001 mol L^{-1} and T = 298.15 K,
    4) pH = 5, I = 0.7 mol L^{-1} and T = 298.15 K.

196

6.2 Spectrophotometric apparatus and CAR determination

Spectrophotometric determination of CAR was performed in aqueous solutions using a Varian Cary 50 UV-Vis spectrophotometer, described in Chapter 2. Spectrophotometric determination of the CAR molecule at its maximum absorption ($\lambda = 209$ nm) was carried out. To obtain a broad linear range, Absorbance *vs*. Concentration, spectrophotometric measurements on standard CAR solutions were performed under different pH conditions (pH = 2.5 for HCl, pH = 7.0 for Phosphate Buffer (PB), pH = 10.0 for NaOH). The best results were acquired in acidic environment with a linear range between 2 and 50 µmol L^{-1} CAR concentration.

6.3 Voltammetric apparatus and Pb^{2+} detection

Electrochemical measurements were performed in KCl (0.1 mol L^{-1}) aqueous solutions and at room temperature. The PC-controlled electrochemical workstation, described in Chapter 2, with the three-electrode cell configuration (Metrohm DropSens Screen-Printed electrodes (SPEs), DRP-DSC4MM 72098), connected to the Autolab potentiostat-galvanostat type III (Eco Chieme) with an IME663 interface, was used. The Screen-Printed Carbon Electrodes (SPCEs) employed are also described in Chapter 2. They were polished with distilled water (conductivity < 0.1 µS cm^{-1}), plunged in H$_2$SO$_4$ solution (0.1 mol L^{-1}) and under a stream of nitrogen, before each measurement. The Differential Pulse Voltammetry (DPV) technique was used with the following conditions: Pb^{2+} electrodeposition potential: -0.6V, electrodeposition time: 45 s, scan rate: $-0.6 \leq$ E/V *vs*. Ag/AgCl ≤ -0.2 V, potential step: 20 mV, amplitude: 25 mV.

6.4 CAR-Thermo Scientific™ UltraLink™ Biosupport coupling reaction

A solution of CAR (**1**) (0.002 g, 86.25 μmol) and Thermo Scientific™ UltraLink™ Biosupport (**2**, AZ) (0.250 g, 57.5 μmol) was kept in touch in PB (pH = 7.0), under constant and mild agitation. After 4h, the solution was centrifuged (1500 rpm for 20 min), in order to separate the solid aggregates from the supernatant, and separated. The obtained white compound (**3**), AZCAR, was washed with PB and dried at room temperature. To determine the amount of grafted CAR (μmol), the supernatant was diluted and unbounded CAR determined by UV-Vis analysis.

The conjugation of CAR (**1**) on the AZ (**2**) exploited the high reactivity of the azlactones grafted on the polymer backbone toward nucleophiles (*i.e.*, primary amines) by a ring-opening addition reaction [172] (Figure 6.4). The coupling reaction, leading to AZCAR (**3**), was carried out under different experimental conditions, such as AZ:CAR ratio (from 1:1 to 1:1.5), reaction time (from 2 to 6 hours), and with or without the addition of an eluotropic salt (*i.e.*, sodium citrate). The best coupling efficiency (78.3%) was obtained using the 1:1.5 AZ:CAR ratio for 4 h in the absence of eluotropic salt. The amount of grafted CAR was calculated by difference between the initial CAR concentration and the residual one in the supernatant after the coupling reaction. As above-mentioned, the efficiency coupling percentage was 78.3% and the actual loading was 0.6 wt %.

Compounds (**1**)-(**3**) were characterized by using the PerkinElmer simultaneous Thermal Analyzer STA6000, from 30 to 500 °C, scan rate 20°/min, N_2 as purge gas (flow rate 40 ml/min).
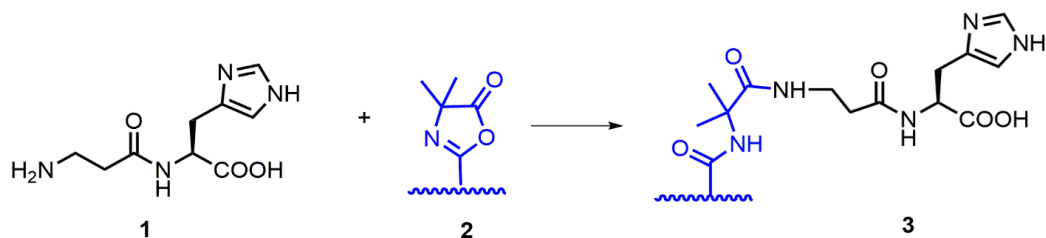
Scheme 4. Schematic representation of the coupling reaction between CAR (**1**) and AZ (**2**).

Clear evidence of CAR grafted on AZ was proven by thermogravimetric analysis (TGA) under inert atmosphere with linear heating, differential scanning calorimetry (DSC) and differential thermal analysis (DTA) (Figure 6.4).
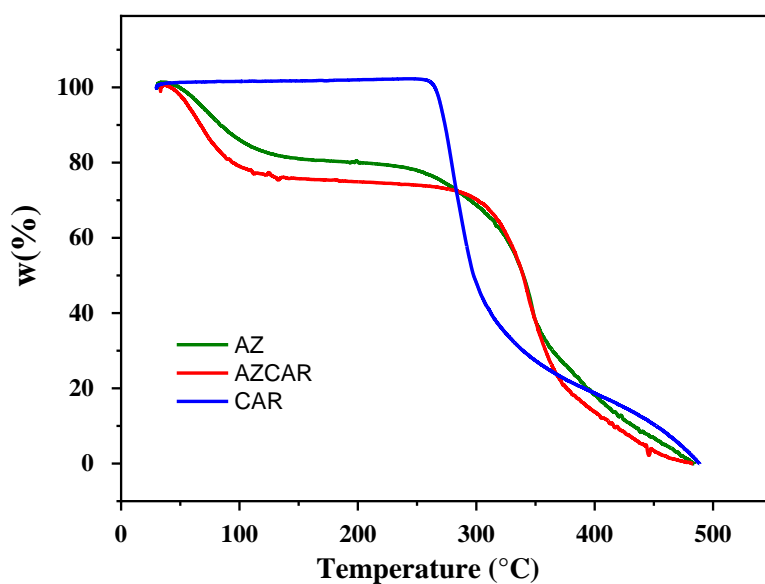
(a)
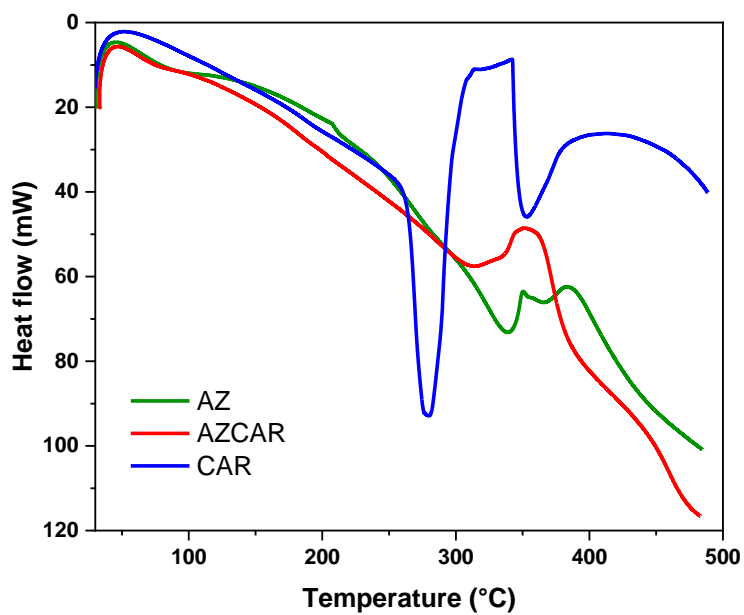
(b)
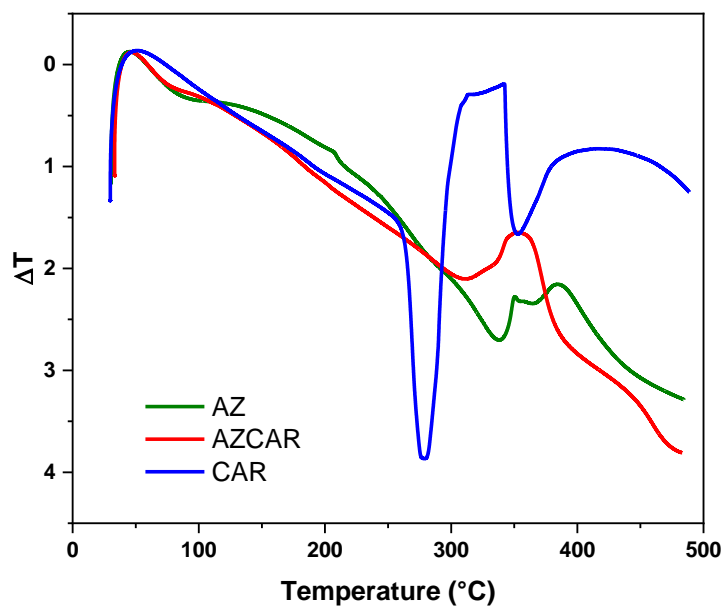
(c)

Figure 6.4. (**a**) TGA, (**b**) DSC and (**c**) DTA profiles of CAR, AZ and AZCAR compounds.

According to the literature [173], the initial thermal decomposition of CAR was detected at about 268 °C, then a continuous weight loss (~ 53%) was observed up to 300 °C (Figure 6.4 (a)). AZ and AZCAR exhibited a similar TGA profile with a first thermal step (~ 20 wt %) from 30 to 100 °C and a second event from 280 to 400 °C, corresponding to an additional 32 wt % and 37 wt %, respectively. The highest weight loss of AZCAR clearly indicated a change in the thermal stability of the polyacrylamide/azlactone copolymer after CAR grafting. In the DSC profiles (Figure 6.4 (b)), CAR revealed an endothermic peak at 280 °C, corresponding to the melting point as reported in the literature [173], and a second one at 351 °C. Moreover, DSC analysis on AZ and AZCAR showed two different trends with two endothermic ones at 338 °C and 366 °C for AZ and an exothermic peak for AZCAR at 351 °C. Similar behavior is observed in the DTA profiles shown in Figure 6.4 (c).

6.5 Batch adsorption study

The adsorption capacity of AZCAR toward Pb^{2+} was investigated depending on the contact time (hours) between adsorbent and adsorbate, initial concentrations (mg L^{-1}) of adsorbate, amount (mg) of adsorbent, pH and ionic strength (mol L^{-1}). All adsorption experiments were performed at room temperature by placing a weighted amount (10 to 30 mg) of the AZCAR adsorbent material in an Erlenmeyer flask containing $Pb(NO_3)_2$ (30 to 70 mg L^{-1}) in KNO_3. This salt was used to fix the ionic strength ($0.001 \leq I \leq 0.7$ mol L^{-1}) and the MOPS buffer to fix the pH ($6.5 \leq pH \leq 7.9$). Higher or lower pH values were adjusted by adding small aliquots of standard NaOH or HNO_3 solutions, respectively. The solutions were mildly stirred (150 rpm) for the prefixed time using an orbital mixer (IKA˙HS 260 basic) before measuring Pb^{2+} concentrations (mg L^{-1}) in the supernatant by DPV.

The first phase of the adsorption study concerned the assessment of the time required to reach equilibrium between adsorbent and adsorbate. For this purpose, 20 mg of AZCAR was put in contact with a solution (26 mL) containing Pb^{2+} (30 mg L^{-1}), at pH = 5.9 and I = 0.15 mol L^{-1}. The amount of Pb^{2+} remaining in the solution was measured at prefixed times.

The adsorption capacity and removal rate (%) were calculated through the following reactions:

$$Q = \frac{(C_0 - C_f)V}{S} \tag{4.1}$$

$$R\% = \frac{(C_0 - C_f)100}{C_0} \tag{4.2}$$

where C_0 and C_f (mg L^{-1}) are the initial and final concentrations of the Pb^{2+} solutions, respectively. In equation (4.1), V (mL) is the volume of the solutions and S the amount (mg) of adsorbent. Q and $R\%$ values of the above-mentioned solution (26 mL), containing AZCAR and Pb^{2+} (30 mg L^{-1}), are given in Table 6.1. The trend of removal rate (%) *vs*. contact time (h) is shown in Figure 6.5. As can be seen, the $R\%$ values increase in the first 24 hours, and then remain constants. This test was repeated by varying the initial conditions (20 mg of AZCAR, 50 mg L^{-1} of Pb^{2+}, pH = 8.1, I = 0.7 mol L^{-1}), as described in Table 6.1. Once again, 24 hours was sufficient to achieve equilibrium between adsorbent and adsorbate. Therefore, all subsequent tests were performed by keeping AZCAR and Pb^{2+} in contact for 24 hours.

In regard to the speciation study and assessment of the sequestering ability of the Pb^{2+}-CAR system under different ionic strength and temperature conditions, widely described in Chapter 4, it was possible to precisely reduce the experimental measurements for batch tests. The different experimental parameters, pH, ionic

strength, amount of adsorbent and concentration of the adsorbate, were taken into account each time.
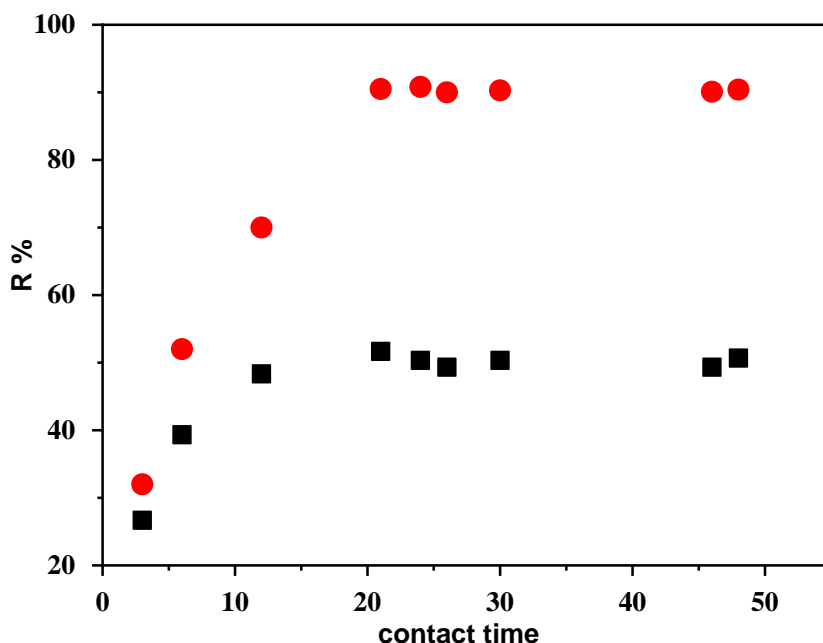
Figure 6.6. Removal rate % *vs.* contact time of the AZCAR toward Pb^{2+}.
Experimental conditions:
(■) 20 mg AZCAR, 30 mg L^{-1} Pb^{2+}, pH = 5.9 and I = 0.15 mol L^{-1},
(●) 20 mg AZCAR, 50 mg L^{-1} Pb^{2+}, pH = 8.1, I = 0.7 mol L^{-1}

In the first set of measurements, the pH was ranged from 5.5 to 9.1. As expected from previous speciation studies, an increase in pH resulted in a significant growth in the removal efficiency of AZCAR, with the $R\%$ value that varies from 64.0 (at pH = 5.52) to 99.4 (at pH = 9.12).

The ionic strength range ($0.001 \leq I/$ mol $L^{-1} \leq 0.7$) provides an opposite and less significant effect on the absorption capacity of the adsorbent. Therefore, a decrease in R % from 99.0 to 90.8 is observed as the ionic strength increases. The adsorption capacity of AZCAR is almost constant as its amount increases. This important

aspect highlights that the available active sites of AZCAR can be fully used at a low dosage at $7.75 \leq pH \leq 8.78$ and $I = 0.15$ mol L^{-1}. The adsorption capacity of the adsorbent enhances as the adsorbate concentration increases. In this case, the $R\%$ value ranges from 31.7 (at the lowest concentration of Pb^{2+} (30 mg L^{-1}) to 99.5 (at 70 mg L^{-1} of Pb^{2+}) at a given ionic strength ($I = 0.7$ mol L^{-1}) and pH (7.33). For instance, by changing both ionic strength ($I = 0.15$ mol L^{-1}) and pH (5.60) parameters, the adsorption capacity of AZCAR decreases to 21.0, despite the high concentration of Pb^{2+} (80 mg L^{-1}). The last two results were obtained by varying the adsorbent:adsorbate ratio and pH.

In addition, considering that the cost of polluted water decontamination can be reduced by trying to recycle the adsorbent material, desorption experiments were useful to evaluate its possible reuse. Indeed, since the low adsorption ability of AZCAR occurred for pH < 6.0, desorption tests were performed on samples 3 and 4, using HNO_3 up to pH ≈ 4.0. The metal resulted totally released in the solution. Therefore, to check the reuse capacity, the pH of the solutions was brought back to the starting one and the adsorption capacity was checked after 24 hours. These laboratory experiments were successfully managed, and AZCAR showed outstanding reuse capacity after the first cycle with negligible decrease in removal efficiency. Therefore, it can be considered a suitable adsorbent material for the effective Pb^{2+} removal from contaminated natural waters.

Table 6.1. Batch adsorption results.

Sample n.	Contact time (hours)	V solution (mL)	AZCAR mg	C_0 (Pb^{2+}) mg L^{-1}	pH	I mol L^{-1}	C_f (Pb^{2+}) mg L^{-1}	Q	R%
1	3	26	20	30	5.9	0.15	22.0	10.4	26.7
	6						18.2	15.3	39.3
	12						15.5	18.9	48.3
	21						14.5	20.1	51.7
	24						14.9	19.6	50.3
	26						15.2	19.2	49.3
	30						14.9	19.6	50.3
	46						15.2	19.2	49.3
	48						14.8	19.8	50.7
2	3	20	20	50	8.1	0.7	34	16	32
	6						24	26	52
	12						15	35	70
	21						475	45.3	90.5
	24						4.6	45.4	90.8
	26						5	45	90
	30						4.85	45.1	90.3
	46						4.95	45	90.1
	48						4.8	45.2	90.4
3	24	20	20	50	5.52	0.7	18	32	64.0
4	24	20	20	50	8.10	0.7	4.6	45.4	90.8
5	24	20	20	50	9.12	0.7	0.9	49.1	98.2
6	24	20	20	50	7.32	0.001	0.5	49.5	99.0
7	24	20	20	50	8.50	0.15	0.6	49.4	98.8
4	24	20	20	50	8.10	0.7	4.6	45.4	90.8
8	24	20	10	50	7.75	0.15	0.6	98.8	98.8
9	24	20	20	50	8.50	0.15	0.6	49.4	98.8
7	24	20	30	50	8.78	0.15	0.3	33.1	99.3
10	24	20	20	30	6.99	0.7	20.5	9.5	31.7
4	24	20	20	50	8.10	0.7	4.6	45.4	90.8
11	24	20	20	70	7.33	0.7	0.35	69.7	99.5
12	24	11	20	80	5.60	0.15	63.2	9.2	21.0
13	24	20	30	30	8.30	0.15	0.4	19.7	98.6
14	24	26	20	30	6.99	0.15	14.9	19.6	50.3

6.6 Final remarks and future perspectives

The speciation study performed on the Pb^{2+}-CAR system turned out of great importance in this thesis. The results, concerning the complexing and sequestering abilities of CAR toward the toxic metal cation, are described in Chapter 4 and exploited here.

Taking advantage of simulations of CAR sequestration, a CAR-based resin (AZCAR) was synthetized. The adsorption capacity of AZCAR was found to be mainly affected by the pH effect, with respect to the ionic strength and amount variations, confirming the trend obtained with the speciation studies.

This was employed to apply CAR molecule in an emerging analytical purpose, which regards the removal of heavy metals, such as Pb^{2+}, from natural waters. This budding aspect is given by the staggering growth and bioaccumulation of environmental pollutants, as the lead, and the main need to use natural materials for its removal from aquatic ecosystems.

However, the promising results reported in this Chapter need to be augmented by more thoroughly investigating desorption processes and possible reuse, as well as adsorptive capacities against other metals.

Chapter 7

Conclusions and future perspectives

Since the 1950s, an exponential number of studies have been published on the structure, role, function, and biological activity of carnosine under different experimental and clinical conditions. Further progress is needed to fully unveil the broad therapeutic potential of this dipeptide, to determine consequently how bioavailability is related to routes of administration, dose, and duration of treatment [9].

The comprehensive speciation study disclosed in this thesis could be of fundamental help in understanding the bioavailability of carnosine and its complex species under different conditions of ionic strength and temperature. The thermodynamic behavior of carnosine was analyzed by a synergistic combination of experimental techniques and supplemented by computational methods. Considering the therapeutic potential of this intriguing dipeptide, this detailed investigation of its acid-base properties provides a useful description of the different species in which it is distributed under conditions simulating natural systems.

On the basis of the speciation study, thermodynamic interaction parameters of carnosine and bivalent metal cations (M^{2+}) were explored over a wide range of ionic strength ($0.1 \leq I/\ mol\ L^{-1} \leq 1$) and temperature ($288.15 \leq T/K \leq 310.15$). Potentiometry was the main analytical technique used for these speciation studies in NaCl aqueous solutions, sometimes supported by UV-Vis spectrophotometry, ^{1}H

NMR and MS. In this way, structural information and coordination modes of the complex species were obtained. Sequestering ability of carnosine toward the metal cations was also assessed in conditions simulating physiological (pH = 7.4 and I = 0.15 mol L^{-1}) and seawater (pH = 8.1 and I = 0.7 mol L^{-1}) ones.

This exhaustive analysis made it possible to establish the best conditions of ionic strength and temperature under which the subsequently synthetized carnosine derivatives could be used. In fact, the easily modified carnosine molecule yielded the following two amide-containing products:

i)   ferrocenyl-carnosine (FcCAR),

ii)   pyrene-carnosine (PyCAR).

Both compounds were studied by potentiometry and UV-Vis spectrophotometry in NaCl aqueous solution at I = 0.15 mol L^{-1} and T = 298.15K. In this way, their acid-base behaviors were defined and compared with that of the progenitor carnosine. The complexing ability of FcCAR and PyCAR was also investigated toward Zn^{2+}, Cd^{2+}, Hg^{2+} and Pb^{2+} by UV-Vis spectrophotometry. Zn^{2+} and Cd^{2+} gave weak interactions with FcCAR and PyCAR, and, therefore, were not further considered.

The former, FcCAR, was investigated electrochemically as a metal probe. In particular, it was tested with respect to Mn^{2+}, Cu^{2+}, Hg^{2+} and Pb^{2+}. Promising results were obtained for the Hg^{2+}-FcCAR system on Screen-Printed Carbon Electrodes (SPCEs), on which a strategic modification was advanced to improve electrochemical performance. For this aim, MultiWalled CarbonNanotubes modified with cyclodextrins (MWCNT-CD) were used. This approach resulted in increased peak currents. However, further investigation is needed to evaluate possible interference with other metal cations or the type of interactions between FcCAR and MWCNT-CD.

The second analog, PyCAR, was designed as a luminescent metal sensor. To date, however, only a UV-Vis spectrophotometric study in NaCl aqueous solutions at I =

0.15 mol L^{-1} and T = 298.15 K has been performed to evaluate the strength of interactions with metal cations.

Furthermore, carnosine (CAR) was grafted on a commercial polyacrylamide/azlactone copolymer (AZ) and the resulting carnosine-based resin, AZCAR, was used for Pb^{2+} removal, showing good removal efficiency under conditions simulating natural waters.

Finally, we are critically considering the aforementioned key points for future perspectives, including:

  i)   Exploiting the physicochemical properties of FcCAR and PyCAR to synthetize fluorescent metal nanocluster (NCs) as potential organic dyes in bio-imaging [174].

  ii)   Evaluating the adsorption capacity of AZCAR with respect to other heavy metals.

The therapeutic potential of carnosine is widely described in the literature, even if its pharmaceutical use is limited by the degrading activity of human *carnosinases*, which greatly reduces the carnosine bioavailability [9]. Carnosine is a nontoxic and well-tolerated dipeptide with no known drug interactions or perilous side effects. In this scenario, different administration routes have also been tested, including intranasal, oral, intracerebroventricular, intraperitoneal, intravenous, intralateral cerebroventricular, intravitreal, intragastric, and intrathecal. The oral and intraperitoneal routes are the most widely used [9]. Interestingly, the antioxidant role of carnosine has also been tested in cataracts [175]. Currently, the only treatment for cataracts is surgical removal and subsequent replacement of the natural lens with an artificial one. Therefore, non-invasive techniques and potential drugs, as eye-drops, are needed for the treatment of cataracts. For this purpose, carnosine has also gradually drawn attention, so much so that it is considered an ideal candidate for ophthalmic therapy. However, carnosine is unable to penetrate into the eye as an eye-drop [175, 176].

To overcome these issues regarding the bioavailability of the dipeptide in biological tissues, several attempts have been done and new strategies are emerging in the literature [3, 9]. Some of these methods have already involved combining carnosine with other molecules or replacing it with carnosine-like properties compounds, such as anserine [22, 101, 177], N-acetyl-carnosine (NAC) [175, 176], a naturally occurring L-carnosine enantiomer, D-Carnosine and a reduced L-carnosine derivative, that is carnosinol [23, 177, 178].

Regarding drug delivery, laboratory experiments are underway to study the interactions between carnosine and amphiphilic cyclodextrins. In this scenario, combining carnosine with other molecules could also be helpful in conveying the actions of human dipeptidases and favoring the transport of carnosine in biological tissues with high metal content. Carnosine may act as a metal sequestering agent.

Finally, chemical derivatization of carnosine is a promising approach to obtain carnosinase-resistant therapeutic molecules. The dipeptide was modified either at the level of the amino group of the β-alanine residue or at the level of the carboxyl group of the L-histidine, depending on the importance of these two groups for the bioactivity [3]

In confirmation, considering that Mass Spectrometry has shown that carnosine interacts with some M^{2+} *via* the amino group of the β-alanine residue, we would like to pay attention to the carboxylic group of L-carnosine. It could be a skillfully modifiable target group to propose synthetic and clever carnosine derivatives, including for bio-sensing applications.

Acknowledgements

It would have been impossible to carry out this research project without the passionate input of my Ph.D. Supervisor Professor Claudia Foti. Without her support I could never have done it. I thank her for choosing me and her continuous loyalty.

I would like to express a sincere gratitude to my second scientific guide, Professor Ottavia Giuffrè.

A deep thanks goes to Doctor Antonino Mazzaglia, who also put me in touch with Professor Alex Fragoso, whom I thank because he gave me the opportunity to work in his group at the Department of Chemical Engineering of the Universitat Rovira I Virgili, Tarragona, Spain. There, I learned to live with myself. I took care of my sense of duty and discovered my strong sense of responsibility. There, I also learned that authentic relationships know no boundaries. During that period, I was found all the advice, suggestions and support of Professor Anna Piperno absolutely helpful. I thank her because she is a friendly source of inspiration. I also thank all the people, who gave a valuable support to the development of the topics discussed herein: Professor Angela Scala, Professor Massimiliano Cordaro, Professor Donatella Aiello, Professor Anna Napoli and Doctor Giuseppe Cassone. I also thank Professor Carmelo Sgarlata and Professor Gianluca Giorgi for the enjoyable time spent together in Catania and Erice, respectively.

A precious place in my heart is occupied by Prof. Maria Pia Ballato, whom I thank for always being by my side.

Finally, I must express the deepest gratitude to my family for the everyday unconditional love and encouragement, and… to my boyfriend, Stefano, for the numerous proofs of love shown to me in this special period.

References

1.   Solana-Manrique C, Sanz FJ, Martínez-Carrión G, Paricio N: **Antioxidant and Neuroprotective Effects of Carnosine: Therapeutic Implications in Neurodegenerative Diseases**. *Antioxidants (Basel)* 2022, **11**(848):1-17.

2.   She J, Fu L, Zheng X, Li J, Wang L, Yu B, Ju J: **Characterization of a new L-carnosine synthase mined from deep-sea sediment metagenome**. *Microbial Cell Factories* 2022, **21**(1):1-10.

3.   Chevalot I, Arab-Tehrany E, Husson E, Gerardin C: **Application of Carnosine and Its Functionalised Derivatives**. In: *Industrial Biotechnology of Vitamins, Biopigments, and Antioxidants.* 2016: 421-444.

4.   Branham ML, Singh P, Bisetty K, Sabela M, Govender T: **Preparation, Spectrochemical, and Computational Analysis of L-Carnosine (2-[(3-Aminopropanoyl)amino]-3-(1H-imidazol-5-yl)propanoic Acid) and Its Ruthenium (II) Coordination Complexes in Aqueous Solution**. *Molecules* 2011, **16**(12):10269-10291.

5.   Trombley PQ, Horning MS, Blakemore LJ: **Interactions between carnosine and zinc and copper: implications for neuromodulation and neuroprotection**. *Biochemistry (Mosc)* 2000, **65**(7):807-816.

6.   Holeček M: **Histidine in Health and Disease: Metabolism, Physiological Importance, and Use as a Supplement**. *Nutrients* 2020, **12**(3):1-20.

7.   Boldyrev AA, Aldini G, Derave W: **Physiology and pathophysiology of carnosine**. *Physiol Rev* 2013, **93**(4):1803-1845.

8.   Caruso G, Godos J, Castellano S, Micek A, Murabito P, Galvano F, Ferri R, Grosso G, Caraci F: **The Therapeutic Potential of Carnosine/Anserine Supplementation against Cognitive Decline: A Systematic Review with Meta-Analysis**. *Biomedicines* 2021, **9**(3):1-17.

9.   Caruso G: **Unveiling the Hidden Therapeutic Potential of Carnosine, a Molecule with a Multimodal Mechanism of Action: A Position Paper**. *Molecules* 2022, **27**(10):1-14.

10.   Yang H, Hou X, Xing L, Tian F: **Carnosine and bone (Review)**. *Molecular medicine reports* 2023, **27**(1):1-11.

11. Takahashi S, Anzai J-i: **Recent Progress in Ferrocene-Modified Thin Films and Nanoparticles for Biosensors**. *Materials* 2013, **6**(12):5742-5762.

12. Moriuchi T: **Helical Chirality of Ferrocene Moieties in Cyclic Ferrocene-Peptide Conjugates**. *European Journal of Inorganic Chemistry* 2022, **2022**(5):1-10.

13. Templeton DM, Ariese F, Cornelis R, Danielsson L-G, Muntau H, van Leeuwen HP, Lobinski R: **Guidelines for terms related to chemical speciation and fractionation of elements. Definitions, structural aspects, and methodological approaches (IUPAC Recommendations 2000)**. *Pure and Applied Chemistry* 2000, **72**(8):1453-1470.

14. Abate C, Foti C, Giuffrè O: **Removal of Hg^{2+} and CH_3Hg^+ by a polyphosphonate ligand from water**. *Journal of Physics: Conference Series* 2021, **1960**(1):1-8.

15. Carnamucio F, Foti C, Cordaro M, Giuffrè O: **Study on Metronidazole Acid-Base Behavior and Speciation with Ca^{2+} for Potential Applications in Natural Waters**. *Molecules* 2022, **27**(17):1-13.

16. Dissette V, Bignozzi CA, Valacchi G, Pecorelli A, Manfredini S, Vertuani S: **Evaluation of the Transepidermal Penetration of a Carnosine Complex in Gel Formulation by 3D Skin Models**. *Cosmetics* 2018, **5**(4):1-9.

17. Kawahara M, Tanaka KI, Kato-Negishi M: **Zinc, Carnosine, and Neurodegenerative Diseases**. *Nutrients* 2018, **10**(2):1-20.

18. Tang W, Liu H, Ooi TC, Rajab NF, Cao H, Sharif R: **Zinc carnosine: Frontiers advances of supplement for cancer therapy**. *Biomedicine & Pharmacotherapy* 2022, **151**:1-8.

19. Berezhnoy DS, Stvolinsky SL, Lopachev AV, Devyatov AA, Lopacheva OM, Kulikova OI, Abaimov DA, Fedorova TN: **Carnosine as an effective neuroprotector in brain pathology and potential neuromodulator in normal conditions**. *Amino Acids* 2019, **51**(1):139-150.

20. Karton A, O'Reilly RJ, Pattison DI, Davies MJ, Radom L: **Computational Design of Effective, Bioinspired HOCl Antioxidants: The Role of**

Intramolecular Cl$^+$ and H$^+$ Shifts. *Journal of the American Chemical Society* 2012, **134**(46):19240-19245.

21. Wojnarowicz A, Sharma PS, Sosnowska M, Lisowski W, Huynh TP, Pszona M, Borowicz P, D'Souza F, Kutner W: **An electropolymerized molecularly imprinted polymer for selective carnosine sensing with impedimetric capacity**. *J Mater Chem B* 2016, **4**(6):1156-1165.

22. Schön M, Mousa A, Berk M, Chia WL, Ukropec J, Majid A, Ukropcová B, de Courten B: **The Potential of Carnosine in Brain-Related Disorders: A Comprehensive Review of Current Evidence**. *Nutrients* 2019, **11**(6):1-26.

23. Chmielewska K, Dzierzbicka K, Inkielewicz-Stepniak I, Przybyłowska M: **Therapeutic Potential of Carnosine and Its Derivatives in the Treatment of Human Diseases**. *Chemical Research in Toxicology* 2020, **XXXX**:A-R.

24. Ali S, Rasul A, Latif N, Aleem SB, Zia R, Khan B: **Effect of Levo-Carnosine on Biomarkers of Oxidative Stress and Hepatotoxicity in Cisplatin-Treated Male Sprague Dawley Rats**. *Pakistan Armed Forces Medical Journal* 2022, **72**(4):1334-1338.

25. El-Ashmawy NE, Khedr EG, Doghish AS, Elballal MS: **Carnosine and crocin ameliorate oxidative stress in rats with rhabdomyolysis-induced acute kidney injury through upregulating HO-1 gene expression**. *Food Bioscience* 2022, **49**:1-11.

26. Kalyankar GD, Meister A: **Enzymatic synthesis of carnosine and related beta-alanyl and gamma-aminobutyryl peptides**. *J Biol Chem* 1959, **234**(12):3210-3218.

27. Winnick RE, Winnick T: **Carnosine-anserine synthetase of muscle I. Preparation and properties of soluble enzyme from chick muscle**. *Biochim Biophys Acta* 1959, **31**(1):47-55.

28. Drozak J, Veiga-da-Cunha M, Vertommen D, Stroobant V, Van Schaftingen E: **Molecular identification of carnosine synthase as ATP-grasp domain-containing protein 1 (ATPGD1)**. *J Biol Chem* 2010, **285**(13):9346-9356.

29. Ketabi S, Rahmani L: **Carbon nanotube as a carrier in drug delivery system for carnosine dipeptide: A computer simulation study**. *Materials Science & Engineering C* 2017, **73**:173-181.

30. Banerjee S, Poddar MK: **Carnosine research in relation to aging brain and neurodegeneration: A blessing for geriatrics and their neuronal disorders**. *Arch Gerontol Geriatr* 2020, **91**:1-10.

31. Hanson HT, Smith EL: **Carnosinase: an enzyme of swine kidney** *Journal of Biological Chemistry* 1949, **179**(2):789-801.

32. Perry TL, Hansen S, Love DL: **Serum-carnosinase deficiency in carnosinaemia**. *Lancet* 1968, **1**(7554):1229-1230.

33. Torreggiani A, Tamba M, Fini G: **Binding of copper(II) to carnosine: Raman and IR spectroscopic study**. *Biopolymers* 2000, **57**(3):149-159.

34. Hasanein P, Kazemian-Mahtaj A, Khodadadi I: **Bioactive peptide carnosin protects against lead acetate-induced hepatotoxicity by abrogation of oxidative stress in rats**. *Pharmaceutical Biology* 2016, **54**(8):1458-1464.

35. Jukić I, Kolobarić N, Stupin A, Matić A, Kozina N, Mihaljević Z, Mihalj M, Šušnjara P, Stupin M, Ćurić Ž B *et al*: **Carnosine, Small but Mighty-Prospect of Use as Functional Ingredient for Functional Food Formulation**. *Antioxidants* 2021, **10**(7):1-31.

36. Aldini G, de Courten B, Regazzoni L, Gilardoni E, Ferrario G, Baron G, Altomare A, D'Amato A, Vistoli G, Carini M: **Understanding the antioxidant and carbonyl sequestering activity of carnosine: direct and indirect mechanisms**. *Free Radic Res* 2021, **55**(4):321-330.

37. Derave W, De Courten B, Baba SP: **An update on carnosine and anserine research**. *Amino Acids* 2019, **51**(1):1-4.

38. Gaunitz F, Hipkiss AR: **Carnosine and cancer: a perspective**. *Amino Acids* 2012, **43**(1):135-142.

39. Shen F, Regmi D, Islam M, Raja Somu D, Merk V, Du D: **Effects of zinc and carnosine on aggregation kinetics of Amyloid-β40 peptide**. *Biochemistry and Biophysics Reports* 2022, **32**:1-7.

40. Radrezza S, Carini M, Baron G, Aldini G, Negre-Salvayre A, D'Amato A: **Study of Carnosine's effect on nude mice skin to prevent UV-A damage**. *Free Radical Biology and Medicine* 2021, **173**:97-103.

41. Pamplona R: **Advanced lipoxidation end-products**. *Chem Biol Interact* 2011, **192**(1-2):14-20.

42. Ihara H, Kakihana Y, Yamakage A, Kai K, Shibata T, Nishida M, Yamada KI, Uchida K: **2-Oxo-histidine-containing dipeptides are functional oxidation products**. *J Biol Chem* 2019, **294**(4):1279-1289.

43. Bertinaria M, Rolando B, Giorgis M, Montanaro G, Guglielmo S, Buonsanti MF, Carabelli V, Gavello D, Daniele PG, Fruttero R *et al*: **Synthesis, physicochemical characterization, and biological activities of new carnosine derivatives stable in human serum as potential neuroprotective agents**. *J Med Chem* 2011, **54**(2):611-621.

44. Medvidović-Kosanović M, Stanković Ex Šter A, Jozanović Horvat M, Drulak M, Ilić M: **Electrochemical and UV/VIS Study of L-Histidine and Its Complexes with Cobalt and Nickel**. *Croatica Chemica Acta* 2018, **91**(4):1-6.

45. Pal A, Ranjan Bhatta S, Thakur A: **Recent advances in the development of ferrocene based electroactive small molecules for cation recognition: A comprehensive review of the years 2010–2020**. *Coordination Chemistry Reviews* 2021, **431**:1-63.

46. Hu Y, Li X, Zhi X, Cong W, Huang B, Chen H, Wang Y, Li Y, Wang L, Fang C *et al*: **RANKL from bone marrow adipose lineage cells promotes osteoclast formation and bone loss**. *EMBO Rep* 2021, **22**(7):1-14.

47. Maeno M, Ito-Kato E, Suzuki N, Takada T, Takayama T, Ito K, Otsuka K: **Effect of beta-alanyl-L-histidinato zinc on the differentiation pathway of human periodontal ligament cells**. *Life Sci* 2004, **74**(20):2493-2504.

48. Ortiz M, Botero ML, Fragoso A, O'Sullivan CK: **Amperometric Detection of Creatinine in Clinical Samples Based on Gold Electrode Arrays Fabricated Using Printed Circuit Board Technology**. *Electroanalysis* 2020, **32**(12):3054-3059.

49.   Zuaznabar-Gardona JC, Fragoso A: **Electrochemistry of redox probes at thin films of carbon nano-onions produced by thermal annealing of nanodiamonds**. *Electrochimica Acta* 2020, **353**:1-12.

50.   Zuaznabar-Gardona JC, Fragoso A: **A wide-range solid state potentiometric pH sensor based on poly-dopamine coated carbon nano-onion electrodes**. *Sensors and Actuators, B: Chemical* 2018, **273**:664-671.

51.   Bartolome JP, Fragoso A: **Preparation and characterization of carbon nano-onions by nanodiamond annealing and functionalization by radio-frequency Ar/O_2 plasma**. *Fullerenes Nanotubes and Carbon Nanostructures* 2017, **25**(5):327-334.

52.   Wajs E, Molina-Ontoria A, Nielsen TT, Echegoyen L, Fragoso A: **Supramolecular solubilization of cyclodextrin-modified carbon nano-onions by host-guest interactions**. *Langmuir* 2015, **31**(1):535-541.

53.   Skoog DA, Holler FJ, Crouch SR: **Principles of instrumental analysis**, 6th ed. edn: Thomson Brooks/Cole; 2007.

54.   Skoog DA, West DM, Holler FJ, Crouch SR: **Fundamentals of analytical chemistry**, 9th ed. edn: Brooks/Cole, Cengage Learning; 2014.

55.   De Robertis A, De Stefano C, Giuffré O, Sammartano S: **Binding of carboxylic ligands by protonated amines**. *Journal of the Chemical Society, Faraday Transactions* 1996, **92**(21):4219-4226.

56.   Frassineti C, Alderighi L, Gans P, Sabatini A, Vacca A, Ghelli S: **Determination of protonation constants of some fluorinated polyamines by means of ^{13}C NMR data processed by the new computer program HypNMR2000. Protonation sequence in polyamines**. *Anal Bioanal Chem* 2003, **376**(7):1041-1052.

57.   Silverstein RM, Webster FX, Kiemle DJ, Bryce DL: **Identificazione spettrometrica di composti organici**, 3 ed. edn: Casa Editrice Ambrosiana; 2016.

58.   Radionova A, Filippov I, Derrick PJ: **In pursuit of resolution in time-of-flight mass spectrometry: A historical perspective**. *Mass Spectrom Rev* 2016, **35**(6):738-757.

59.   Cai Y-H, Lin C-H, Wang Y-S: **Theoretical study of the impact of ion acceleration parameters on the mass resolving power in linear MALDI time-of-flight mass spectrometry**. *International Journal of Mass Spectrometry* 2022, **471**:1-8.

60.   Aiello D, Carnamucio F, Cordaro M, Foti C, Napoli A, Giuffrè O: **Ca^{2+} Complexation With Relevant Bioligands in Aqueous Solution: A Speciation Study With Implications for Biological Fluids**. *Frontiers in Chemistry* 2021, **9**:1-15.

61.   Aiello D, Siciliano C, Mazzotti F, Di Donna L, Risoluti R, Napoli A: **Protein Extraction, Enrichment and MALDI MS and MS/MS Analysis from Bitter Orange Leaves (*Citrus aurantium*)**. *Molecules* 2020, **25**(7):1-19.

62.   Giuffrè O, Aiello D, Chillè D, Napoli A, Foti C: **Binding ability of arsenate towards Cu^{2+} and Zn^{2+}: thermodynamic behavior and simulation under natural water conditions**. *Environmental Science: Processes & Impacts* 2020, **22**(8):1731-1742.

63.   Liu J, Xu Y, Liu S, Yu S, Yu Z, Low SS: **Application and Progress of Chemometrics in Voltammetric Biosensing**. *Biosensors (Basel)* 2022, **12**(7):1-19.

64.   Torre R, Costa-Rama E, Nouws HPA, Delerue-Matos C: **Screen-Printed Electrode-Based Sensors for Food Spoilage Control: Bacteria and Biogenic Amines Detection**. *Biosensors (Basel)* 2020, **10**(10):1-26.

65.   Łysoń M, Górska A, Paczosa-Bator B, Piech R: **Nimesulide Determination on Carbon Black-Nafion Modified Glassy Carbon Electrode by Means of Adsorptive Stripping Voltammetry**. *Electrocatalysis* 2021, **12**(6):641-649.

66.   Zuaznabar-Gardona JC, Fragoso A: **Development of highly sensitive IgA immunosensors based on co-electropolymerized L-DOPA/dopamine carbon nano-onion modified electrodes**. *Biosensors and Bioelectronics* 2019, **141**:1-7.

67.   Frisch MJ, al. e: **Gaussian 09**. *Gaussian, Inc, Wallingford, CT* 2009.

68.   Becke AD: **Density-functional exchange-energy approximation with correct asymptotic behavior**. *Physical Review A* 1988, **38**(6):3098-3100.

69.   Lee C, Yang W, Parr RG: **Development of the Colle-Salvetti correlation-energy formula into a functional of the electron density**. *Physical Review B* 1988, **37**(2):785-789.

70.   Stephens PJ, Devlin FJ, Chabalowski CF, Frisch MJ: **Ab Initio Calculation of Vibrational Absorption and Circular Dichroism Spectra Using Density Functional Force Fields**. *The Journal of Physical Chemistry* 1994, **98**(45):11623-11627.

71.   Vosko SH, L. W, Nusair M: **Accurate Spin-Dependent Electron Liquid Correlation Energies for Local Spin Density Calculations: A Critical Analysis**. *Canadian Journal of Physics* 1980, **58**:1200-1211.

72.   Tomasi J, Mennucci B, Cammi R: **Quantum Mechanical Continuum Solvation Models**. *Chemical Reviews* 2005, **105**(8):2999-3094.

73.   Chandra AK, Goursot A: **Calculation of Proton Affinities Using Density Functional Procedures: A Critical Study**. *The Journal of Physical Chemistry* 1996, **100**(28):11596-11599.

74.   Wolken JK, Tureček F: **Proton affinity of uracil. A computational study of protonation sites**. *Journal of the American Society for Mass Spectrometry* 2000, **11**(12):1065-1071.

75.   Kühne TD, Iannuzzi M, Del Ben M, Rybkin V, Seewald P, Stein F, Laino T, Khaliullin RZ, Schütt O, Schiffmann Fea: **P2K: An electronic structure and molecular dynamics software package - Quickstep: Efficient and accurate electronic structure calculations**. *The Journal of chemical physics 2020* 2020, **152**(19):1-47.

76.   Goedecker S, Teter M, Hutter J: **Separable dual-space Gaussian pseudopotentials**. *Physical Review B* 1996, **54**(3):1703-1710.

77.   Perdew JP, Burke K, Ernzerhof M: **Generalized Gradient Approximation Made Simple**. *Physical Review Letters* 1996, **77**(18):3865-3868.

78.   Grimme S, Antony J, Ehrlich S, Krieg H: **A consistent and accurate ab initio parametrization of density functional dispersion correction (DFT-D) for the 94 elements H-Pu**. *The Journal of chemical physics* 2010, **132**(15):154104.

79.   Grimme S, Ehrlich S, Goerigk L: **Effect of the damping function in dispersion corrected density functional theory**. *Journal of Computational Chemistry* 2011, **32**(7):1456-1465.

80.   Bussi G, Donadio D, Parrinello M: **Canonical sampling through velocity rescaling**. *The Journal of chemical physics 2007* 2007, **126**(1):1-7.

81.   De Stefano C, Sammartano S, Mineo P, Rigano C: **Computer Tools for the Speciation of Natural Fluids**. In., A. Gianguzza, E. Pellizzetti and S. Sammartano, Kluwer Academic Publishers, Dordrecht, The Netherlands, edn edn: Marine Chemistry: An Environmental Analytical Chemistry Approach; 1997: 71-83.

82.   Gans P, Sabatini A, Vacca A: **Determination of equilibrium constants from spectrophometric data obtained from solutions of known pH : The program pHab**. *Annali Di Chimica* 1999, **89**:45-49.

83.   Frassineti C, Ghelli S, Gans P, Sabatini A, Moruzzi MS, Vacca A: **Nuclear magnetic resonance as a tool for determining protonation constants of natural polyprotic bases in solution**. *Anal Biochem* 1995, **231**(2):374-382.

84.   Alderighi L, Gans P, Ienco A, Peters D, Sabatini A, Vacca A: **Hyperquad simulation and speciation (HySS): a utility program for the investigation of equilibria involving soluble and partially soluble species**. *Coordination Chemistry Reviews* 1999, **184**(1):311-318.

85.   De Stefano C, Gianguzza A, Milea D, Pettignano A, Sammartano S: **Sequestering ability of polyaminopolycarboxylic ligands towards dioxouranium(VI) cation**. *Journal of Alloys and Compounds* 2006, **424**:93-104.

86.   De Stefano C, Milea D, Porcino N, Sammartano S: **Speciation of Phytate Ion in Aqueous Solution. Sequestering Ability toward Mercury(II) Cation in NaClaq at Different Ionic Strengths**. *Journal of Agricultural and Food Chemistry* 2006, **54**(4):1459-1466.

87.   De Stefano C, Milea D, Porcino N, Sammartano S: **Speciation of phytate ion in aqueous solution. Cadmium(II) interactions in aqueous NaCl at different ionic strengths**. *Anal Bioanal Chem* 2006, **386**(2):346-356.

88.   De Stefano C, Gianguzza A, Piazzese D, Porcino N, Sammartano S: **Sequestration of biogenic amines by alginic and fulvic acids**. *Biophys Chem* 2006, **122**(3):221-231.

89.   Giacalone A, Gianguzza A, Pettignano A, Sammartano S: **Sequestration of organometallic compounds by natural organic matter. Binding of trimethyltin(IV) by fulvic and alginic acids**. *Applied Organometallic Chemistry* 2006, **20**:706-717.

90.   Crea F, De Stefano C, Foti C, Milea D, Sammartano S: **Chelating agents for the sequestration of mercury(II) and monomethyl mercury(II)**. *Curr Med Chem* 2014, **21**(33):3819-3836.

91.   Gianguzza A, Giuffrè O, Piazzese D, Sammartano S: **Aqueous solution chemistry of alkyltin(IV) compounds for speciation studies in biological fluids and natural waters**. *Coordination Chemistry Reviews* 2012, **256**(1):222-239.

92.   Mirzahosseini A, Molaei M, Mazák K, Pálla T, Köteles I, Varró N, Mándity I, Noszál B: **Species-specific acid-base characterization of carnosine and homocarnosine using nuclear magnetic resonance**. *Chemical Physics Letters* 2022, **808**:1-6.

93.   Lytkin AI, Barannikov VP, Badelin VG, Krutova ON: **Enthalpies of acid dissociation of l-carnosine in aqueous solution**. *Journal of Thermal Analysis and Calorimetry* 2020, **139**(6):3683-3689.

94.   Martell AE, Smith RM, Motekaitis RJ: **Critically Selected Stability Constants of Metal Complexes**. In: *National Institute of Standard Technology, Garthersburg, MD*. 2004.

95.   May PM, Murray K: **Database of Chemical Reactions Designed To Achieve Thermodynamic Consistency Automatically**. *Journal of Chemical & Engineering Data* 2001, **46**(5):1035-1040.

96.   Pettit LD, Powell KJ: **IUPAC Stability Constants Database, Academic Software**. In: *IUPAC*. 2001.

97.   Abate C, Cassone G, Cordaro M, Giuffrè O, Mollica-Nardo V, Ponterio RC, Saija F, Sponer J, Trusso S, Foti C: **Understanding the behaviour of carnosine in aqueous solution: an experimental and quantum-based computational investigation on acid–base properties and complexation**

mechanisms with Ca²⁺ and Mg²⁺. *New Journal of Chemistry* 2021, **45**(43):20352-20364.

98. Jozanović Horvat M, Sakac N, Jakobovic D, Sak-Bosnar M: **Analytical Characterization and Quantification of Histidine Dipeptides, Carnosine and Anserine by Modeling of Potentiometric Titration Data**. *International Journal of Electrochemical Science* 2015, **10**:5787-5799.

99. Abate C, Aiello D, Cordaro M, Giuffrè O, Napoli A, Foti C: **Binding ability of L-carnosine towards Cu²⁺, Mn²⁺ and Zn²⁺ in aqueous solution**. *Journal of Molecular Liquids* 2022, **368**:1-12.

100. Peiretti PG, Medana C, Visentin S, Giancotti V, Zunino V, Meineri G: **Determination of carnosine, anserine, homocarnosine, pentosidine and thiobarbituric acid reactive substances contents in meat from different animal species**. *Food Chem* 2011, **126**(4):1939-1947.

101. Jozanović Horvat M, Medvidović-Kosanović M, Sak-Bosnar M: **Voltammetric Characterization and Determination of Histidine Dipeptides - Carnosine and Anserine**. *International Journal of Electrochemical Science* 2015, **10**:6548-6557.

102. Surdy P, Rubini P, Buzás N, Henry B, Pellerito L, Gajda T: **Interaction of dimethyltin(IV)²⁺ cation with gly-gly, gly-his, and some related ligands. A new case of a metal ion able to promote peptide nitrogen deprotonation in aqueous solution**. *Inorganic Chemistry* 1999, **38**(2):346-352.

103. Gajda T, Henry B, Delpuech J-J: **Multinuclear NMR and potentiometric study on tautomerism during protonation and zinc(II) complex formation of some imidazole-containing peptide derivatives**. *Journal of the Chemical Society, Perkin Transactions 2* 1994(1):157-164.

104. Kaden T, Zuberbühler A: **256. Zusammensetzung und Struktur von Komplexen des einwertigen Kupfers mit Imidazolderivaten**. *Helvetica Chimica Acta* 1966, **49**(7):2189-2195.

105. Daniele PG, Prenesti E, Ostacoli G: **Ultraviolet–circular dichroism spectra for structural analysis of copper(II) complexes with aliphatic and aromatic ligands in aqueous solution**. *Journal of the Chemical Society, Dalton Transactions* 1996(15):3269-3275.

106. Sóvágó I, Farkas E, Gergely A: **Studies on transition-metal–peptide complexes. Part 7. Copper(II) complexes of dipeptides containing L-histidine**. *Journal of the Chemical Society, Dalton Transactions* 1982(11):2159-2163.

107. Farkas E, Sóvágó I, Gergely A: **Studies on transition-metal–peptide complexes. Part 8. Parent and mixed-ligand complexes of histidine-containing dipeptides**. *Journal of the Chemical Society, Dalton Transactions* 1983(8):1545-1551.

108. Daniele PG, Prenesti E, Zelano V, Ostacoli G: **Chemical relevance of the copper(II)-l-carnosine system in aqueous solution: A thermodynamic and spectrophotometric study**. *Spectrochimica Acta Part A: Molecular Spectroscopy* 1993, **49**(9):1299-1306.

109. Brookes G, Pettit LD: **Thermodynamics of formation of complexes of copper(II) and nickel(II) ions with glycylhistidine, β-alanylhistidine, and histidylglycine**. *Journal of the Chemical Society, Dalton Transactions* 1975(20):2112-2117.

110. Lenz GR, Martell AE: **Metal Chelates of Some Sulfur-Containing Amino Acids**. *Biochemistry* 1964, **3**(6):745-750.

111. Bonomo RP, Bruno V, Conte E, De Guidi G, Mendola DL, Maccarrone G, Nicoletti F, Rizzarelli E, Sortino S, Vecchio G: **Potentiometric, spectroscopic and antioxidant activity studies of SOD mimics containing carnosine**. *Dalton Transactions* 2003(23):4406-4415.

112. Daniele PG, Amico P, Ostacoli G: **Heterobinuclear Cu(II) L-carnosine complexes with Cd(II) or Zn(II) in aqueous solution**. *Inorganica Chimica Acta* 1982, **66**:65-70.

113. Agarwal RP, Perrin DD: **Stability constants of complexes of copper(II) ions with some histidine peptides**. *Journal of the Chemical Society, Dalton Transactions* 1975(3):268-272.

114. Medvidovic-Kosanović M, Stanković A, Drulak M, Sak-Bosnar M: **Potentiometric, electrochemical and UV/VIS investigation of a copper (II) complex with β-alanyl-L-histidine**. *International Journal of Electrochemical Science* 2018, **13**(6):5323-5332.

115. Baes CF, Mesmer RE: **The Hydrolysis of Cations**. New York, USA: John Wiley & Sons; 1976.

116. Foti C, Giuffrè O: **Interaction of Ampicillin and Amoxicillin with Mn^{2+}: A Speciation Study in Aqueous Solution**. *Molecules* 2020, **25**(14):1-16.

117. Powell KJ, Brown PL, Byrne RH, Gajda T, Hefter G, Sjöberg S, Wanner H: **Chemical speciation of environmentally significant metals with inorganic ligands Part 2: The Cu^{2+}-OH^-, Cl^-, CO_3^{2-}, SO_4^{2-}, and PO_4^{3-} systems (IUPAC Technical Report)**. *Pure and Applied Chemistry* 2007, **79**(5):895-950.

118. Powell KJ, Brown PL, Byrne RH, Gajda T, Hefter G, Leuz A-K, Sjöberg S, Wanner H: **Chemical speciation of environmentally significant metals with inorganic ligands. Part 5: The Zn^{2+} + OH^-, Cl^-, CO_3^{2-}, SO_4^{2-}, and PO_4^{3-} systems (IUPAC Technical Report)**. *Pure and Applied Chemistry* 2013, **85**(12):2249-2311.

119. Powell KJ, Brown PL, Byrne RH, Gajda T, Hefter G, Leuz A-K, Sjöberg S, Wanner H: **Chemical speciation of environmentally significant metals with inorganic ligands. Part 4: The Cd^{2+} + OH^-, Cl^-, CO_3^{2-}, SO_4^{2-}, and PO_4^{3-} systems (IUPAC Technical Report)**. *Pure and Applied Chemistry* 2011, **83**(5):1163-1214.

120. Powell KJ, Brown PL, Byrne R, Gajda T, Hefter G, Sjöberg S, Wanner H: **Chemical speciation of environmentally significant heavy metals with inorganic ligands part 1: The Hg^{2+}- Cl^-, OH^-, CO_3^{2-}, SO_4^{2-}, and PO_4^{3-} aqueous systems**. *Pure and Applied Chemistry* 2005, **77**(4):739-800.

121. Powell KJ, Brown PL, Byrne RH, Gajda T, Hefter G, Leuz A-K, Sjöberg S, Wanner H: **Chemical speciation of environmentally significant metals with inorganic ligands. Part 3: The Pb^{2+} + OH^-, Cl^-, CO_3^{2-}, SO_4^{2-}, and PO_4^{3-} systems (IUPAC Technical Report)**. *Pure and Applied Chemistry* 2009, **81**(12):2425-2476.

122. Gaggelli E, Valensin G: **^1H and ^{13}C NMR relaxation investigation of the calcium complex of β-alanyl-L-histidine (carnosine) in aqueous solution**. *Journal of the Chemical Society, Perkin Transactions 2* 1990(3):401-406.

123. Dutka TL, Lamboley CR, McKenna MJ, Murphy RM, Lamb GD: **Effects of carnosine on contractile apparatus Ca^{2+} sensitivity and sarcoplasmic**

reticulum Ca²⁺ release in human skeletal muscle fibers. *J Appl Physiol (1985)* 2012, **112**(5):728-736.

124. Boldyrev AA: **Problems and perspectives in studying the biological role of carnosine**. *Biochemistry (Mosc)* 2000, **65**(7):751-756.

125. Beneduci A, Corrente GA, Marino T, Aiello D, Bartella L, Di Donna L, Napoli A, Russo N, Romeo I, Furia E: **Insight on the chelation of aluminum(III) and iron(III) by curcumin in aqueous solution**. *Journal of Molecular Liquids* 2019, **296**:1-10.

126. Ommati MM, Jamshidzadeh A, Heidari R, Sun Z, Zamiri MJ, Khodaei F, Mousapour S, Ahmadi F, Javanmard N, Shirazi Yeganeh B: **Carnosine and Histidine Supplementation Blunt Lead-Induced Reproductive Toxicity through Antioxidative and Mitochondria-Dependent Mechanisms**. *Biol Trace Elem Res* 2019, **187**(1):151-162.

127. He J, Rössner N, Hoang MTT, Alejandro S, Peiter E: **Transport, functions, and interaction of calcium and manganese in plant organellar compartments**. *Plant Physiology* 2021, **187**(4):1940-1972.

128. Baran EJ: **Metal complexes of carnosine**. *Biochemistry (Mosc)* 2000, **65**(7):789-797.

129. Chmielewska K, Dzierzbicka K, Inkielewicz-Stępniak I, Przybyłowska M: **Therapeutic Potential of Carnosine and Its Derivatives in the Treatment of Human Diseases**. *Chemical Research in Toxicology* 2020, **33**(7):1561-1578.

130. Hewlings S, Kalman D: **A Review of Zinc-L-Carnosine and Its Positive Effects on Oral Mucositis, Taste Disorders, and Gastrointestinal Disorders**. *Nutrients* 2020, **12**(3):1-12.

131. Suzuki H, Fujiwara M, Kodama H, Kamikonya N, Niwa Y, Yoshimura N, Kunimoto R, Takaki H, Yamakado K: **Protective Effect of Polaprezinc and Hyperbaric Oxygen Therapy on Radiation-induced Small Intestinal Damage in Mice**. *In Vivo* 2022, **36**(5):2218-2223.

132. Mineo P, Vitalini D, La Mendola D, Rizzarelli E, Scamporrino E, Vecchio G: **Electrospray mass spectrometric studies of L-carnosine (beta-alanyl-L-histidine) complexes with copper(II) or zinc ions in aqueous solution**. *Rapid Commun Mass Spectrom* 2002, **16**(7):722-729.

133. Anke M, Ihnat M, Stoeppler M: **Elements and their compounds in the environment: occurrence, analysis and biological relevance**, 2nd completely rev. and enl. ed. edn. Weinheim: Wiley-VCH; 2004.

134. Gupta P, Rahm CE, Jiang D, Gupta VK, Heineman WR, Justin G, Alvarez NT: **Parts per trillion detection of heavy metals in as-is tap water using carbon nanotube microelectrodes**. *Analytica Chimica Acta* 2021, **1155**:1-11.

135. Chowdhury IR, Chowdhury S, Mazumder MAJ, Al-Ahmed A: **Removal of lead ions (Pb^{2+}) from water and wastewater: a review on the low-cost adsorbents**. *Applied Water Science* 2022, **12**(8):1-33.

136. Lakshmi R, Raja V, Sabarathinam C, Sekar C, Neelakantan MA: **Industrial impact on groundwater quality with special reference to Cr^{2+} and Pb^{2+} in coastal aquifers**. *Environmental Monitoring and Assessment* 2021, **193**:1-17.

137. Ghosh S, Othmani A, Malloum A, Ke Christ O, Onyeaka H, AlKafaas SS, Nnaji ND, Bornman C, Al-Sharify ZT, Ahmadi S *et al*: **Removal of mercury from industrial effluents by adsorption and advanced oxidation processes: A comprehensive review**. *Journal of Molecular Liquids* 2022, **367**:1-19.

138. Walters JG, Ahmed S, Terrero Rodríguez IM, O'Neil GD: **Trace Analysis of Heavy Metals (Cd, Pb, Hg) Using Native and Modified 3D Printed Graphene/Poly(Lactic Acid) Composite Electrodes**. *Electroanalysis* 2020, **32**(4):859-866.

139. Bretti C, Cigala RM, Crea F, Foti C, Sammartano S: **Solubility and activity coefficients of acidic and basic non-electrolytes in aqueous salt solutions. 3. Solubility and activity coefficients of adipic and pimelic acids in NaCl(aq), $(CH_3)_4NCl(aq)$ and $(C_2H_5)_4NI(aq)$ at different ionic strengths and at t = 25 °C**. *Fluid Phase Equilibria* 2008, **263**(1):43-54.

140. Raposo J, Zuloaga O, Olazabal Ma, Madariaga J: **Development of a Modified Bromley Methodology for the estimation of ionic media effects on solution equilibria: Part 5. The chemical model of boric acid in aqueous solution at 25°C and comparison with arsenious acid**. *Fluid Phase Equilibria* 2003, **207**:81-95.

141.	Pettit LD, Powell K: **The IUPAC stability constants database**. *Chem Int* 2006, **56**:14-15.

142.	Dobbie H, Kermack WO: **Complex-formation between polypeptides and metals. 2. The reaction between cupric ions and some dipeptides**. *Biochem J* 1955, **59**(2):246-257.

143.	Sunatsuki Y, Motoda Y, Matsumoto N: **Copper(II) complexes with multidentate Schiff-base ligands containing imidazole groups: Ligand-complex or self-complementary molecule?** *Coordination Chemistry Reviews* 2002, **226**:199-209.

144.	Moustafa EM, Korany M, Mohamed NA, Shoeib T: **Carnosine complexes and binding energies to some biologically relevant metals and platinum containing anticancer drugs**. *Inorganica Chimica Acta* 2014, **421**:123-135.

145.	Wang C-Z, Ichiyanagi H, Sakaguchi K, Feng X, Elsegood MRJ, Redshaw C, Yamato T: **Pyrene-Based Approach to Tune Emission Color from Blue to Yellow**. *The Journal of Organic Chemistry* 2017, **82**(14):7176-7182.

146.	Kim S-Y, Kim M-J, Ahn M, Lee K-M, Wee K-R: **Systematic energy band gap control of pyrene based donor-acceptor-donor molecules for efficient chemosensor**. *Dyes and Pigments* 2021, **191**:1-9.

147.	Ponniah S J, Barik SK, Thakur A, Ganesamoorthi R, Ghosh S: **Triazolyl Alkoxy Fischer Carbene Complexes in Conjugation with Ferrocene/Pyrene as Sensory Units: Multifunctional Chemosensors for Lead(II), Copper(II), and Zinc(II) Ions**. *Organometallics* 2014, **33**(12):3096-3107.

148.	Medvidović-Kosanović M: **Potentiometric, electrochemical and UV/VIS investigation of a copper (II) complex with β-alanyl-L-histidine**. *International Journal of Electrochemical Science* 2018, **13**:5323-5332.

149.	Sipa K, Brycht M, Leniart A, Urbaniak P, Nosal-Wiercińska A, Pałecz B, Skrzypek S: **β-Cyclodextrins incorporated multi-walled carbon nanotubes modified electrode for the voltammetric determination of the pesticide dichlorophen**. *Talanta* 2018, **176**:625-634.

150.   Arman A, Sağlam Ş, Üzer A, Apak R: **Electrochemical determination of nitroaromatic explosives using glassy carbon/multi walled carbon nanotube/polyethyleneimine electrode coated with gold nanoparticles**. *Talanta* 2022, **238**(Pt 1):1-9.

151.   Hu Y, Wang C, Zhao P, Zhang L, Fei J, Xie Y: **A novel catechin electrochemical sensor based on a two-dimensional MOFs material derivative Zn doped carbon nanosheets and multi-walled carbon nanotubes composite film**. *Talanta* 2022, **246**:1-7.

152.   Mazzaglia A, Scala A, Sortino G, Zagami R, Zhu Y, Sciortino MT, Pennisi R, Pizzo MM, Neri G, Grassi G *et al*: **Intracellular trafficking and therapeutic outcome of multiwalled carbon nanotubes modified with cyclodextrins and polyethylenimine**. *Colloids and Surfaces B: Biointerfaces* 2018, **163**:55-63.

153.   Cardiano P, Fazio E, Lazzara G, Manickam S, Milioto S, Neri F, Mineo PG, Piperno A, Lo Schiavo S: **Highly untangled multiwalled carbon nanotube@polyhedral oligomeric silsesquioxane ionic hybrids: Synthesis, characterization and nonlinear optical properties**. *Carbon* 2015, **86**:325-337.

154.   Trapani M, Scala A, Mineo PG, Pistone A, Díaz-Moscoso A, Fragoso A, Monsù Scolaro L, Mazzaglia A: **Thiolated amphiphilic β-cyclodextrin-decorated gold colloids: Synthesis, supramolecular nanoassemblies and controlled release of dopamine**. *Journal of Molecular Liquids* 2021, **336**:1-10.

155.   Mazzaglia A, Di Natale G, Tosto R, Scala A, Sortino G, Piperno A, Casaletto MP, Riminucci A, Giuffrida ML, Mineo PG *et al*: **KLVFF oligopeptide-decorated amphiphilic cyclodextrin nanomagnets for selective amyloid beta recognition and fishing**. *Journal of Colloid and Interface Science* 2022, **613**:814-826.

156.   Piperno A, Mazzaglia A, Scala A, Pennisi R, Zagami R, Neri G, Torcasio SM, Rosmini C, Mineo PG, Potara M *et al*: **Casting Light on Intracellular Tracking of a New Functional Graphene-Based MicroRNA Delivery System by FLIM and Raman Imaging**. *ACS Applied Materials and Interfaces* 2019, **11**(49):46101-46111.

157.   Takenaka H, Sato S, Takenaka S: **Electrochemical Detection of Duplex DNA Using Intercalation-Triggered Decomplexation of Ferrocene with β-Cyclodextrin**. *Electroanalysis* 2013, **25**(8):1827-1830.

158.   Trapani M, Mazzaglia A, Piperno A, Cordaro A, Zagami R, Castriciano MA, Romeo A, Monsù Scolaro L: **Novel Nanohybrids Based on Supramolecular Assemblies of Meso-tetrakis-(4-sulfonatophenyl) Porphyrin J-aggregates and Amine-Functionalized Carbon Nanotubes**. In: *Nanomaterials.* vol. 10; 2020: 1-14.

159.   Lavastre I, Besançon J, Brossiert P, Moise C: **The use of metallocenic esters of n-hydroxysuccinimide for metallohapten synthesis**. *Applied Organometallic Chemistry* 1991, **5**(3):143-149.

160.   Nikolić D, Poleksić V, Skorić S, Tasić A, Stanojević S, Rašković B: **The European Chub (Squalius cephalus) as an indicator of reservoirs pollution and human health risk assessment associated with its consumption**. *Environmental Pollution* 2022, **310**:1-14.

161.   Blanco A, Pignata ML, Lascano HR, Salazar MJ, Rodriguez JH: **Lead uptake and translocation pathways in soybean seedlings: the role of ion competition and transpiration rates**. *Environ Sci Pollut Res Int* 2021, **28**(16):20624-20636.

162.   Kumar KY, Muralidhara HB, Nayaka YA, Balasubramanyam J, Hanumanthappa H: **Hierarchically assembled mesoporous ZnO nanorods for the removal of lead and cadmium by using differential pulse anodic stripping voltammetric method**. *Powder Technology* 2013, **239**:208-216.

163.   Es'haghi Z, Heidari T, Mazloomi E: **In situ pre-concentration and voltammetric determination of trace lead and cadmium by a novel ionic liquid mediated hollow fiber-graphite electrode and design of experiments via Taguchi method**. *Electrochimica Acta* 2014, **147**:279-287.

164.   Tosato M, Lazzari L, Marco VD: **Revisiting Lead(II)-1,4,7,10-tetraazacyclododecane-1,4,7,10-tetraacetic Acid Coordination Chemistry in Aqueous Solutions: Evidence of an Underestimated Thermodynamic Stability**. *ACS Omega* 2022, **7**(18):15596-15602.

165. Radi S, Toubi Y, El-Massaoudi M, Bacquet M, Degoutin S, Mabkhot YN: **Efficient extraction of heavy metals from aqueous solution by novel hybrid material based on silica particles bearing new Schiff base receptor**. *Journal of Molecular Liquids* 2016, **223**:112-118.

166. Beaugeard V, Muller J, Graillot A, Ding X, Robin J-J, Monge S: **Acidic polymeric sorbents for the removal of metallic pollution in water: A review**. *Reactive and Functional Polymers* 2020, **152**:1-20.

167. Politayeva NA, Smyatskaya YA, Dolbnya IV, Kasobov LS, Rakhimov DB, Zaripova DA: **Research of pH influence on sorption properties of sorbents on a basis of residual biomass of microalgae Chlorella sorokiniana and duckweed Lemna minor**. 2019, **124**(E3S Web Conf.):1-4.

168. https://www.thermofisher.com/order/catalog/product/53110#/53110.

169. Kushwaha N, Kushwaha S: **Synthetic approaches and biological significance of oxazolone moieties: A review**. *Biointerface Research in Applied Chemistry* 2022, **12**(5):6460-6486.

170. Barreca D, Neri G, Scala A, Fazio E, Gentile D, Rescifina A, Piperno A: **Covalently immobilized catalase on functionalized graphene: effect on the activity, immobilization efficiency, and tetramer stability**. *Biomaterials Science* 2018, **6**(12):3231-3240.

171. Neri G, Scala A, Barreca F, Fazio E, Mineo PG, Mazzaglia A, Grassi G, Piperno A: **Engineering of carbon based nanomaterials by ring-opening reactions of a reactive azlactone graphene platform**. *Chemical Communications* 2015, **51**(23):4846-4849.

172. Piperno A, Scala A, Risitano F, Grassi G: **Oxazol-5-(4H)-Ones. Part 1. Synthesis and Reactivity as 1,3-dipoles**. *Current Organic Chemistry* 2014, **18**(21):2691-2710.

173. Vranes M, Panić J, Tot A, Papović S, Gadžurić S, Podlipnik C, Bester-Rogac M: **From amino acids to dipeptide: The changes in thermal stability and hydration properties of β-alanine, L-histidine and L-carnosine**. *Journal of Molecular Liquids* 2021, **328**:1-13.

174. Li H, Chen J, Huang H, Feng J-J, Wang A-J, Shao L-X: **Green and facile synthesis of l-carnosine protected fluorescent gold nanoclusters for cellular imaging**. *Sensors and Actuators B: Chemical* 2016, **223**:40-44.

175. Dubois VD, Bastawrous A: **N-acetylcarnosine (NAC) drops for age-related cataract**. *Cochrane Database Syst Rev* 2017, **2**(2):1-16.

176. Wang L, Liu W, Huang X: **An approach to revolutionize cataract treatment by enhancing drug probing through intraocular cell line**. *Libyan J Med* 2018, **13**(1):1-10.

177. Rezzani R, Favero G, Ferroni M, Lonati C, Moghadasian MH: **A carnosine analog with therapeutic potentials in the treatment of disorders related to oxidative stress**. *PLoS One* 2019, **14**(4):1-18.

178. Anderson EJ, Vistoli G, Katunga LA, Funai K, Regazzoni L, Monroe TB, Gilardoni E, Cannizzaro L, Colzani M, De Maddis D *et al*: **A carnosine analog mitigates metabolic disorders of obesity by reducing carbonyl stress**. *J Clin Invest* 2018, **128**(12):5280-5293.